UC Berkeley
UC Berkeley Electronic Theses and Dissertations

Title
Halogen-Based Plasma Etching of Novel Field-Effect Transistor Gate Materials

Permalink
https://escholarship.org/uc/item/4kr1v34v

Author
Kiehlbaugh, Kasi Michelle

Publication Date
2009

Peer reviewed|Thesis/dissertation

eScholarship.org Powered by the California Digital Library
University of California

Halogen-Based Plasma Etching of Novel Field-Effect Transistor Gate Materials

by

Kasi Michelle Kiehlbaugh

A dissertation submitted in partial satisfaction of the

requirements for the degree of

Doctor of Philosophy

in

Chemical Engineering

in the

Graduate Division

of the

University of California, Berkeley

Committee in charge:

Professor David B. Graves, Chair
Professor Jeffrey A. Reimer
Professor Michael A. Lieberman

Fall 2009

Halogen-Based Plasma Etching of Novel Field-Effect Transistor Gate Materials

© 2009

by Kasi Michelle Kiehlbaugh

Abstract

Halogen-Based Plasma Etching of Novel Field-Effect Transistor Gate Materials

by

Kasi Michelle Kiehlbaugh

Doctor of Philosophy in Chemical Engineering

University of California, Berkeley

Professor David B. Graves, Chair

Vacuum Beam Studies of Ruthenium Etching

Ru is known to have two volatile oxidation products, RuO_3 and RuO_4, although the etch rate is negligible when Ru is exposed to an O_2 plasma discharge. The introduction of a small amount of additive gas, such as Cl_2, has been shown to increase the Ru etch rate sixfold. The reason for this dramatic shift in etching is poorly understood, primarily because it is difficult if not impossible to study plasma-surface interactions in a plasma environment. The unique capabilities of the beam system have made it possible to explore the mechanism of Ru etching. It has been shown that under 500 eV Ar^+ ion bombardment, the addition of O radicals lowered the etch rate by a factor of 2.5. This process was relatively insensitive to temperature over the range studied (room temperature to ~175°C). It was also shown that O radicals alone spontaneously etched Ru at a very slow rate over the entire temperature range.

Statistical Analysis of Polysilicon Etching and Gate Profile Evolution in Dual-Doped Polysilicon Gates

Polysilicon gate etching for the 90nm lithography node and below requires extremely precise control of the gate CD and profile. Generally speaking, the current requirement for Gate CD control is that the 3 sigma should less than ~5nm for all gates, including across the chip, across the wafer, wafer-to-wafer, lot-to-lot, and tool-to-tool variations. Similarly, for gate sidewall angle control, the 3 sigma angle variation should be less than ~1 degree, inclusive of all sources of variation. This is particularly challenging for technologies which employ dual-doped gates, since the chemistry and physics of the etching process induces a different profile evolution between gates with different doping.

The goal of this project was to identify a parameter space where the differences in gate profile evolution across different polysilicon dopant types were minimized. Blanket etch rates and patterned wafers were used to determine the effect of different gate etch process variables on the gate profile. The materials studied were undoped polysilicon and polysilicon that had been doped with P, As, Sb, and B. Prediction models were created for the blanket etch rate studies that were used to optimize the processing conditions and to propose some simple mechanisms that identify which species are adsorbed on the surface.

DEDICATION

To going downstream…

TABLE OF CONTENTS

Dedication i
Table of Contents ii
List of Figures iv
List of Tables vii
Acknowledgments ix
Chapter 1: Introduction 1
Plasma Fundamentals 1
Plasma Etching 1
Novel Materials: High-κ Dielectrics and Metal Gates 2
Plasma Beam Systems 4
Chapter 2: Experimental Methods 6
System Overview 6
Main Chamber 7
Sample Carousel 7
Modulated Beam Mass Spectrometry 9
Mechanical Pumps 11
Pressure Measurement 13
Gas Containment and Delivery 18
Quartz Crystal Microbalance 20
Ion Gun and Faraday Cup 20
Inductively Coupled Plasma Radical Source 21
Surface Wave Radical Source 22
Chapter 3: Characterization of the System 26
Residual Gas Analysis 26
Modulated-Beam Mass Spectroscopy 27
Characterization of the Ion Flux From the Ion Source 28
Characterization of the Ion Flux From the Surface Wave Radical Source 29
Etch Rate Measurements 30
Sample Temperature Control 31
Temperature Dependence of QCM 32
Chapter 4: Preliminary Vacuum Beam Studies of Ruthenium Etching 35
Introduction 35
Experimental Results and Discussion 36
Conclusions 39
Chapter 5: A Statistical Analysis of Polysilicon Etching and Gate Profile Evolution in Dual-Doped Polysilicon Gates 40
Background 40
Experimental Methods 44
Designed Experiment #1: Factorial Design 44
Fractional Factorial 44
Doped wafers 47
Undoped wafers 51

Full factorial 53
Doped wafers 54
Undoped wafers 57
Residual Analysis 59
Test of Normality Assumption 60
Doped wafers 60
Undoped wafers 61
Test of Equal Variance Assumption 62
Doped wafers 62
Undoped wafers 66
Inclusion of a covariate 70
Uniformity analysis 72
Designed Experiment #2: Box-Behnken Response Surface Design 79
P-doped etch rate 82
As-doped etch rate 82
Sb-doped etch rate 82
B-doped etch rate 82
Undoped etch rate 82
P-doped etch uniformity 83
As-doped etch uniformity 83
Sb-doped etch uniformity 83
B-doped etch uniformity 84
Undoped etch uniformity 84
Designed Experiment #3: Gate Profile Studies as a Function of Power and CHF3 94
CHF3 flow rate 95
Source Power 99
Conclusions 103
References 105
Appendix 110
Full Factorial with covariate for doped wafers 110
Full Factorial with covariate for undoped wafers 117
Full Factorial Uniformity analysis for doped wafers 124
Full Factorial Uniformity analysis for undoped wafers 131
Designed Experiment #2 Etch Rate 138
P-doped wafers 138
As-doped wafers 144
Sb-doped wafers 150
B-doped wafers 156
Undoped wafers 162
Designed Experiment #2 Uniformity 168
P-doped wafers 168
As-doped wafers 174
Sb-doped 180
B-doped wafers 186
Undoped wafers 192

LIST OF FIGURES

Figure 1: (a) anisotropic and (b) isotropic etching profiles 2
Figure 2: MOSFET device scaling[7] 2
Figure 3: Schematic of a metal-oxide-semiconductor field effect transistor (MOSFET)[7]..... 3
Figure 4: Top cross-section view of the experimental apparatus. P=turbomolecular pump, QMS=quadropole mass spectrometer, S=sample, C=carousel, CB=beam chopper blade, W=view port, G=gas supply, V=gate valve. Original drawing courtesy of Dr. John Coburn. 6
Figure 5: Cross-sectional side view of the chamber showing the carousel, dewar, and ion gun. Courtesy of Dr. John Coburn. 8
Figure 6: Three-dimensional computer-generated representation of a stable ion path.[23] ... 10
Figure 7: NEMA 5-15 (left) and NEMA 6-15 (right) grounded connectors for mechanical pumps. 12
Figure 8: Cross-sectional view (left) and side view (right) of a Granville-Phillips Series 275 Convectron Gauge 13
Figure 9: Granville-Phillips Series 303 Vacuum Process Controller Model B 15
Figure 10: Granville-Phillips Series 307 Vacuum Gauge Controller 15
Figure 11: Granville-Phillips nude Bayard-Alpert-type Ionization Gauge 16
Figure 12: (a) Granville-Phillips 274 Glass Bayard-Alpert type Ionization Gauge and (b) Granville-Phillips 355 Micro-Ion Gauge 17
Figure 13: Size comparison between Granville-Phillips 274 Glass Bayard-Alpert type Ionization Gauge (left) and Granville-Phillips 355 Micro-Ion Gauge (right) 17
Figure 14: Gas cabinet and manifold for hazardous gases. Inert gases occupy the outside panel. Two of the three gas lines are clearly visible inside the cabinet. 19
Figure 15: HP 5334A Universal Counter 20
Figure 16: Cross-sectional side view of the Faraday cup.[27] Its position on the carousel is indicated in Figure 5. 21
Figure 17: Keithley Model 6485 5-1/2 digit Picoammeter with 10fA Resolution 21
Figure 18: Cross-sectional view of the inductively coupled plasma (ICP) radical source.[27] 22
Figure 19: Photograph of surface wave plasma source with an ignited Ar plasma 23
Figure 20: Residual gas background in vacuum beam system. Gas load was primarily water vapor and pump oil adsorbed on chamber walls. 26
Figure 21: MBMS detection of step input of Ar 28
Figure 22: Effect of raster value on current density from the ion gun 29
Figure 23: Current density measured from surface wave radical source as a function of microwave power 30
Figure 24: Example of QCM etch rate measurements. (a) 500 eV Ar^+ and (b) 1000 eV Ar^+ 31
Figure 25: Sample temperature dependence on heater power 32
Figure 26: Temperature dependent behavior of QCM 33
Figure 27: QCM temperature calibration curve for deviation from room temperature (a) from vendor and (b) measured experimentally 34
Figure 28: Sputter yield of Ru as a function of temperature in the presence of O radicals 36
Figure 29: Raw QCM signal as a function of time for a Ru-coated QCM crystal exposed to O radicals and Ar^+ ions 37

Figure 30: Spontaneous etch rate of Ru in the presence of O radicals as a function of temperature 38
Figure 31: QCM traces of Ru etching in the presence of O radicals and O radicals combined with Ar^+ ions as a function of time for a range of temperatures 39
Figure 32: Illustration of dual-doped gate structure[7] 40
Figure 33: TEM images from four wafers with different doping characteristics and different sidewall angles 41
Figure 34: Typical endpoint detection trace of the three gate etch steps when simultaneously etching polysilicon of different doping types. EPD=endpoint detection.[76] 43
Figure 35: Half normal plot for the fractional factorial doped wafer etch rate data 48
Figure 36: Half normal plot for the fractional factorial undoped wafer etch rate data 51
Figure 37: Half normal plot for the full factorial doped wafer etch rate data 54
Figure 38: Half normal plot for the full factorial undoped wafer etch rate data 57
Figure 39: Residual by predicted plots for (a) doped and (b) undoped wafers 59
Figure 40: Plots of the studentized residuals as a function of starting film thickness for the (a) doped and (b) undoped wafers 70
Figure 41: Improved residuals as a function of starting thickness after the addition of the starting thickness covariate to the model for the (a) doped and (b) undoped wafers 72
Figure 42: Contour plot of the surface generated by the prediction equations for the doped:undoped etch rate ratio showing the effect of source power and CHF3. He/O2=1 75
Figure 43: Contour plot of the surface generated by the prediction equations for the doped:undoped etch rate ratio showing the effect of source power and CHF3. He/O2=-1. 76
Figure 44: Optimal settings for simultaneously minimizing the etch rate differences and minimizing the across-wafer variance. Desirability weights: d:un=1 and integration statistic=.5. 78
Figure 45: Region of the optimum found by overlying the d:un and uniformity equations... 79
Figure 46: Graphical representation of factor levels for a Box-Behnken design for three factors. 81
Figure 47: Response surface plots of the etch rate as a function of CHF3 and He/O2 for phosphorus- and antimony-doped polysilicon at low, mid, and high settings of the source power. Left column is P-doped film at (a) 250 W, (b) 325 W, and (c) 400 W. Right column is Sb-doped film at (d) 250 W, (e) 325 W, and (f) 400 W 85
Figure 48: Response surface plots of the etch rate as a function of CHF3 and He/O2 for arsenic-doped and undoped polysilicon at low, mid, and high settings of the source power. Left column is As-doped film at (a) 250 W, (b) 325 W, and (c) 400 W. Right column is undoped film at (d) 250 W, (e) 325 W, and (f) 400 W 86
Figure 49: Response surface plots of the etch rate as a function of CHF3 and He/O2 for boron-doped polysilicon at low, mid, and high settings of the source power: (a) 250 W, (b) 325 W, and (c) 400 W. 87
Figure 50: Contour plots of etch rate ratio as a function of source power and CHF3. From left to right for each row: 20, 60, and 100 sccm He/O2. From top to bottom: P:un, As:un, Sb:un, and B:un. 90
Figure 51: Optimal settings for simultaneously minimizing the etch rate differences and minimizing the across-wafer variance for phosphorus-doped films. Desirability weights: P:un=1 and integration statistic=.5. 91
Figure 52: Optimal settings for simultaneously minimizing the etch rate differences and minimizing the across-wafer variance for arsenic-doped films. Desirability weights: As:un=1 and integration statistic=.5. 92

Figure 53: Optimal settings for simultaneously minimizing the etch rate differences and minimizing the across-wafer variance for antimony-doped films. Desirability weights: Sb:un=1 and integration statistic=.5 93
Figure 54: Optimal settings for simultaneously minimizing the etch rate differences and minimizing the across-wafer variance for boron-doped films. Desirability weights: B:un=1 and integration statistic=.5 94
Figure 55: Sidewall angle as a function of CHF3 flow rate for all dopant cases 95
Figure 56: Sidewall angle as a function of CHF3 flow rate for phosphorus doped samples.. 96
Figure 57: Sidewall angle as a function of CHF3 flow rate for arsenic doped samples 97
Figure 58: Sidewall angle as a function of CHF3 flow rate for antimony doped samples..... 98
Figure 59: Sidewall angle as a function of source power for all dopant cases 99
Figure 60: Sidewall angle as a function of source power for phosphorus doped samples.... 100
Figure 61: Sidewall angle as a function of source power for arsenic doped samples 101
Figure 62: Sidewall angle as a function of source power for antimony doped samples..... 102
Figure 63: SIMS profile of phosphorus dopant distribution within the gate structure. "As implanted" refers to the condition before annealing, not to the chemical species arsenic. 103

LIST OF TABLES

Table 1: High and low settings for each of the four factors studied in the fractional factorial design 45
Table 2: Design matrix for fractional factorial study of etch rate. Highlighted run #5 represents the current process on record (POR). 45
Table 3: Etch rate results of Designed Experiment #1. Etch rate is in units of Å/s and the factor levels have been coded for ease of analysis. Randomized order. 46
Table 4: Table of contrasts for fractional factorial doped wafer etch rate data showing which terms are potentially significant and any confounded terms..... 48
Table 5: JMP output for least squares regression analysis of fractional factorial doped wafers reduced model..... 50
Table 6: Table of contrasts for fractional factorial undoped wafer etch rate data showing which terms are potentially significant and any confounded terms. 51
Table 7: JMP output for least squares regression analysis of fractional factorial undoped wafers reduced model 52
Table 8: Etch rate results of foldover portion of Designed Experiment #1. Etch rate is in units of Å/s and the factor levels have been coded for ease of analysis. Randomized order. 53
Table 9: Table of contrasts for the full factorial doped wafer etch rate data showing which terms are potentially significant 55
Table 10: JMP output for least squares regression analysis of full factorial doped wafer reduced model..... 56
Table 11: Table of contrasts for the full factorial undoped wafer etch rate data showing which terms are potentially significant..... 57
Table 12: JMP output for least squares regression analysis of full factorial undoped wafer reduced model..... 59
Table 13: JMP output testing the normality assumption for the residuals of the doped wafer model 61
Table 14: JMP output testing the normality assumption for the residuals of the undoped wafer model..... 62
Table 15: JMP output testing the assumption of equal variance for the residuals of the doped wafer model..... 65
Table 16: JMP output testing the assumption of equal variance for the residuals of the undoped wafer model..... 69
Table 17: Final model for the doped wafer etch data from the full factorial design, including starting thickness as a covariate..... 71
Table 18: Final model for the undoped wafer etch data from the full factorial design, including starting thickness as a covariate..... 71
Table 19: Final model for the doped wafer uniformity, including starting thickness as a covariate 73
Table 20: Final model for the undoped wafer uniformity, including starting thickness as a covariate 74
Table 21: Factor settings for the three factors studied in the Box-Behnken response surface design 80

Table 22: Box-Behnken design matrix and resulting etch rates for wafers doped with P, As, Sb, B, and no dopant. The runs are listed in the randomized order in which they were run.81
Table 23: Box-Behnken prediction models for the five film types 83
Table 24: Box-Behnken prediction models for the etch rate uniformity for the five film types. 84

ACKNOWLEDGMENTS

I would like to acknowledge the support of the following people:

- Mark, my family
- Dave Graves, John Coburn, Harold Winters, Dave Fraser, Mike Lieberman, Jeff Reimer
- Joe Vegh, Yoshie Kimura and Gary Lee, Dustin Nest, Mark Goldman, Monica Titus, Yuki Sakiyama, Misha Sorokin, Dave Humbird, Dave Hsu, Mark Nierode, Matt Radtke, Yassine Kabouzi
- Class of 2002, David Durkee, Jeff Nye, Enrique Iglesia, Arup Chakraborty, Henrik Wallman
- Paul Zimmerman, Mike Rowell
- Pie Queens, Matt Tsang, Hank Ibser, Jo Adamkewicz, Kath Ratcliff, Ethan Schlenker, BTP, Hang Time, Classy
- Eric Tonnis, Mike Vyvoda, Mark Kiehlbauch, Frank Greer, Gowri Kota, Adam Thorsness
- Jim Bernhart, Isis, Darren Rhodes
- Matt Owen, Amish Patel, Brad Holmes, Sam Wilcke, Erica Worthington, Tim Zimmerman
- Sarah Stewart, Jack Hamson
- Victor Wu, Diane Euser
- Dr. Sue Bell, Dr. Carol Morrison, Dr. Stephen Langer, Dr. Mark Balabanis, Bethany Williams
- SRC, Ginny Wiggins, NSF, EPA, TI, Steve Vitale, Chris Borst, Allen Bowling
- Hans Gabathuler, Pfeiffer
- Aileen Harris, Eric Granlund, Henry Chan, Steve Hoagland, Yi-Min Hsieh, Barbara Harris, Trish Schaible, Stacey Shulman, Rocio Sanchez, Angela Wilkes
- Jerry Kiser, Steve Willett, Ken Kardell, Byron Braasch, Don Reimer, Dennis McDermott, Ellen Hargus, Thelda Delamarter, John Kennedy, Mike Ortmann

CHAPTER 1: INTRODUCTION

Plasma-assisted processing is an important technology in integrated circuit (IC) fabrication. As many as one-third of the hundreds of processing steps utilize the unique, low-temperature reactivity of partially ionized plasma discharges.[1] These steps include etching, thin film deposition, pattern development, doping, and photoresist removal. I focused on etching.

PLASMA FUNDAMENTALS

A plasma discharge is created when a gas is ionized, either fully or partially, liberating electrons from their bound state to atoms and molecules. The resulting highly reactive atomic and molecular radicals, ions, free electrons, and neutral feedstock species make up the plasma discharge. The positively- and negatively-charged components in the discharge are able to move independently, making the plasma electrically conductive and thus strongly responsive to electromagnetic fields.

Fully-ionized plasmas, found abundantly in nature (i.e., the sun, lightning, flames, and auroras) are in thermal equilibrium, meaning all the components of the plasma are at the same temperature and all the molecules are fully ionized. In contrast, the low-pressure discharges of interest to the semiconductor manufacturing community are only partially ionized and the plasma density is typically only a small fraction of the neutral gas density. Partially ionized discharges are in a non-equilibrium state and cannot sustain themselves without externally-supplied electrical power. The mobile electrons receive the bulk of the applied electrical power, meaning the electron temperature greatly exceeds the temperature of the rest of the species in the discharge. This temperature difference makes it possible for the near-room temperature reactive radicals to provide activation energy to a surface without heating it. Additional activation energy is provided to the substrate by the positively-charged ions that are accelerated toward all grounded surfaces by the large potential gradient at the physical boundaries of the plasma.

PLASMA ETCHING

It is the combination of reactive neutrals (atoms and molecular radicals) and directional ion bombardment that make plasma-assisted processing so powerful and unique.[2-5] The synergistic etching effect of reactive neutrals and ion bombardment is ten times higher than either pure chemical etching or pure sputtering by ion bombardment alone.[6] This behavior is seen in systems where the etch products are volatile and can be thought of as ion-assisted chemical etching. Accelerating the desorption of product species near the ion impact site gives plasma-assisted processes the ability to selectively create highly anisotropic features, where etching occurs only in one direction because of the combined effects of the chemical etch, sidewall redeposition, and directional ion bombardment. The anisotropy of plasma-assisted etching has clear processing advantages over other techniques, such as liquid-based "wet" etching or gas-phase etching with molecular gases where the etch rates are isotropic, or occurring in all directions equally (Figure 1).[1]

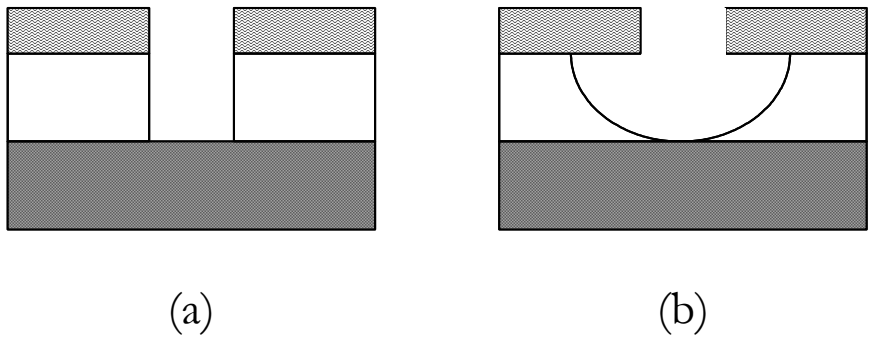

Figure 1: (a) anisotropic and (b) isotropic etching profiles

Interestingly, the continual increase in microprocessor speeds that even the general public has come to expect would not be possible without the anisotropic etching capabilities of plasma discharges. Performance enhancements such as faster switching speeds and lower power dissipation have primarily come from simply making the size of the individual transistor smaller. For a given device generation, all geometries in the transistor are scaled down by a single scaling factor (Figure 2), while the power-supply voltage is typically kept constant.[7] As the dimensions are reduced, the fabrication tolerances on those dimensions are also proportionally reduced, making the feature undercutting that is characteristic of isotropic etching techniques completely unacceptable.[1]

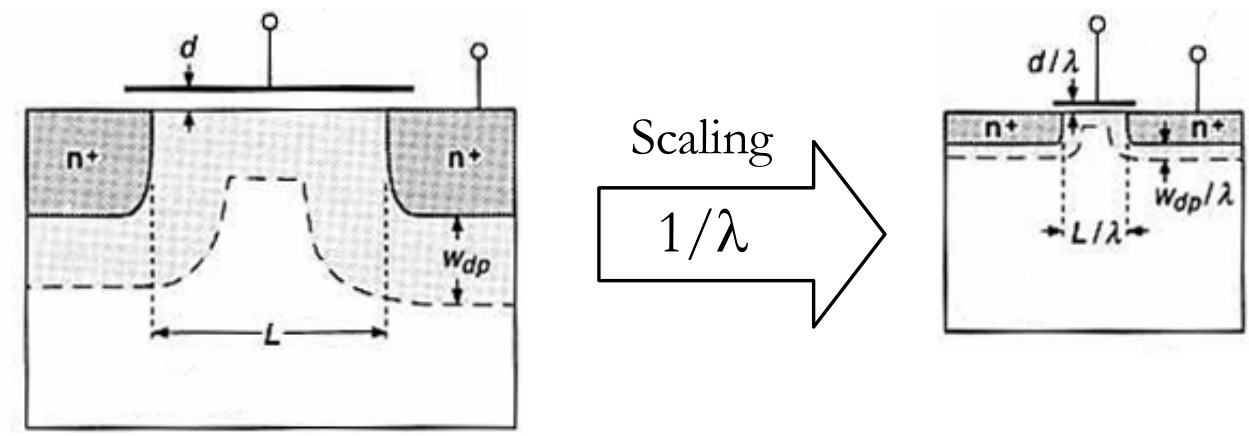

Figure 2: MOSFET device scaling[7]

NOVEL MATERIALS: HIGH-κ DIELECTRICS AND METAL GATES

Continued scaling not only requires the precisely-defined structures that plasma-assisted etching can produce, it also requires the industry to explore new materials that will allow the scaling to continue beyond the physical limits of the silicon-based technologies that have been the industry standard since its beginning.[8] For example, the silicon dioxide layer that forms the gate dielectric region of the metal-oxide-semiconductor field-effect transistor (MOSFET—Figure 3) has been thinned down from ~100 nm in the 1970s to 1.2 nm in today's state-of-the-art devices. Unfortunately, direct

tunneling of electrons from the gate electrode into the conduction band of the underlying silicon channel becomes a serious problem below this length scale, leading to catastrophic dielectric breakdown and device failure.[9]

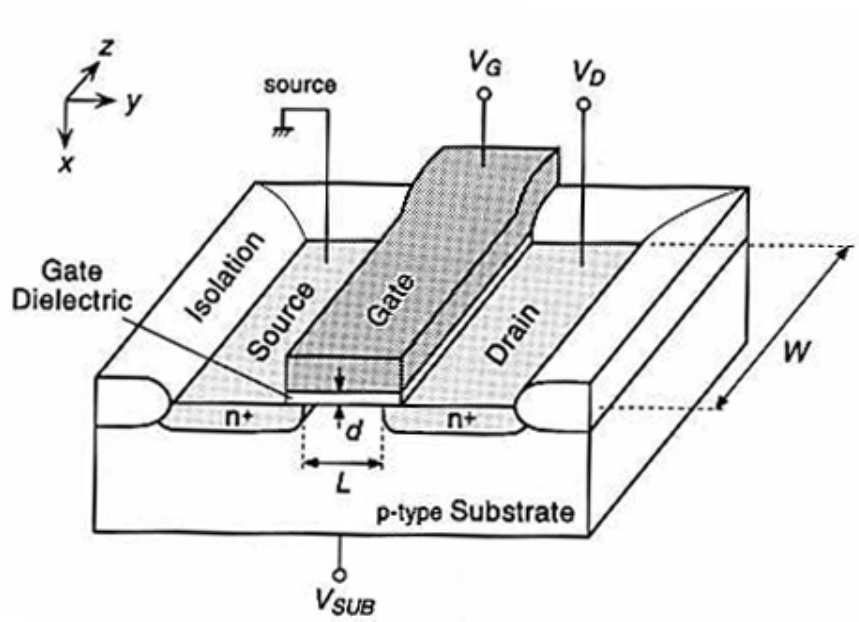

Figure 3: Schematic of a metal-oxide-semiconductor field effect transistor (MOSFET)[7]

Since the capacitance of the dielectric layer is both directly proportional to its dielectric constant κ and inversely proportional to its thickness t, one seemingly straightforward way to address this scaling problem would be to switch to a dielectric material with a higher dielectric constant than SiO_2. The physical thickness of the dielectric could be increased without affecting the capacitance, and hence the design and scaling parameters of the circuit.[7] As seen in Figure 3, the gate dielectric layer has interfaces with both the silicon substrate below and the gate electrode above. For the transistor to function as designed, these interfaces must be thermodynamically stable within the temperature range used to fabricate the device.

The current gate electrode material is negatively-doped polycrystalline silicon (n^+ poly-Si), which is fairly unreactive with the underlying SiO_2 dielectric layer. Unfortunately, the same is not true for the high-κ films that are currently being investigated, most of which are known to react with n^+ poly-Si to form unwanted metal silicides that negatively affect device performance.[10] The need for chemical stability at the high-κ/electrode interface is one of several issues that has led to focused research efforts on metal gate materials.

Replacing the n^+ poly-Si with an appropriately chosen metal electrode can eliminate the interfacial reactivity problem. Unsuitable candidate-metals can be predicted with thermodynamics and eliminated: if an oxide of the metal exists and has a highly negative Gibbs energy of formation, the metal will reduce the underlying dielectric and the metal/dielectric interface will not be stable. Oxygen solubility is another indicator of metal/dielectric interface stability. Metals with a high

oxygen solubility cause redistribution of the oxygen within the dielectric, again creating an unstable interface. By taking into account these thermodynamic considerations, a candidate gate metal can be selected that will have a stable interface with the underlying oxide.[11]

Thermodynamic stability is not enough to qualify a given metal as a potential gate material. The field of acceptable metals is further narrowed by eliminating those that are not compatible with the processes used to build the device. For example, the metal must be thermally stable upon annealing. It must also produce volatile etch products so that it can be etched in a plasma discharge via the ion-assisted chemical etching mechanism.

Metals offer several advantages over poly-Si. The direct tunneling mechanism mentioned above in regard to dielectric breakdown also negatively affects the n-doped poly-Si gate. Electron tunneling draws dopant atoms from the poly-Si bulk toward the dielectric interface, depleting the bulk gate region of negative charge-carriers and affecting the capacitive behavior of the device. Metal gates are a promising alternative because they suffer virtually no depletion.[7, 10]

In addition to providing stable interfaces on high-κ materials and eliminating gate depletion effects, metal gate materials exhibit low resistivity, which increases signal transmission speed. They also have work functions in the appropriate range that align well with the conduction and valence band edges of Si. Candidate metals and conducting metal oxides include Ru, RuO_2, Ir, IrO_2, Pt, Ta, TaN, TaC, Ti, TiN, W, Mo, MoN, Hf, HfN, Ni, and Co. Preliminary data on Ru etching will be presented in Chapter 4.

PLASMA BEAM SYSTEMS

One of the main reasons that experimental evidence in support of proposed surface reaction mechanisms is not more abundant in the literature is that the complicated, highly coupled nature of the plasma environment makes it almost impossible to take the kind of measurements that would be necessary. Measuring volatile reaction products directly is not possible since any species desorbing from the surface will reenter the plasma discharge where it will likely be ionized or broken down into radicals. The short mean free path and highly reactive discharge environment precludes the use of nearly all conventional surface science techniques.[12] This fact underscores the need for fundamental studies that can tease out the details of the surface chemistry and make it possible to approach process design with chemical insight rather than brute force.

At the industrial level, most process development is highly empirical.[12] Too much going on inside the reactor to decouple the contribution that each parameter or species has on the outcome. Plasma physics, gas-phase chemistry, surface physics and surface chemistry all play a role.[1] The desire to reduce the complexity of the system and in doing so, make it possible to answer surface-related questions like the ones raised by the ruthenium system led researchers to develop beam-based ultra-high vacuum (UHV) systems where surface science measurements are possible.[13-17]

These beam systems were designed with the knowledge that reactive neutral radicals (both atomic and molecular) and energetic positive ions are the most important species in plasma-assisted etching processes, and so they imitate the plasma with a beam of neutral radicals and an independently controllable beam of inert ions that are directed at the surface of interest. All studies in such a beam

system focus on the spontaneous reaction of neutral species on or with a solid surface that produces volatile products, or the related system where the reaction is stimulated by energetic positive ion bombardment.[12] Beam-based studies are not limited to etching reactions. It is also possible to investigate radical recombination,[18, 19] plasma-assisted deposition,[20] and surface functional group modifications[21, 22] in this type of system.

The radical beam is created by generating a plasma discharge in a small external source that is separated from the UHV chamber by one or more differential pumping orifices. In a similar manner, the ions are generated externally in a commercial ion gun that is also separated from the chamber by a small orifice. Inert ions are used to simplify the interpretation of the results by limiting the source of chemical reactivity to the neutral radical beam. The volatile products that are formed can be detected in several ways; the most common of which is modulated beam mass spectrometry.[12]

In the type of beam system described above, the researcher has complete control over what the surface is exposed to and so can very clearly delineate the surface effect of different species in a given plasma discharge system. Knowing the identity of desorbed reaction products often makes it possible to deduce the surface mechanisms and so gain insight into the surface reaction kinetics for specific plasma chemistries. I worked with such a beam system, described in detail in Chapter 2, and used it to do some preliminary studies investigating the mechanisms of Ru etching.

CHAPTER 2: EXPERIMENTAL METHODS

SYSTEM OVERVIEW

The vacuum beam system that was used to conduct the Ru etching studies was equipped with a differentially-pumped modulated-beam mass spectrometer (MBMS) to detect desorbed surface reaction products and reflected species, and a quartz crystal microbalance (QCM) to precisely measure etch rates. It had two beam sources: a commercial ion gun for positive ion generation and a small microwave plasma source for radical generation. A rotatable carousel with heating and cooling capabilities held multiple samples. The carousel also held the QCM and a faraday cup for ion gun characterization. Two thermocouple leads on the carousel enabled measurement of the sample surface temperature during experiments. The degree of vacuum in the system was monitored by several ion and Baratron gauges and was maintained by seven turbomolecular pumps and four mechanical pumps. A computer performed simultaneous data acquisition of the signals from the MBMS, QCM, thermocouples, and main chamber pressure gauge. Lecture bottles of reactive and inert gases were housed in a small gas cabinet attached to the system and were admitted to the beam sources via a pressure-reducing leak valve. The gas processing lines could be pumped out by a fourth mechanical pump as needed. Figure 4 shows an overview of the main components of the system as viewed from above.

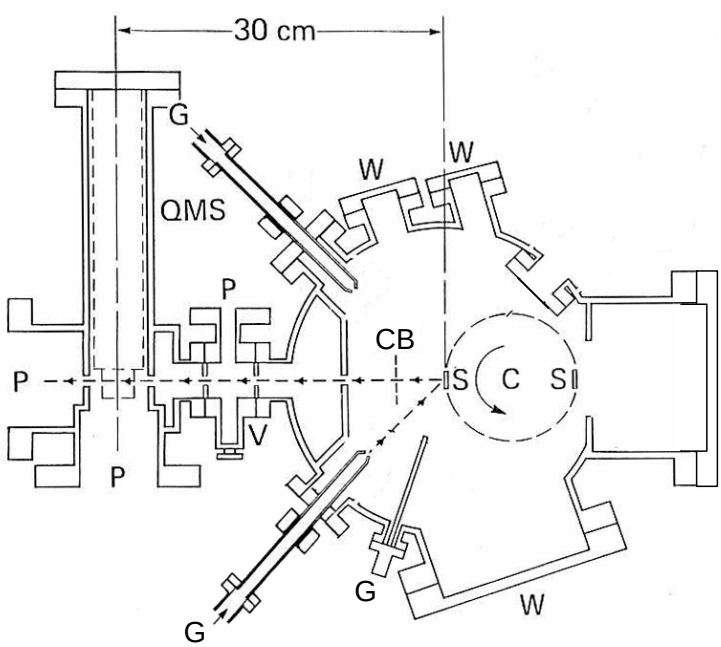

Figure 4: Top cross-section view of the experimental apparatus. P=turbomolecular pump, QMS=quadropole mass spectrometer, S=sample, C=carousel, CB=beam chopper blade, W=view port, G=gas supply, V=gate valve. Original drawing courtesy of Dr. John Coburn.

MAIN CHAMBER

The main processing chamber was a 30 cm diameter cylinder and was pumped by an Osaka Vacuum TG2003M Magnetically Suspended Turbomolecular Pump with a pumping speed of 2000 L/s. It was equipped with numerous ports that were used to mount the beam sources and various pieces of analytic equipment. The base pressure in the main chamber was typically in the 10^{-8} Torr range during idle periods and in the 10^{-6} Torr range when the beam sources were active. The low pressure was needed to allow the ion and radical beams to travel unimpeded to the surface by establishing a mean free path that was greater than the dimensions of the chamber. The top lid of the system was connected to the main chamber via a two-stage differentially pumped rotary seal (Thermionics RNN-600) to which the sample carousel was also attached. It had a dedicated turbomolecular pump (Pfeiffer TMU 071 P) that was mounted on the northeast side of the system next to the main chamber. Both valves connecting the rotary seal to the pumps needed to be open whenever the system was under vacuum. The left port on the flange, marked "First Stage," was connected directly to Mechanical Pump #2, while the right port, marked "Second Stage," was connected to the TMU 071 turbopump, which was backed by Mechanical Pump #2. A shut-off valve allowed this entire branch to be isolated from the mechanical pump in the event that it was not being used. In that case, the two shut-off valves on the flange needed to be closed as well.

SAMPLE CAROUSEL

Samples were mounted in the system on a rotating carousel with eight positions. Each carousel position could hold up to two samples. Two of the positions were used to hold the Faraday cup and the QCM, although these could be removed and replaced with additional samples if needed. Conversely, additional QCMs or other analytical equipment could be added. The ability to analyze up to sixteen samples in a single experimental run was a very powerful feature of the system. Sixteen different materials could all be exposed to identical processing conditions simply by rotating each sample into the beams. The results could then be directly compared without any need to consider run-to-run variations.

The octagonal sample-mounting plate was connected to the rotating flange on the top of the chamber via a hollow, cylindrical dewar. The outer wall of the dewar experienced vacuum, while the internal volume was open to the environment, at atmospheric pressure (Figure 5). The dewar could be filled with liquid nitrogen or other low-temperature-liquid baths to cool the carousel and attached samples down to ~80 K. The samples could also be heated to various temperatures with a cartridge heater placed in the dewar. The mounting flange had 360 degrees of rotational freedom in either direction, and also had x, y, and z translation so that samples could be precisely aligned in front of the QMS aperture.

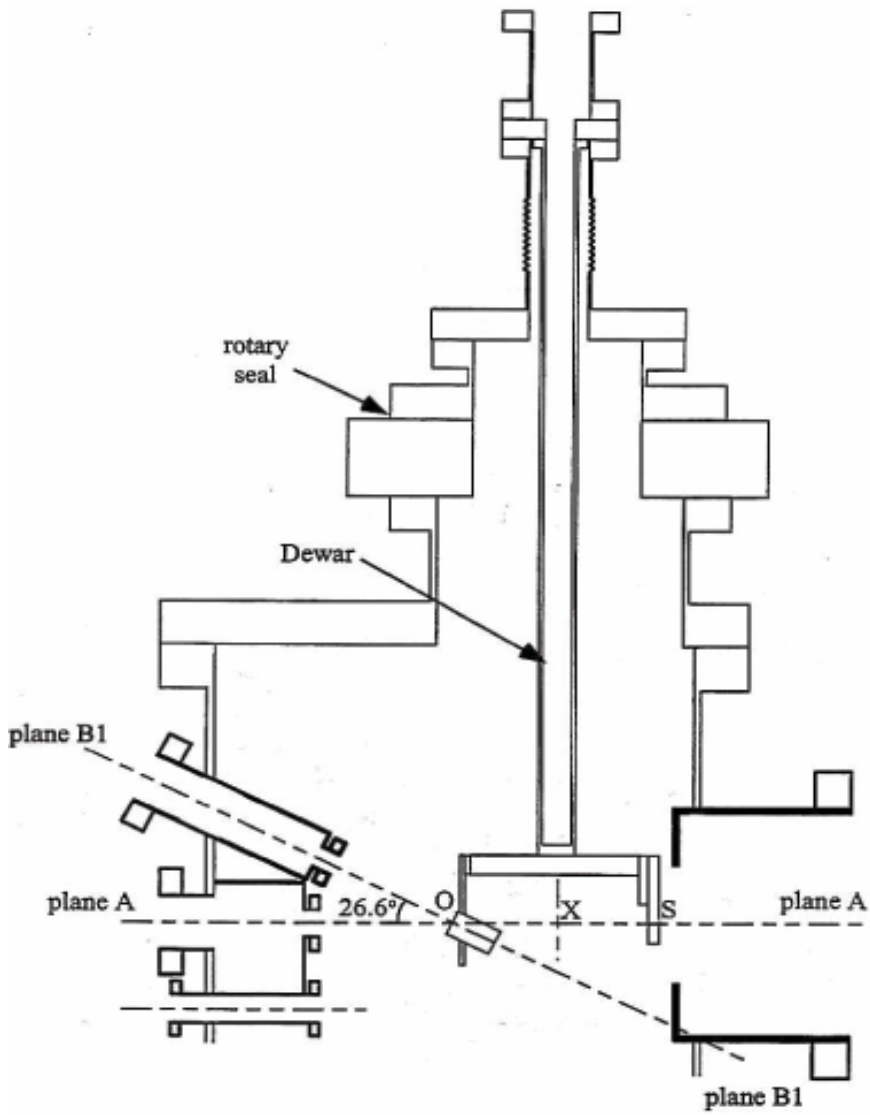

Figure 5: Cross-sectional side view of the chamber showing the carousel, dewar, and ion gun. Courtesy of Dr. John Coburn.

The original heater was a small resistive-heating element, mounted in a cylindrical block of copper. The heater could not be removed from the dewar and so was exposed to liquid nitrogen on a regular basis. This heating element was able to heat samples to 350 K. I replaced this heater with a 500 W cartridge heater that could be removed from the dewar before liquid nitrogen was introduced. A heater "jacket," consisting of two concentric, copper sleeves was designed to encase the cartridge heater and aid heat transfer to the samples. The jacket remained in the dewar at all times. Stable sample temperatures up to 560 K were demonstrated with this new design at only 50% of the heater's power output. The cartridge heater was operated at lower-than-100% power via a voltage regulator. Two type-k thermocouple leads that were mounted to the carousel were used to measure surface temperatures.

MODULATED BEAM MASS SPECTROMETRY

The MBMS portion of the system consisted of a differentially pumped quadropole mass spectrometer (QMS), a beam chopper, and a lock-in amplifier. The QMS chamber could be isolated from the main chamber by a differentially pumped gate valve. The QMS (Balzers QMG 420) was used to detect the neutral species evolved or reflected from the sample surface mounted on the carousel. It was separated from the main chamber by a ¼-inch-diameter aperture and four stages of differential pumping.

Differential pumping brought the background pressure in the mass spectrometer chamber (10^{-10} Torr) substantially below the pressure in the main chamber during processing (10^{-6} Torr). This pressure difference yielded a significantly higher signal-to-noise ratio because the background "noise" signal was reduced, making it possible to detect smaller fluxes of desorbed species. It also ensured that the mean free path of the species desorbed or reflected from the surface was sufficiently long in order to prevent gas-phase collisions before detection.

The QMS was mounted perpendicular to the main-chamber axis and was operated in cross-beam mode so as to reduce the fast-particle-induced background signal.[12] The distance from the sample surface to the QMS ionization volume was 30 cm.

To further improve the signal-to-noise ratio, the flux of species from the surface was mechanically modulated by a beam chopper operating at 25 Hz. This modulated-beam procedure was used to distinguish between the QMS signals from the species originating at the surface and those coming from the background gas. When the blades of the beam chopper were open, the volatile surface-reaction products were able to directly enter the QMS chamber. When the beam-chopper blades closed, these species could no longer pass through the aperture to reach the QMS because the line-of-sight path was blocked. The background species entered the QMS chamber regardless of the position of the beam-chopper blades.

The modulated, analog signal from the QMS was processed by a lock-in amplifier (EG&G 5208) operated in X-Y mode, which was then recorded by the computerized data-acquisition program running in LabVIEW. It was possible to detect species with this technique that had beam-to-background ratios as small as 10%, meaning reaction products could clearly be seen, even with a relatively high base-pressure in the main chamber.

The reference signal from the unit that drove the beam chopper was very sensitive to electrical and mechanical interference from a variety of sources, including the Tesla coil used to strike the plasma in the radical source and rotational motion of the carousel. The signal would change from a single sine wave at 25 Hz to multiple simultaneous sine waves of various amplitudes. This modified signal could not be interpreted by the lock-in amplifier and so it was unable to lock in on any of the surface species being detected by the mass spectrometer.

Unsuccessful attempts were made to electrically isolate the driver unit to eliminate this problem. The wire connections on both the chamber feed-through and the unit itself were also replaced. Since no acceptable solution to this problem was found, it was necessary to monitor the reference signal from the driver unit at all times during experiments. An oscilloscope was used for this purpose. If the

signal changed, the reference signal cable on the driver unit needed to be temporarily unplugged for a few seconds. When it was plugged back in, the signal would return to normal and experimentation could continue.

The QMS operated by detecting the mass-to-charge ratio of the gas-phase species present in the ionization volume of the instrument. The molecules were ionized, directed through a mass separator, and then detected. Positive ions were first created by electron-impact ionization with electrons generated from a hot filament. They were then drawn through the mass separator, an RF quadropole in this case.

The RF quadropole mass separator consisted of four cylindrical rods that formed a band-pass filter though the superposition of DC and RF fields. For a given tuning condition, ions of a particular mass were able to move through a large number of stable, periodic oscillations while traveling in the z-direction (Figure 6). Species with any other mass-to-charge ratio had unstable paths and were discarded before they reached the detector.[23]

The Balzers QMS on the system had two detector settings: Faraday cup or secondary electron multiplier. The current measured by the detector was proportional to the gas-phase density of species that formed ions with the selected mass-to-charge ratio.[24] By sweeping the RF and DC potentials linearly in time, a mass range could be scanned.

Figure 6: Three-dimensional computer-generated representation of a stable ion path.[23]

It was crucial that the QMS ionization volume be lined up precisely along the central axis of the chamber or it would not be possible to detect species evolved from the surface. The QMS unit was mounted to the chamber via a flange with an adjustable bellows.[1]

The position of the QMS ionization volume could be visually inspected from the west end of the system through the viewport on the fourth stage of differential pumping. The ionization volume was encompassed by a hollow rectangular box, the four edges of which needed to be just visible around the perimeter of the circular port separating the third and fourth stages of pumping. If the QMS ionization volume was positioned incorrectly, either the left or right edge of the rectangular box

[1] Unless the modulated signal from the lock-in amplifier is no longer detectable for even a model system such as silicon etching with chlorine, the mass spectrometer bellows should never be adjusted for any reason.

would be visible as a solid line cutting across the viewable space. This positioning was so important because it was the small volume inside the box that was sampled by the mass spectrometer. Unless this volume encompassed the line-of-sight path to the surface (which lay along the central axis), the modulated signal from the surface would be so low that it would be indistinguishable from the background, even if a very large flux of species was coming from the surface.

MECHANICAL PUMPS

Four mechanical pumps were used for initial chamber evacuation from atmosphere and to back the seven turbomolecular pumps that generated ultrahigh vacuum within the chamber. The main chamber turbomolecular pump was backed by a Welch 1397 Duoseal belt-driven, rotary-vane mechanical vacuum-pump, with a free air displacement of 500 liters/minute. This pump will be referred to as Mechanical Pump #1. The first stage of differential pumping was backed by an Alcatel 2033 dual-stage, rotary-vane mechanical vacuum-pump, with a free air displacement of 765 liters/minute (Mechanical Pump #2). These two mechanical pumps were separated by a valve that could be opened during system roughing to allow the atmospheric-pressure gas load to be pumped out more quickly. Mechanical Pump #2 also backed both stages of the differentially pumped rotary seal that supported the carousel. The second, third, and fourth stages of differential pumping in the MBMS section were backed by a Welch 1402 Duoseal belt-driven, rotary-vane mechanical vacuum-pump, with a free air displacement of 160 liters/minute (Mechanical Pump #3). The gas-line turbomolecular pump was backed by a Welch 1400 Duoseal belt-driven, rotary-vane mechanical vacuum pump, with a free air displacement of 25 liters/minute (Mechanical Pump #4).

All the mechanical pumps had electro-pneumatic valves at the inlet so that they could be quickly isolated from the system via a control panel if needed. These valves failed closed upon power failure so the system was protected from mechanical-pump-oil backstreaming into the chamber in the event of a power outage. They were controlled via mechanical switches on the control panel. The panel was not specifically designed for the existing setup of the system, and so had several unused switches.

Each mechanical pump was fitted with an oil trap to reduce backstreaming of mechanical-pump oil into the system. Several of these traps were filled with copper gauze, which was replaced in 2003.

Each mechanical pump and its vacuum connections were connected to the system in the same way for continuity and easy maintenance. The inlet to each mechanical pump was connected to a pressure-relief valve that could be used to bring the body of the pump to atmospheric pressure when the pump was turned off. This was important as it prevented back-streaming of the pump oil. The next item in the pump stack was the oil trap. Mechanical Pumps #1 and #4 had copper gauze traps, while Mechanical Pumps #2 and #3 had permanent molecular-sieve traps that could be heated if necessary to liberate the absorbed oil. Convectron gauges were located at this point in the pump stack so that the base pressure of the mechanical pump could be monitored. After the oil trap, an electro-pneumatic valve was connected to a controller that could be used to independently operate each valve. The valves were controlled with compressed air.

The College of Chemistry had problems with water appearing in the compressed-air lines on several occasions. This caused some major damage to the electrical equipment when it got wet

unexpectedly. Because the lab was located on the lowest level of the building and was nearest to the building's air compressors, any failure of the compressors affected our lab the most severely. On multiple occasions, water got into the body of the electro-pneumatic valves and several of them had to be replaced. The water also damaged several turbopump controllers which had to be rebuilt. To prevent further damage, a sheet of plastic was placed over the turbopump controllers and tubing was put in place to redirect any unexpected water delivered to the electro-pneumatic valves via the compressed-air line into the drain on the floor.

A wooden enclosure measuring 41" deep by 73.5" wide by 20" high was built around the four mechanical pumps used on the system. The main purpose of the enclosure was to reduce the noise level in the laboratory, but it also served the secondary purpose of providing a raised platform from which to access the north side of the system. This "back" side of the system would be very difficult to access otherwise. The enclosure was lined with sound insulation foam to further reduce the noise level. The front of the enclosure was fitted with two barn-door-style hinged doors, which allowed access to the pumps inside for maintenance and repair.

After the initial installation of the enclosure, it was noted that the ambient temperature inside the enclosure was well above the recommended operating temperature for the mechanical pumps, so a small 5-inch-diameter fan was installed on the east face of the enclosure to generate air flow and lower the temperature to an acceptable level.[2]

All the mechanical pumps were plugged into outlets on the power strip located above the pump enclosure. Mechanical Pumps #3 and #4 used standard NEMA 5-15 grounded connectors for 15A/125V electricity and had on/off toggle switches on the power cord. Mechanical Pumps #1 and #2 used NEMA 6-15 grounded connectors, with blades rotated 90 degrees, for 15A/250V electricity (Figure 7). These pumps had to be unplugged manually. The plug for Mechanical Pump #2 did not fit snugly into the outlet. It fell out of the outlet on one occasion during processing, causing several days of downtime while the system base-pressure recovered.[3]

Figure 7: NEMA 5-15 (left) and NEMA 6-15 (right) grounded connectors for mechanical pumps.

Each mechanical-pump exhaust port was connected to the hazardous-exhaust lines for the building. It is important that the pump exhaust never be released into the room, as it contains all of the

[2] The electrical cable for this fan is easy to unplug accidentally, so care must be taken when working around the system to ensure that this fan is always operating.

[3] Extreme care must be taken when working in the vicinity of the pump cables so as not to accidentally unplug this pump and shock the system with atmospheric pressure.

process gases used in the system, as well as fragmented pump oil that should not be inhaled. The extra ports on the exhaust manifold should be capped at all times.

The mechanical pumps were filled with TKO-19 Ultra Hydrocarbon Pump Fluid from Kurt J. Lesker Company. This oil was hydro-treated to provide good ultimate vacuum and low backstreaming. The oil should be changed on a regular basis, particularly when hazardous and corrosive gases are used regularly. It is recommended that that the pump oil be changed at least every six months.

PRESSURE MEASUREMENT

The operating pressure in each of the four mechanical pumps was monitored with a separate Granville-Phillips Series 275 Convectron Gauge.

Pressure in a vacuum system can be measured in a variety of ways. An indirect-reading gauge calculates the pressure by measuring a gas property that changes in a predictable manner with changes in gas density. These gas properties include momentum transfer (viscosity), charge generation (ionization), and energy transfer (thermal conductivity).[25]

Thermal conductivity can be used to determine the pressure by monitoring the heat transfer between a heated wire and its surroundings. The change in temperature is detected by either directly monitoring the temperature of the wire, or by monitoring the resistance of the heated wire. When the resistance is measured with a Wheatstone bridge circuit, the device is called a Pirani gauge. If the temperature is directly measured with a thermocouple, it is called a thermocouple gauge.

Convectron gauges use the wire-resistance monitoring technique, and so are convection-enhanced Pirani-type gauges. They provide reliable, fast response measurements from 1×10^{-4} to 10 Torr. Convectron gauges have a millisecond response time, making them preferable to thermocouple-type gauges, which take seconds to respond and have a smaller pressure window.

Figure 8: Cross-sectional view (left) and side view (right) of a Granville-Phillips Series 275 Convectron Gauge

Several operating guidelines need to be considered when installing and operating a Convectron gauge. If the gauge will be used to measure pressures greater than 1 Torr, the tube must be mounted with its axis aligned horizontally. Although the gauge will read correctly below 1 Torr when mounted in any position, erroneous readings will result at pressures above 1 Torr if the tube axis is not horizontal. Because the gauge calculates pressure indirectly via temperature changes, it is

important to locate the gauge away from internal and external heat sources, in an area where the ambient temperature is reasonably constant. The pressure indication depends on the gas type as well as the pressure, so the controller needs to be properly calibrated to the gas in use in the system. The factory default is N_2 (air uses the same settings).

Bayard-Alpert ion gauges are another type of indirect pressure-gauge. They measure the pressure by monitoring the gas property of charge-generation, specifically the ionization of the gas species present in the chamber. This type of gauge can reliably measure pressure in the ultra-high vacuum region, over the range from 10^{-10} to 10^{-3} Torr.

The gauge is a triode consisting of three elements: a filament (the cathode), a helical grid, and a central collector wire (the anode). The gauge utilizes the principle of thermionic emission, where a charged and heated metal filament composed of thoria-coated iridium emits electrons from its surface. The electrons are liberated because their thermal vibrational energy surpasses the work function of the metal.[4]

The stream of electrons from the filament is attracted to the helical grid by a positive DC potential (+150 V), in the process ionizing a fraction of the gas molecules they encounter in the space between the filament and the grid. The positive ions created by electron collision are drawn to the negatively charged central collector wire (-30 V). The ion current generated is then amplified and interpreted as a pressure by the pressure gauge controller.

The low-pressure sensitivity of hot-cathode ion gauges is limited by the photoelectric effect. Electrons hitting the helical grid produce x-ray photons (a phenomenon known as Bremsstrahlung) that then generate additional electrons via the photoelectric effect when they interact with nearby surfaces. The additional photoelectrons also ionize gas molecules, producing noise in the ion collector that can dominate at very low pressures. This limits the range of Bayard-Alpert-type hot-cathode ion gauges to 10^{-10} Torr.

Both Convectron gauges and Bayard-Alpert ion gauges need to be connected to a controller that can perform the necessary mathematical operations to continuously convert the raw signal, wire resistance and current, respectively, into a pressure measurement. Two such controllers were used in this research: a Granville-Phillips Series 303 Vacuum Process Controller Model B and a Granville-Phillips Series 307 Vacuum Gauge Controller.

The Granville-Phillips Series 303 Vacuum Process Controller Model B (Figure 9) is a programmable, microprocessor-controlled vacuum-system controller that operated two ionization-gauge tubes

[4] The current from a heated wire depends exponentially on the temperature of the wire, following a mathematical form similar to the Arrhenius equation. The emitted current density J (A/m^2) is related to temperature T by the equation $J = AT^2e^{-W/kT}$, where T is the metal temperature in Kelvin, W is the work function of the metal, and k is the Boltzmann constant. The proportionality constant A, known as Richardson's constant, is given by $A = 4\pi mk^2e/h^3 = 1.20173 \times 10^6 Am^{-2}K^{-2}$, where m and $-e$ are the mass and charge of an electron, and h is Planck's constant.

simultaneously, as well as two Series 275 Convectron gauges.[5] It was capable of monitoring pressures from 5 x 10^{-11} Torr to atmospheric pressure (760 Torr).

The unit was programmed via the front-panel controls, and was set to read in units of Torr. For accurate measurements, the sensitivity of the controller had to be programmed to match the type of ion gauge being used. For glass-tubulated Bayard-Alpert gauges, the factory default of 10/Torr for N_2 was appropriate. For the nude-gauge design, the ion gauge (IG) sensitivity of the controller needed to be set to 25/Torr for N_2. If gases other than N_2 or air were being pumped, the relative sensitivity of the gauge for that gas needed to be programmed into the controller.[6]

Figure 9: Granville-Phillips Series 303 Vacuum Process Controller Model B

The Granville-Phillips Series 307 Vacuum Gauge Controller (Figure 10) measured pressure from 5 x 10^{-12} Torr to atmospheric pressure (760 Torr). Two ion gauges could be operated sequentially, along with two Convectron gauges simultaneously. As with the 303 Controller, the sensitivity needed to be set manually to match the type of ion gauge being used. The controller was set to 10/Torr for Gauge A, the glass tubulated gauge used to monitor the pressure in the ion-gun cavity. The other connection was not in active use, but was available to monitor the pressure in one of the stages of differential pumping if additional cables had been available.

Figure 10: Granville-Phillips Series 307 Vacuum Gauge Controller

On the system, each of the four Convectron gauges was connected to one of the two controllers, which digitally reported the pressure in units of Torr. Mechanical Pumps #1 and #3 were connected to the Granville-Phillips 307 Vacuum Gauge Controller. Mechanical Pump #1 was monitored on Display A and Mechanical Pump #3 on Display B. The cable plugs connecting the gauges to the controller were a dark blue that matched the neck of the gauge and were cylindrical in shape. Mechanical Pumps #2 and #4 were connected to the Granville-Phillips Series 303 Vacuum Process Controller, with Mechanical Pump #2 on the CG1 display and Mechanical Pump #4 on the CG2 display. The cable plugs for these gauges were a light blue color that matched the neck of the gauge

[5] See Section 3-45 of the Series 303 instruction manual for more details. Instruction manuals for all commercial equipment on the system have been collected and catalogued in the lab.

[6] The Granville Phillips 303 pressure gauge controller that was originally used with the system malfunctioned in 2004 but has been kept in the lab for spare parts should any be needed for the new 303 controller. The controller has been discontinued, so it is important to have spare parts available.

and were conical in shape. All four mechanical-pump pressures could be monitored simultaneously with this arrangement, making it easier to monitor the health of the pumps, as well as closely monitor the pump-down process for any unexpected behavior.

Ion gauges were distributed throughout the ultra-high vacuum portion of the system to monitor the pressure at various points. A nude Bayard-Alpert hot-cathode ionization gauge (Figure 11) was situated in a port of the main chamber and was used to monitor the pressure during both idle periods and during processing to ensure the pressure did not rise above 1 x 10^{-6} Torr. This was important both for the health of the pumps and to keep the mean free path of the reactants and products in the necessary range. This gauge was attached to the IG1 display of the 303 controller.

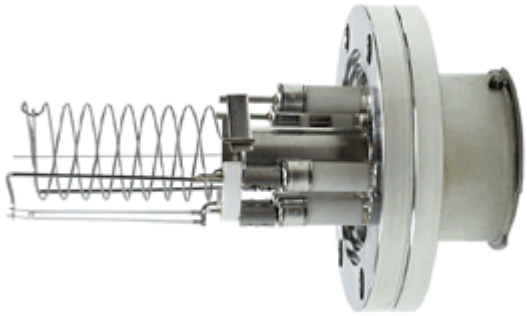

Figure 11: Granville-Phillips nude Bayard-Alpert-type Ionization Gauge

A tubulated glass gauge (Granville-Phillips 274 Glass Bayard-Alpert-type Ionization Gauge) (Figure 12a) was located on one branch of a four-way cross attached to one of the ports of the main chamber.[7] This gauge monitored the pressure of inert gas (typically Ar) in the ion gun cavity so that the proper flux of ions could be delivered to the sample. It was connected to the Gauge A display of the 307 controller. The operating pressure needed to be approximately 1 x 10^{-4} Torr for optimal functioning of the gun.

[7] A spare glass tubulated gauge is available in lab should the one currently on the system break, although it is **strongly** advised that when it needs to be replaced, the glass gauge be replaced instead with a Granville-Phillips 355 Micro-Ion Gauge (Figure 12b). The Micro-Ion Gauge is much smaller (Figure 13) and therefore easier to install within this complex, tightly-packed vacuum system. It would be much easier to add additional radical or electron sources to the system if the large, fragile glass gauge were removed. The Micro-Ion Gauge is also more rugged, has a wider pressure range, is more burnout resistant and produces less heat than a glass gauge. It is only slightly more expensive than a glass gauge.

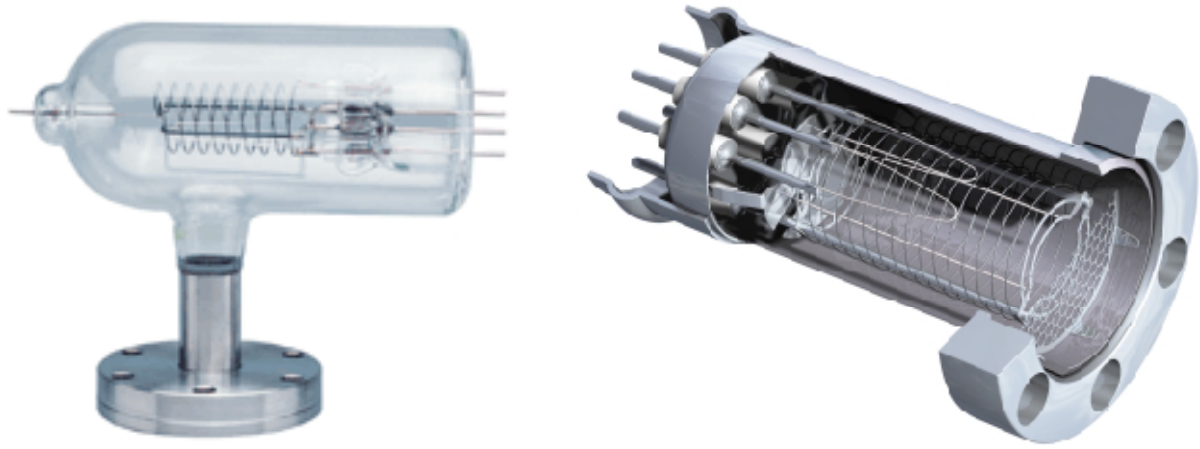

(a) (b)

Figure 12: (a) Granville-Phillips 274 Glass Bayard-Alpert type Ionization Gauge and (b) Granville-Phillips 355 Micro-Ion Gauge

Figure 13: Size comparison between Granville-Phillips 274 Glass Bayard-Alpert type Ionization Gauge (left) and Granville-Phillips 355 Micro-Ion Gauge (right)

The differentially-pumped mass spectrometer section of the system contained three nude ion gauges that could be used to monitor the pressure in the different stages of differential pumping. The first gauge was located on the back side of the gate valve that separated the two sections of the system. This gauge monitored the second stage of differential pumping. The first stage of pumping had no pressure gauge.

The second gauge was located on the elbow opposite the mass spectrometer and monitored the third stage of differential pumping. The third gauge was located in the top port of the four-way cross, past the mass spectrometer section, in the fourth stage of differential pumping. This section was commonly referred to as the "beam dump" since it pumped away the gases that had already passed through the mass spectrometer ionizer. Of these three gauges, the one on the third stage was the only one hooked up to a controller due to the limited number of available cables. This gauge was chosen because it gave the best estimate of the pressure inside the mass spectrometer. It was connected to the IG2 display of the 303 controller.

In addition to the Bayard-Alpert-style ionization gauges, a Balzers Compact Full Range pressure gauge was attached to the main chamber and was capable of monitoring the pressure continuously

over the entire pressure range: from atmosphere down to ultra-high vacuum. Of all the gauges on the system, this one was the most important and useful for running the system. It made it possible to verify that the ion gauges were reading properly, as well as pump down the system and bring it up to atmosphere safely.[8] The gauge had an RS-232 interface that was connected to the LabVIEW data collection system that I designed and programmed, allowing for continuous monitoring and recording of the pressure in the chamber during processing.

During idle, the base pressure in the main chamber was typically 1×10^{-8} Torr. The base pressure in the mass spectrometer section was typically 1×10^{-10} Torr. During processing with the radical source, typical chamber pressures were 5×10^{-6} Torr, with 5×10^{-9} Torr in the mass spectrometer section.

I installed a pressure burst disc on the top of the main chamber, in order to protect the system from overpressure with nitrogen when the chamber was brought to atmosphere. The Balzers dual gauge was the only way to determine when the chamber had been brought to atmospheric pressure. The system was designed to handle negative pressures with ease, not to be pressurized positively above atmospheric pressure. Over-pressurizing the chamber with nitrogen would be dangerous and could shatter the glass components on the system, including the quartz radical source, the glass-tubulated ion gauge, and the multiple quartz viewports. The pressure burst disc was installed to prevent this. It was designed to rupture when the chamber pressure reached a value of 25 psi (1293 Torr), a value that the glass components should be able to sustain. It was important to carefully monitor the pressure via the Balzers dual gauge as the chamber was being back-filled with nitrogen so that it could be turned off as soon as the pressure reached 760 Torr.[9]

GAS CONTAINMENT AND DELIVERY

No acceptable solution for the safe storage and delivery of toxic and corrosive gases such as fluorine, chlorine, bromine, etc. had been implemented by previous researchers. A small gas cabinet was purchased that could be mounted on the reactor cart, immediately adjacent to the system to minimize the distance to the gas inlet on the radical source. The gas cabinet could house up to four lecture bottles internally. A permanently-mounted gas manifold system was designed and constructed that allowed up to three reactive gases and one inert gas to be mixed in the radical source. Only the bottle needed to be removed when a processing line was no longer needed. Each gas line had a variable leak valve that was used to reduce the pressure to an appropriate level before being admitted to the source. The delivery lines for each gas had an isolation valve before they joined the common delivery line so that the lines could be isolated when not in use and protected from cross-contamination. A dedicated mechanical pump and turbopump stack were used to pump down the lines at the beginning and end of an experiment to 1×10^{-8} Torr.

The initial design only included a mechanical pump, but it was found that the gas lines needed to be at the same level of vacuum as the chamber for everything to proceed smoothly when the valve was opened between them. Without the turbopump in place, the pressure difference was so large (six orders of magnitude) that the main chamber received a large pressure shock each time the gas line was opened. It took several hours for the system to recover from this before an experiment could

[8] The head of the gauge can get contaminated with time and may need to be removed from the system and cleaned.

[9] Never leave the nitrogen line open to the chamber unattended!

begin, with corrosive gases flowing the entire time. The addition of the turbopump to bring the gas line pressure down to ultra-high vacuum level eliminated this problem.

A N_2 purge line was built into the manifold, along with bypass valves around each leak valve so that the entire manifold could be purged with nitrogen prior to removing the gas bottle. This was done both to prevent the release of hazardous gases and to maintain the purity of the process lines. Inert gases were housed on the outside of the gas cabinet and had the same gas line design as the reactive gases. A capacitance manometer pressure gauge at the entrance to the radical source was used to determine the partial pressure of each gas added to the blend entering the radical source. Figure 14 shows a three-dimensional schematic of the gas cabinet and gas delivery system.

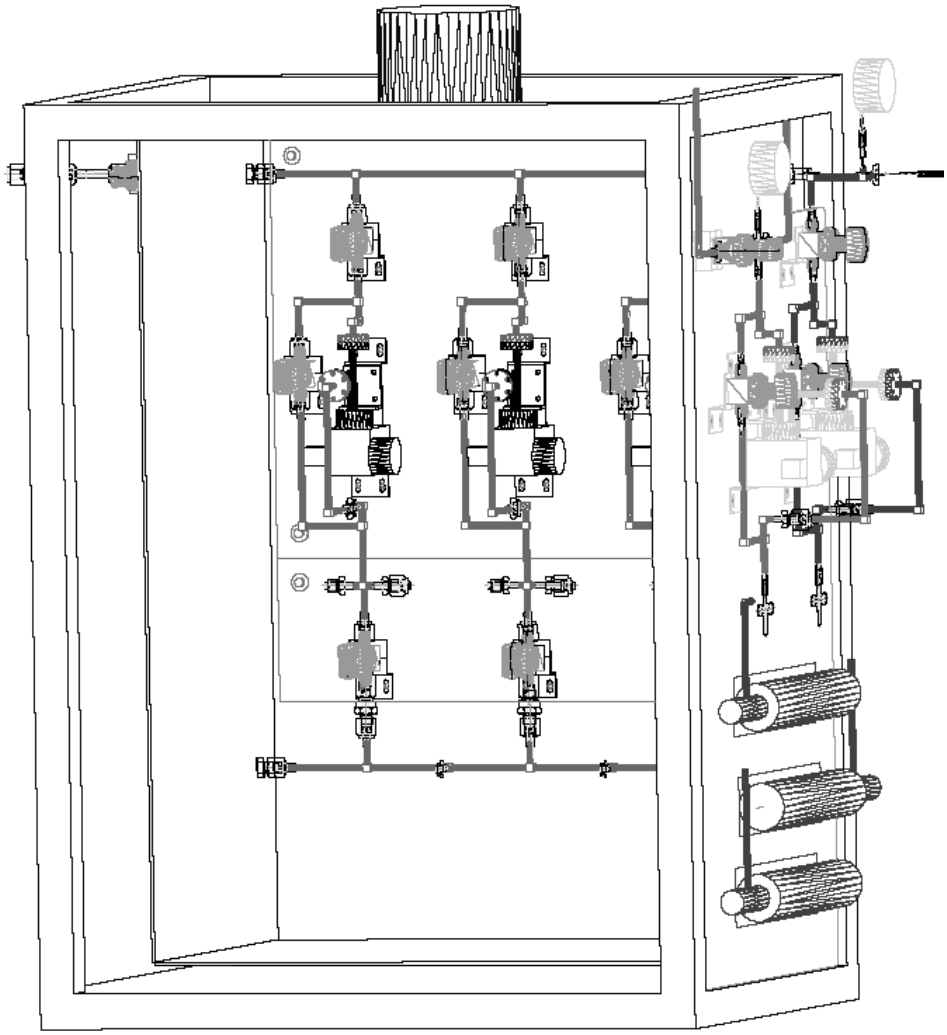

Figure 14: Gas cabinet and manifold for hazardous gases. Inert gases occupy the outside panel. Two of the three gas lines are clearly visible inside the cabinet.

QUARTZ CRYSTAL MICROBALANCE

The QCM was used to conduct *in-situ* measurements of etching and deposition rates. 6 MHz AT-cut quartz crystals with gold electrodes were used. The film of interest was deposited onto the crystal prior to installation in the system. The piezoelectric quartz crystal was made to oscillate in the thickness shear mode at its resonant frequency by applying a small potential (± 5V) using a feedback network of a closed loop system.[26] Since the resonant frequency of the crystal was proportional to its mass, small changes in the resonant frequency could be correlated to small changes in mass from the addition or removal of surface species. A change of 1 Hz corresponded to a mass change of 12.3 x 10^{-9} g/cm^2. A frequency counter (HP 5334A Universal Counter, Figure 15) with 0.1 Hz frequency resolution was used to detect the frequency changes. I interfaced the frequency counter via RS-232 to the LabVIEW data collection program where the frequency changes could be recorded and plotted in real time.

Figure 15: HP 5334A Universal Counter

Quartz crystals are highly sensitive to temperature changes, on the order of 0.1 Hz/°C, but will operate very reliably at stable temperatures. The carousel heater was able to maintain stable temperatures for extended periods of time, making the QCM a very valuable tool for studies of the effect of temperature on surface chemistry. This topic will be discussed in more detail in the next chapter.

ION GUN AND FARADAY CUP

A commercial ion gun (Phi Electronics Model 04-191) was used to create inert positive ions (500/1000 eV) for surface ion bombardment. Argon was typically used as the inert feed gas. The ion gun was mounted to the main chamber, directly above the MBMS system at an angle of 26.6° from the sample surface normal. A flux of Ar^+ ions ranging from 5 x 10^{12} to 5 x 10^{13} ions/cm^2/s could be generated by varying the Ar pressure in the ion gun chamber.

Ions were generated in the ion gun cavity by electron impact ionization. The electrons were generated via thermionic emission from a heated tungsten filament. The electrons were then given the necessary energy to cause ionization by being accelerated away from the filament toward the positively biased steel cage enclosing the filament. Once created, the ions were drawn to the negatively-biased grid at the open end of the filament casing and were then focused into a beam by a series of ion lenses. The beam could be rastered across the surface for even treatment of the entire sample by scanning the relative voltages of the ion lenses.

The flux of ions arriving at the sample surface was measured by a Faraday cup mounted on the sample carousel. The Faraday cup was mounted to the carousel at an angle of 26.6° in order to be aligned with the ion gun axis. The Faraday cup consisted of a cylindrical current-collection chamber with a 2 mm diameter aperture (Figure 16). The outer casing was grounded and electrically isolated from the internal collection surface. The positive current created by ion impact was detected by a picoammeter (Keithley Model 6485, Figure 17) that was connected via RS-232 to the LabVIEW data collection program where the current measurements could be recorded and plotted in real time.

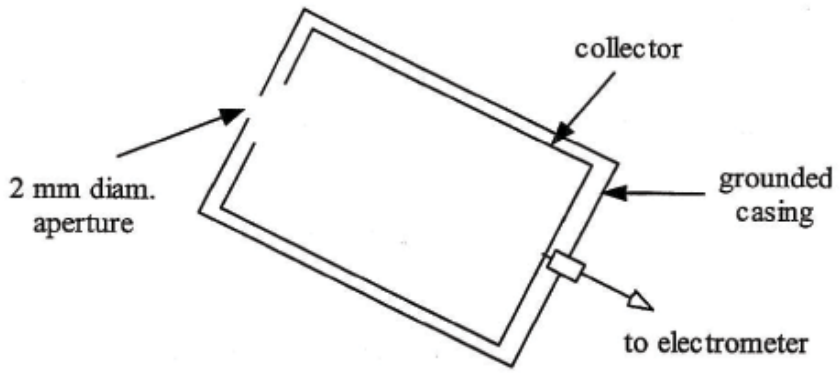

Figure 16: Cross-sectional side view of the Faraday cup.[27] Its position on the carousel is indicated in Figure 5.

Figure 17: Keithley Model 6485 5-1/2 digit Picoammeter with 10fA Resolution

INDUCTIVELY COUPLED PLASMA RADICAL SOURCE

The first radical source used on the system, designed by Dr. Gowri Kota,[27] consisted of two concentric quartz tubes fused together at one end (Figure 18). Gas was admitted to the inner tube

from the gas delivery system. The pressure was maintained in the 100 to 500 mTorr range. Radicals were generated by an inductively coupled plasma (ICP) discharge generated inside the inner tube. A small aperture (6 mm in diameter) at the fused end of the inner tube allowed the radical species to effuse into the main chamber. The plasma discharge extended throughout the entire length of the inner cylinder. The five-turn inductive coil used to drive the plasma was housed in the outer tube. The coil was driven at 13.56 MHz, using 100 to 400 W of RF power from a solid state RF power generator (ENI Model OEM-6AM-1) through a capacitive matching network.

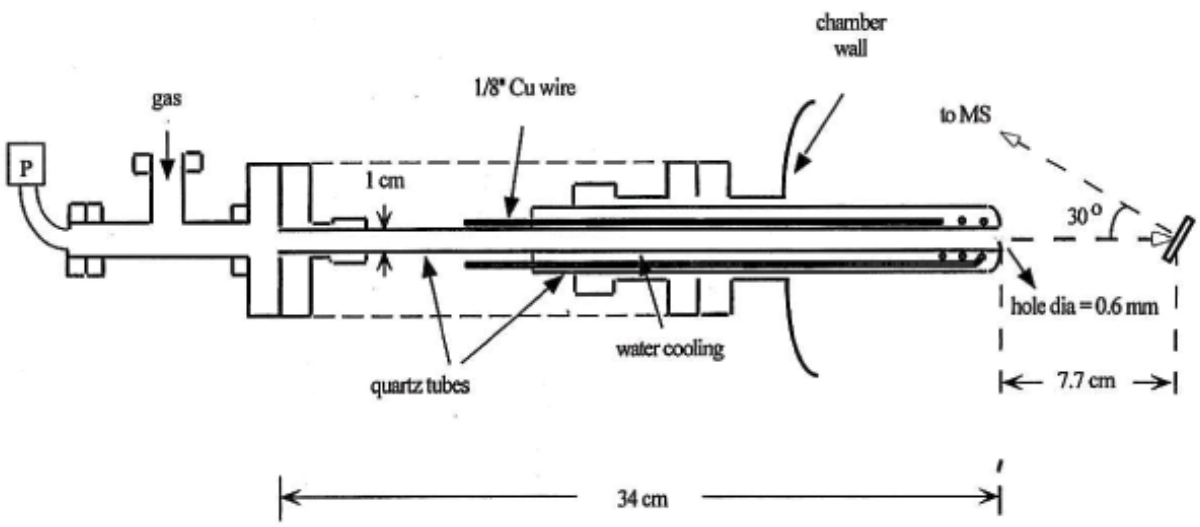

Figure 18: Cross-sectional view of the inductively coupled plasma (ICP) radical source.[27]

Cooling was needed because of the heating that occurred in the coil and at the walls of the inner tube. The double-wall design allowed the annular region housing the coil to be kept at atmospheric pressure and cooled with cooling water, even though it extended well inside the chamber. The tip of the radical source was supposed to be 7.7 cm from the sample surface, but was in fact 10 cm from the sample surface.[28] A design of this sort, where the plasma discharge existed in the space immediately before the aperture into the sample chamber, was necessary for species such as Cl and Br that had high recombination rates on surfaces. This design ensured that a sufficient flux of dissociated atoms arrived at the surface. The source was best suited for dissociating simple diatomic molecules, ensuring data interpretation did not become too complicated.

SURFACE WAVE RADICAL SOURCE

Since the ICP radical source was producing less than desirable results as a result of at-the-time undocumented changes made to the source design prior to my ownership of the equipment,[28] I decided to replace the ICP radical source with a new source of my own design (shown in Figure 19), based on a design originating from Michel Moisan's research group at the Université de Montréal in Quebec, Canada. The new source, known as a surface wave plasma source, operates using the principles of surface wave transmission from microwave field theory. A surface wave is an electromagnetic, nonuniform plane wave that propagates along the interface between differing media, guided by the refractive index gradient. Surface waves demonstrate the following

characteristics: 1) the field components of the wave diminish with distance from the interface, 2) the optical energy does not get converted into other forms of energy, and 3) the wave does not have a component normal to the interface.[29]

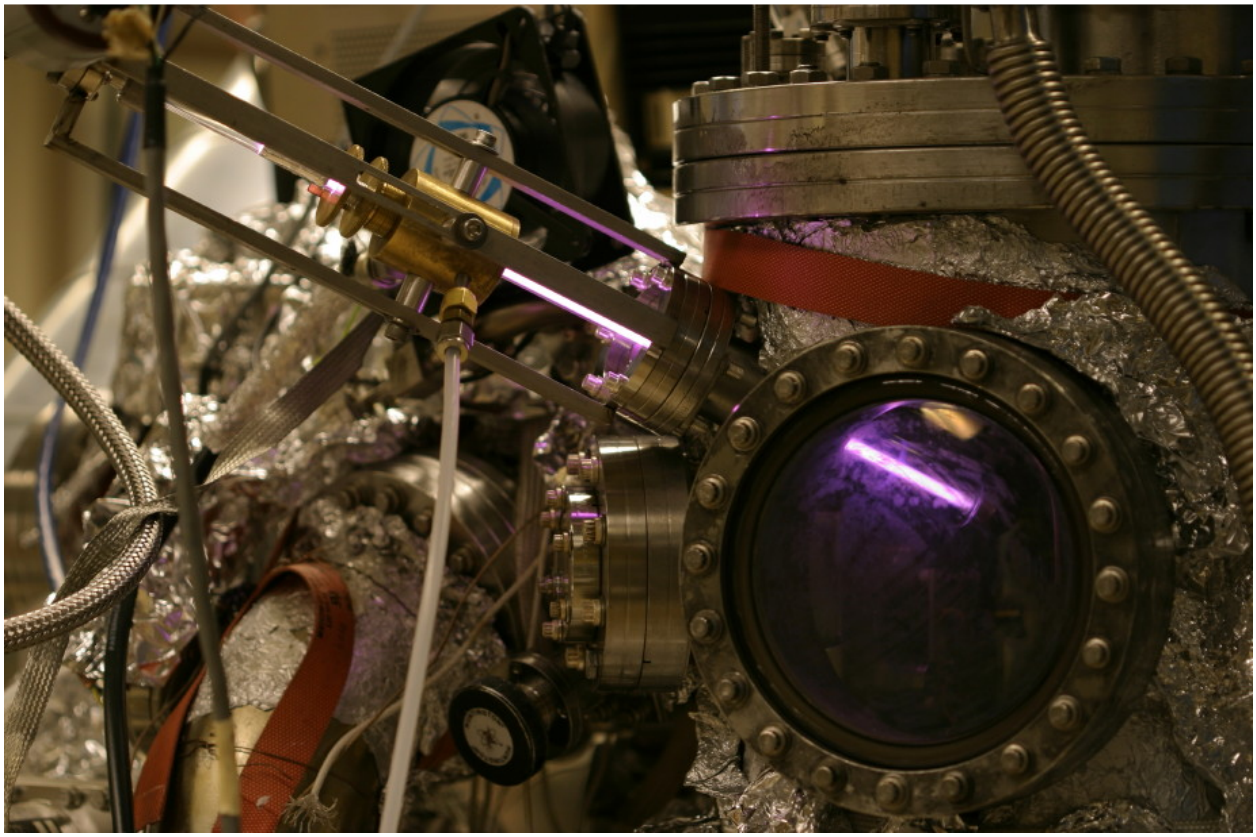

Figure 19: Photograph of surface wave plasma source with an ignited Ar plasma

The basic design of the radical source is a straight cylindrical dielectric discharge tube surrounded by a wave launcher. The wave launcher has two basic components: a microwave frequency field applicator that provides the electromagnetic field configuration required to excite a guided wave and an impedance-matching network that optimizes the microwave power transfer from the generator to the plasma. These components are not necessarily physically separated; they can be part of one integral unit. A integrated wave launcher known as a surfatron[30] was obtained from the Groupe de Physique des Plasmas at the Université de Montréal. The launcher launches a surface wave along the thin walls of the quartz tube. The gas inside the tube interacts with this wave in such a way that energy is transferred between the wave and the gas, making it possible to sustain a plasma discharge. The level of ionization and length of the plasma column can be controlled by varying several controls on the surfatron launcher (via matching). Please see Chapter 5 of the book *High Density Plasma Sources* for additional information on the design details and theory of operation of the surfatron wave launcher.[31]

Several different designs for the dielectric discharge component of the surface wave plasma source were considered. All involved quartz tubing, since the surface wave requires a dielectric material to

avoid high frequency power heating. The factors that needed to be considered in choosing the design were the available locations for the source, the size of the port, the distance to the sample, the need to not obscure other system components such as the ion gun, how to best mate the source with the system, how to cool it, how to support the launcher around the source, the distance the launcher should be from the system wall, and how to ignite it.

The choice was made to use a metal-to-glass seal to eliminate the glass compression fitting that was used in the past for the ICP source. Compression fittings leak and so the ultimate base pressure they can achieve is not as low as conflat metal seals. A compression fitting was still used to connect the gas line to the source in order to simplify the design and construction. The original design did include a glass-to-metal seal on both ends, but it was determined that there would be no way to put the launcher on the source with this design, unless the launcher was put on the tube before the glass-blowing occurred. The diameter of the inner tube that houses the plasma was chosen because it would provide the largest plasma volume and potentially the largest radical flux to the surface for the given surfatron launcher. The launcher has removable tube inserts that allow tubes of 6.5, 7.5, or 8.5 mm to be used.

The glass-to-metal piece was purchased from an outside vendor and given to the College of Chemistry glass shop to have the inner tube put in and the tip sealed off. A pinhole opening approximately 6-7 mm in diameter (smallest possible size that can be made by the glass blower) was placed at the tip of the inner tube to allow the radicals to enter the chamber. The outer tube extends the full length of the source and provides air cooling to the entire length of the plasma column. Dry nitrogen is hooked up to the surfatron launcher to cool the portion of the tube it surrounds, and a fan was run to circulate the air around the remainder of the tube.

The gas flow rate through the source can be varied over a wide range, but the source seems to operate most stably when the pressure is between 100-200 mTorr. The column length and measured radical flux gradually decrease over time because the regulator used on the gas cylinder is a single-stage regulator. Single stage regulators step the pressure down in a single step, and as the pressure upstream of the regulator drops, the pressure supplied to the reactor slowly decays. Dual-stage regulators are available to eliminate this issue, but are more expensive and were not considered necessary for this application. The source has a single gas line connection, but because of the structure of the gas delivery system, a variety of gases can be blended together before they arrive at the source.

The source tube is composed entirely of quartz except for the glass-to-metal fitting described above and is surrounded by a stainless steel cage that serves two purposes. The cage provides physical protection to the source and also holds the launcher in position around the quartz tube.

The tip of the source was positioned as close as possible to the sample surface on the carousel, without compromising line of sight from the ion gun. The previous ICP radical source was several inches further away from the sample, and I believe that this was a primary reason that that source never provided the expected radical fluxes.

The source was placed in the angled 2 ¾" port on the front side of the main chamber. This position was chosen because it required minimal reconfiguring of the other components of the system. The

ICP radical source that was located in the port below this was removed, as was its matching network. The chosen port provided a clear line-of-sight to the sample surface without obstructing the path of the ion gun. The port size was the minimum needed to allow passage of both the tube containing the discharge and the larger surrounding cooling tube. Because the entrance to the mass spectrometer section occupies the chamber position normal to the surface, all sources of radicals and ions will necessarily be at some angle to the surface, so the angle of the chosen port was not a specific consideration in placing the radical source. The large port that housed the ICP radical source is another location that could be used in the future if an additional radical source was added to the system.

The length of the plasma column from the surfatron launcher to the tip of the quartz tube is on the order of 12". The surfatron launcher can be moved along the length of the inner quartz tube, and it was found that the source performed better with the surfatron launcher closer to the chamber.

The launcher is connected to a 2.45 GHz microwave generator via a coaxial cable. The length of the cable is important for efficiently transferring the power from the generator to the launcher. My initial experiments were all run with a several-foot-long cable before I realized this. The first cable that was used actually melted because of the poorly attached plug on one end. It was only possible to get the discharge to the tip of the quartz tube with the microwave power turned all the way up and an argon-only plasma. When the long cable was replaced with the shortest possible cable, it became possible to get the discharge to the tip with much lower power input; now, a setting of only 60-70% is needed and a full-length discharge can be achieved with gases like O_2 present. The ion output from the radical source was characterized and is discussed in the next chapter. It was found that when the discharge reaches nearly all the way to the tip, a measurable flux of ions can be detected with the Faraday cup. When the plasma is all the way to the tip, a negative current is detected, indicating that the orifice for the source encompasses the plasma sheath and electrons are streaming from the source into the chamber. The radical flux from the source was also characterized, but the results were inconclusive. This result is most likely not due to any failure of the radical source to produce radicals, but rather because the mass spectrometer was improperly positioned during all experiments that I ran on the system during my graduate tenure. This grievous error was detected at the very end of my experimentation and corrected, although not before the surface wave radical source was characterized. Even with the misaligned mass spectrometer, an increase in radical species and a decrease in molecular species while the plasma was running were observed, but these observations cannot be quantified without further experimentation.

CHAPTER 3: CHARACTERIZATION OF THE SYSTEM

I conducted a series of basic experiments to characterize the behavior of the various components of the system. These experiments were done in some cases to choose an optimal operating condition and in others to quantify the behavior of an inherently complex process so that it could be better understood.

RESIDUAL GAS ANALYSIS

One of the most basic, yet most important experiments that I performed during the initial characterization of the system involved using the QMS to determine the composition of the background gas inside the system. The modulated beam capabilities were not used for this experiment because the species of interest were those that the modulation would remove from the signal. The mass spectrum of the system background gas is shown in Figure 20.

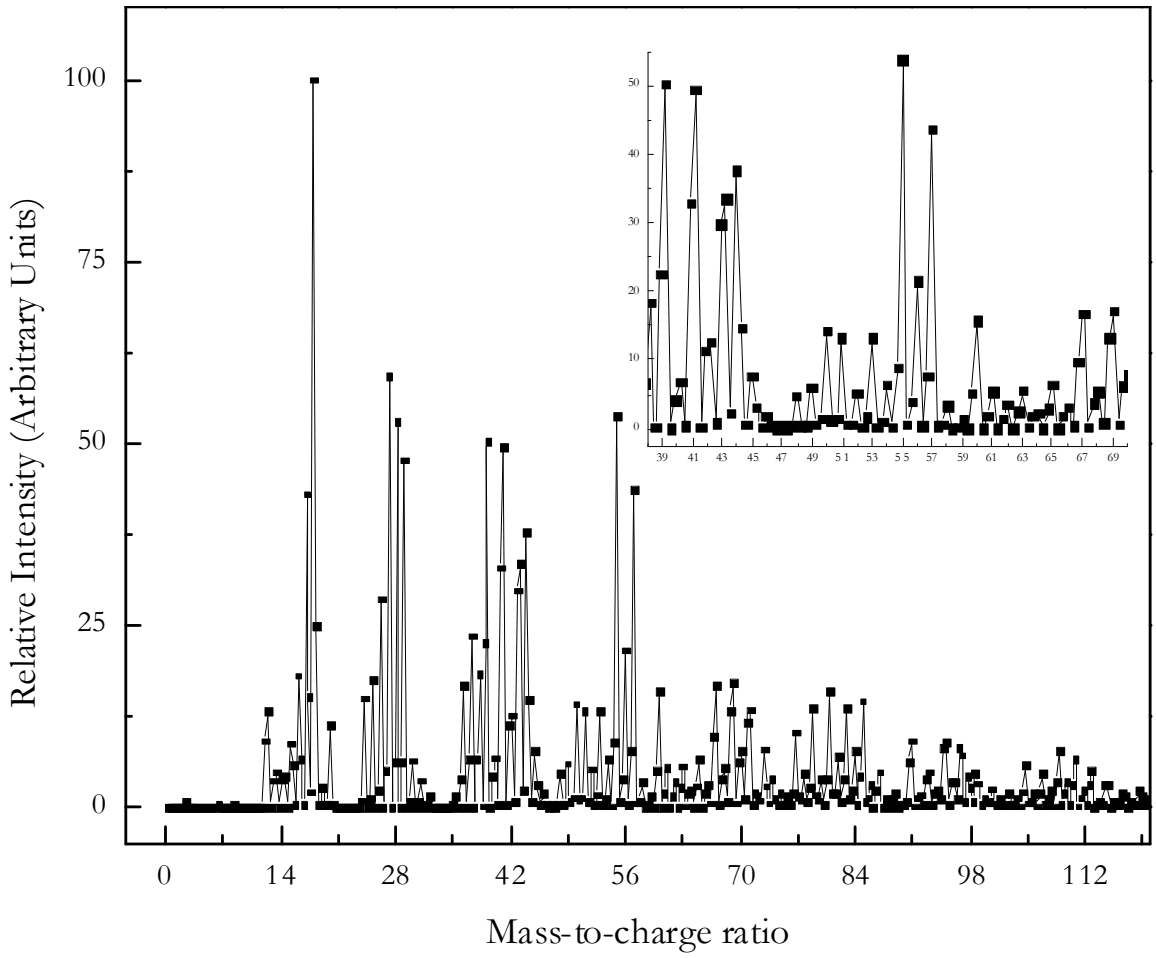

Figure 20: Residual gas background in vacuum beam system. Gas load was primarily water vapor and pump oil adsorbed on chamber walls.

When molecules are ionized, fragments with several different mass-to-charge ratios are created. The differences in the fragments are primarily the result of dissociative ionization, isotopic mass differences, and multiple ionization. The pattern of fragments, called a cracking pattern, forms a type of molecular fingerprint that can be used to help identify the presence of a particular gas species.[23] Evidence of water vapor contamination in the system was readily identifiable by the large peak at M/z=18 and the associated smaller peaks at 16 and 17 that are also part of the fingerprint. This was expected, as water vapor is known to be the primary gas load (desorbing from the walls) in an unbaked vacuum system. Glass and steel that has been exposed to room ambient for extended periods may contain up to 100 monolayers of water vapor that will slowly desorb over time when put under vacuum.[23]

The spectrum also shows fragments that are characteristic of organic molecules, most likely originating from backstreaming of the organic pump oils used in the mechanical pumps. The fingerprint of saturated straight-chain hydrocarbon oil is characterized by groups of fragment peaks centered 14 mass units apart. These clusters coincide with the number of carbon atoms in the chain. The C_1 cluster appear in the mass range 12 to 16, C_2 clusters from 24 to 30, C_3 species from 36 to 44, and so on. In most hydrocarbon oils, the fragments at mass numbers 39, 41, 43, 55, 57, 67, and 69 are particularly stable and their presence is a guarantee of hydrocarbon contamination.[23] The inset in Figure 20 shows this region of the spectrum in more detail and confirms the presence of hydrocarbons in the system. The presence of water vapor and hydrocarbon oils can be greatly reduced with a ~200°C bake for 24 hours to remove the surface gas,[32] and this was later done.

MODULATED-BEAM MASS SPECTROSCOPY

In this experiment, a small volume of argon gas was introduced into the gas delivery line upstream of the leak valve. The leak valve was then opened completely for a brief period of time (~1 minute). During this time, argon gas entered the chamber and was reflected off of the sample and through the MBMS aperture. The leak valve was then closed and the system was allowed to return to equilibrium. Figure 21 shows the signal that was detected by the lock-in amplifier during this experiment. The step input of Ar can very clearly be seen in this plot of signal intensity as a function of time. Slight signal decay during the time the leak valve was open is also evident. This was caused by the decreasing Ar pressure on the upstream side of the leak valve. Only a finite dose of Ar was used for the experiment rather than a continuous flow. As the pressure decreased on the upstream side of the leak valve, the flux of Ar atoms arriving at the surface also decreased. These data illustrate the ability of the MBMS system to remove background noise and to very clearly detect the flux of species coming from the surface.

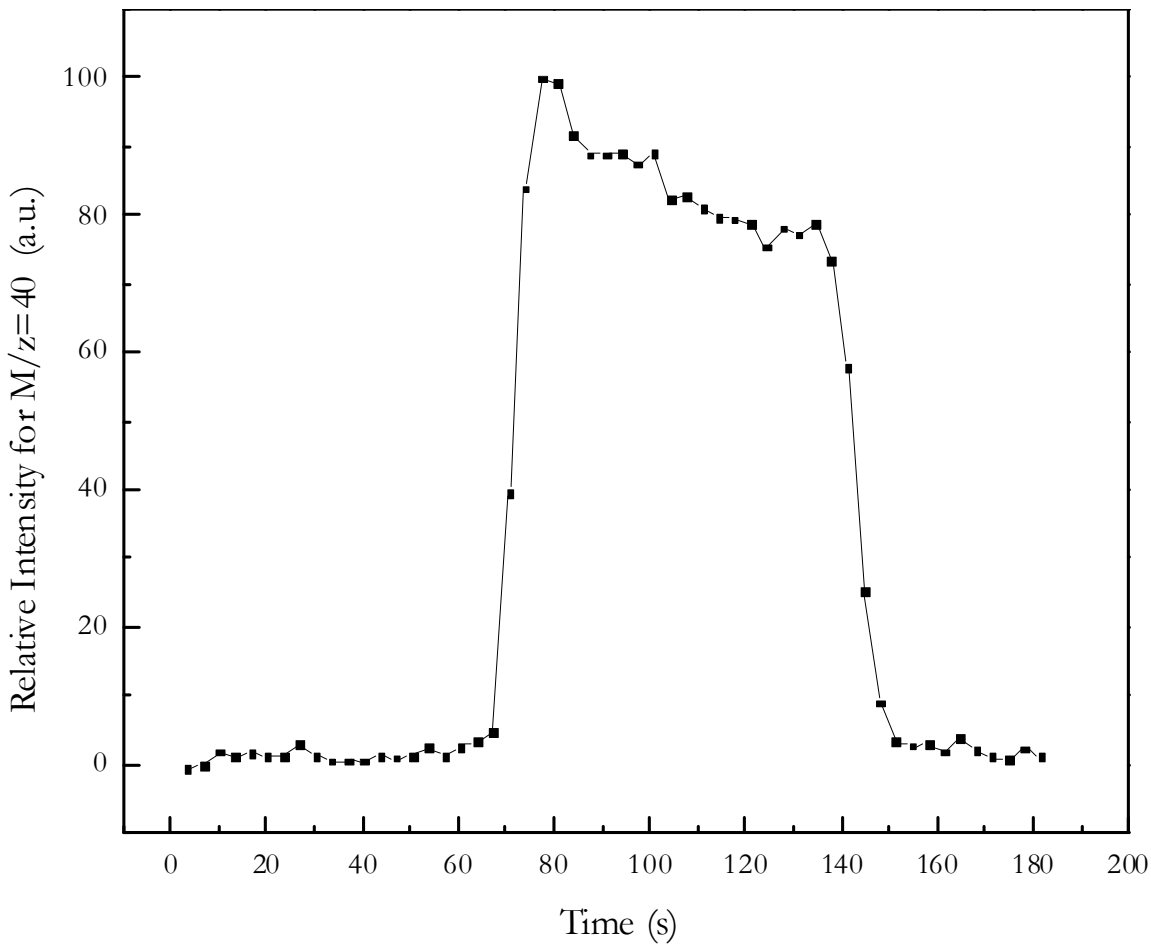

Figure 21: MBMS detection of step input of Ar

CHARACTERIZATION OF THE ION FLUX FROM THE ION SOURCE

The behavior of the ion gun for different raster values was explored in order to understand how this setting affected the mean value of the current density and its variance. The spot size increases as the raster value increases. The experiment was conducted using 500 eV Ar^+ ions and measured with the Faraday cup; the results are shown in Figure 22.

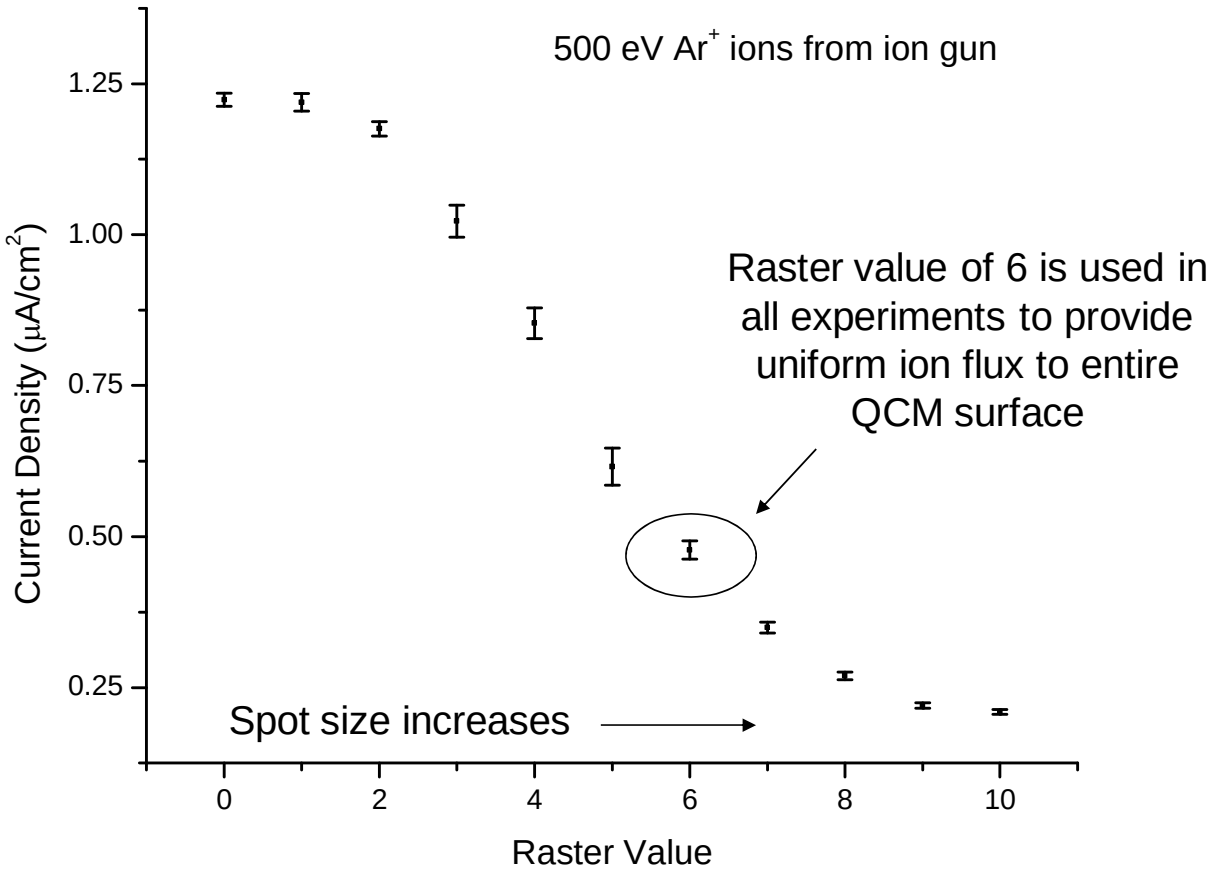

Figure 22: Effect of raster value on current density from the ion gun

CHARACTERIZATION OF THE ION FLUX FROM THE SURFACE WAVE RADICAL SOURCE

The newly designed surface wave radical source was characterized with the Faraday cup, just as the ion gun was, to determine if it was producing a measurable amount of ions. For a 120 mTorr Ar discharge, it did indeed produce not only a detectable amount of ions, but rather a surprisingly large amount at higher power settings. The ion flux from the radical source was a strong function of the discharge column length. In fact, when the discharge reached the end of the quartz tube, as shown in Figure 23 below, the current density was comparable to the ion gun densities. The addition of O_2 brought the current density down to negligible levels.

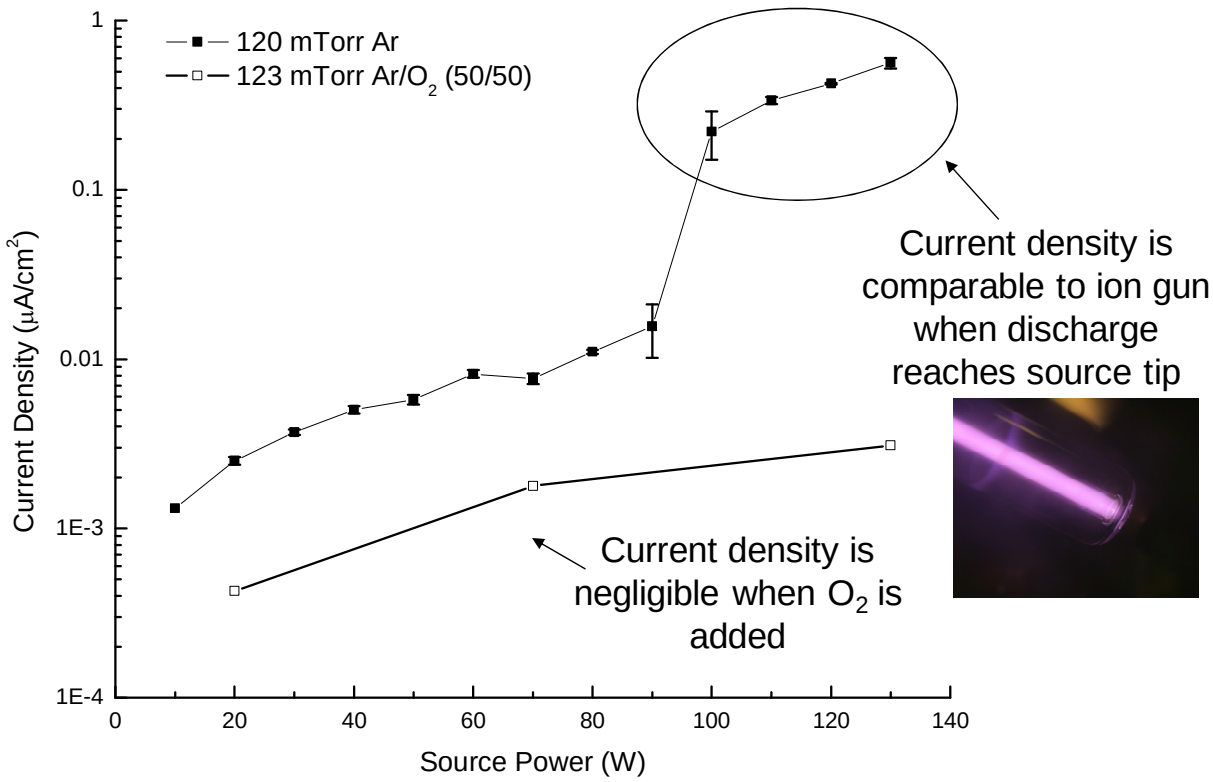

Figure 23: Current density measured from surface wave radical source as a function of microwave power

ETCH RATE MEASUREMENTS

This experiment was conducted to investigate the effects of Ar^+ ion bombardment on the etch rate of a gold-coated QCM crystal. Figure 24 shows the effect of 500 and 1000 eV Ar^+ on the resonant frequency of the QCM. The resonant frequency increased toward 6 MHz as material was removed from the surface. Gold atoms were sputtered off at a constant rate in both cases, although the specific rate clearly depended on the energy of the bombarding ions. The etch rate can be calculated from the slope of the frequency change with time and was determined to be 1.2 Å/min for 500 eV Ar^+ and 2.8 Å/min for 1000 eV Ar^+. These results were expected, since the higher energy ions are capable of removing more material per ion impact than the lower energy ions. The slight decrease in frequency that was observed when the ion beam was turned off was caused by the adsorption of a monolayer of water on the surface of the QCM, illustrating how sensitive this technique is to minute mass changes.

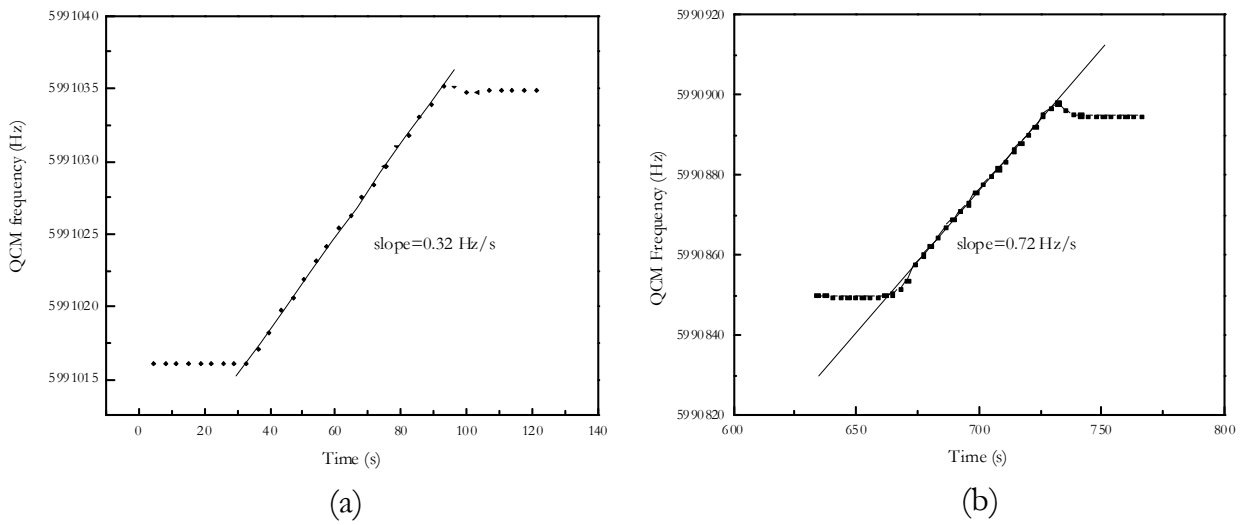

Figure 24: Example of QCM etch rate measurements. (a) 500 eV Ar^+ and (b) 1000 eV Ar^+

SAMPLE TEMPERATURE CONTROL

Figure 25 demonstrates the temperature response of the samples on the carousel when the cartridge heater was turned on and maintained at a constant power level. The samples were initially at room temperature. When 30% power was supplied to the heater, a 463 K (190°C) surface temperature was obtained. This temperature is very stable, even over extended periods of time (22 hours). A stable surface temperature of 557 K (284°C) was then demonstrated at 50% power. Unlike the first temperature ramp where the steady-state temperature was approached gradually, a slight overshoot of the temperature occurred during the second ramp. These differences in behavior are a result of the way the experiment was conducted at each point. In the first case, the power input was set directly to 30% and not changed. In the second case, the power input was set to 60% to increase the heating rate and then turned down to 50% once the desired temperature range was reached. Because of the large thermal mass of the carousel, the time scales for heating and cooling were relatively long. It took several hours to reach a stable temperature: six hours to reach 463K, three hours to then reach 557 K, and longer than twelve hours to return to room temperature.

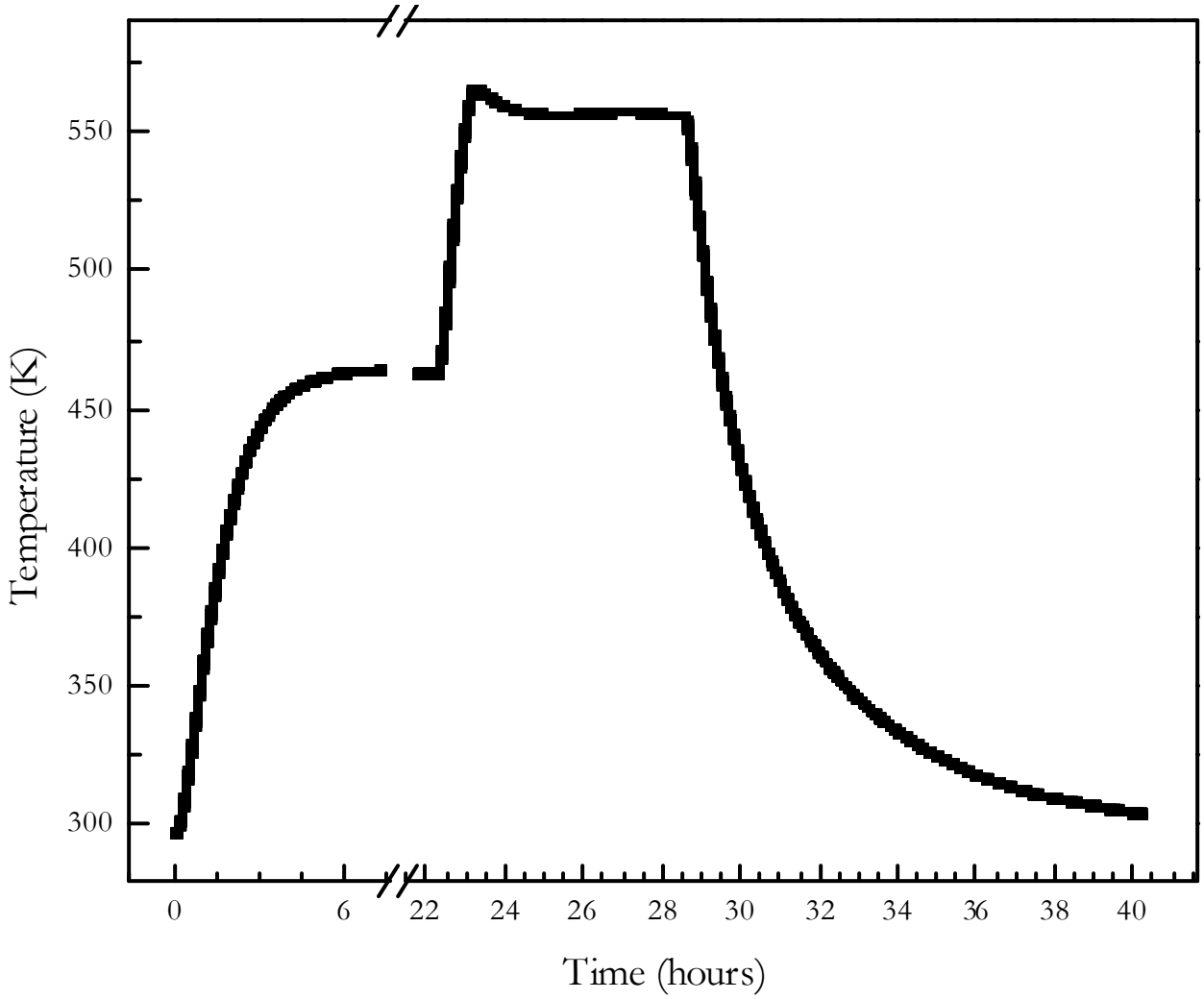

Figure 25: Sample temperature dependence on heater power

TEMPERATURE DEPENDENCE OF QCM

In the final set of experimental data that was collected to characterize the basic functions of the beam system, the temperature dependence of the QCM was investigated. The frequency changes of the QCM were monitored during the temperature-ramp experiments described above. The results are presented in Figure 26 and very clearly show the strong dependence of the frequency on changes in temperature. If properly calibrated, the QCM could actually be used as a way to measure temperature.[26] The frequency changes faithfully mirrored the temperature changes that were recorded. These data show the importance of having stable surface temperatures when trying to correlate QCM frequency changes to etching or deposition rates.

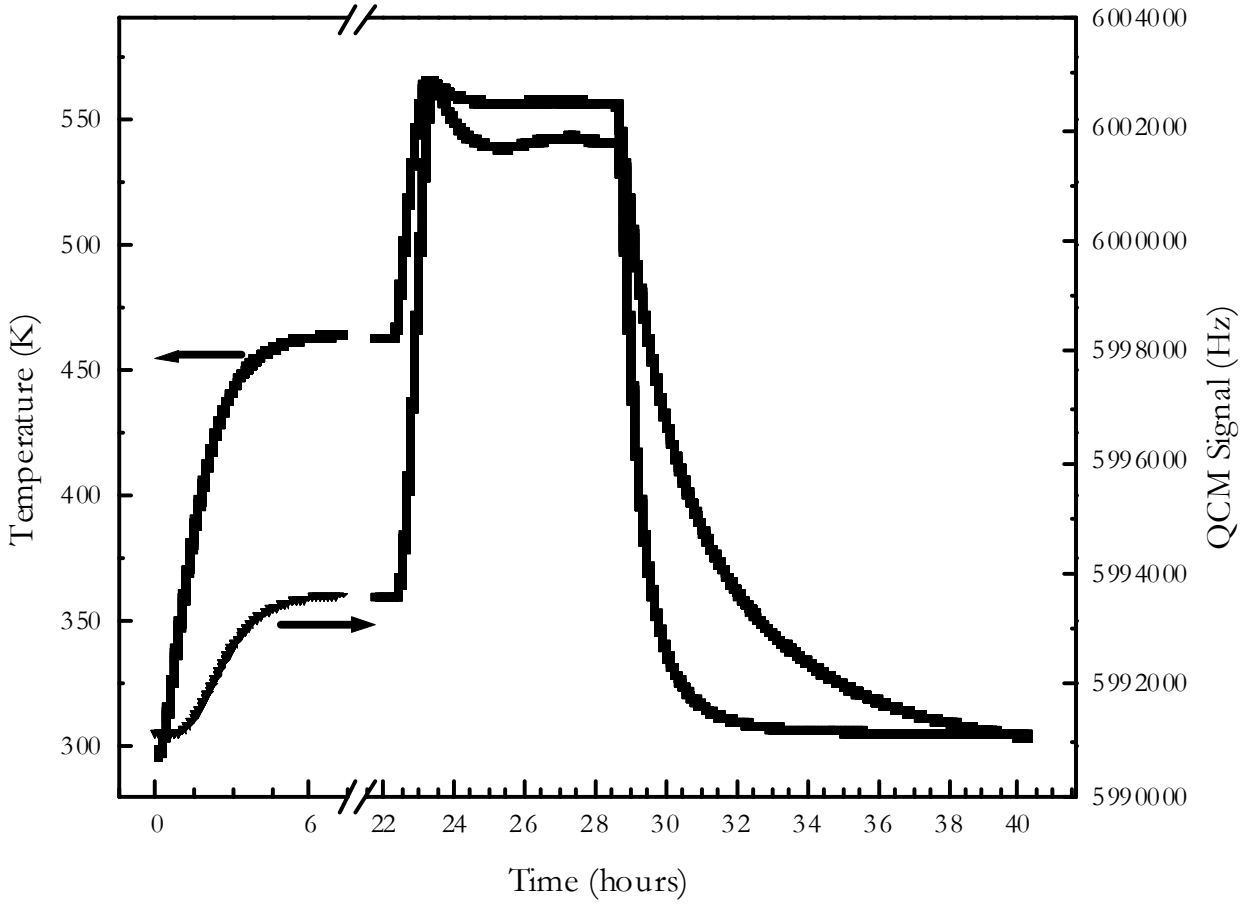

Figure 26: Temperature dependent behavior of QCM

Having said that, however, if one has the temperature calibration curve for the specific crystal being used, it is possible to correct for small fluctuations in surface temperature that may have occurred during the experiment. These calibration curves have been compiled for most commercially-available crystals and can often be obtained from the manufacturer upon request. The specific degree of the cut of the crystal determines the exact temperature response that a given crystal will have. For proprietary reasons, manufacturers will not provide information about the exact cut of the crystal, but rather will give a range that the crystal falls within (Figure 27a). For this reason, it is very useful to experimentally produce the calibration curve for the crystal in use so that accurate corrections can be made to the frequency measurement when temperature fluctuations occur. Figure 27b contains the calibration curve for my crystal. It is a replotting of the data shown in Figure 26 for the temperature region immediately above room temperature. By comparing the curves in Figure 27 (a) and (b), it can be deduced that the crystal is a 3° AT cut specimen.

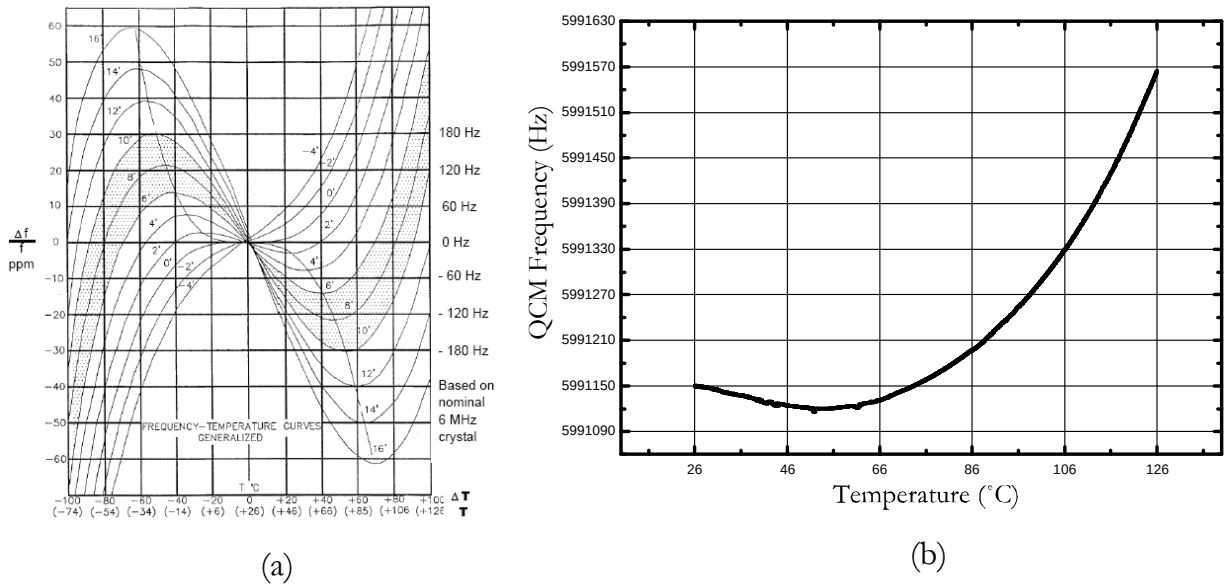

Figure 27: QCM temperature calibration curve for deviation from room temperature (a) from vendor and (b) measured experimentally

CHAPTER 4: PRELIMINARY VACUUM BEAM STUDIES OF RUTHENIUM ETCHING

INTRODUCTION

Ruthenium (Ru) and its conducting metal oxide, RuO_2, are candidate materials for the gate metal electrode that exhibit all of the necessary traits described in Chapter 1. They have high work functions (~5eV), excellent thermal stability, and low resistivities.[33, 34] Ru and RuO_2 have been shown to be stable on a variety of high-κ materials.[11, 35, 36] They can be etched by plasma discharges,[37, 38] although the details of the etching mechanism are still unclear, as will be discussed in detail below. Two volatile etch products, RuO_3 and RuO_4, have been experimentally identified for RuO_2 plasma-assisted etching.[39] The same volatile products are assumed for Ru plasma-assisted etching[37, 40] (based on high-temperature studies of the ruthenium-oxygen system conducted in the 1960s[41-43]) but have not been measured.

In order to initiate etching by creating the volatile oxidation products of Ru, researchers have exposed Ru and RuO_2 to pure O_2 plasma discharges and obtained surprisingly low etch rates, on the order of 100 Å/min for both materials. For comparison, the etch rate of doped poly-Si etching is on the order of 30 Å/s. When additive gases are introduced in small amounts (0-20% by gas flow rate, depending on the additive), the etch rate increases dramatically, six-fold in many cases. The etch rate decreases as more additive is introduced.[38, 39, 44-47] Work done in my research group by Cheng-Che Hsu[48, 49] confirms these finding. In an Ar/O_2 plasma, he reports an etch rate of 50 Å/min. With the addition of Cl_2 up to 20% by flow rate, the etch rate increases to 300 Å/min. Further addition of Cl_2 beyond 20% decreases the etch rate.

This rate-enhancing behavior is very poorly understood. The chemical nature of the additive appears to play a major role in the extent of rate-enhancement, although no systematic studies have been done to clarify this issue. CF_4,[38, 39, 46] CF_3CFH_2,[44, 45] SF_6,[45, 46] N_2,[39, 45] CCl_4,[46] and Cl_2[37, 39] have all been used as additives for RuO_2 etching, while Cl_2[37, 40], BCl_3, [40] CHF_3, [40] SF_6, [40] and CF_4[50] are the Ru etching additives reported in the literature. F-bearing and Cl-bearing species appear to have at least qualitatively similar effects on the etch rate, while N_2 seems to have a much smaller effect.[39, 45]

Theories and competing models abound about the role additives play in etching, but virtually nothing has been done to experimentally verify or refute these ideas. Additives are known to enhance the O radical density in the gas phase,[39, 51, 52] and it has been proposed that this is the only role they play in the etching process—that they do not participate in the surface reaction at all.[39, 45] Other researchers have proposed that an additive in some way catalyzes the surface reaction up to a point[44] but poisons the surface beyond some critical coverage by occupying O adsorption sites or forming a residue.[45] Another proposed model suggests that the reactive component of the additive (typically F or Cl) actually gets incorporated into volatile reaction products.[38]. Hsu's measurements of Ru-containing oxychloride ions in the discharge[48] imply that this may be a valid model. It has also been suggested that Cl_xO_y or F_xO_y radicals are formed in the discharge and that these are the primary etching species.[53]

EXPERIMENTAL RESULTS AND DISCUSSION

The beam system was used to explore these proposed models in more detail. The preliminary work was conducted with O radicals. Additional experiments involving Cl radicals were planned; due to equipment difficulties, it was not possible to carry out those experiments.

The sputter yield of Ru in the presence of O radicals (generated by the surface wave radical source) and Ar^+ ions was measured with a Ru-coated QCM crystal. The MBMS system was also operated during these experiments, but no reaction products were detectable. Figure 28 shows the results of this experiment for 500 eV Ar^+ ions. The presence of O radicals reduced the sputter yield by a factor of 2.5 at all temperatures. Temperature had little influence on the sputter yield in the presence of O radicals, except at the highest temperature of ~175°C.

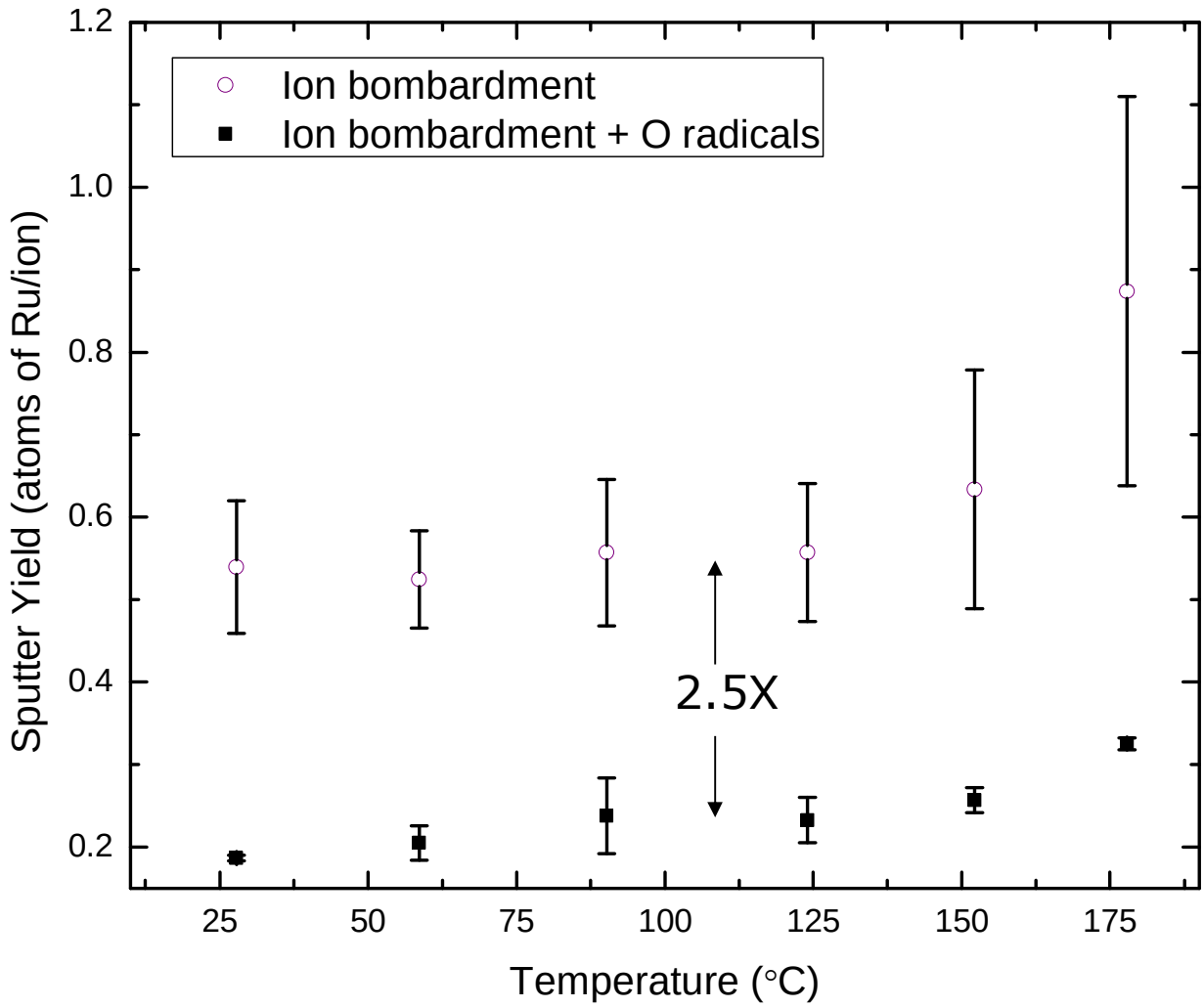

Figure 28: Sputter yield of Ru as a function of temperature in the presence of O radicals

Figure 29 below shows the raw QCM trace when the Ru surface was sequentially exposed to O radicals, Ar^+ ions and O radicals, O radicals, and finally, Ar^+ ions. An interesting and unexpected result was obtained and is circled in the figure: the O radicals alone spontaneously etched the Ru.

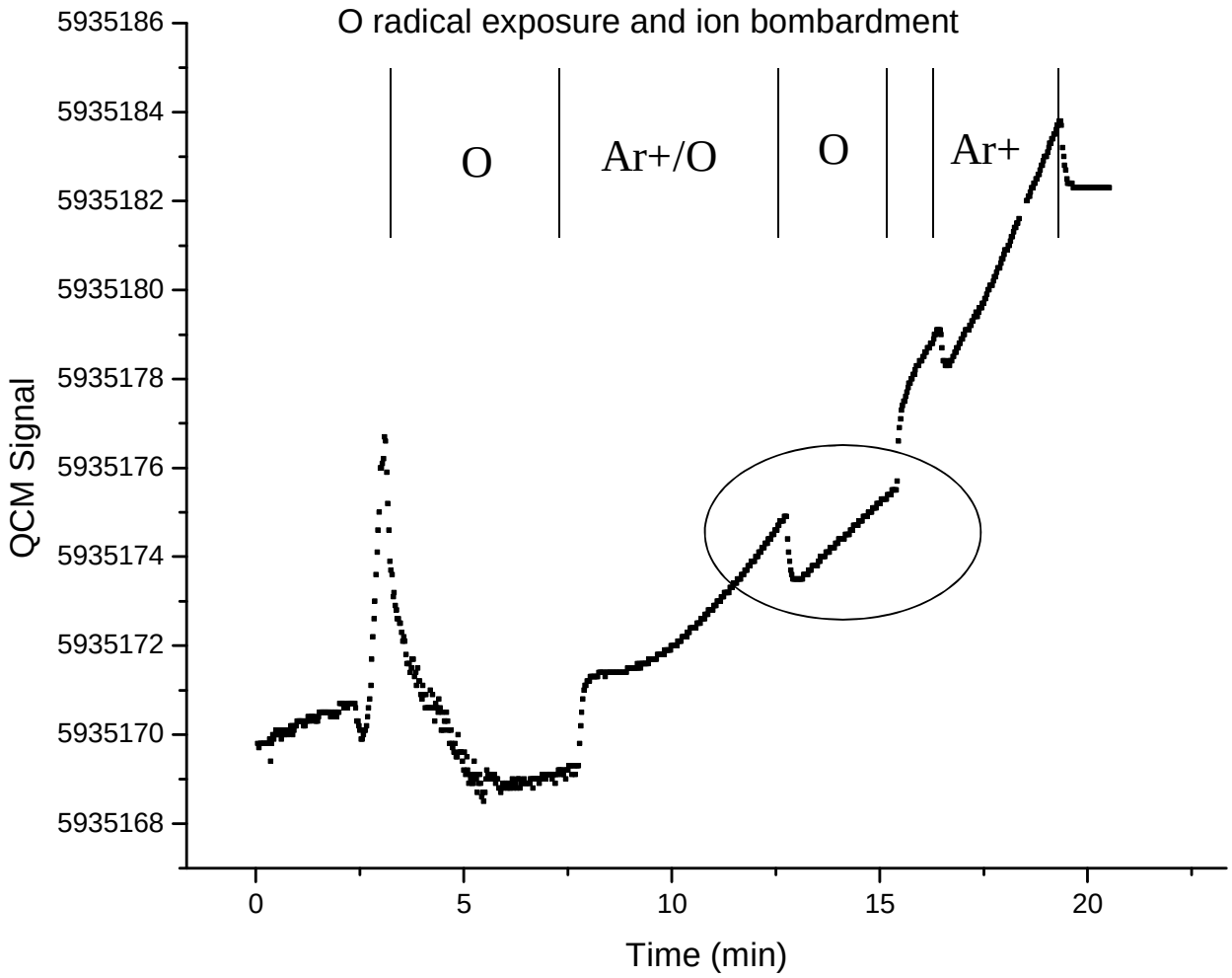

Figure 29: Raw QCM signal as a function of time for a Ru-coated QCM crystal exposed to O radicals and Ar^+ ions

The ability of O radicals to spontaneously etch Ru was not anticipated and has not been reported in the literature. This phenomenon was studied in more detail over a range of temperatures. The results are shown below in Figure 30. The small but measureable etch rate initially decreased as the temperature increased above room temperature, but then increased dramatically at and above 125°C.

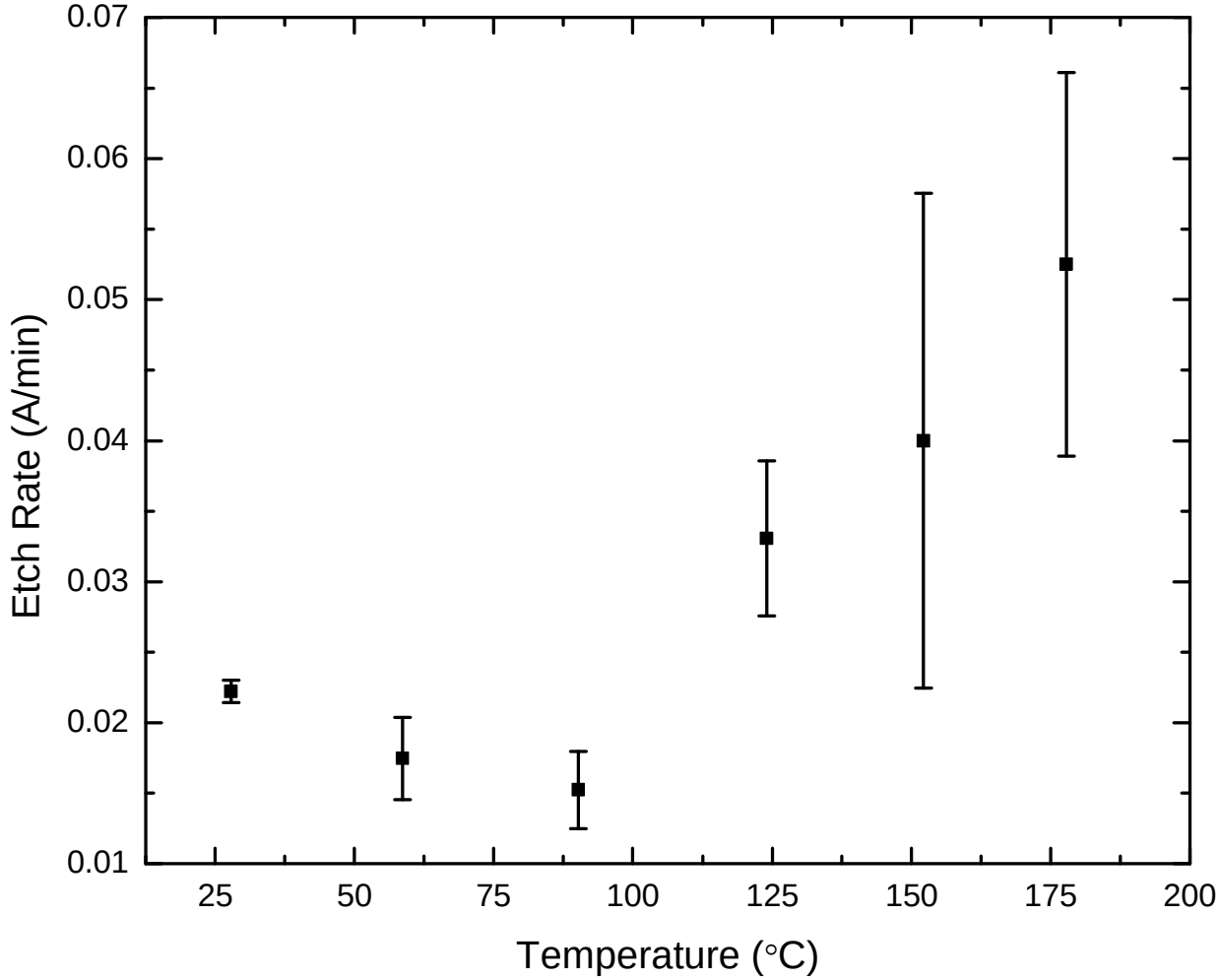

Figure 30: Spontaneous etch rate of Ru in the presence of O radicals as a function of temperature

The final detail to note is that the substrate temperature affected how quickly the spontaneous etch began. In Figure 31 below, the QCM response as a function of time is shown for a range of temperatures. The first part of each trace represents the period when the Ru surface was exposed to only O radicals from a 50/50 mixture of Ar/O_2 in the surface wave radical source. The step increase that occurs on each curve near the end is the point at which the ion gun was turned on. The behaviour of the curve before the ion gun was turned on is the portion of interest. Particularly for the room temperature experiment, the surface took much longer to reach its steady-state value than it did at higher temperatures. The 178°C curve also exhibits an interesting deviation from the other curves in that the uptake period where the surface was gaining mass, presumably through the adsorption of O radicals, was much longer than it was for lower temperatures, perhaps indicating that a temperature-dependent threshold for the O adsorption mechanism exists for this system.

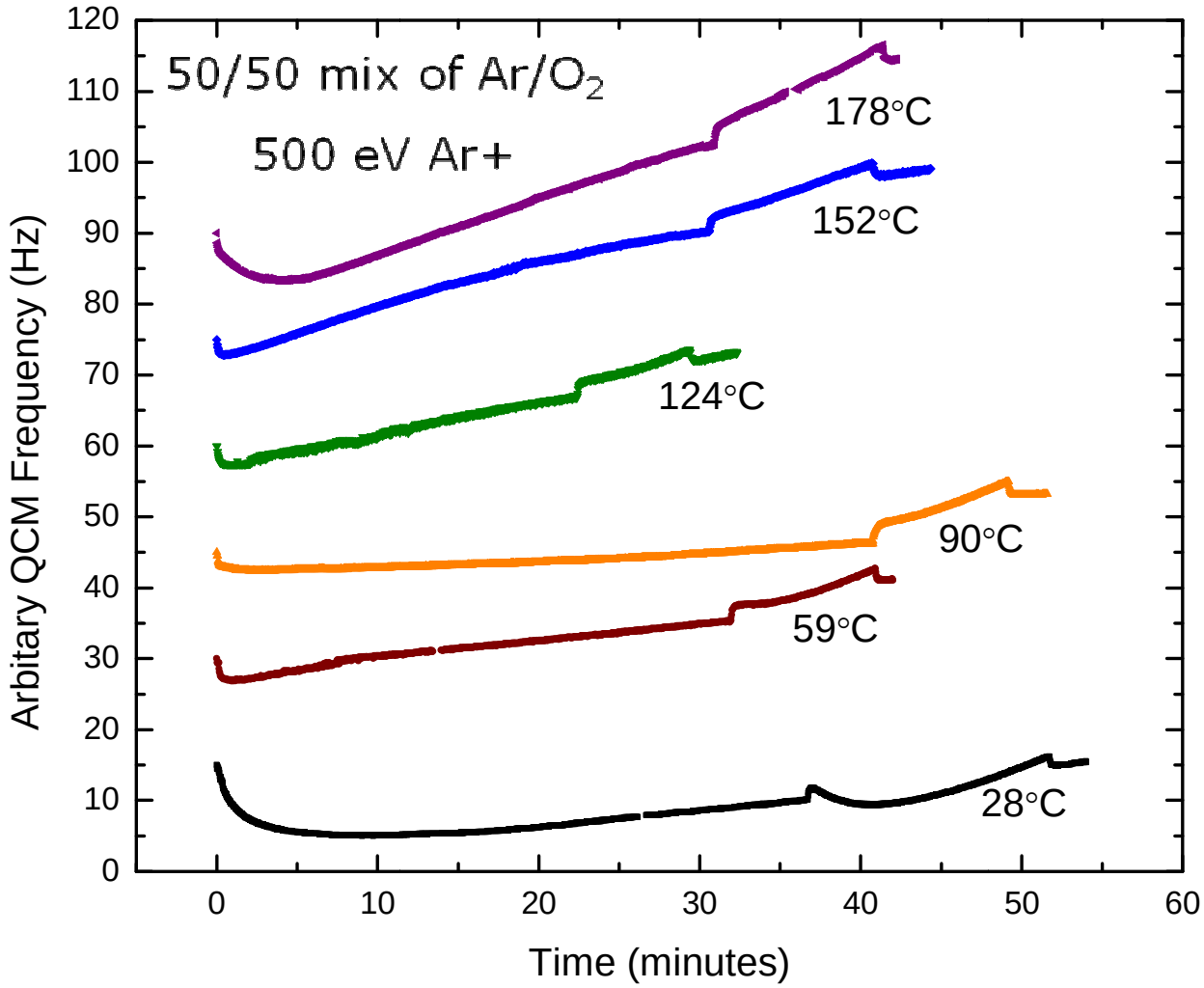

Figure 31: QCM traces of Ru etching in the presence of O radicals and O radicals combined with Ar^+ ions as a function of time for a range of temperatures

CONCLUSIONS

Ru is known to have two volatile oxidation products, RuO_3 and RuO_4, although the etch rate is negligible when Ru is exposed to an O_2 plasma discharge. The introduction of a small amount of additive gas, such as Cl_2, has been shown to increase the Ru etch rate sixfold. The reason for this dramatic shift in etching is poorly understood, primarily because it is difficult if not impossible to study plasma-surface interactions in a plasma environment. The unique capabilities of the beam system have made it possible to explore the mechanism of Ru etching. It has been shown that under 500 eV Ar^+ ion bombardment, the addition of O radicals lowered the etch rate by a factor of 2.5. This process was relatively insensitive to temperature over the range studied (room temperature to ~175°C). It was also shown that O radicals alone spontaneously etched Ru at a very slow rate over the entire temperature range.

CHAPTER 5: A STATISTICAL ANALYSIS OF POLYSILICON ETCHING AND GATE PROFILE EVOLUTION IN DUAL-DOPED POLYSILICON GATES

I completed a six-month internship in the research and development division of Texas Instruments in the fall of 2005 and conducted a portion of my Ph.D. research in their facilities. The following chapter contains the details of those experiments, which focused on statistical design and analysis of polysilicon etching experiments.

BACKGROUND

Dual-doped gate technology has extended the life of polysilicon as a gate material. Dual-doped polysilicon gates were introduced in the late 1980s. This approach reduces the threshold voltages needed to operate the device by independently tailoring the work functions of the gate for each channel in the device.[7, 54, 55]

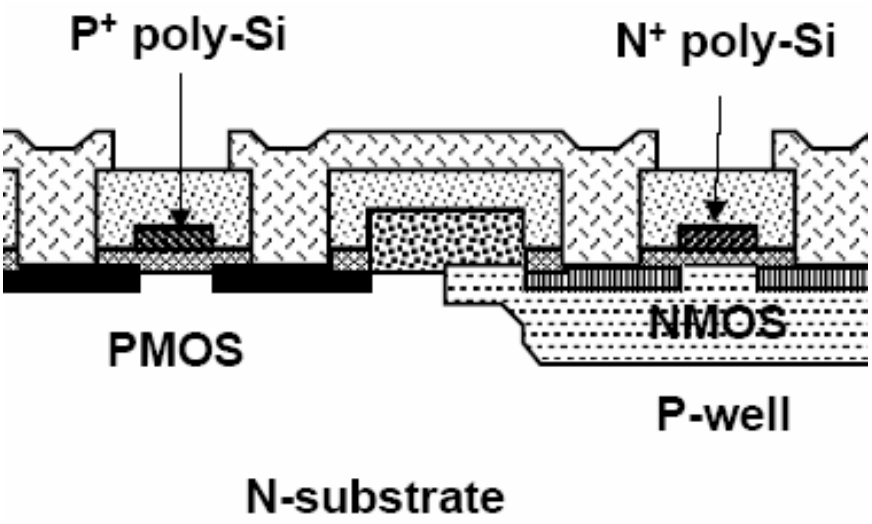

Figure 32: Illustration of dual-doped gate structure[7]

As dimensions shrink, the shape of gate becomes more important. Up to this point, the width of the gate (referred to as the critical dimension or CD) has been the primary concern for optimizing device performance. Smaller length scales enhance the effects of other features such as notches, "feet", sidewall angle, and substrate recess.[56]

Sub-90 nm process nodes require precise dimensional control of both the gate critical dimension (CD) and the profile shape. The 3 sigma variation in gate CD must be less than 5 nm for all gates. The 3 sigma variation in sidewall angle should be less than approximately 1 degree. This is inclusive of all sources of variation: across chip, across wafer, wafer-to-wafer, lot-to-lot, tool-to-tool, and day-to-day.[56-58]

It is well-known that doping affects the poly-Si etch rate, with n-doped poly-Si etching faster than undoped or p-doped poly-Si.[1, 59-68] The precise dimensional control required as device scaling continues is very difficult to achieve because of this etch rate difference. The difference in doping changes the etching behavior of the two gate structures. As a result, p+ and n+ gates on the same wafer take on different profiles (Figure 33), causing device performance to suffer.

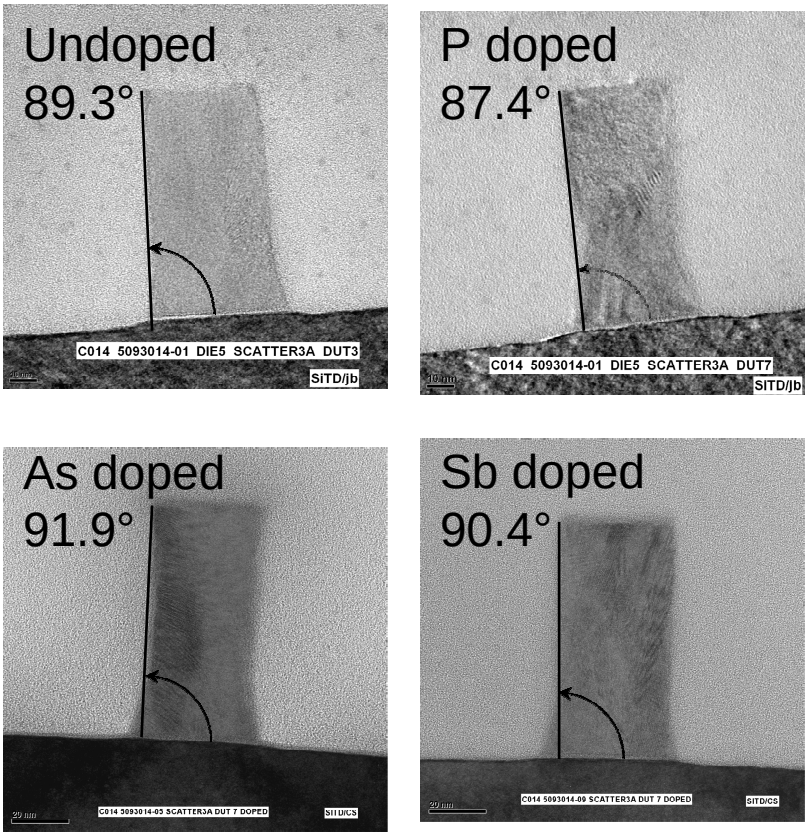

Figure 33: TEM images from four wafers with different doping characteristics and different sidewall angles

The goal of this research was to minimize the differences in the sidewall angle between gates with different dopants. Many variables affect the etching behavior of polysilicon, among them feature size, pattern density, dopant, doping level, annealing conditions, processing temperature, plasma frequency, power inputs, and etching chemistry.[69-71] These last two parameters are easiest to vary in an industrial setting when the overall process involves thousands of interrelated processing steps. In order to understand how the etching chemistry affects the etch rate of doped and undoped polysilicon, it is important to understand why etch rates differences are observed in the first place.

Several theories exist in the literature regarding why n-doped polysilicon etches faster than undoped polysilicon. Initial theories involved heating effects or the dopant atoms themselves reacting to form volatile products.[60, 63, 72] It was later realized that it was the additional electrons, rather than the donor atoms themselves, that were making the difference.

Berg et al. observed that for $CFCl_3$ discharges, the etch rates were not primarily dependent on the actual dopant concentration, but rather on the degree of activation of the dopants as measured by the sheet resistivity. They proposed that the electrical activity of the bulk and surface plays an important role in the rate of adsorption of active species and therefore on the etch rate.[71]

Mogab and Levinstein suggested that the effect of doping on the free carrier concentration is responsible. As with Berg et al., only electrically activated P-doped material exhibited an increased etch rate in C_2F_6-Cl_2 discharges. They note that the presence of free electrons stimulates etching, whereas holes have no effect.[61]

Baldi and Beardo confirm the theory that it is the active carrier concentration, or position of the Fermi level, that determines the etch rate by using Hall-effect measurements on wafers etched in CF_4-CF_3Cl-O_2 discharges. They point out that the same effect is observed for different dopant species (P and As) and for different etching species (F, Cl, and Br), leading them to conclude that the etch rate of polysilicon is determined by the rate of chemisorptions of halogen atoms, which in turn is influenced by the availability of free electrons.[65] With regard to the different halogen atoms, the effect is very strong for Cl, but is weak for F.[1] Of note, the etch rate enhancement is not observed unless the doping level is high enough to make the semiconductor degenerate.[73] This understanding of the nature of the etch process can now be used to select new chemistries for simultaneously etching both materials.

Even for much larger dimensions, dual-doped gates have always provided a processing challenge because of their different etching behaviors under the same processing conditions.[74, 75] While it is of course not possible to change the nature of the materials, it is possible to seek a processing space where the differences are minimized.

The gate etch process has three basic steps: 1) breakthrough, which removes the native oxide from the polysilicon, 2) the main etch step, which removes ~70% of unmasked polysilicon height without exposing the gate oxide, and 3) overetch, which removes the remaining polysilicon from the gate oxide.[74, 76, 77] The main etch step is the focus of this study. All other processing steps were held constant throughout the experiments.

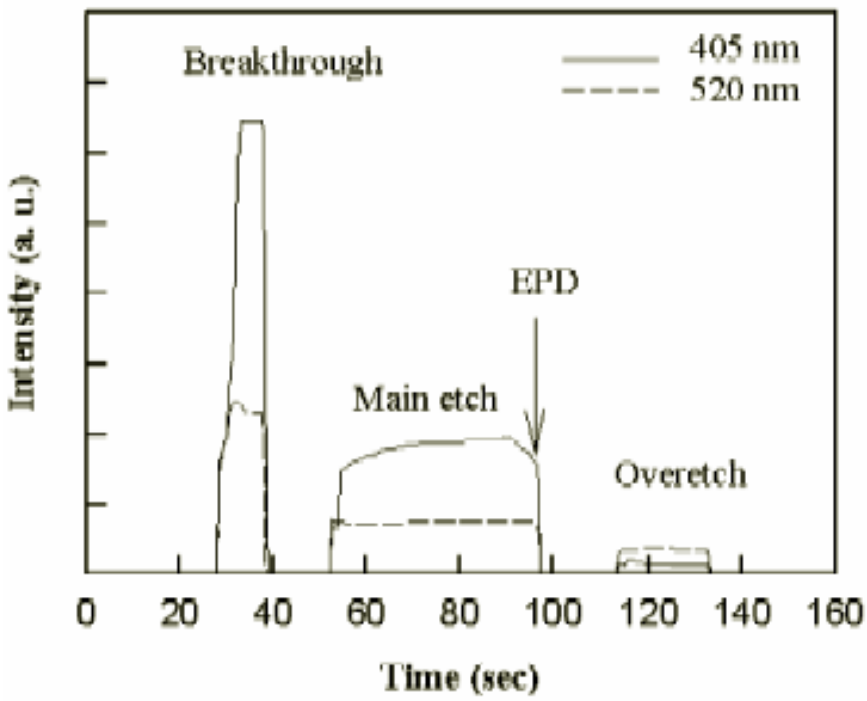

Figure 34: Typical endpoint detection trace of the three gate etch steps when simultaneously etching polysilicon of different doping types. EPD=endpoint detection.[76]

The chemistry in use for the main etch step when my experiments were conducted was a Cl_2-HBr-O_2 mixture. This mixture is standard in the industry for etching polysilicon, and it generally provides good profile control, small CD variation, and highly selective etching of polysilicon with respect to the mask and gate oxide.[78-81] However, the chemistry needs to be further optimized for sub-90 nm processes as the tolerances on acceptable variation become tighter. This chemistry is known to form SiO_xCl_y passivation layers on the feature sidewalls, helping to produce an anisotropic etch.[69, 82, 83] This passivation layer also deposits on the chamber walls, requiring frequent chamber cleaning.[78] The gate etch profile is primarily determined by the characteristics of the passivation layer.[80] It has been shown that the addition of CF_4 to the standard chemistry changes the nature of the sidewall film, generating a thicker, chlorine-rich SiO_x-CF_y mixed passivation layer on the silicon sidewalls and producing a subsequently more uniform etch between dense and isolated silicon structures[78-81, 84] It has been suggested that this might also apply to n^+- and p^+-doped polysilicon layers.[79, 81] The addition of CF_4 has the added benefit of keeping the chamber walls clean as well if the CF_4/O_2 ratio is kept around 4.[78, 79, 81]

In addition to chemistry, another main determiner of etch rates and profiles are the power inputs to the system. Based on the only two studies in the literature that directly address the simultaneous etching of dual-doped polysilicon gates,[74, 76] I determined that ion density (as determined by the source power) would be the only non-chemical parameter that I would study as it was the most influential factor.

In summary, a review of the literature suggested the following influential power and chemistry parameters for the main etch step:

- Adding fluorine-bearing species to the standard Cl_2-HBr-O_2 chemistry
- Varying the F/O_2 ratio
- Varying the ion density (source power)

EXPERIMENTAL METHODS

After clearly identifying the challenge—to minimize the etch rate and sidewall angle differences between simultaneously etched doped and undoped polysilicon gates and to minimize the across-wafer variance—the next step was choose the types of experiments I would run. I chose to do a set of sequential studies so that I could build upon my knowledge as I progressed through the experimentation process. I also chose to use design of experiments methodology so that the resulting data could be statistically analyzed and interpreted objectively, without bias with regard to my expectations of the outcome or misinterpretation of insignificant random noise.[85, 86]

All etching experiments were conducted on 200 mm wafers in the KFAB facility at Texas Instruments in Dallas, Texas, using a commercial high density plasma system made by Applied Materials, Inc. The decoupled plasma source (DPS2) silicon etch system is described in detail elsewhere.[79, 87] Thickness measurements taken with a KLA-Tencor OptiProbe ellipsometer were used to quantify the etch rate. Except for the parameters described in detail below, the remaining process conditions was kept constant (bias power=100 W, Cl_2=50 sccm, HBr=200 sccm, and pressure=5 mTorr).

DESIGNED EXPERIMENT #1: FACTORIAL DESIGN

FRACTIONAL FACTORIAL

A two-level fractional factorial design was used as a factor screening experiment to investigate the effects of source power, CHF_3, CF_4, and O_2 on the etch rate of phosphorus-doped and undoped polysilicon blanket films. The starting thickness was on the order of 2500 Å and the phosphorus-doped wafers were doped with a dose of 5E15 cm^{-2} at 40 keV. The initial design was a one-half fraction of the 2^4 design (a 2^{4-1} design, involving 8 runs for each type of wafer for 16 total runs). This design choice allowed me to determine which main effects were important, as well as identify if interactions between any of the factors was significant, something not possible with typical one-factor-at-a-time experimentation. The setting for each factor are shown in Table 1 below. The source power settings, CF_4, and O_2 settings were chosen based on the ranges found in literature[76, 79, 84] and the current baseline process. The He/O_2 ratio was 5:1, so a flow rate of 20 sccm He/O_2 contains 4 sccm of O_2. CHF_3 was available on the etch tool because it is used in the breakthrough

step to remove the native oxide from the polysilicon prior to the main etch. It was included as an alternative F-bearing gas, and the flow rate was set based on the minimum possible flow rate that the tool could produce.

Factor	Low	High
Power (W)	250	400
CF_4 (sccm)	0	25
CHF_3(sccm)	0	40
He/O_2 (sccm)	20	80

Table 1: High and low settings for each of the four factors studied in the fractional factorial design

The table of treatment combinations (known as the design matrix) is given in Table 2; a plus sign represents the high level of the factor and a minus sign, the low level. The runs were randomized, but are presented here in standard order. Highlighted run #5 represents the current process on record (POR). The design was build around this known good processing condition to maximize the likelihood of obtaining meaningful results, and to be able to compare with the current baseline process.

Run	Pattern	Power	CF4	He/O2	CHF3
1	−−−−	250	0	20	0
2	−−++	250	0	80	40
3	−+−+	250	25	80	0
4	−++−	250	25	20	40
5	**+−−+**	**400**	**0**	**80**	**0**
6	+−+−	400	0	20	40
7	++−−	400	25	20	0
8	++++	400	25	80	40

Table 2: Design matrix for fractional factorial study of etch rate. Highlighted run #5 represents the current process on record (POR).

The thickness of each film was measured just before etching at 17 locations across the wafer surface. Each wafer was etched for 20 seconds and then the thickness was measured again. The etch rate was calculated as the difference between the average thickness before and after etch divided by the amount of time etched.

The resulting etch rates are shown in **Error! Reference source not found.Error! Reference source not found.**, where etch rate is in units of Å/s. The factor levels have been coded for ease of later analysis. The results are presented in the randomized order in which they were run.

doping	source power	CF4	O2	CHF3	avg ER
1	1	-1	1	-1	31.86
1	-1	-1	-1	-1	25.44
1	-1	1	1	-1	25.06
1	-1	1	-1	1	23.42
1	-1	-1	1	1	24.04
1	1	-1	-1	1	29.76
1	1	1	1	1	30.86
1	1	1	-1	-1	31.90
-1	1	-1	1	-1	32.36
-1	-1	-1	-1	-1	25.50
-1	-1	1	1	-1	25.00
-1	-1	1	-1	1	23.63
-1	-1	-1	1	1	24.27
-1	1	-1	-1	1	28.88
-1	1	1	1	1	28.62
-1	1	1	-1	-1	30.62

Table 3: Etch rate results of Designed Experiment #1. Etch rate is in units of Å/s and the factor levels have been coded for ease of analysis. Randomized order.

In order to facilitate analysis of the results, the variables were converted from their original units to dimensionless coded variables according to the following formulas:

$$x_1 = \frac{power - (power_{low} + power_{high})/2}{(power_{high} - power_{low})/2}$$

$$x_2 = \frac{CF_4 - \left(CF_{4_{low}} + CF_{4_{high}}\right)/2}{\left(CF_{4_{high}} - CF_{4_{low}}\right)/2}$$

$$x_3 = \frac{O_2 - \left(O_{2_{low}} + O_{2_{high}}\right)/2}{\left(O_{2_{high}} - O_{2_{low}}\right)/2}$$

$$x_4 = \frac{CHF_3 - \left(CHF_{3_{low}} + CHF_{3_{high}}\right)/2}{\left(CHF_{3_{high}} - CHF_{3_{low}}\right)/2},$$

where $-1 \leq x_i \leq 1$. Coded design variables make the analysis and model fitting easier to interpret for several reasons. Because the model coefficients are all dimensionless, their magnitudes are directly comparable, and they measure the effect of changing each of the design factors over a one-unit interval. By having them all on a common scale, it is easy to identify the most important variables by simply comparing the relative size of the factor effects: the larger the effect, the more important the variable. In addition, all the parameters are estimated with the same precision, meaning the standard error for each coefficient is the same.[85] The standard error, which is used to calculate confidence intervals, is defined as the square root of the variance:

$$se(\hat{\beta}) = \sqrt{V(\hat{\beta})} = \sqrt{\frac{MS_E}{n2^k}},$$

where n is the number of observations and 2k is the number of treatments.

A statistical analysis of the etch rate data was performed using JMP. Each wafer type is treated as an individual data set, meaning that results are generated for two separate fractional designs and a prediction model is created for each wafer type. This approach makes it possible to see if the factors affect the two wafer types in different ways, and it makes it possible to find a design space where the differences between the two materials is minimized. The ratio of the doped etch rate to the undoped etch rate (d:un) is used for this purpose.[74]

Doped wafers

The initial JMP output from the screening analysis for the doped wafers is shown below in Figure 35 and Table 4. Because the JMP software is not capable of producing subscripts for the chemical formulas, they will be presented from this point forward both in the text and in figures without the subscript.

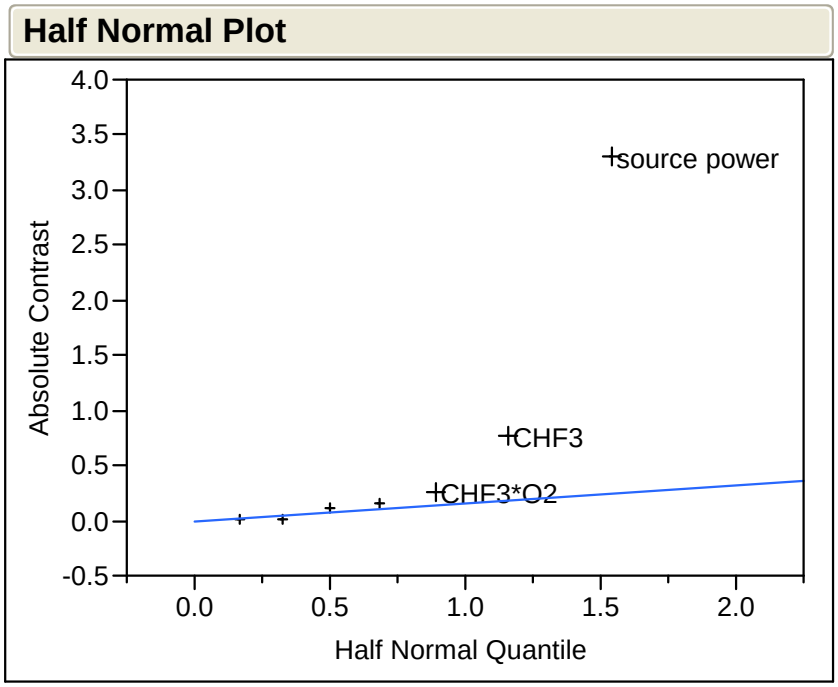

Figure 35: Half normal plot for the fractional factorial doped wafer etch rate data

Contrasts

Term	Contrast	Lenth t-Ratio	Individual p-Value	Aliases
source power	3.30179	21.26	0.0003*	
CHF3	-0.77354	-4.98	0.0088*	
O2	0.16211	1.04	0.2516	
CF4	0.01775	0.11	0.9225	
source power*CHF3	-0.01374	-0.09	0.9407	O2*CF4
source power*O2	0.10356	0.67	0.4690	CHF3*CF4
CHF3*O2	0.26649	1.72	0.0935	source power*CF4

Table 4: Table of contrasts for fractional factorial doped wafer etch rate data showing which terms are potentially significant and any confounded terms.

The half-normal probability plot of effects shows the absolute value of the effect estimates plotted against their cumulative normal probabilities. Effects that lie along the line are negligible, while large effects fall far from the line.

For the doped wafers, source power, CHF3, and CHF3*O2 are the important effects to include in the model. Surprisingly, CF4 had no effect on the etch rate. Because of the limited number of data points in the design, the interaction terms are all aliased with each other, meaning it is impossible to distinguish between one effect and another in the model. The 2^{4-1} fractional factorial design is a resolution IV design, meaning no main effect is aliased with any other main effect or with any two-

factor interaction, but two-factor interactions are aliased with each other. In this case, it is not possible to tell if the effect observed for the CHF3*O2 interaction is actually from the CHF3*O2 interaction or is rather from the CF4*source power interaction. Additional experimentation was needed to dealias these terms, which is described in more detail below.

The same information about which terms contribute to the resulting etch rate can be obtained from inspecting the p-values of the effects in the table of contrasts. The p-value is the probability of obtaining a test statistic at least as extreme as the one that was actually observed, assuming that the null hypothesis is true. One rejects the null hypothesis if the p-value is smaller than or equal to the chosen significance level α (alpha). A p-value less than α=.1 is considered marginally significant, a value less than α=.05 is significant, and a value less than α=.01 is highly significant. The individual p-value for source power was <0.0001, for CHF3 was 0.0084, and for CHF3*O2 was 0.0941.

A reduced model was constructed, incorporating only the terms that do not lie on the half-normal line. The JMP output is shown in Table 5. According to Montgomery et. al., it was not necessary to include the hierarchical terms in the model (i.e., if a model contains high-order terms, it is common practice to include all of the lower-order terms that contain it),[88] so only significant terms were included.

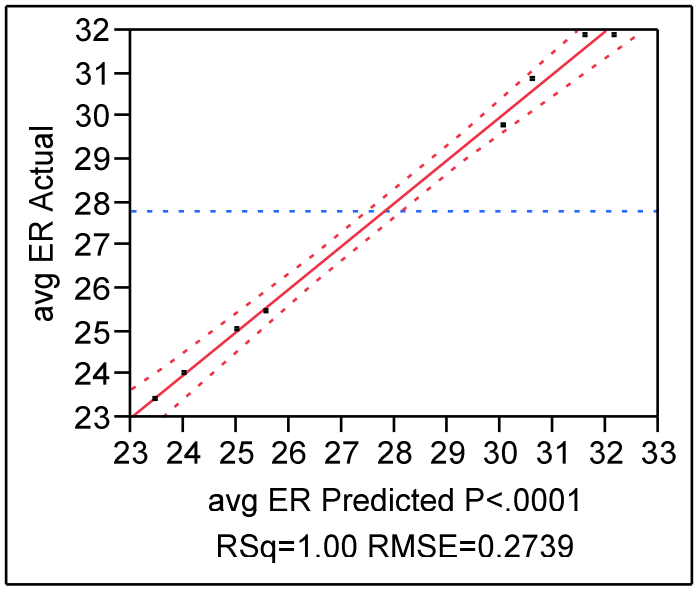

Summary of Fit

RSquare	0.996769
RSquare Adj	0.994346
Root Mean Square Error	0.273883
Mean of Response	27.79215
Observations (or Sum Wgts)	8

Analysis of Variance

Source	DF	Sum of Squares	Mean Square	F Ratio

Source	DF	Sum of Squares	Mean Square	F Ratio
Model	3	92.569610	30.8565	411.3556
Error	4	0.300047	0.0750	**Prob > F**
C. Total	7	92.869658		<.0001*

Parameter Estimates

Term	Estimate	Std Error	t Ratio	Prob>|t|
Intercept	27.792151	0.096832	287.01	<.0001*
source power	3.3017904	0.096832	34.10	<.0001*
CHF3	-0.77354	0.096832	-7.99	0.0013*
CHF3*O2	0.266489	0.096832	2.75	0.0513

Effect Tests

Source	Nparm	DF	Sum of Squares	F Ratio	Prob > F
source power	1	1	87.214561	1162.677	<.0001*
CHF3	1	1	4.786919	63.8155	0.0013*
CHF3*O2	1	1	0.568131	7.5739	0.0513

Press

Press	Press RMSE
1.2001892699	0.38732888

Table 5: JMP output for least squares regression analysis of fractional factorial doped wafers reduced model

The CHF3*O2 term is just beyond the (somewhat arbitrary) cutoff for statistical significance and is aliased with the source power*CF4 term. It is clear that source power and CHF3 have an impact on the etch rate, but because of the marginal significance of the interaction term and the aliasing, the way in which these two terms interact is unclear. In order to clarify the situation, additional experimentation was conducted, which is described in detail after the analysis of the undoped wafer results.

Undoped wafers

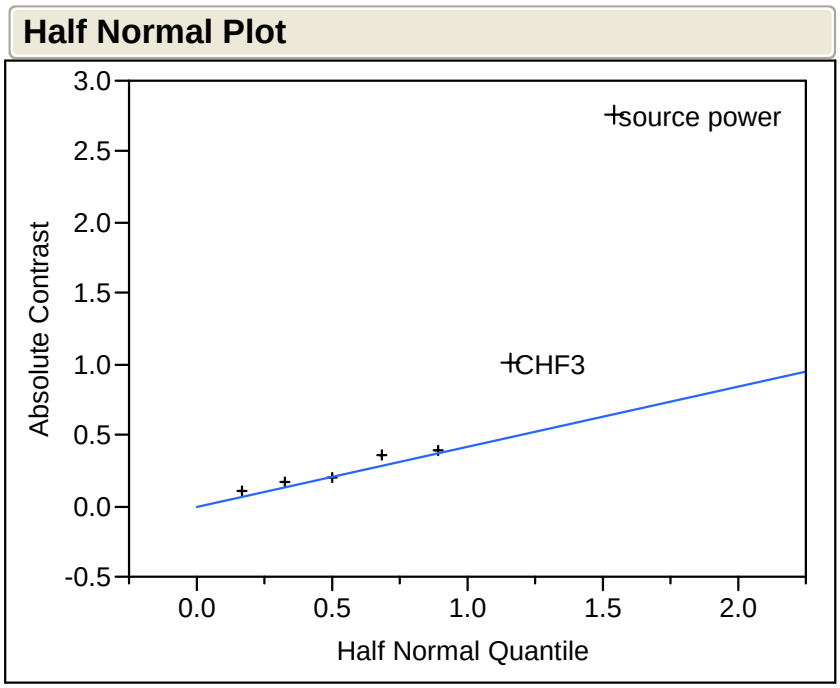

Figure 36: Half normal plot for the fractional factorial undoped wafer etch rate data

Contrasts

Term	Contrast		Lenth t-Ratio	Individual p-Value	Aliases
source power	2.75968		6.55	0.0052*	
CHF3	-1.00855		-2.39	0.0419*	
CF4	-0.39114		-0.93	0.2981	
O2	0.20203		0.48	0.6889	
source power*CHF3	-0.35946		-0.85	0.3333	CF4*O2
source power*CF4	-0.10662		-0.25	0.8324	CHF3*O2
CHF3*CF4	0.16845		0.40	0.7381	source power*O2

Table 6: Table of contrasts for fractional factorial undoped wafer etch rate data showing which terms are potentially significant and any confounded terms.

A reduced model was constructed as above containing only the significant terms (Table 7).

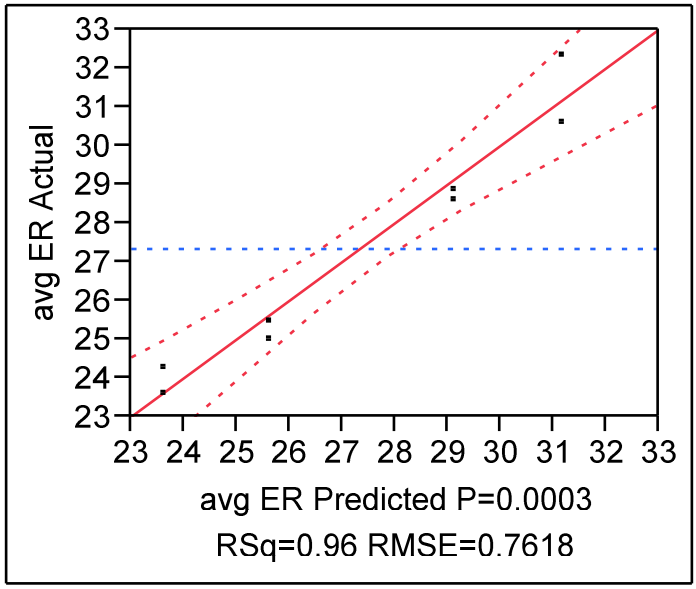

Summary of Fit

RSquare	0.959675
RSquare Adj	0.943544
Root Mean Square Error	0.761847
Mean of Response	27.35946
Observations (or Sum Wgts)	8

Analysis of Variance

Source	DF	Sum of Squares	Mean Square	F Ratio
Model	2	69.063922	34.5320	59.4957
Error	5	2.902055	0.5804	**Prob > F**
C. Total	7	71.965977		0.0003*

Lack Of Fit

Source	DF	Sum of Squares	Mean Square	F Ratio
Lack Of Fit	1	1.0336683	1.03367	2.2130
Pure Error	4	1.8683871	0.46710	**Prob > F**
Total Error	5	2.9020553		0.2111
				Max RSq
				0.9740

Parameter Estimates

Term	Estimate	Std Error	t Ratio	Prob>|t|
Intercept	27.359463	0.269354	101.57	<.0001*
source power	2.7596765	0.269354	10.25	0.0002*
CHF3	-1.008551	0.269354	-3.74	0.0134*

Press

Press	Press RMSE
7.4292615951	0.96366887

Table 7: JMP output for least squares regression analysis of fractional factorial undoped wafers reduced model

It is clear from the initial analysis of the fractional factorial data that source power and CHF3 are the most important factors affecting the etch rate. Increasing source power enhances the etch rate, while increasing CHF3 suppresses the etch rate. Oxygen appeared to have an enhancing effect on the etch rate of doped wafers in the presence of CHF3, but this cannot be stated with certainty without further experimentation. The predictive power of the doped model is much higher than the undoped model (as determined by the value of the PRESS statistic, smaller is better), indicating there is a source of variation present in the data that has not been taken into account by the model. PRESS is an acronym for Prediction Error Sum of Squares, which is computed as the sum of the squared prediction errors obtained by predicting the *i*th data point with a model that includes all observations except the *i*th one.[85, 89]

In order to dealias the interaction terms for the doped wafer data, the original fractional factorial was augmented with a foldover design containing 16 more wafers; that is, the other half of the one-half fraction was run to create a full 2^4 factorial design.

FULL FACTORIAL

With a full factorial design, it is possible to estimate each main effects as well as any interactions without having them confounded with other terms. According to the sparsity of effects principle, higher order interactions (e.g., CHF3*CF4*O2) will typically be negligible and their mean squares can be used to estimate the random error. The foldover design matrix and the resulting etch rates are shown in Table 8.

doping	source power	CF4	O2	CHF3	avg ER
1	-1	-1	1	-1	25.16
1	1	-1	1	1	30.36
1	-1	1	1	1	23.81
1	1	1	1	-1	31.53
1	-1	-1	-1	1	23.82
1	1	-1	-1	-1	31.46
1	-1	1	-1	-1	25.30
1	1	1	-1	1	29.93
-1	-1	-1	1	-1	25.80
-1	1	-1	1	1	30.78
-1	-1	1	1	1	23.98
-1	1	1	1	-1	32.32
-1	-1	-1	-1	1	23.99
-1	1	-1	-1	-1	32.23
-1	-1	1	-1	-1	25.45

Table 8: Etch rate results of foldover portion of Designed Experiment #1. Etch rate is in units of Å/s and the factor levels have been coded for ease of analysis. Randomized order.

The foldover data was combined with the original fractional factorial data, and a JMP screening analysis was conducted on the full data sets for the doped and undoped wafers, just as was done for the fractional factorial portion.

Doped wafers

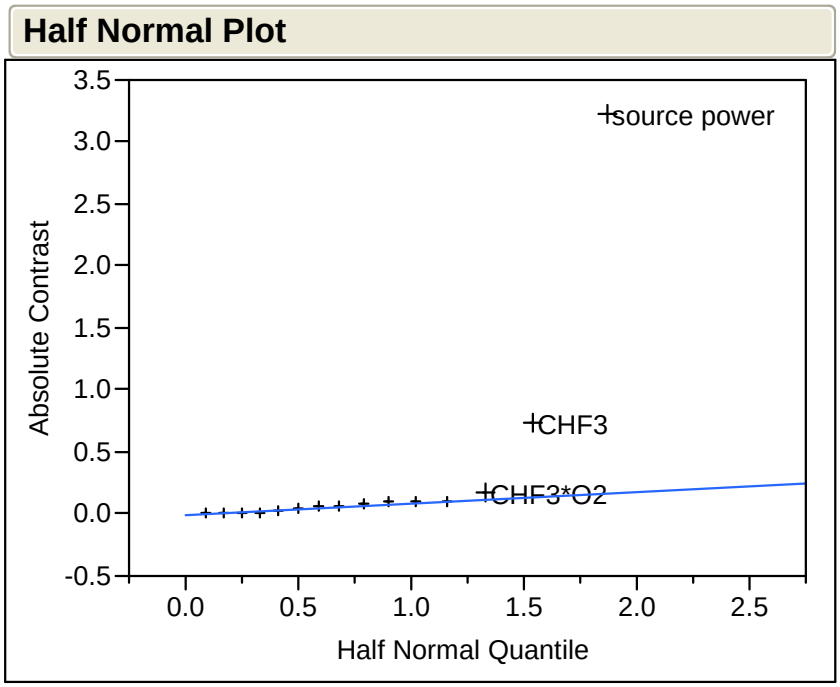

Figure 37: Half normal plot for the full factorial doped wafer etch rate data

Contrasts

Term	Contrast	Lenth t-Ratio	Individual p-Value
source power	3.22634	36.03	<.0001*
CHF3	-0.73224	-8.18	0.0007*
O2	0.10241	1.14	0.2408
CF4	-0.00553	-0.06	0.9566
source power*CHF3	0.00103	0.01	0.9910
source power*O2	0.09233	1.03	0.2891
CHF3*O2	0.16412	1.83	0.0851
source power*CF4	0.10237	1.14	0.2410
CHF3*CF4	0.01123	0.13	0.9125
O2*CF4	-0.01477	-0.16	0.8829
source power*CHF3*O2	0.02328	0.26	0.8172
source power*CHF3*CF4	0.05969	0.67	0.5002
source power*O2*CF4	-0.04130	-0.46	0.6839
CHF3*O2*CF4	0.07545	0.84	0.3742
source power*CHF3*O2*CF4	0.06001	0.67	0.4886

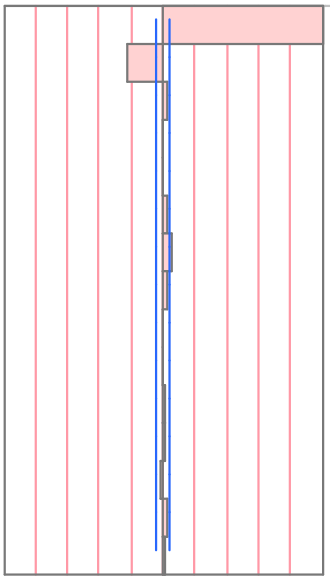

Table 9: Table of contrasts for the full factorial doped wafer etch rate data showing which terms are potentially significant

The same terms are significant for the full factorial data set. The interaction term CHF3*O2 was indeed responsible for the observed effect. It was necessary to complete the full factorial design to determine this. The reduced model is shown below in Table 10.

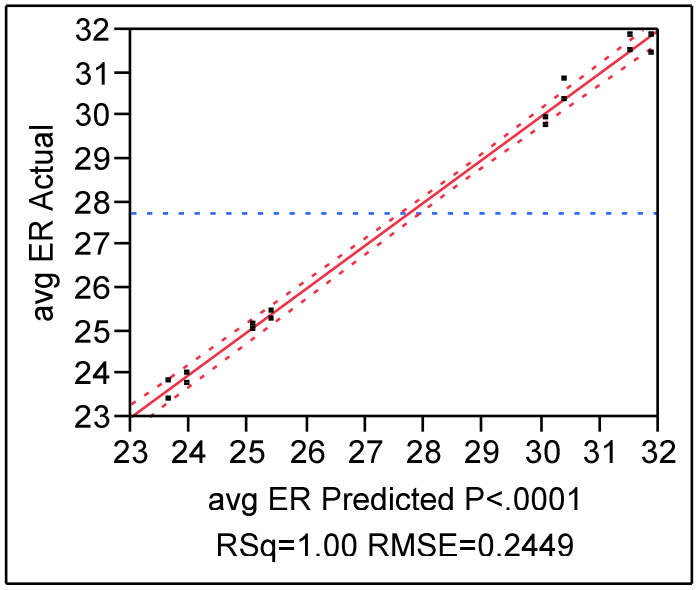

Summary of Fit

RSquare	0.995918
RSquare Adj	0.994898
Root Mean Square Error	0.244873
Mean of Response	27.73215
Observations (or Sum Wgts)	16

Analysis of Variance

Source	DF	Sum of Squares	Mean Square	F Ratio
Model	3	175.55775	58.5193	975.9294
Error	12	0.71955	0.0600	**Prob > F**
C. Total	15	176.27730		<.0001*

Lack Of Fit

Source	DF	Sum of Squares	Mean Square	F Ratio
Lack Of Fit	4	0.31288685	0.078222	1.5388
Pure Error	8	0.40666418	0.050833	**Prob > F**
Total Error	12	0.71955103		0.2795
				Max RSq
				0.9977

Parameter Estimates

Term	Estimate	Std Error	t Ratio	Prob>|t|
Intercept	27.732145	0.061218	453.01	<.0001*
source power	3.2263364	0.061218	52.70	<.0001*
CHF3	-0.732241	0.061218	-11.96	<.0001*
O2*CHF3	0.1641232	0.061218	2.68	0.0200*

Effect Tests

Source	Nparm	DF	Sum of Squares	F Ratio	Prob > F
source power	1	1	166.54794	2777.531	<.0001*
CHF3	1	1	8.57883	143.0696	<.0001*
O2*CHF3	1	1	0.43098	7.1875	0.0200*

Press

Press	Press RMSE
1.2792018316	0.28275451

Table 10: JMP output for least squares regression analysis of full factorial doped wafer reduced model

The PRESS statistic has increased a bit from 1.20 to 1.28, indicating the predictive value of this model has degraded a bit for the larger dataset.

Undoped wafers

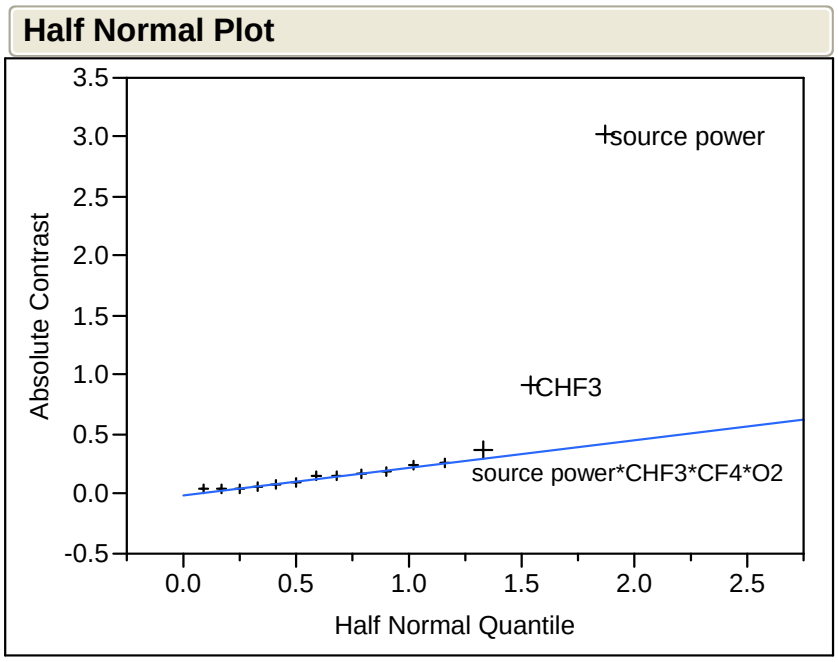

Figure 38: Half normal plot for the full factorial undoped wafer etch rate data

Contrasts

Term	Contrast	Lenth t-Ratio	Individual p-Value
source power	3.03210	13.33	0.0003*
CHF3	-0.92390	-4.06	0.0066*
CF4	-0.23946	-1.05	0.2678
O2	0.15548	0.68	0.4679
source power*CHF3	-0.18938	-0.83	0.3712
source power*CF4	-0.05265	-0.23	0.8303
CHF3*CF4	0.07130	0.31	0.7714
source power*O2	0.09715	0.43	0.6921
CHF3*O2	-0.05396	-0.24	0.8269
CF4*O2	-0.17008	-0.75	0.4227
source power*CHF3*CF4	0.04655	0.20	0.8484
source power*CHF3*O2	-0.15168	-0.67	0.4846
source power*CF4*O2	-0.08465	-0.37	0.7293
CHF3*CF4*O2	-0.27243	-1.20	0.2152
source power*CHF3*CF4*O2	-0.37539	-1.65	0.1056

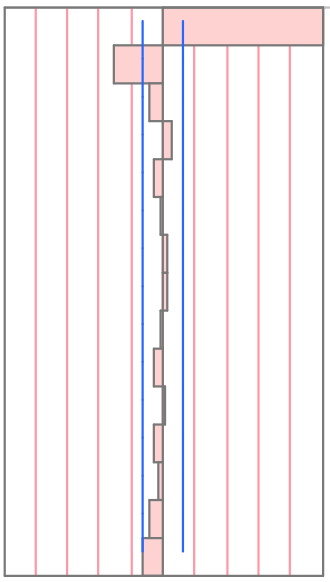

Table 11: Table of contrasts for the full factorial undoped wafer etch rate data showing which terms are potentially significant

The reduced model for the undoped wafers is shown in Table 12.

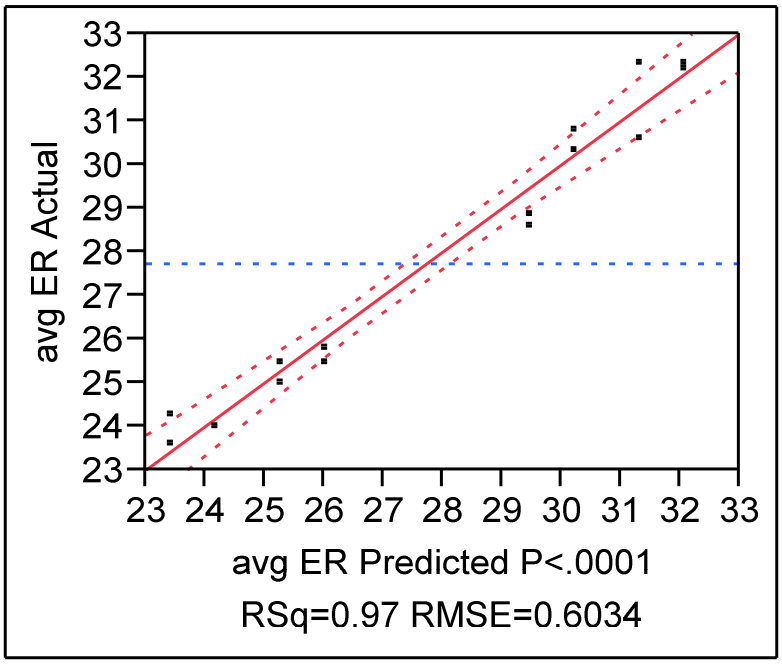

Summary of Fit

RSquare	0.973897
RSquare Adj	0.967371
Root Mean Square Error	0.603399
Mean of Response	27.73485
Observations (or Sum Wgts)	16

Analysis of Variance

Source	DF	Sum of Squares	Mean Square	F Ratio
Model	3	163.01038	54.3368	149.2397
Error	12	4.36909	0.3641	**Prob > F**
C. Total	15	167.37947		<.0001*

Parameter Estimates

Term	Estimate	Std Error	t Ratio	Prob>|t|
Intercept	27.734849	0.15085	183.86	<.0001*
source power	3.0321029	0.15085	20.10	<.0001*
CHF3	-0.923897	0.15085	-6.12	<.0001*
source power*CF4*O2*CHF3	-0.375386	0.15085	-2.49	0.0285*

Effect Tests

Source	Nparm	DF	Sum of Squares	F Ratio	Prob > F
source power	1	1	147.09837	404.0157	<.0001*
CHF3	1	1	13.65737	37.5109	<.0001*
source power*CF4*O2*CHF3	1	1	2.25463	6.1925	0.0285*

Press

Press	Press RMSE

Press	Press RMSE
7.7672686243	0.6967455

Table 12: JMP output for least squares regression analysis of full factorial undoped wafer reduced model

The PRESS statistic has increased in this case as well from 7.43 to 7.77. It is very unlikely that the presence of the 4-factor interaction term is actually explaining a real 4-way interaction effect. This term is rarely if ever significant when a full factorial design is used to study a physical system.[85] Instead, what this result is indicating is that there is a consistent, measurable component of variation in the system that has not been accounted for by the four design factors (source power, CF4, O2, CF3). This source of variation needs to be identified for the model to be useful in explaining or predicting the behavior of the studied system.

RESIDUAL ANALYSIS

One way to identify this unknown component of variation is through a residual analysis. Although the R^2 and R^2adjusted values look good for both models and all the model terms are significant, it is important to check the adequacy of the model before it is adopted, especially with the suspicious 4-way interaction term in the undoped model. This check is done with a residual analysis. A residual is the difference between the actual and predicted value of an observation. Two assumptions were made in the analysis of variance procedure that need to be tested. It was assumed that the errors (residuals) were normally and independently distributed with mean zero and constant but unknown variance. Analyzing the residuals will reveal if these assumptions have been violated. If the model is adequate, the residuals should be normally distributed, structureless, and display constant variance across the levels of the factors and the response. This analysis is done graphically.

The first plot to investigate is the residual by predicted plot, shown below in Figure 39 for both doped and undoped wafers.

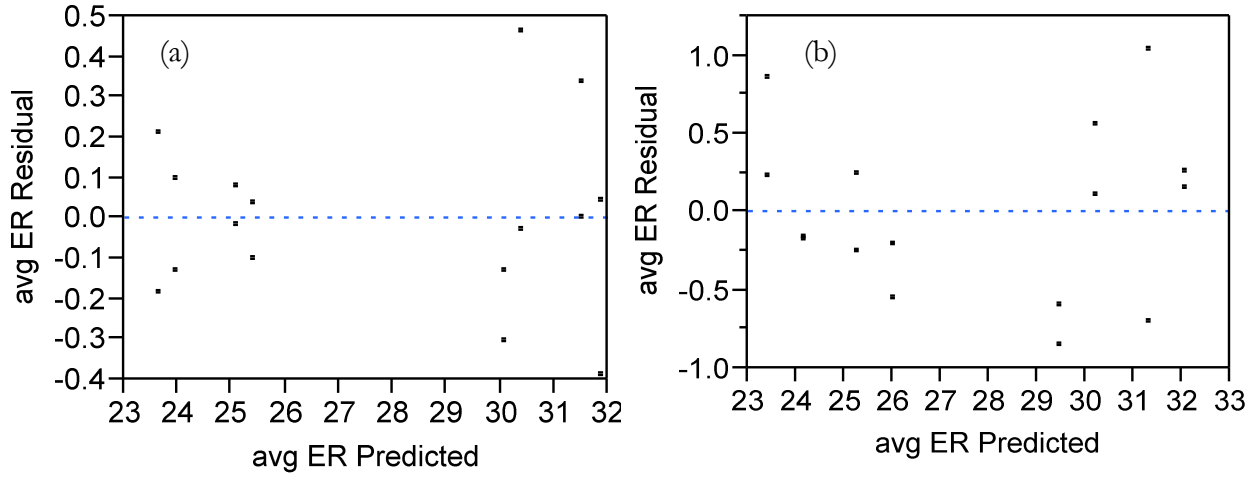

Figure 39: Residual by predicted plots for (a) doped and (b) undoped wafers

The residuals in both plot above show some structure that is concerning. The variance is larger at higher etch rates, indicating the homogeneous variance assumption may be violated, and there appears to be a downward-trending pattern at lower etch rates for the undoped wafers.

The normality assumption is tested next, using the studentized residuals, which normalizes the variance to a value of unity if the model is correct. Data is given first for the doped wafers (Table 13), then the undoped wafers (Table 14).

Test of Normality Assumption

DOPED WAFERS

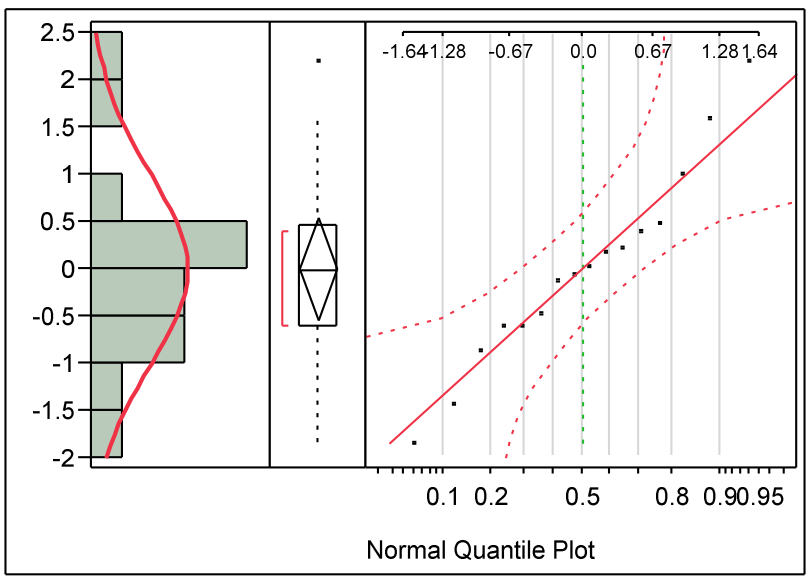

Normal(-2e-15,1.0328)

Moments

Mean	-2.07e-15
Std Dev	1.0327956
Std Err Mean	0.2581989
Upper 95% Mean	0.5503379
Lower 95% Mean	-0.550338
N	16

Fitted Normal
Parameter Estimates

Type	Parameter	Estimate	Lower 95%	Upper 95%
Location	μ	-2.07e-15	-0.550338	0.5503379
Dispersion	σ	1.0327956	0.7629311	1.5984486

-2log(Likelihood) = 45.4386494007794

Goodness-of-Fit Test

Shapiro-Wilk W Test

W	Prob<W
0.976079	0.9249

Note: Ho = The data is from the Normal distribution. Small p-values reject Ho.

Table 13: JMP output testing the normality assumption for the residuals of the doped wafer model

UNDOPED WAFERS

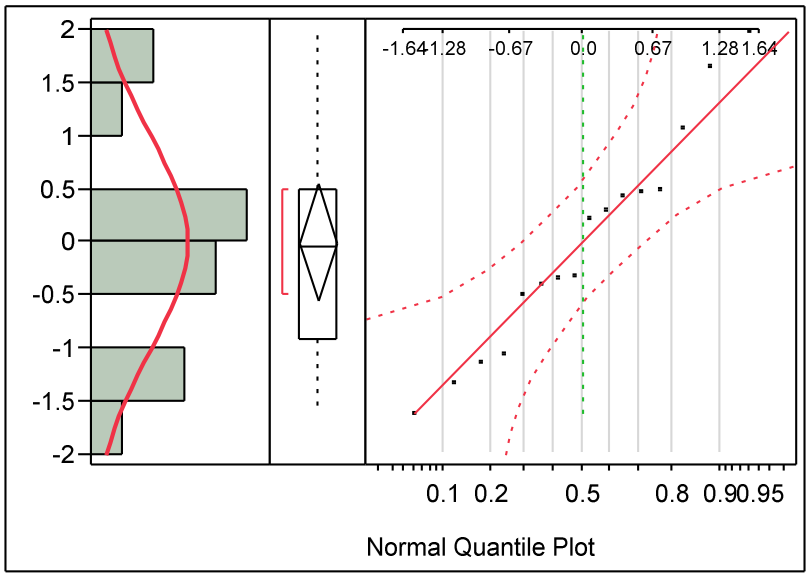

Normal(-4e-15,1.0328)

Moments

Mean	-3.84e-15
Std Dev	1.0327956
Std Err Mean	0.2581989
Upper 95% Mean	0.5503379
Lower 95% Mean	-0.550338
N	16

Fitted Normal
Parameter Estimates

Type	Parameter	Estimate	Lower 95%	Upper 95%
Location	μ	-3.84e-15	-0.550338	0.5503379
Dispersion	σ	1.0327956	0.7629311	1.5984486

-2log(Likelihood) = 45.438649400768

Goodness-of-Fit Test

Shapiro-Wilk W Test

W	Prob<W
0.964835	0.7496

Note: Ho = The data is from the Normal distribution. Small p-values reject Ho.

Table 14: JMP output testing the normality assumption for the residuals of the undoped wafer model

Both sets of residuals are normally distributed, so that model assumption has not been violated. The final component of the residual analysis involves plotting the residuals as a function of each of the factors. A series of statistical tests for equality of variance is included after each residual plot to quantify any observed nonhomogeneity. The results for the doped wafer model are shown below in Table 15.

Test of Equal Variance Assumption

DOPED WAFERS

Oneway Analysis of Studentized Resid avg ER By doping By source power doping=1

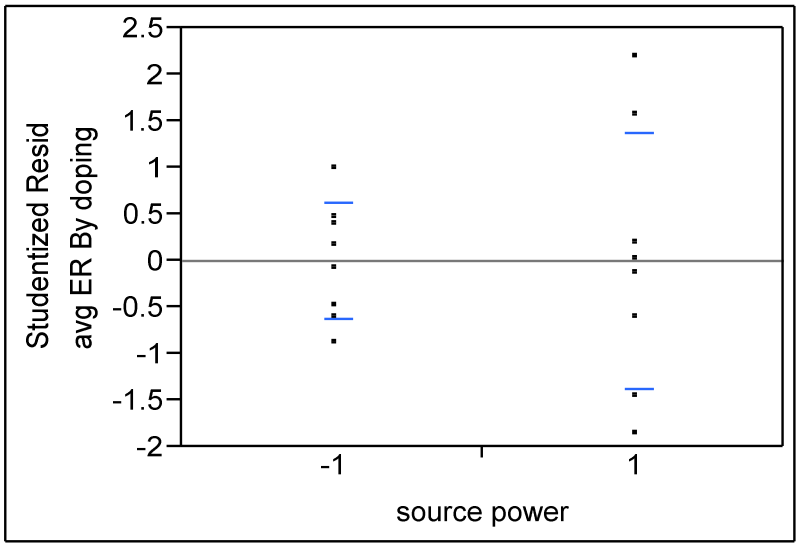

Tests that the Variances are Equal

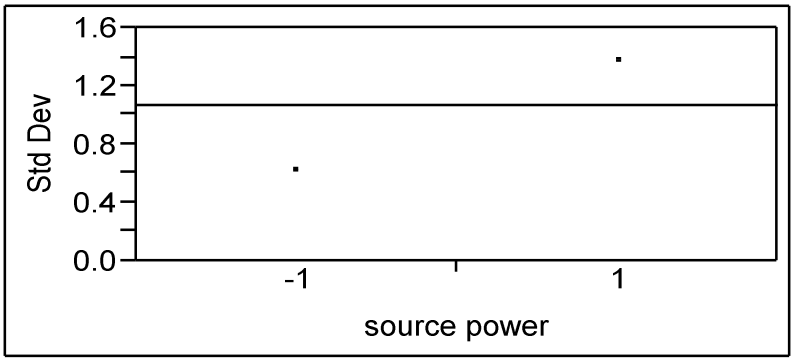

Level	Count	Std Dev	MeanAbsDif to Mean	MeanAbsDif to Median
-1	8	0.629181	0.508790	0.508790
1	8	1.374717	1.004409	1.004409

Test	F Ratio	DFNum	DFDen	p-Value
O'Brien[.5]	3.3252	1	14	0.0896
Brown-Forsythe	2.3281	1	14	0.1493
Levene	2.3481	1	14	0.1477
Bartlett	3.6406	1	.	0.0564
F Test 2-sided	4.7739	7	7	0.0562

Oneway Analysis of Studentized Resid avg ER By doping By CF4 doping=1

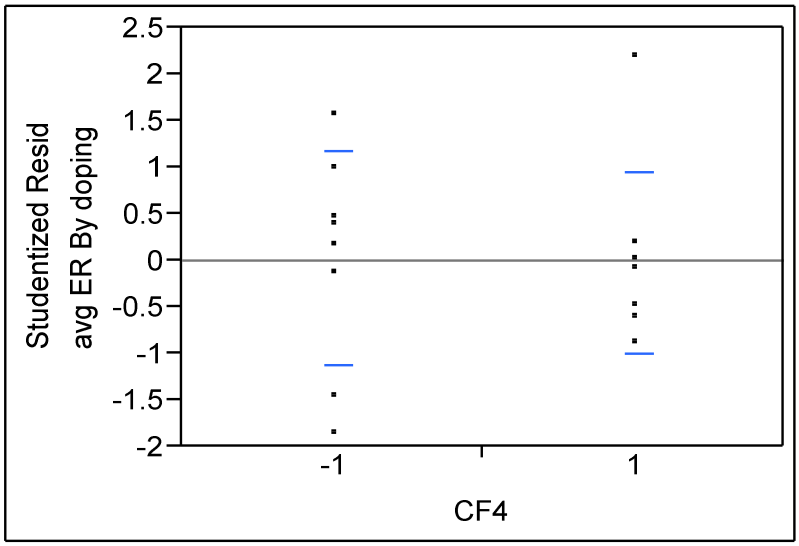

Tests that the Variances are Equal

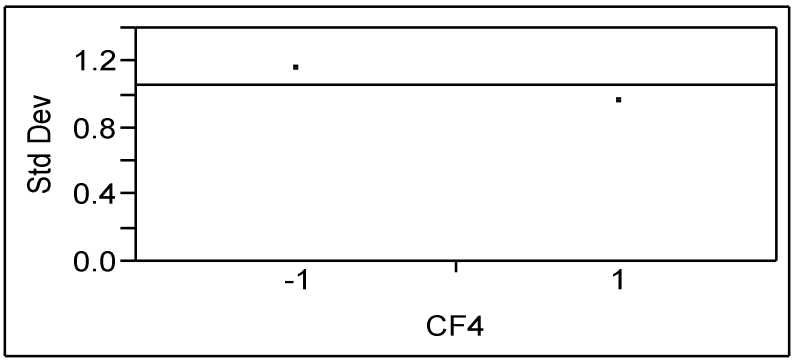

Level	Count	Std Dev	MeanAbsDif to Mean	MeanAbsDif to Median
-1	8	1.156995	0.8723466	0.8338575
1	8	0.972379	0.6278115	0.6178799

Test	F Ratio	DFNum	DFDen	p-Value
O'Brien[.5]	0.1744	1	14	0.6826
Brown-Forsythe	0.3107	1	14	0.5860
Levene	0.4962	1	14	0.4927
Bartlett	0.1964	1	.	0.6576
F Test 2-sided	1.4158	7	7	0.6579

Oneway Analysis of Studentized Resid avg ER By doping By O2 doping=1

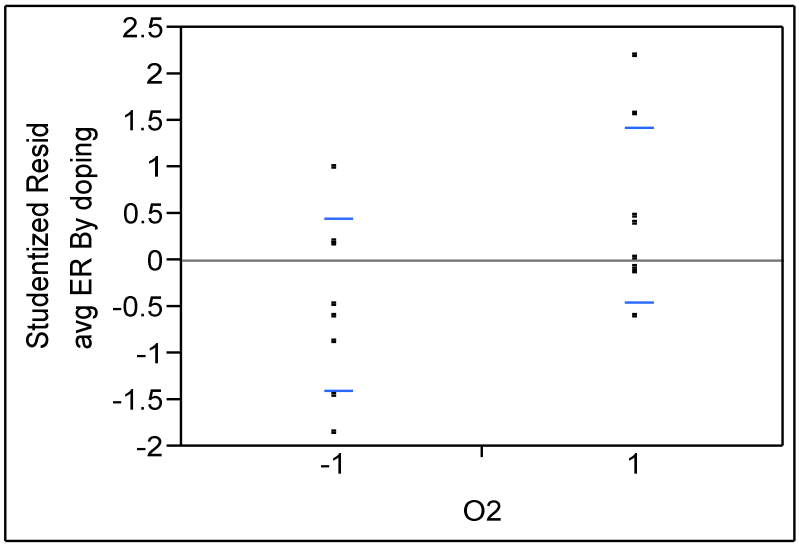

Tests that the Variances are Equal

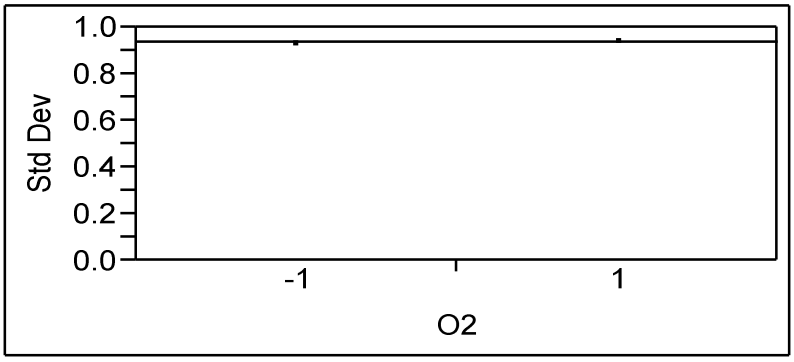

Level	Count	Std Dev	MeanAbsDif to Mean	MeanAbsDif to Median
-1	8	0.9277380	0.7083480	0.7078344
1	8	0.9444218	0.7042805	0.6784448

Test	F Ratio	DFNum	DFDen	p-Value
O'Brien[.5]	0.0030	1	14	0.9570
Brown-Forsythe	0.0093	1	14	0.9247
Levene	0.0002	1	14	0.9885
Bartlett	0.0021	1	.	0.9637

Test	F Ratio	DFNum	DFDen	p-Value
F Test 2-sided	1.0363	7	7	0.9637

Oneway Analysis of Studentized Resid avg ER By doping By CHF3 doping=1

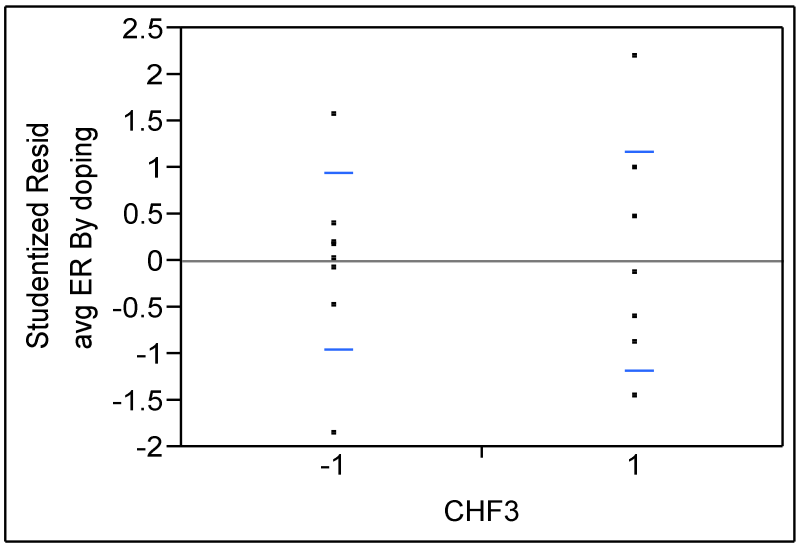

Tests that the Variances are Equal

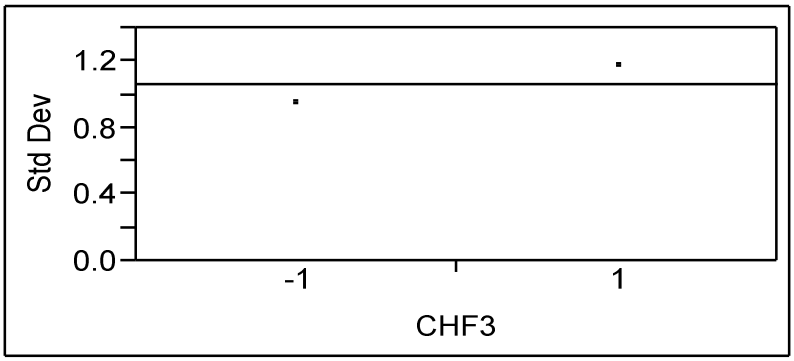

Level	Count	Std Dev	MeanAbsDif to Mean	MeanAbsDif to Median
-1	8	0.953318	0.5973839	0.5917105
1	8	1.173414	0.9158155	0.8826899

Test	F Ratio	DFNum	DFDen	p-Value
O'Brien[.5]	0.2608	1	14	0.6175
Brown-Forsythe	0.5825	1	14	0.4580
Levene	0.8824	1	14	0.3635
Bartlett	0.2799	1	.	0.5968
F Test 2-sided	1.5151	7	7	0.5971

Table 15: JMP output testing the assumption of equal variance for the residuals of the doped wafer model

The variance increases significantly from low to high source power. That, combined with the fact that the variance increases as the etch rate increases, indicates that the underlying assumptions used to create the model have been violated and something needs to be done to improve the model, either a transformation or the inclusion of additional variables. The results for the undoped wafer model are shown below in Table 16.

UNDOPED WAFERS

Oneway Analysis of Studentized Resid avg ER By doping By source power doping=-1

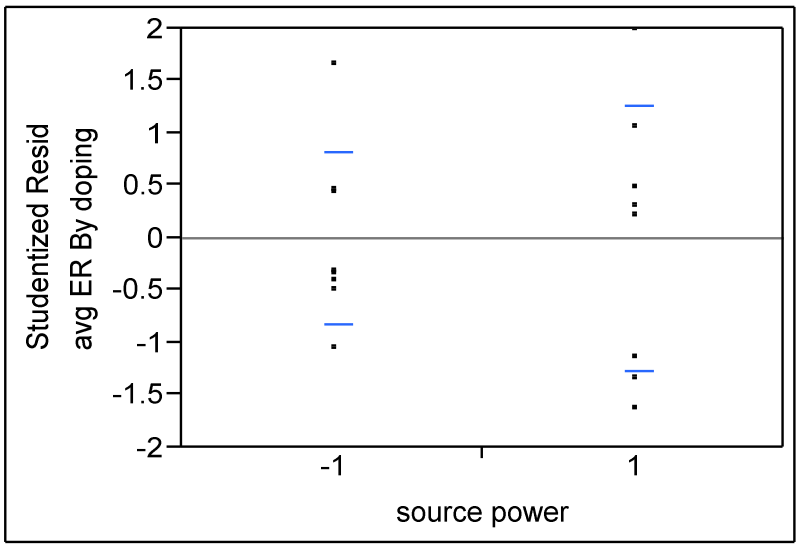

Tests that the Variances are Equal

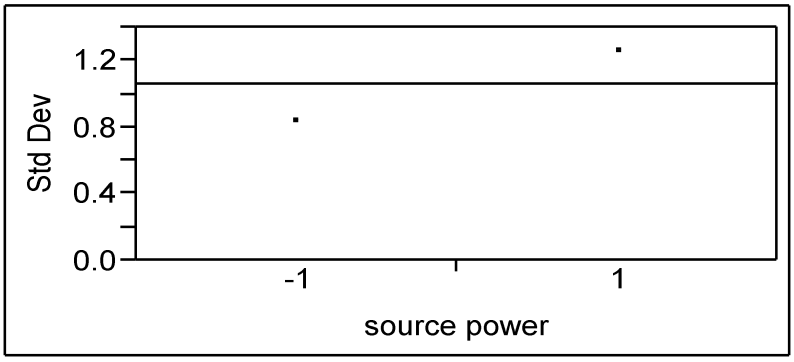

Level	Count	Std Dev	MeanAbsDif to Mean	MeanAbsDif to Median
-1	8	0.833110	0.642522	0.5647933
1	8	1.261603	1.018844	0.9630947

Test	F Ratio	DFNum	DFDen	p-Value
O'Brien[.5]	1.5418	1	14	0.2348

Test	F Ratio	DFNum	DFDen	p-Value
Brown-Forsythe	1.1982	1	14	0.2921
Levene	1.8053	1	14	0.2004
Bartlett	1.0942	1	.	0.2955
F Test 2-sided	2.2932	7	7	0.2958

Oneway Analysis of Studentized Resid avg ER By doping By CF4 doping=-1

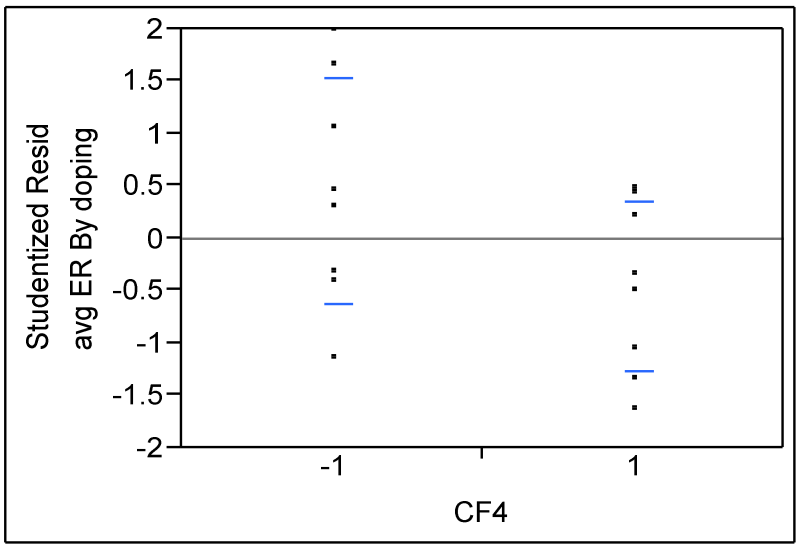

Tests that the Variances are Equal

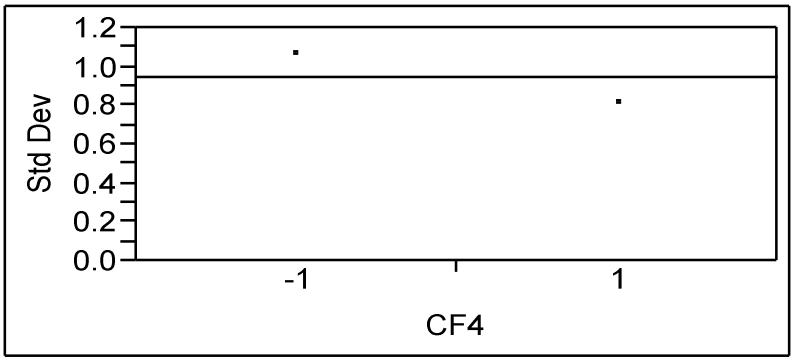

Level	Count	Std Dev	MeanAbsDif to Mean	MeanAbsDif to Median
-1	8	1.069481	0.8396214	0.8396214
1	8	0.813604	0.6623195	0.6623195

Test	F Ratio	DFNum	DFDen	p-Value
O'Brien[.5]	1.0139	1	14	0.3311
Brown-Forsythe	0.4962	1	14	0.4927
Levene	0.5043	1	14	0.4893
Bartlett	0.4826	1	.	0.4873
F Test 2-sided	1.7279	7	7	0.4876

Oneway Analysis of Studentized Resid avg ER By doping By O2 doping=-1

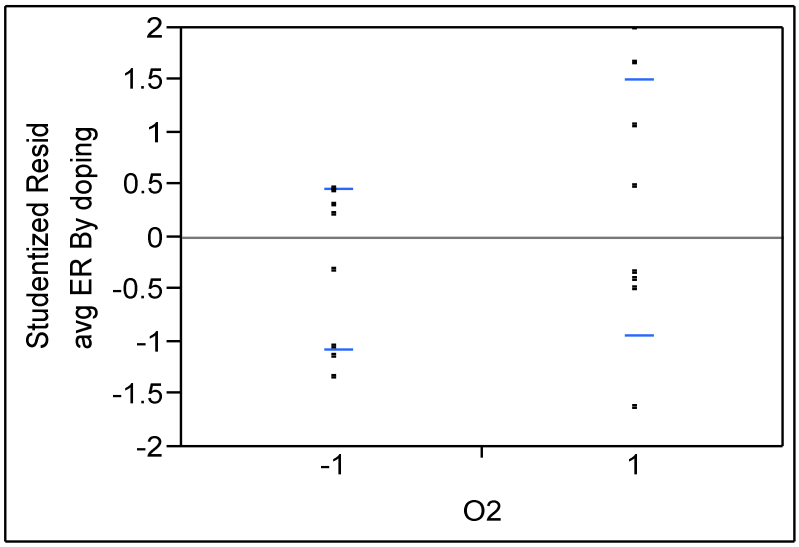

Tests that the Variances are Equal

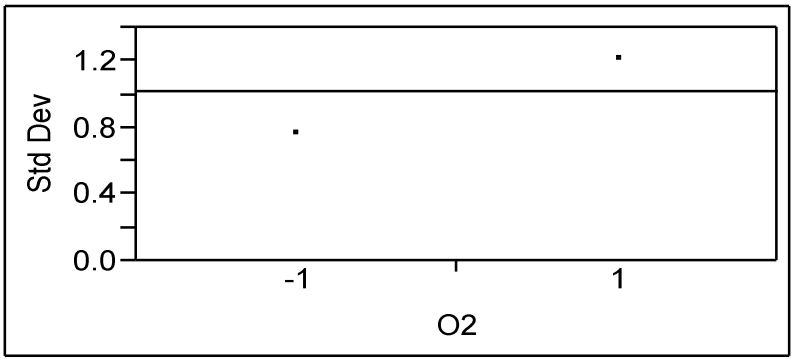

Level	Count	Std Dev	MeanAbsDif to Mean	MeanAbsDif to Median
-1	8	0.765257	0.657778	0.657778
1	8	1.223823	1.003588	1.003588

Test	F Ratio	DFNum	DFDen	p-Value
O'Brien[.5]	2.3276	1	14	0.1494
Brown-Forsythe	1.6882	1	14	0.2148
Levene	2.1851	1	14	0.1615
Bartlett	1.3903	1	.	0.2384
F Test 2-sided	2.5575	7	7	0.2386

Oneway Analysis of Studentized Resid avg ER By doping By CHF3 doping=-1

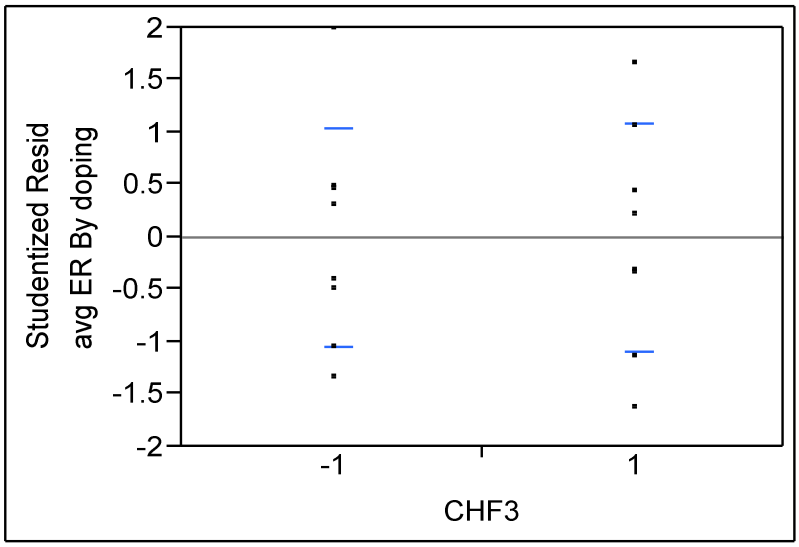

Tests that the Variances are Equal

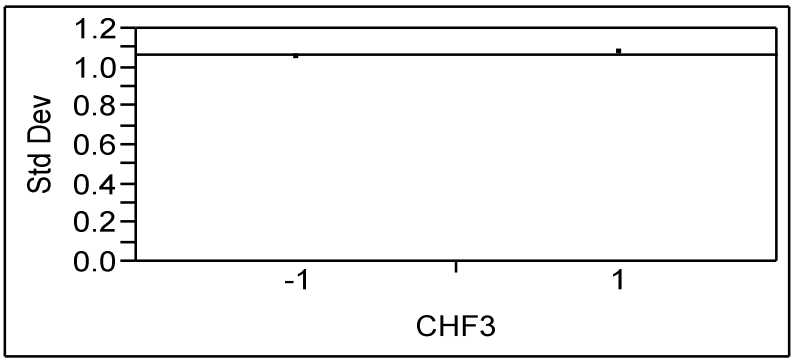

Level	Count	Std Dev	MeanAbsDif to Mean	MeanAbsDif to Median
-1	8	1.054527	0.8145645	0.8145645
1	8	1.083369	0.8468012	0.8468012

Test	F Ratio	DFNum	DFDen	p-Value
O'Brien[.5]	0.0064	1	14	0.9371
Brown-Forsythe	0.0117	1	14	0.9155
Levene	0.0117	1	14	0.9152
Bartlett	0.0048	1	.	0.9450
F Test 2-sided	1.0554	7	7	0.9451

Table 16: JMP output testing the assumption of equal variance for the residuals of the undoped wafer model

Although the variance assumptions have been met by the model for the undoped wafers for each of the factors, the plot of the residuals versus the predicted value shown in Figure 39 revealed structure in the residuals. The models for both wafer types need to be improved.

Transformations are one possible way to correct assumption violations, but several transformations of the response variable (etch rate) were tested and none of them corrected the nonequal variances. Another way to improve a model is to identify nuisance variables that were not controlled but may have influenced the response. These nuisance variables are known as covariates. These variables can be analyzed using analysis of covariance (ANCOVA).

In this designed experiment, the starting thickness of the wafer was a potential covariate. A plot of the studentized residuals as a function of this variable for the undoped wafer model (Figure 40b) shows a clear increasing trend, which suggests that including this variable in the model as a covariate could reduce the unexplained error component of the model, improving the fit and predictive value of the model, as well as potentially correcting the nonuniform variance issue. The same plot for the doped wafers (Figure 40a) does not show the same obvious trend, suggesting that it may not play as significant or direct a role in the doped wafer model. Inclusion of the covariate for both wafer types is discussed next.

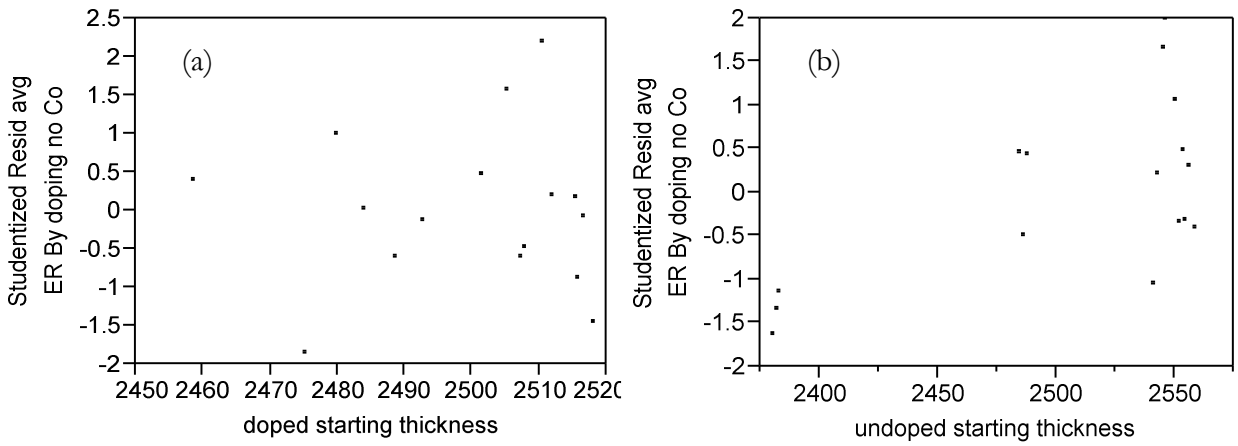

Figure 40: Plots of the studentized residuals as a function of starting film thickness for the (a) doped and (b) undoped wafers

INCLUSION OF A COVARIATE

The entire statistical analysis was repeated with the starting thickness included as a possible covariate term in the model for both wafer types. The covariate was also allowed to interact with the treatments, meaning different slopes between the factors and the factor by covariate interactions were possible. Please see Chapter 15 of Montgomery's *Design and Analysis of Experiments* for a detailed explanation of this technique. The details of the analysis, including the residual analysis are contained in the appendix.

Because the number of possible terms increased dramatically when the covariate and it interactions were added to the model, the screening platform in JMP is no longer the best way to choose the best model. All possible models were evaluated for this step and the model with the lowest AICc (Akaike

information criterion with a second order correction for small sample sizes) that had acceptable residuals was selected. The resulting model for the doped wafers is shown below in Table 17.

Parameter Estimates

Term	Estimate	Std Error	t Ratio	Prob>|t|
Intercept	27.687939	0.029106	951.27	<.0001*
source power	3.254943	0.024276	134.08	<.0001*
CHF3	-0.696408	0.024422	-28.52	<.0001*
doped starting thickness(2458.43,2517.83)	0.1741617	0.043909	3.97	0.0027*
O2*doped starting thickness	0.2259228	0.036414	6.20	0.0001*
O2*CHF3*doped starting thickness	0.3763801	0.03835	9.81	<.0001*

Table 17: Final model for the doped wafer etch data from the full factorial design, including starting thickness as a covariate

The residuals for this model are normally distributed with equal variance, so the model can be accepted as a statistically valid empirical model of the data that can be used for prediction and process optimization. The covariate entered the model as a main effect, along with its interactions with O2 and O2*CHF3. All measures of model adequacy were improved by the inclusion of the starting thickness covariate.

Parameter Estimates

Term	Estimate	Std Error	t Ratio	Prob>|t|
Intercept	27.360871	0.059179	462.34	<.0001*
source power	3.231408	0.053214	60.73	<.0001*
CHF3	-0.851979	0.050994	-16.71	<.0001*
undoped starting thickness(2379.68,2558.41)	0.9010404	0.073729	12.22	<.0001*

Table 18: Final model for the undoped wafer etch data from the full factorial design, including starting thickness as a covariate

The final model for the undoped wafers is shown above in Table 18. Note that the covariate term (i.e., starting thickness of the undoped wafer) had a larger effect on the etch rate than the presence of CHF3, indicating that at least some of the process variability observed between different types of materials is not due to the etching process itself, but rather to the condition of the wafer when it arrives at the tool. This effect was observed for wafer-to-wafer runs, but center-to-edge variability across the wafer could be caused in part by prior processing steps.

The residuals for the undoped model are normally distributed and have constant variance, so the assumptions hold and the chosen model is valid. The covariate has replaced the four-way interaction term, considerably improving the model in the process; the PRESS statistic is now 0.85 instead of 7.77. Finally, the inclusion of starting thickness as a covariate has corrected the increasing trend that was observed for the residuals as a function of starting thickness before it was included (Figure 40). See Figure 41 below.

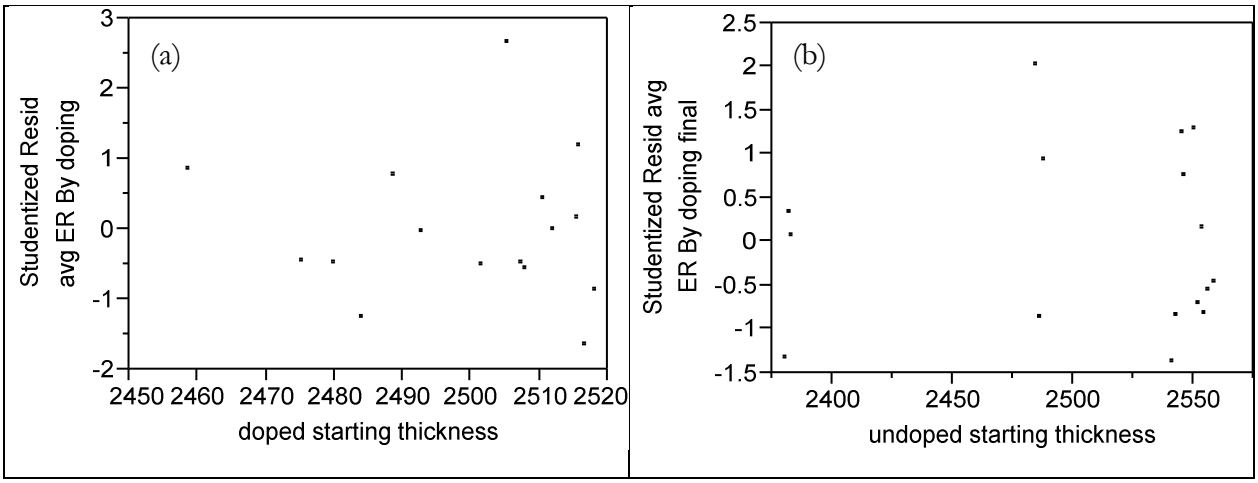

Figure 41: Improved residuals as a function of starting thickness after the addition of the starting thickness covariate to the model for the (a) doped and (b) undoped wafers

The main benefit of an analysis of this type is that it allows you to clearly identify which factors had a significant effect on the response so that they can be studied in more detail in future experiments. The prediction equations are useful for finding optimal operating conditions, and this will be explored in more detail below, but the real power of the factorial method lies in its ability to very efficiently provide useful information about where to focus your future experimental energies.

Source power, CHF3, and starting thickness main effects affected the etch rate for both wafer types. In addition, the doped wafers were sensitive to the interaction of starting thickness with O2 and with CHF3*O2. The doped wafers have a slightly faster etch rate than the undoped wafers at the center of the parameter space, as indicated by the slightly larger value of the intercept (27.69 doped vs. 27.36 undoped). Source power exerted the same influence on the two wafer types (3.25 doped and 3.23 undoped). This was expected, as source power affects the ion density in the discharge and that factor was not expected to interact differently with the two film types. CHF3 suppressed the etch rate in both cases, but had a stronger suppression effect on the undoped wafers (-0.85 undoped vs. -0.70 doped). For both wafer types, thicker wafers etched faster. For doped wafers, increasing O2*thickness combinations increased the etch rate, as did the synergistic effect of CHF3 in the presence of O2 for a given thickness. Although CHF3 acts to suppress the etch rate, the presence of O2 reverses this trend to a small extent.

UNIFORMITY ANALYSIS

The entire analysis to this point has dealt with the average etch rate across the wafer. Another goal of this project was to reduce the within-wafer variance, also known as uniformity. On the length scale of interest to the semiconductor industry (nanometers), small variations in etch rate from the center to the edge of the wafer can cause significant variation in the thickness profile across the wafer and lead to device failures, particularly near the outer edge of the wafer where the differences are often the most extreme.

To quantify the uniformity, the integration statistic proposed by Davis et al. was used.[90] The coefficient of variation (also known as the inverse signal-to-noise ratio) is typically used in the

literature to quantify variance across the wafer. It is the dimensionless ratio between the standard deviation and the mean of a distribution. Because of the assumptions underlying this statistic, it is inappropriate to use in the presence of deterministic patterns in the response over the wafer (such as the commonly seen bull's eye effect). The coefficient of variation assumes that the observations are drawn from a random normal distribution, which is clearly not true when there is an underlying pattern on the wafer. For a highly skewed distribution, the mean is not a good estimate of the "most likely" observation and the standard deviation is not a good indicator of the spread of a skewed distribution. It is therefore likely that the traditional coefficient of variation metric will not produce a reliable estimate of the variation present across a wafer surface. The coefficient of variation also ignores the spatial locations of the data by giving all measurements equal weight. A more appropriate statistic is needed to assess wafer uniformity. Davis et al. develop what they call the integration statistic for this purpose.

The measured responses can be thought of as defining a volume, and the total error in volume can be used as an indicator of the nonuniformity of the response. The error volume is then divided by the target volume to obtain a dimensionless indicator of nonuniformity. The statistic can be represented in the following way:

$$I = \frac{\iint h\big(T - g(r,\theta)\big) r dr d\theta}{Vol_{Target}},$$

where $h(\,)$ is a general loss function such as $|x|$ or x^2 that is necessary if the target volume intersects the error surface, Vol_{Target} is the target volume, T is the target value of the response, and $g(r,\theta)$ is the function representing the response surface.

To generate a function representing the surface, a 2D smooth spline was fit to the measured data. The smooth spline fit was used as an interpolating function and the integral was evaluated numerically on a 30 x 30 grid. This statistic eliminates the problems with the coefficient of variation and incorporates information about the spatial relationship of the data into the metric.

The integration statistic was calculated for the full factorial etch rate data and used as a metric to analyze the variance in the etch rate across the wafer. The variance in the etch rate measurements can be thought of as an independent response that can be affected by the design factors and covariates, just as the etch rate can be. The preceding statistical analysis was applied to this response and the results are documented in Table 19 and Table 20. The details of the analysis can be found in the appendix.

Parameter Estimates

Term	Estimate	Std Error	t Ratio	Prob>|t|
Intercept	0.0102946	0.000227	45.43	<.0001*
source power	0.0004399	0.000227	1.94	0.0761
O2	0.0006187	0.000227	2.73	0.0183*
source power*O2	0.0015071	0.000227	6.65	<.0001*

Table 19: Final model for the doped wafer uniformity, including starting thickness as a covariate

Parameter Estimates

Term	Estimate	Std Error	t Ratio	Prob>|t|
Intercept	0.0106443	0.000243	43.88	<.0001*
O2	0.0006611	0.000234	2.83	0.0165*
CHF3	0.0005324	0.000239	2.23	0.0478*
source power*O2	0.0010256	0.000239	4.30	0.0013*
source power*undoped starting thickness	-0.001193	0.000304	-3.92	0.0024*

Table 20: Final model for the undoped wafer uniformity, including starting thickness as a covariate

The uniformity of both wafer types was affected to the same degree by O2 (0.00062 for doped and 0.00066 for undoped) and the source power*O2 interaction (0.0015 for doped and 0.0010 for undoped). In addition, for the doped wafers, source power alone contributed to the non-uniformity. For the undoped wafers, the presence of CHF3 made the wafers more non-uniform, and the starting thickness affected how much of an effect source power had. Increasing O2 increases the non-uniformity of both wafer types; if non-uniformity is a primary concern, this information should be taken into account when choosing the etching chemistry.

One of the main goals of this study was to find operating conditions where the etch rates of the two materials were the same. To facilitate this, the ratio of the two etch rates d:un was examined, where d:un=1 is optimum, following the example of Kraft et al.[74]. The easiest way to identify the factor settings that will produce the desired ratio of d:un=1 is to examine contour plots of the response surface. This approach makes it possible to view the effect of two factors simultaneously, with any others held constant. Below are two contour plots of the d:un ratio as a function of source power and CHF3, with the starting thicknesses held constant at their median value and the O2 factor set at +1 (He/O2=80 sccm, O2=16 sccm, Figure 42) and -1 (He/O2=20 sccm, O2=4 sccm, Figure 43).

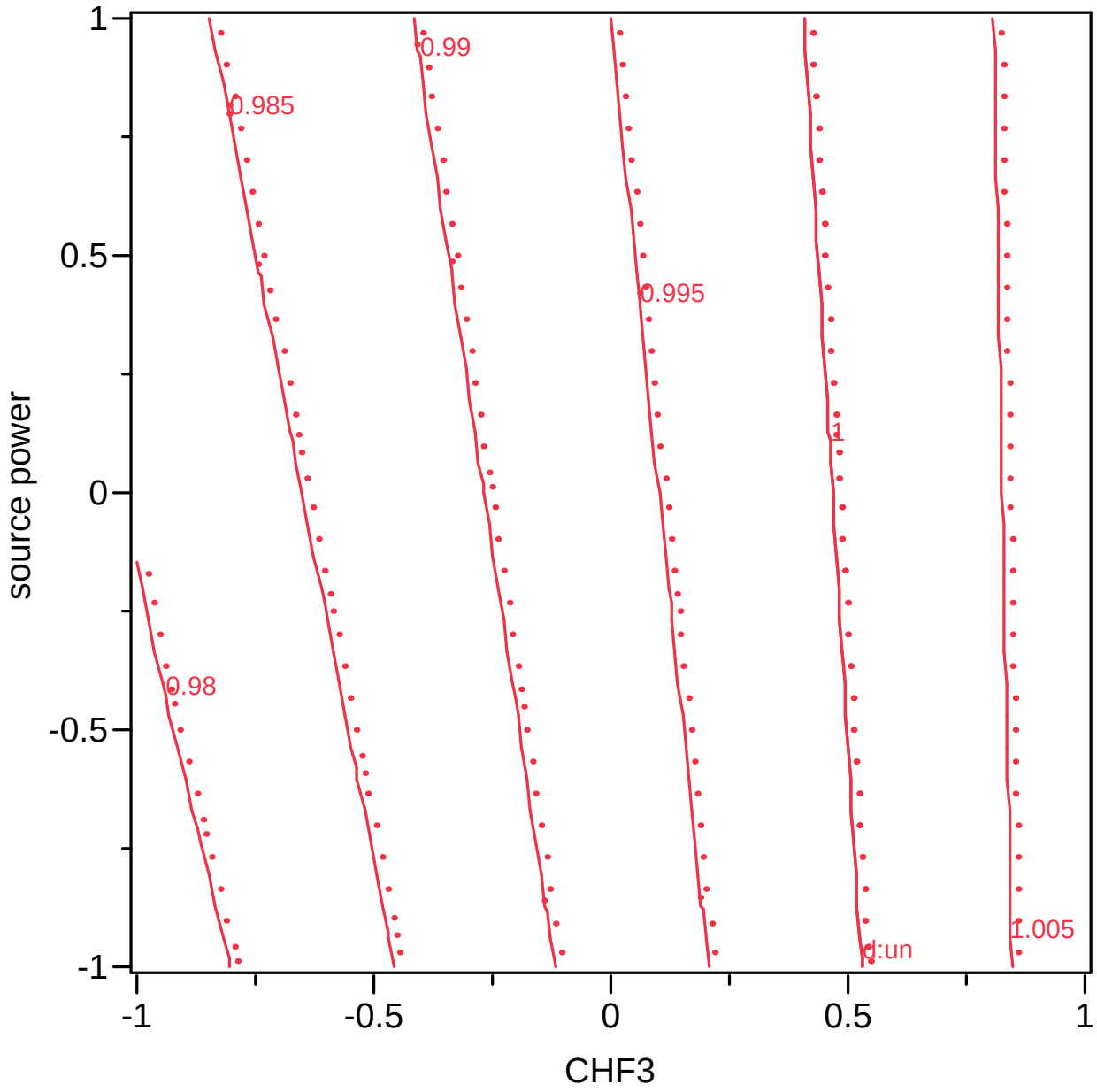

Figure 42: Contour plot of the surface generated by the prediction equations for the doped:undoped etch rate ratio showing the effect of source power and CHF3. He/O2=1.

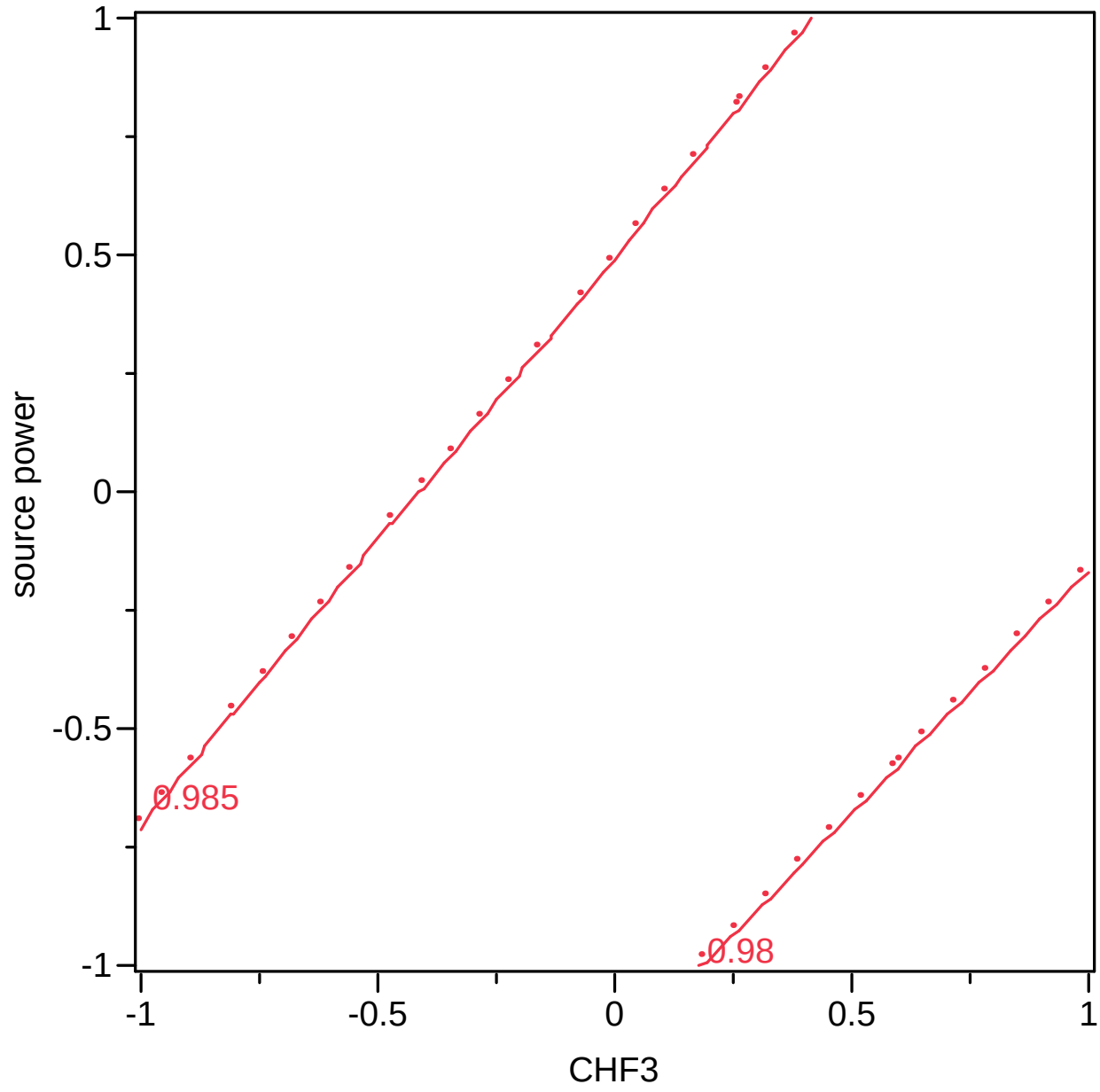

Figure 43: Contour plot of the surface generated by the prediction equations for the doped:undoped etch rate ratio showing the effect of source power and CHF3. He/O2=-1.

It can be seen from the first contour plot that for high levels of He/O2, a value of CHF3 around 0.5 (30 sccm) will produce equal etch rates between the two films. Under these conditions, the response is relatively insensitive to source power, so it could be optimized for other responses without affecting the etch rate. When the level of O2 present in the chamber is reduced to -1 (He/O2=20 sccm, O2=4 sccm), there is no combination of settings that will produce the desired etch rate ratio, and under these conditions the undoped wafers actually etch faster than the doped wafer. These responses are very dependent on the starting thickness of the film, and so, in actual practice, it

would be ideal to have a feed-forward control system programmed with the prediction equation determined here that could use the starting thickness to optimize the response.[58, 91]

These results are very encouraging because they highlight that the currently used recipe (Process on Record—POR) need only be slightly modified with the addition of a moderate amount of readily available CHF3 to produce equal etch rates for the two materials. These results confirm the result predicted by the literature review that the addition of an F-bearing species would help minimize the difference between the etch rates. They are unexpected only in that the effective species turned out to be CHF3 rather than the CF4 that was reported in the literature. To date, no studies have been published describing the effect of adding CHF3 to the standard polysilicon etch chemistry, so this is a new and unique result.

Because source power affects the two wafer types almost equally, CHF3 and O2 settings are the factors that will have the largest influence on the ratio. It is important to note that these results only apply to blanket films. Because of the dramatically different chemistry that occurs on the sidewalls of the gate and the bottom of the trench[81] due to the directionality of the ions, these findings cannot be directly applied to three-dimensional structures without verification. These prediction equations most closely predict the way the bombarded bottom of the feature would etch, since profile control is most strongly related to the composition of the passivation sidewall layer.

The final step in the analysis of the factorial design is to optimize the etch rate ratio and across-wafer uniformity simultaneously. Optimization via desirability functions[92] was conducted in JMP, and the results obtained are shown in Figure 44. The results are consistent with the contour plots above, indicating that within the range of possible setting that will produce d:un=1 (O2=1, CHF3~0.5), utilizing a low source power setting will simultaneously make the etch rate across the wafers more uniform.

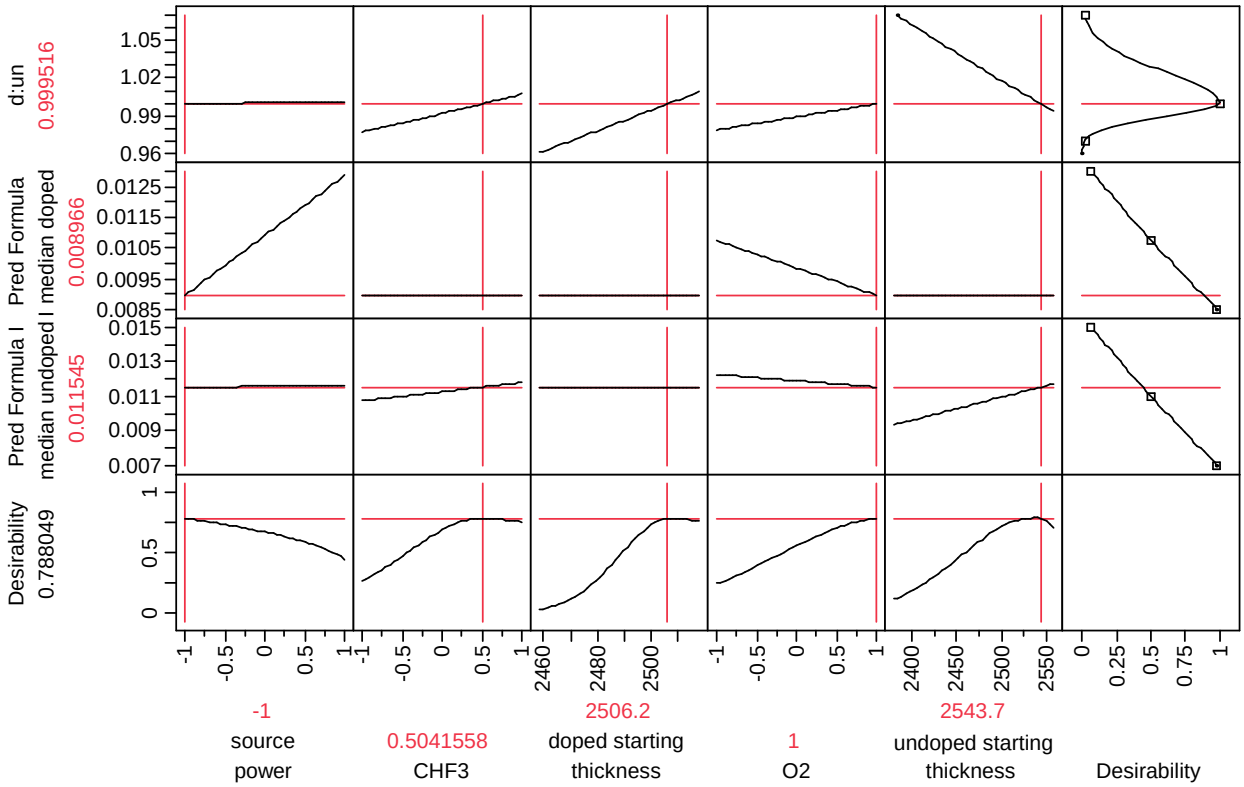

Figure 44: Optimal settings for simultaneously minimizing the etch rate differences and minimizing the across-wafer variance. Desirability weights: d:un=1 and integration statistic=.5.

Another way to view this same information is with an overlay of the contour plots for all three responses (Figure 45). The unshaded region of the plot indicates the regions where all responses are optimized simultaneously.

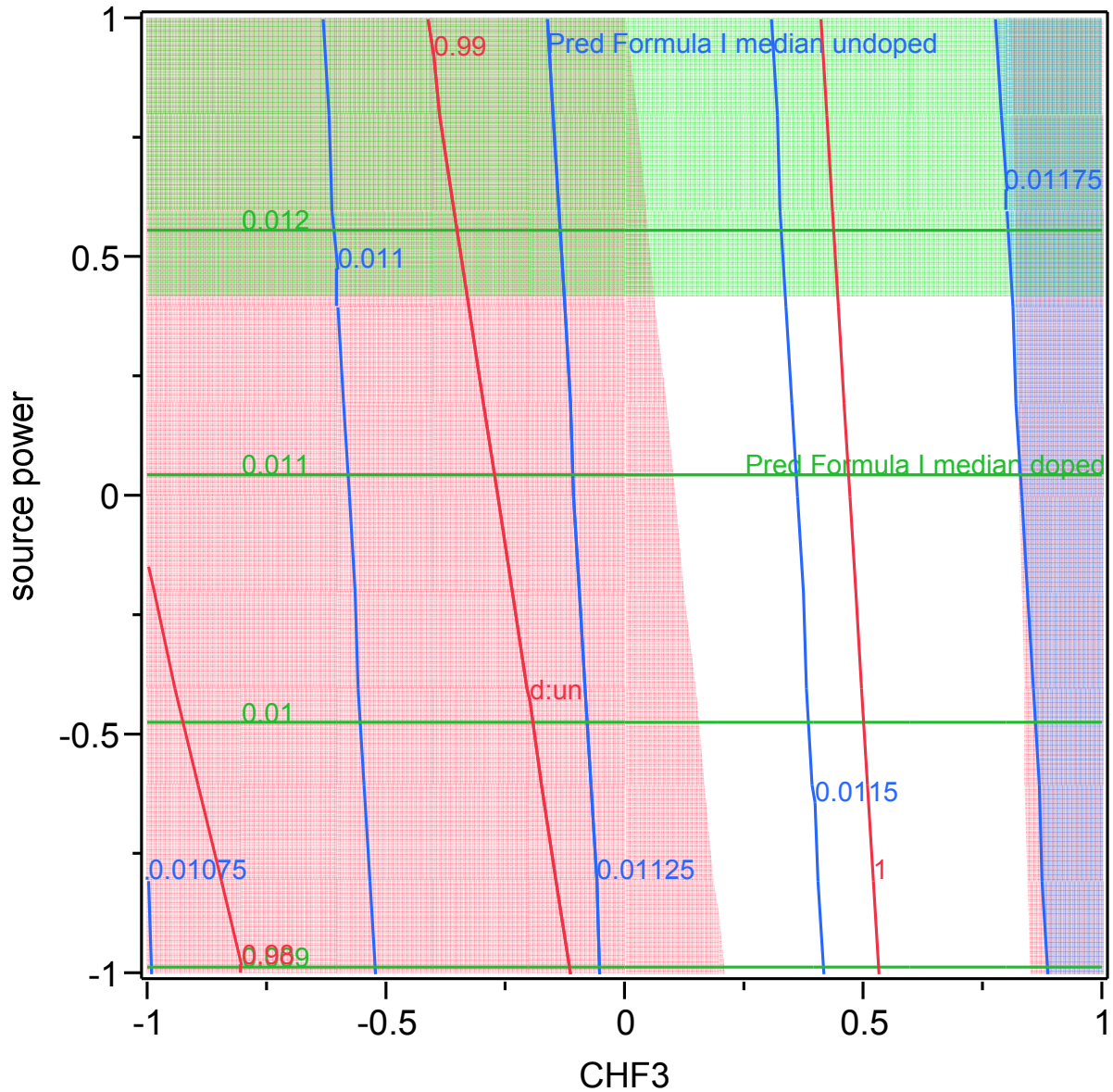

Figure 45: Region of the optimum found by overlying the d:un and uniformity equations

DESIGNED EXPERIMENT #2: BOX-BEHNKEN RESPONSE SURFACE DESIGN

Based on the information obtained from the factorial screening experiment, a number of changes were made in the second set of experiments. The CF4 factor was dropped from the design since it did not make a significant difference in the blanket film etch rate or uniformity for the range investigated. The flow rate may have been too low, but the setting was the same as that reported in the literature for nearly identical processing conditions.[84] Another possible reason for the apparent inertness of CF4 may be the fact that the blanket studies only simulate the etch environment on the

bombarded surfaces of the wafer, and the role of CF4 is in fact primarily about changing the chemistry of the sidewall passivation layer, which does not exist for the blanket films. Based on these arguments, it is interesting to note that an only slightly higher flowrate of CHF3 (40 sccm versus 25 sccm) had such a noticeable impact on the bombarded surfaces, slowing the etch rate when it was present. This indicates that if flowrate was not the problem, the behavior of the two quite similar species is very different in the polysilicon etching environment. The CHF3 appears to be forming a passivating layer on the bombarded surface, whereas CF4 does not, based on both my results and those in the literature.[81, 84]

With only three remaining factors, a Box-Behnken response surface design[85, 86, 93] was chosen to explore the parameter space in more detail and identify possible curvature in the response that was not detectable with the factorial design. The range of the factors was expanded for the CHF3 and He/O2, but encompassed the range studied in the factorial design to facilitate comparisons. Four different dopant types were studied (P, As, Sb, B) in addition to undoped wafers. The blanket film thicknesses were all targeted at 1000Å and the dopant doses were as follows: P=4E15 cm^{-2} at 5 keV, As=2E15 cm^{-2} at 30 keV, Sb=3E15 cm^{-2} at 30keV, and B=4E15 cm^{-2} at 5 keV. The following settings were used, with all remaining factors being the same as given for the factorial experiment.

Factor	Low	Medium	High
Source power (W)	250	325	400
CHF3(sccm)	0	40	80
He/O2 (sccm)	20	60	100

Table 21: Factor settings for the three factors studied in the Box-Behnken response surface design

The Box-Behnken design matrix and resulting etch rates in Å/s for the five wafer types is given below in Table 22. The design is a three-level spherical design with center points, with all points lying on a sphere of radius $\sqrt{2}$ (Figure 46). Three centerpoint replicates were run, as well as a single replicate of the 0-- setting.

Pattern	CHF3	source power	He/O2	P doped	As doped	Sb doped	B doped	undoped
--0	0	250	60	23.48	21.07	21.62	20.32	24.55
-+0	0	400	60	31.47	31.11	30.72	28.54	32.27
++0	80	400	60	29.05	28.58	28.16	27.20	29.59
-0-	0	325	20	28.04	27.48	27.14	24.06	27.76
-0+	0	325	100	27.58	27.04	26.82	22.95	28.55
+0-	80	325	20	23.49	22.20	22.42	20.23	25.16
0++	40	400	100	29.71	29.43	28.68	27.50	30.30
+-0	80	250	60	21.43	17.36	16.85	20.53	21.69
0-+	40	250	100	19.74	18.25	17.96	19.07	22.39
+0+	80	325	100	24.86	23.77	23.22	19.60	25.62
0+-	40	400	20	28.07	27.30	27.01	25.72	28.77
0--	40	250	20	21.74	17.53	16.89	19.78	21.59
0--	40	250	20	23.47	22.90	19.90	21.80	22.88
000	40	325	60	27.29	26.68	25.86	26.08	27.38
000	40	325	60	26.94	26.36	25.59	25.79	27.20
000	40	325	60	26.98	26.57	25.59	25.72	27.25

Table 22: Box-Behnken design matrix and resulting etch rates for wafers doped with P, As, Sb, B, and no dopant. The runs are listed in the randomized order in which they were run.

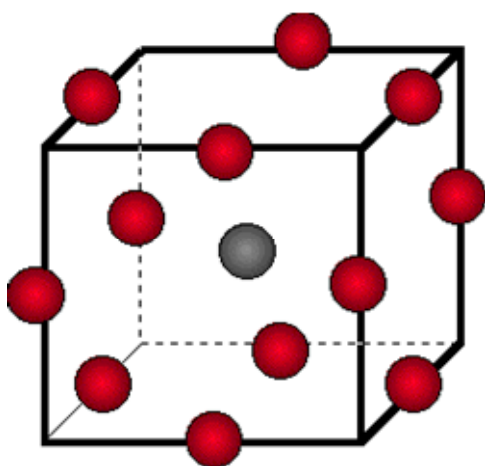

Figure 46: Graphical representation of factor levels for a Box-Behnken design for three factors.

A detailed statistical analysis using linear regression and the least squares procedure was conducted on the etch rate and uniformity data, the details of which are documented in the appendix. The final models for each of the etch rates (Table 23) and uniformity integration statistics (Table 24) are given below. A residual analysis was conducted on all models to ensure the model assumptions were valid. Based on what was learned about the importance of the starting thickness covariate in the factorial experiment, it was included in this analysis as well.

P-doped etch rate

Parameter Estimates

Term	Estimate	Std Error	t Ratio	Prob>|t|
Intercept	26.802964	0.122334	219.10	<.0001*
CHF3(0,80)	-1.229428	0.112052	-10.97	<.0001*
source power(250,400)	4.0305455	0.104373	38.62	<.0001*
CHF3*He/O2	0.7135152	0.156677	4.55	0.0019*
source power*He/O2	1.4943899	0.154467	9.67	<.0001*
He/O2*He/O2	-1.610535	0.182245	-8.84	<.0001*
source power*source power*P starting thickness	1.316621	0.405092	3.25	0.0117*
He/O2*He/O2*P starting thickness	-2.462416	0.371787	-6.62	0.0002*

As-doped etch rate

Parameter Estimates

Term	Estimate	Std Error	t Ratio	Prob>|t|
Intercept	25.039043	0.279213	89.68	<.0001*
CHF3(0,80)	-1.603478	0.39545	-4.05	0.0016*
source power(250,400)	5.2520179	0.378761	13.87	<.0001*
He/O2*He/O2*As starting thickness	-2.337496	0.561924	-4.16	0.0013*

Sb-doped etch rate

Parameter Estimates

Term	Estimate	Std Error	t Ratio	Prob>|t|
Intercept	25.67004	0.092204	278.40	<.0001*
CHF3(0,80)	-1.90997	0.063133	-30.25	<.0001*
source power(250,400)	5.1737588	0.061488	84.14	<.0001*
He/O2(20,100)	0.3676749	0.060963	6.03	0.0005*
CHF3*CHF3	0.4375898	0.090548	4.83	0.0019*
CHF3*source power	0.553125	0.089215	6.20	0.0004*
source power*source power	-1.78035	0.09208	-19.33	<.0001*
CHF3*He/O2	0.4658284	0.089838	5.19	0.0013*
He/O2*He/O2*Sb starting thickness	-1.635677	0.092781	-17.63	<.0001*

B-doped etch rate

Parameter Estimates

Term	Estimate	Std Error	t Ratio	Prob>|t|
Intercept	25.857381	0.068866	375.47	<.0001*
source power(250,400)	3.1655813	0.06181	51.22	<.0001*
CHF3*source power	-1.825481	0.1158	-15.76	<.0001*
CHF3*B starting thickness	-0.850294	0.130445	-6.52	0.0002*
CHF3*source power*B starting thickness	-1.871816	0.24753	-7.56	<.0001*
source power*source power*B starting thickness	3.0337432	0.149792	20.25	<.0001*
CHF3*He/O2*B starting thickness	0.8376722	0.128938	6.50	0.0002*
He/O2*He/O2*B starting thickness	-6.471119	0.178254	-36.30	<.0001*

Undoped etch rate

Parameter Estimates

Term	Estimate	Std Error	t Ratio	Prob>|t|
Intercept	27.266061	0.070382	387.40	<.0001*
CHF3(0,80)	-1.378007	0.04834	-28.51	<.0001*

Term	Estimate	Std Error	t Ratio	Prob>|t|
source power(250,400)	3.6758843	0.049828	73.77	<.0001*
He/O2(20,100)	0.4580102	0.046655	9.82	<.0001*
source power*source power	-0.505072	0.072403	-6.98	<.0001*
source power*source power*undoped starting thickness	-0.549137	0.108536	-5.06	0.0007*
He/O2*He/O2*undoped starting thickness	-0.723457	0.124441	-5.81	0.0003*

Table 23: Box-Behnken prediction models for the five film types

P-doped etch uniformity

Parameter Estimates

Term	Estimate	Std Error	t Ratio	Prob>|t|
Intercept	0.0169995	0.000672	25.30	<.0001*
source power(250,400)	-0.011516	0.000609	-18.90	<.0001*
He/O2(20,100)	0.0100713	0.000647	15.57	<.0001*
CHF3*CHF3	0.0069014	0.000788	8.76	<.0001*
source power*source power	-0.002366	0.00084	-2.82	0.0259*
CHF3*He/O2	-0.011982	0.000871	-13.76	<.0001*
source power*P starting thickness	-0.032686	0.001975	-16.55	<.0001*
He/O2*P starting thickness	0.0327944	0.002056	15.95	<.0001*
He/O2*He/O2*P starting thickness	0.006591	0.001079	6.11	0.0005*

As-doped etch uniformity

Parameter Estimates

Term	Estimate	Std Error	t Ratio	Prob>|t|
Intercept	0.0179464	0.000452	39.73	<.0001*
CHF3(0,80)	0.0067773	0.000602	11.26	<.0001*
CHF3*source power	0.0145185	0.00066	22.00	<.0001*
CHF3*He/O2	-0.004831	0.000707	-6.83	0.0005*
He/O2*He/O2	0.0081418	0.000693	11.75	<.0001*
CHF3*As starting thickness	0.0279342	0.001298	21.52	<.0001*
He/O2*As starting thickness	-0.005541	0.001315	-4.21	0.0056*
CHF3*He/O2*As starting thickness	0.0333202	0.002042	16.31	<.0001*
source power*He/O2*As starting thickness	0.0054968	0.000739	7.43	0.0003*
He/O2*He/O2*As starting thickness	-0.011108	0.001537	-7.23	0.0004*

Sb-doped etch uniformity

Parameter Estimates

Term	Estimate	Std Error	t Ratio	Prob>|t|
Intercept	0.0184928	0.000165	111.94	<.0001*
CHF3(0,80)	0.0070002	0.000154	45.42	<.0001*
CHF3*CHF3	0.0140141	0.000294	47.67	<.0001*
CHF3*source power	0.0025243	0.000234	10.78	<.0001*
He/O2*He/O2	0.0083209	0.000227	36.67	<.0001*
source power*Sb starting thickness	-0.003431	0.00018	-19.05	<.0001*
CHF3*CHF3*Sb starting thickness	-0.08841	0.001404	-62.96	<.0001*
CHF3*source power*Sb starting thickness	-0.131897	0.002186	-60.33	<.0001*
source power*source power*Sb starting thickness	-0.073259	0.001215	-60.28	<.0001*
He/O2*He/O2*Sb starting thickness	0.0660363	0.001221	54.08	<.0001*

B-DOPED ETCH UNIFORMITY

Parameter Estimates

Term	Estimate	Std Error	t Ratio	Prob>|t|
Intercept	0.0130334	0.003058	4.26	0.0021*
CHF3*CHF3	0.0250061	0.003175	7.88	<.0001*
CHF3*source power	0.0289288	0.003756	7.70	<.0001*
source power*source power	-0.021924	0.004863	-4.51	0.0015*
source power*B starting thickness	-0.017991	0.002909	-6.18	0.0002*
CHF3*CHF3*B starting thickness	-0.065518	0.007719	-8.49	<.0001*
He/O2*He/O2*B starting thickness	0.0572969	0.005874	9.75	<.0001*

UNDOPED ETCH UNIFORMITY

Parameter Estimates

Term	Estimate	Std Error	t Ratio	Prob>|t|
Intercept	0.013637	0.00036	37.88	<.0001*
He/O2(20,100)	-0.002218	0.000544	-4.08	0.0028*
source power*source power	0.0031845	0.000399	7.98	<.0001*
He/O2*undoped starting thickness	0.0041089	0.000771	5.33	0.0005*
CHF3*source power*undoped starting thickness	-0.002339	0.000715	-3.27	0.0097*
source power*He/O2*undoped starting thickness	0.004708	0.000536	8.78	<.0001*
He/O2*He/O2*undoped starting thickness	0.0038588	0.000513	7.53	<.0001*

Table 24: Box-Behnken prediction models for the etch rate uniformity for the five film types.

Because of the second-order behaviors in the main effects that can be detected with a design of this type, it is expected that the models will be more complicated. These models are too involved to try to explain each term physically, but a few trends in the most significant terms should be noted. The etch rate at the center point (CHF3=40 sccm, source power=325 W, He/O2=60) was highest for the undoped films and lowest for the As-doped films: As=25.04, Sb=25.67, B=25.86, P=26.80, and undoped=27.27. The effect of source power was again significant for all films types and showed the following trend: B=3.17, undoped=3.68, P=4.03, Sb=5.17, and As=5.25 (i.e., source power becomes more influential on the etch rate as the dopant dose for the n-type dopants decreases). The O2*O2*thickness interaction term was also present in each model: undoped=-7.23, B=-6.47, P=-2.46, As=-2.34, and Sb=-1.63 (following the trend of the periodic table for the n-type dopants). The final term that was present (and expected based on the results of the factorial experiment) in all but the p-type film (B-doped) was CHF3: Sb=-1.91, As=-1.60, undoped=-1.38, and P=-1.23.

The best way to view these second-order regression models is as response surfaces. It is much more intuitive to identify trends in the data visually than by trying to interpret a multiple-term equation, especially when there are second-order terms involved. Response surfaces were plotted as the etch rate (Å/s) as a function of CHF3 and He/O2 flow rates for each of the source power settings (250, 325, and 400 W) in order to identify trends and understand more holistically how each of the factors affected the etch rate.

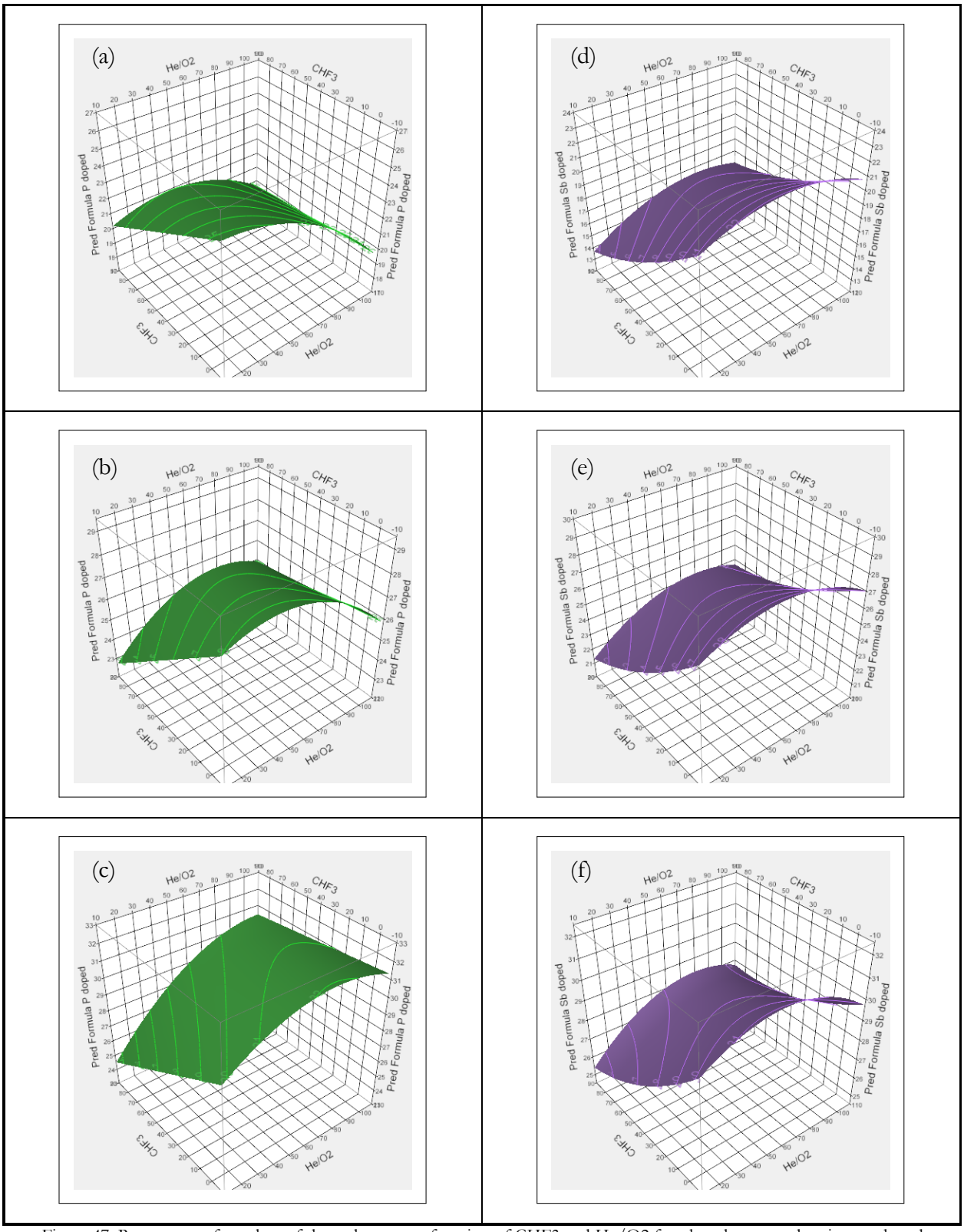

Figure 47: Response surface plots of the etch rate as a function of CHF_3 and He/O_2 for phosphorus- and antimony-doped polysilicon at low, mid, and high settings of the source power. Left column is P-doped film at (a) 250 W, (b) 325 W, and (c) 400 W. Right column is Sb-doped film at (d) 250 W, (e) 325 W, and (f) 400 W.

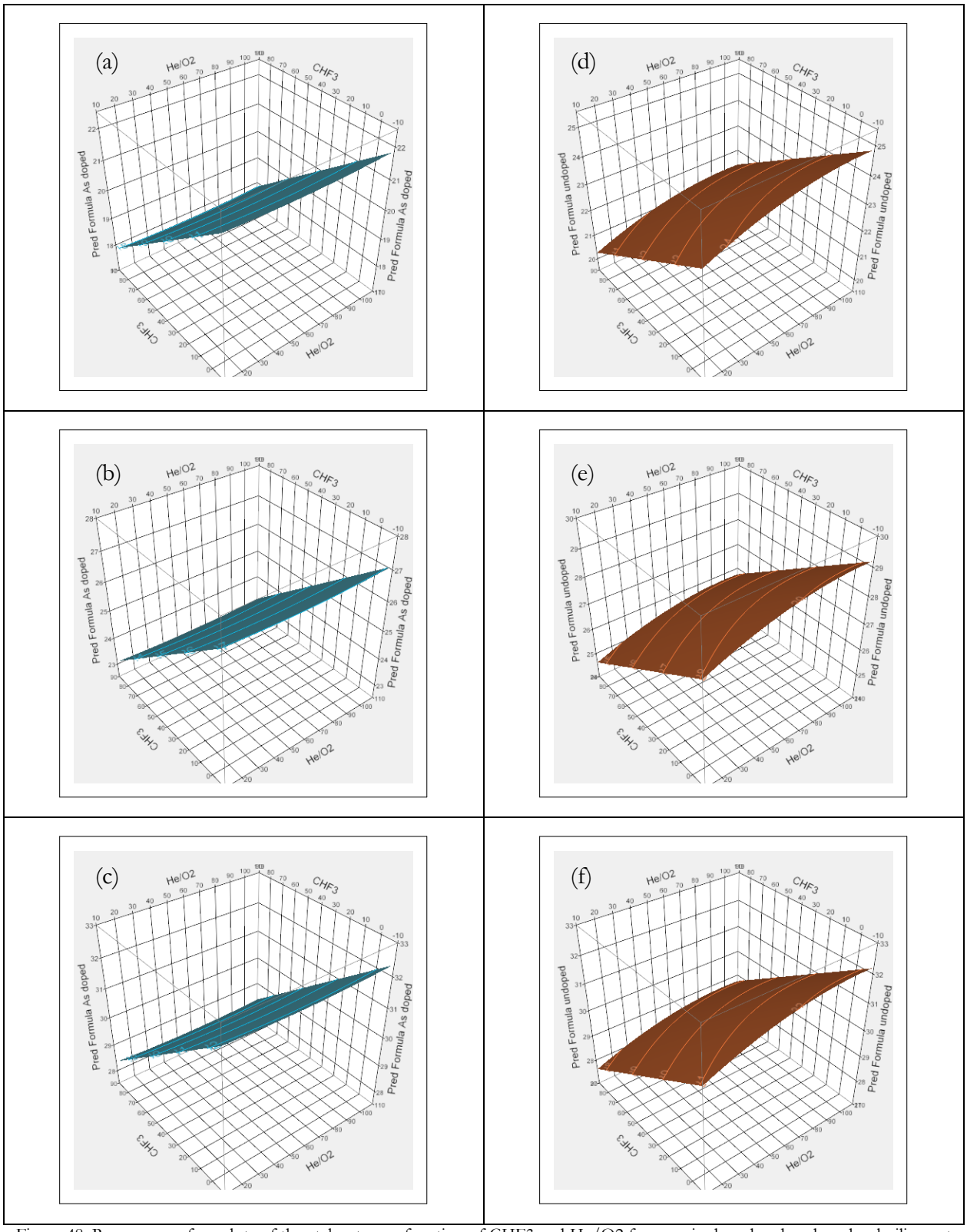

Figure 48: Response surface plots of the etch rate as a function of CHF3 and He/O2 for arsenic-doped and undoped polysilicon at low, mid, and high settings of the source power. Left column is As-doped film at (a) 250 W, (b) 325 W, and (c) 400 W. Right column is undoped film at (d) 250 W, (e) 325 W, and (f) 400 W.

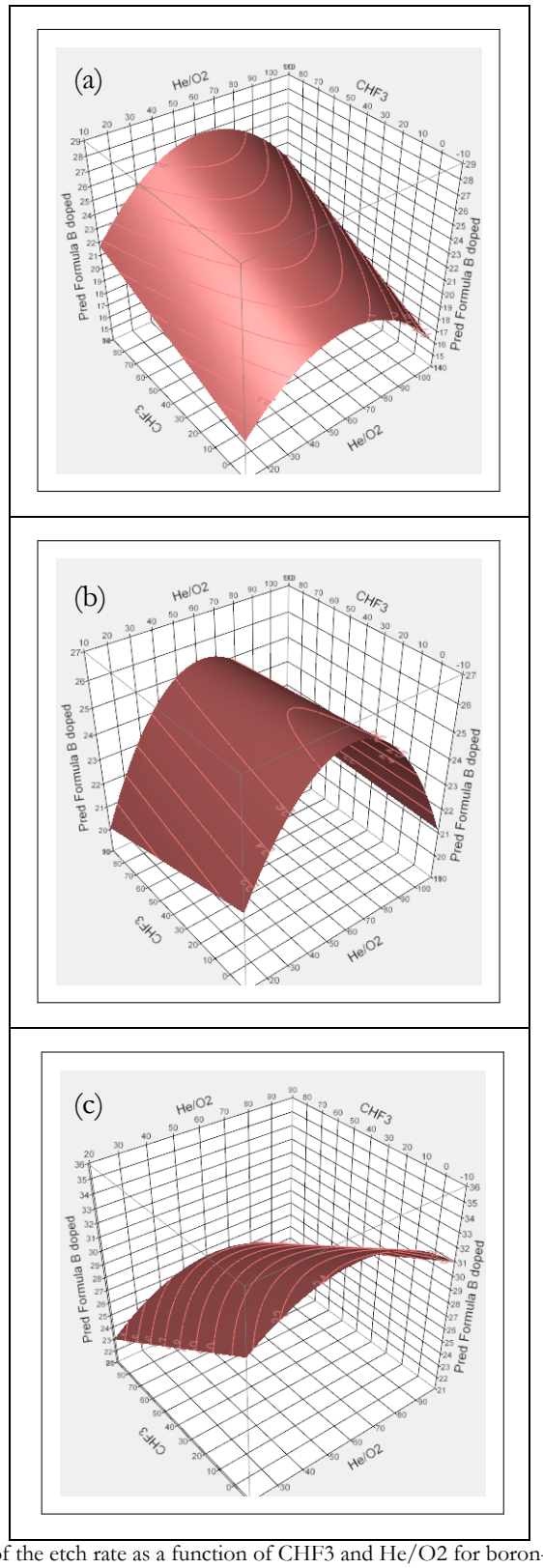

Figure 49: Response surface plots of the etch rate as a function of CHF3 and He/O2 for boron-doped polysilicon at low, mid, and high settings of the source power: (a) 250 W, (b) 325 W, and (c) 400 W.

There are some very interesting trends in the data. For the P-doped films, the etch rate is a linearly decreasing function of CHF3, but demonstrates a parabolic relationship with the flow rate of He/O2. The ion density changes the shape of the response surface as it increases, but those basic relationships do not change. The same trends are observed for Sb-doped films.

The response for the As-doped films is much different; the response surface shows virtually no curvature. The linearly decreasing function of CHF3 is still observed, but the response is very flat with respect to He/O2. Increasing the ion density has no effect on the shape of the response surface; it simply increases the etch rate. For the undoped films, the response surface looks similar to the As-doped films, but there is a slight amount of curvature in the He/O2 response. The same linearly decreasing function of CHF3 is present, and the etch rate is a monotonically increasing function of He/O2. Increasing the ion density only increases the etch rate; it does not change the shape of the response surface.

The situation is more complex for the B-doped films. At low ion densities, the etch rate is actually a linearly *increasing* function of CHF3, which was not observed for any other material. A strong parabolic relationship between the etch rate and the He/O2 flow rate is also noted. As the ion density is increased, the parabolic relationship grows stronger, but the trend for CHF3 reverses itself, and the typical linearly decreasing function of CHF3 is observed. At the highest studied ion density, the same trends are observed, but the parabolic relationship has weakened.

From a surface chemistry perspective, it is possible to draw some qualitative conclusions about the possible chemical mechanisms at work by analyzing the trends observed in experimental data.[94] A reaction rate that is a linearly decreasing function of a chemical species suggests that that species is adsorbed on the surface. A flat or linearly increasing trend suggests that the species is either not adsorbed or the surface coverage is extremely low. A parabolic trend also suggest that the species is adsorbed on the surface. When these principles are applied to the trends observed for the doped polysilicon etching reaction, several tentative conclusions can be drawn.

The films were purposely presented in the order they were in order to highlight the importance of dopant dose on the surface reaction mechanism. As was discussed in the background section of this chapter, the doping effect is a function of the active carrier concentration, rather than the actual chemical identity of the dopant. For that reason, for the purposes of this discussion, I will be focusing on the dopant dose rather than on the dopant species.

For the films dosed with 4E15 cm^{-2} of P, it appears that CHF3 or one of its daughter species and O2/O radicals are all adsorbed on the surface and potentially participate in the rate-limiting reaction step. Ion density does not substantially affect this. The same observations hold for the films dosed with 3E15 cm^{-2} of Sb. For the films dosed with 2E15 cm^{-2} of As, CHF3 is still adsorbed on the surface, but the O2/O species now appear to be primarily in the gas phase or very weakly adsorbed to the surface. For the undoped wafers, the same observations hold, but the role of O2/O has changed in some way. For the films dosed with 2E15 cm^{-2} of the p-type dopant B, the surface mechanisms appear to be a function of ion density in a way that none of the n-type films were. For low ion densities, CHF3 and its daughter species do not adsorb on the surface in any appreciable way, while the O2/O species do. At intermediate and high ion densities, both CHF3/daughters and O2/O adsorb on the surface, as with the higher-dose n-type films.

While these proposed mechanisms are intriguing, it is important to consider them in the larger context of the plasma discharge environment. There are many other species present in the reaction chamber simultaneously that are not being explored here. This technique of deducing reaction mechanisms from rate data was developed in the context of catalysis and may not be applicable in the plasma environment. Nevertheless, these results illustrate some of the fundamental insights into surface chemistry that can be teased from a properly designed experiment.

On a more practical level, the models for each film type were used to calculate the proper timing of the main etch step for the patterned wafers studied in the third and final phase of experiments. Also, as was done with the factorial experiment, the prediction equations can be used to locate optimal processing conditions that will minimize the etch rate differences. Contour plots of the d:un ratio as a function of source power and CHF3 are shown below in Figure 50 for the three levels of He/O2.

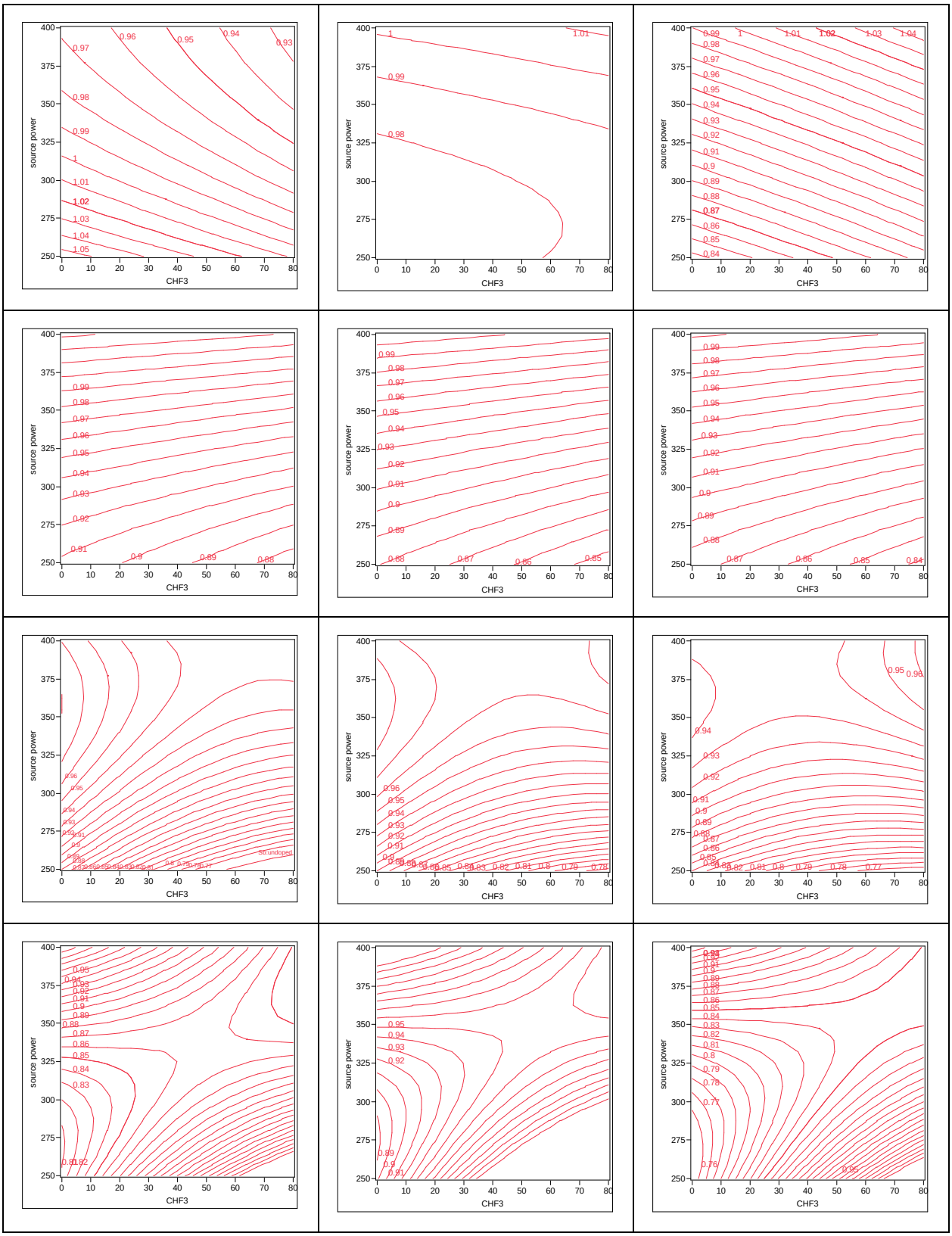

Figure 50: Contour plots of etch rate ratio as a function of source power and CHF3. From left to right for each row: 20, 60, and 100 sccm He/O2. From top to bottom: P:un, As:un, Sb:un, and B:un.

Multiple optimum processing scenarios exist for the phosphorus:undoped films. For arsenic:undoped films, the largest window exists for low He/O2. High source power is required regardless of the He/O2 content. For antimony:undoped films, no processing conditions exist in this parameter space that can produce equal etch rates, and a saddle point exists in the response surface. A saddle point also exists for boron:undoped films, and it appears that high source power and little to no CHF3 for all levels of He/O2 is the direction of the optimum.

To optimize both the etch rate ratio and uniformity simultaneously, the desirability functions mentioned previously were utilized. The results for each of the wafer types are presented below.

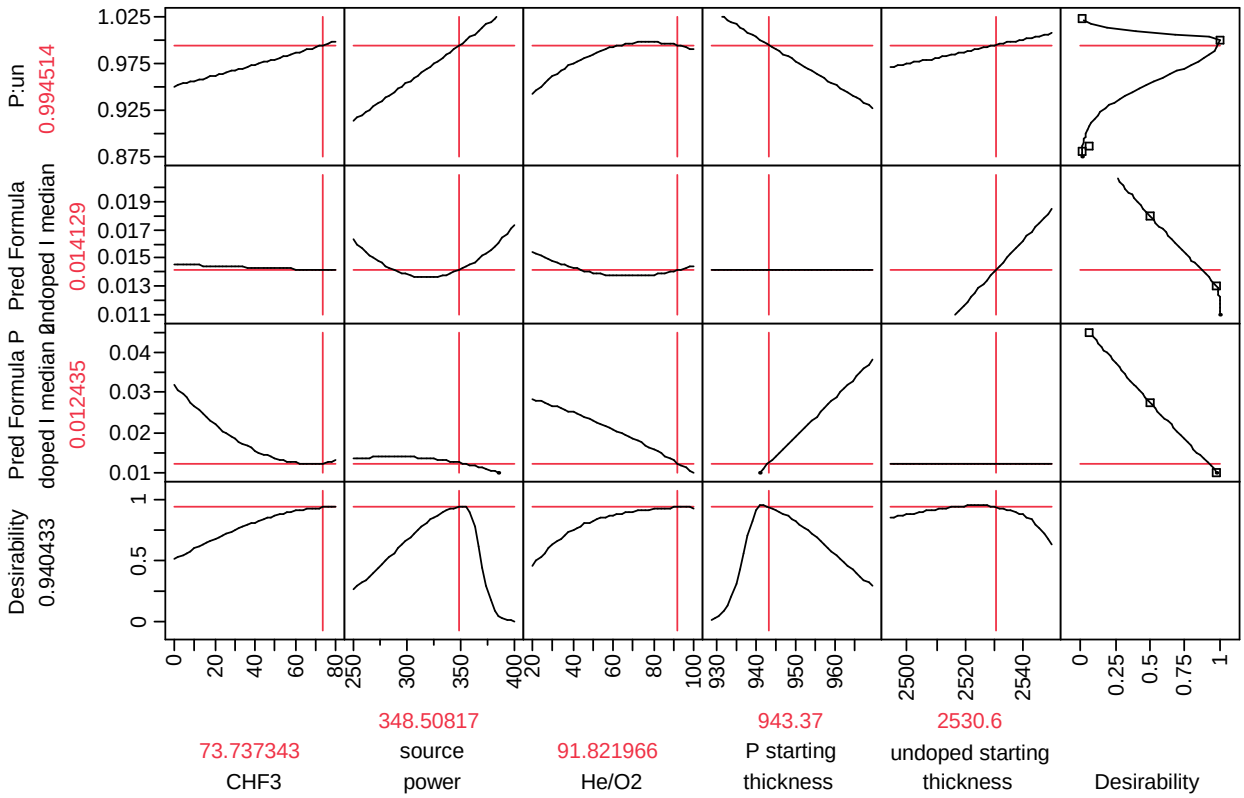

Figure 51: Optimal settings for simultaneously minimizing the etch rate differences and minimizing the across-wafer variance for phosphorus-doped films. Desirability weights: P:un=1 and integration statistic=.5.

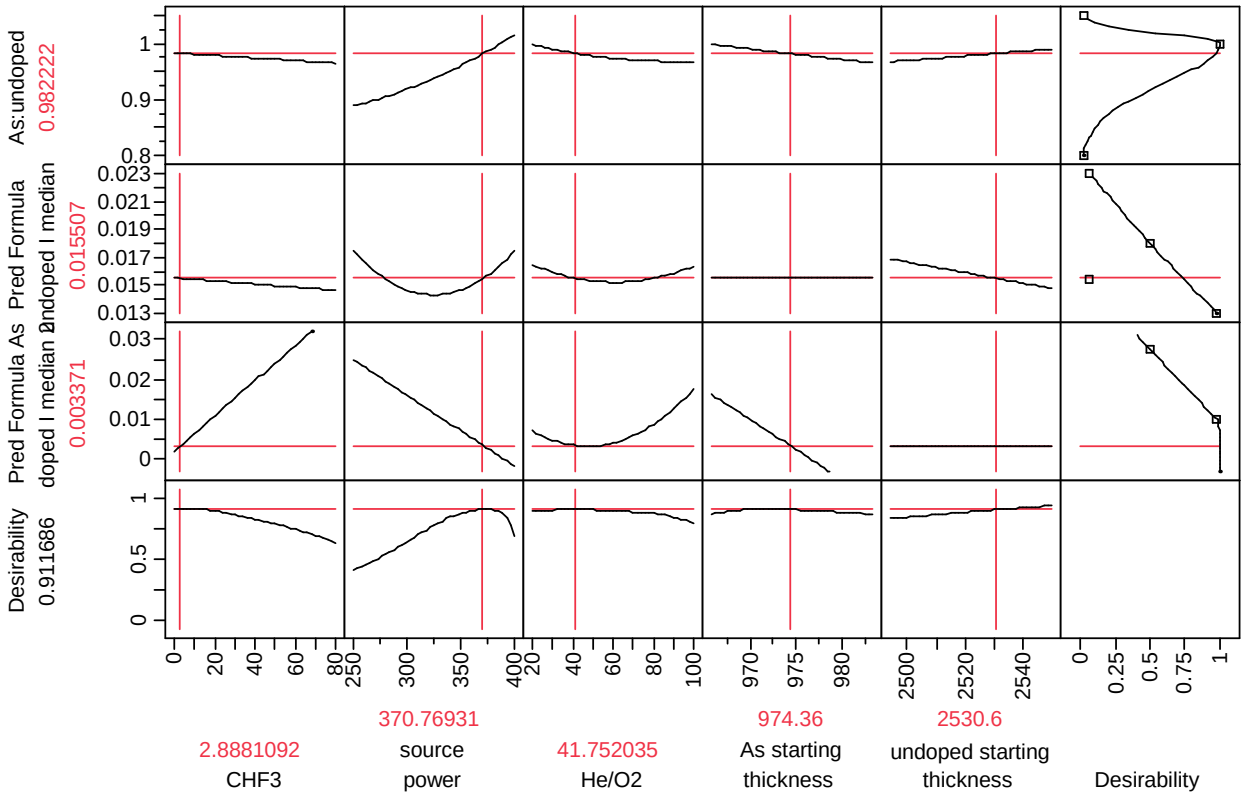

Figure 52: Optimal settings for simultaneously minimizing the etch rate differences and minimizing the across-wafer variance for arsenic-doped films. Desirability weights: As:un=1 and integration statistic=.5.

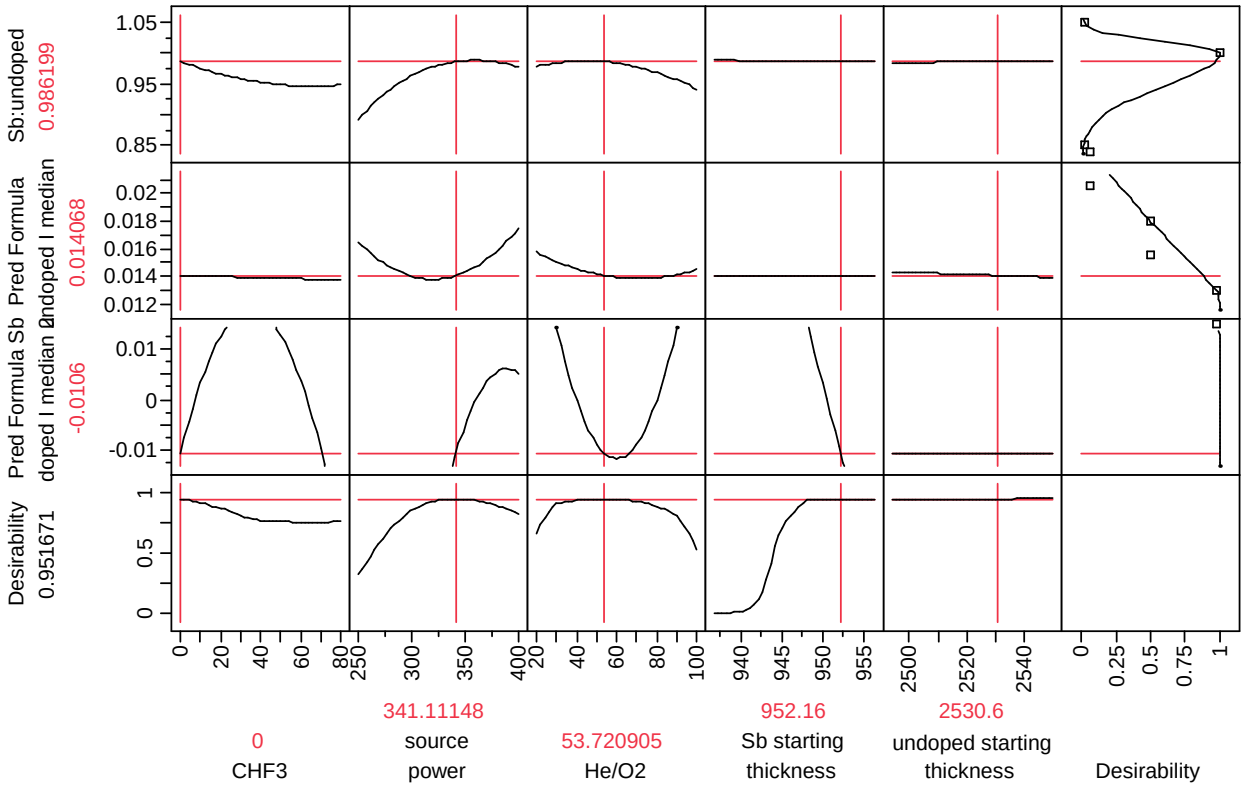

Figure 53: Optimal settings for simultaneously minimizing the etch rate differences and minimizing the across-wafer variance for antimony-doped films. Desirability weights: Sb:un=1 and integration statistic=.5

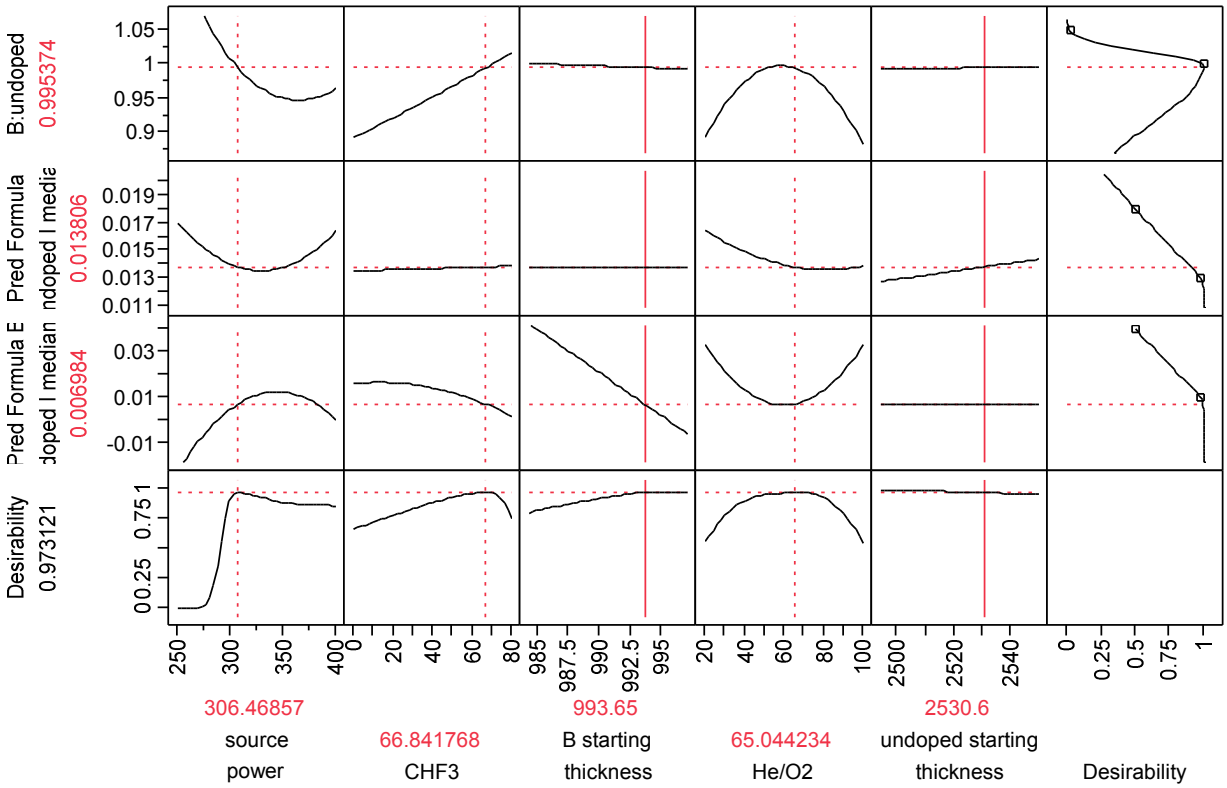

Figure 54: Optimal settings for simultaneously minimizing the etch rate differences and minimizing the across-wafer variance for boron-doped films. Desirability weights: B:un=1 and integration statistic=.5

DESIGNED EXPERIMENT #3: GATE PROFILE STUDIES AS A FUNCTION OF POWER AND CHF3

Twenty-four patterned wafers with polysilicon gates doped with P, As, and Sb were processed using recipes optimized from the results of the previous two designed experiments. The source power was varied to change the ion density and the flow rate of CHF3 was varied to explore the effect of sidewall polymer formation on final gate profile. The optimal etch times were calculated using the model produced in phase 2. The most appropriate parameter space was chosen to capture the desired behavior. The following settings were used:

Power = 400 W CHF3 (sccm) = 0, 40, 53, 66, 80

CHF3 = 66 sccm Power (W) = 250, 325, 400, 475

TEM micrographs of 10 gate structures were created for each wafer (5 each of the doped and undoped gates). The sidewall angle measurements were taken from the TEM images using the Quartz PCIViewer software.

CHF3 FLOW RATE

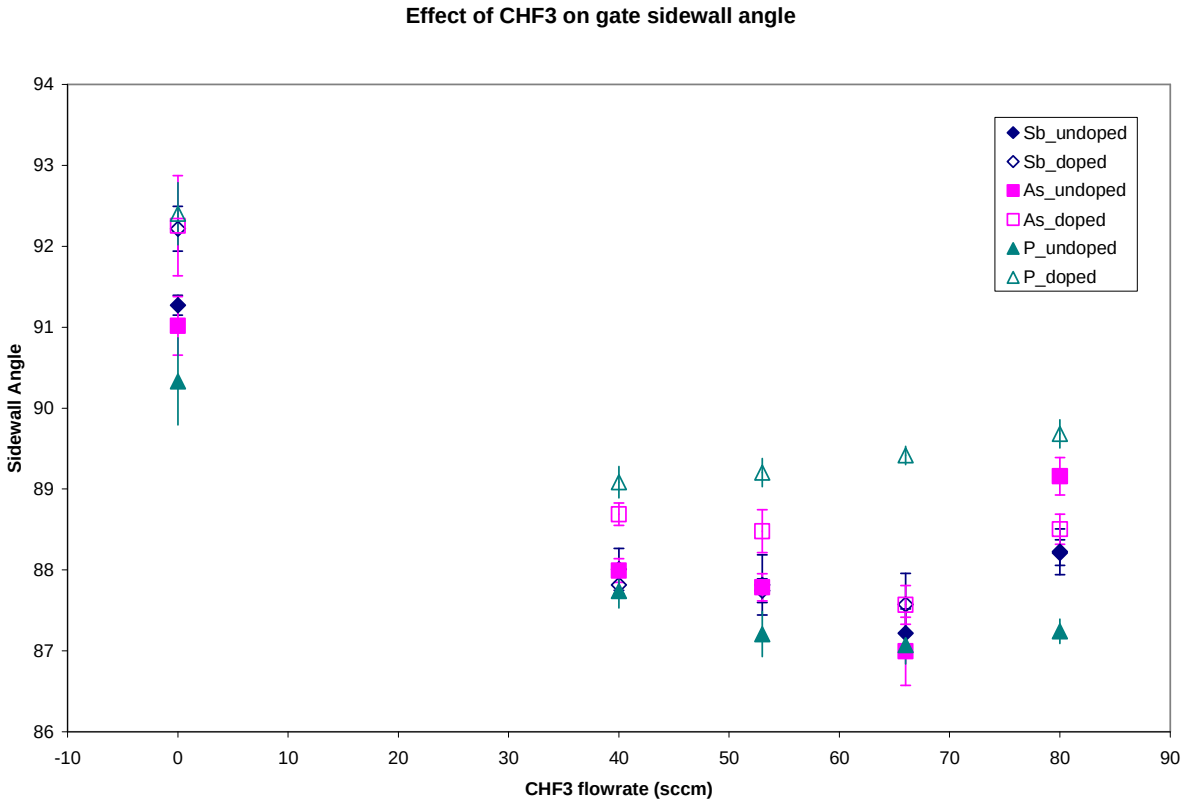

Figure 55: Sidewall angle as a function of CHF3 flow rate for all dopant cases

The effect of CHF_3 on the gate sidewall angle was examined by introducing various flow rates of CHF_3 to the optimized gate etch recipe. The source power for all data was 400 W. The sidewall angles for these experiments fell between 87 and 92.5 degrees. The standard recipe at the time of these experiments did not include CHF_3. For CHF3=0 sccm, the sidewall angle was the highest, the only case to give a greater than 90 degree angle for the sidewall. These profiles also had large "feet", a highly undesirable characteristic that directly affects the transistor performance. For all dopant types, the doped gates had more extreme sidewall angles than the undoped gates. When CHF3 was introduced in any concentration, the sidewall angle decreased approximately 3 degrees. The specific concentration affected the within-wafer variability most noticeably. For CHF3=80 sccm, the sidewall angles for the doped and undoped structures on a wafer are identical for the Sb doped wafers, which was the ultimate goal of this project. The concentrations of CHF3 appear to affect all dopants in a similar way, which agrees with the findings in literature regarding the role of CF4 in changing the chemistry of the sidewall passivation film.

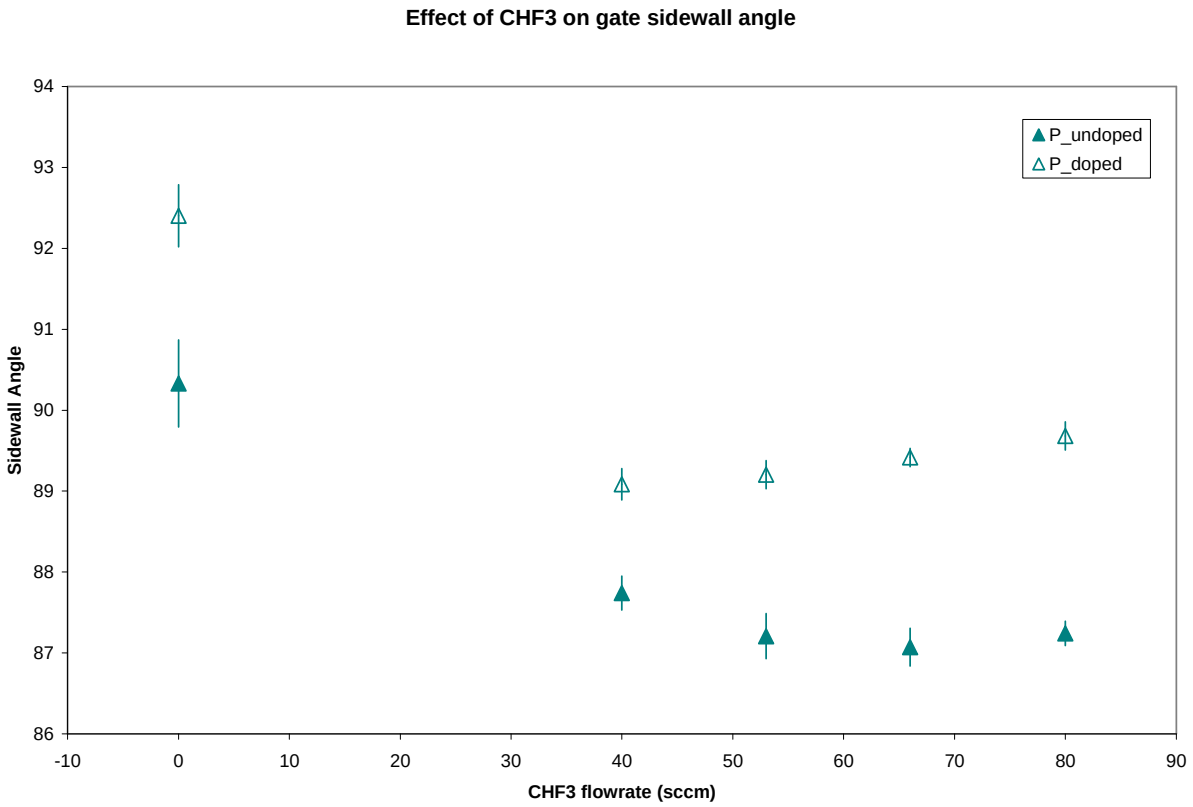

Figure 56: Sidewall angle as a function of CHF3 flow rate for phosphorus doped samples

Phosphorus produced the clearest trends. Without CHF3 present, the sidewall angles for both doped and undoped gates are retrograde (larger than 90 degrees). When CHF3 is introduced, the sidewall angle slowly increases for the phosphorus doped gates, while the angle decreases for the undoped gates. The difference is minimized at CHF3=40 sccm, although the sidewall angles are still more than a degree apart for this case.

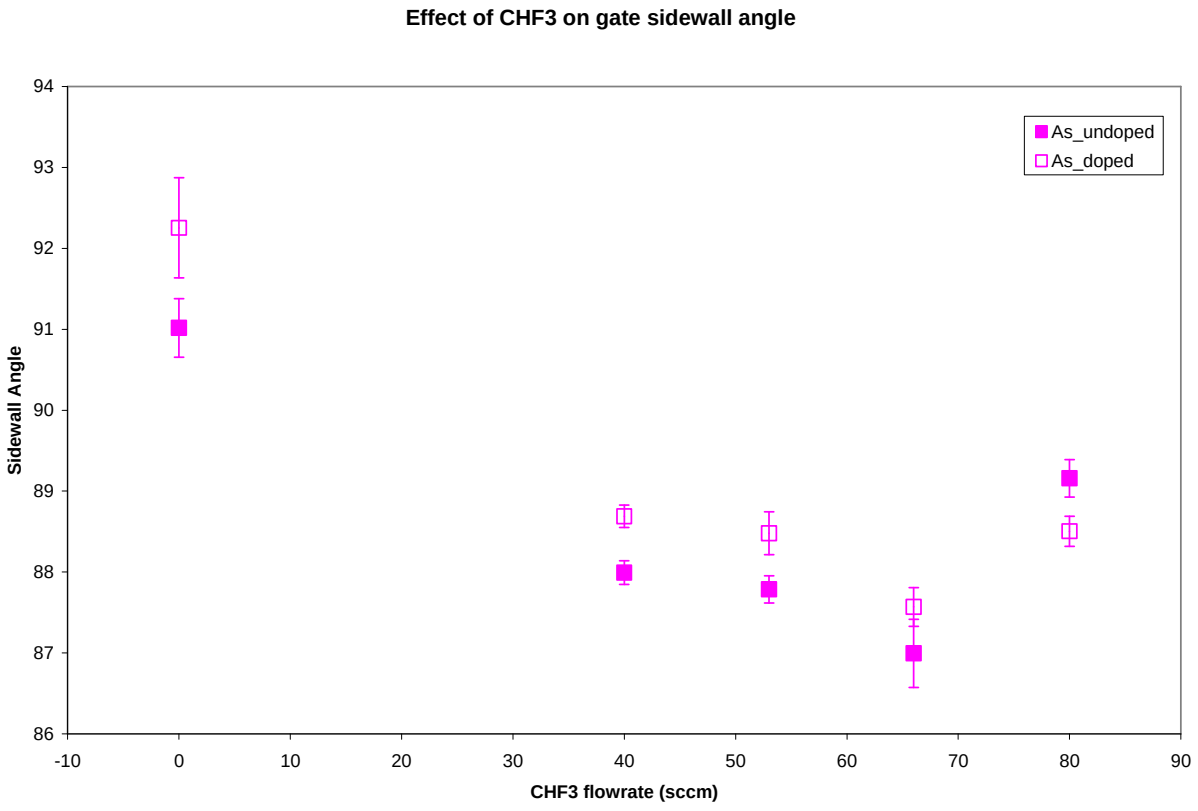

Figure 57: Sidewall angle as a function of CHF3 flow rate for arsenic doped samples

Similar trends are noted for the arsenic case. Without CHF3 present, the sidewall angles are retrograde. For CHF3 flow rates between 40 and 70 sccm, the sidewall angle decreases with increasing CHF3 for both gates. Something unusual happens at the highest CHF3 flow rate of 80 sccm, in that the undoped gate now has a steeper sidewall than the doped gate and the angle has increased for both cases. The optimum setting for As appears to be the CHF3=80 sccm case, since the sidewall angle is closest to the target angle of 89.5 degrees and the difference in angles is minimized.

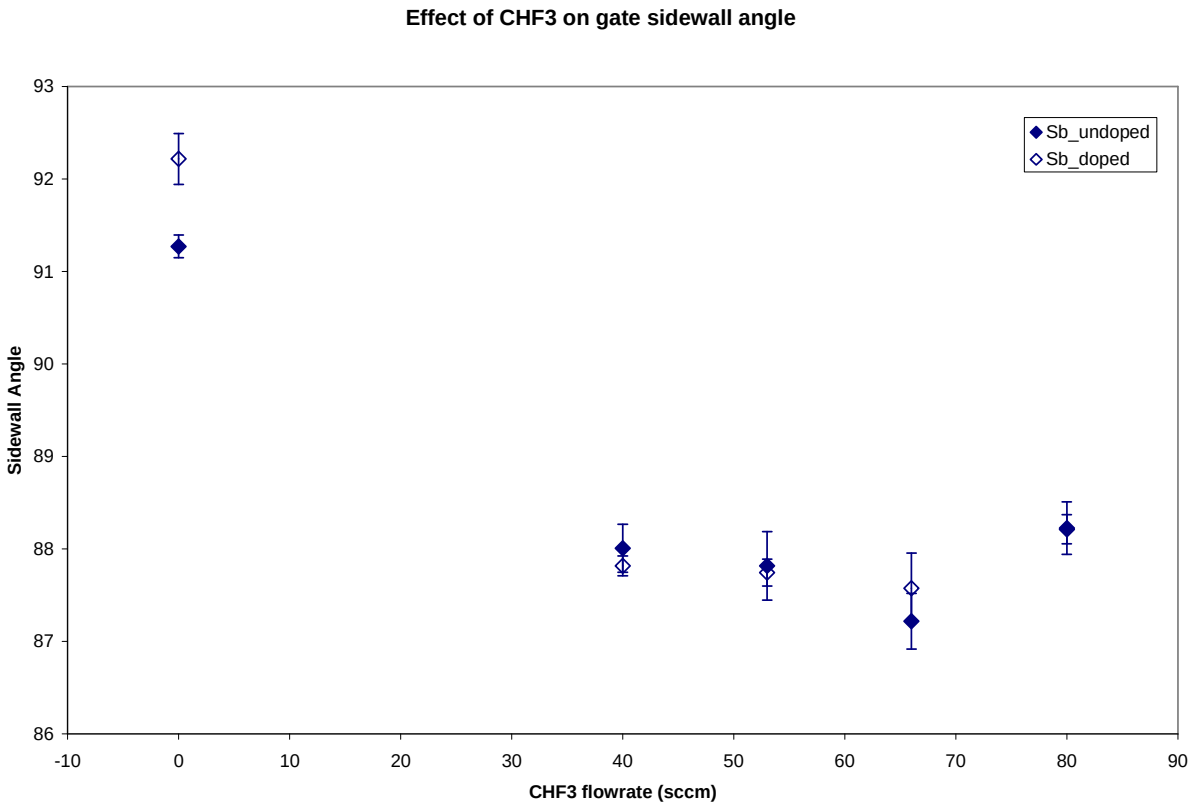

Figure 58: Sidewall angle as a function of CHF3 flow rate for antimony doped samples

Similar observations can be made about the antimony case that were made for the arsenic case. The addition of CHF3 dramatically lowers the sidewall angle, bringing it closer to the target angle. Increasing CHF3 addition causes the sidewall angle to decrease for both doped and undoped samples until the CHF3=80 sccm setting, where the sidewall angle increases to its highest level with CHF3 present. Encouragingly, the undoped and doped gates have identical sidewall angles at this setting, making this the optimum setting for the antimony samples.

SOURCE POWER

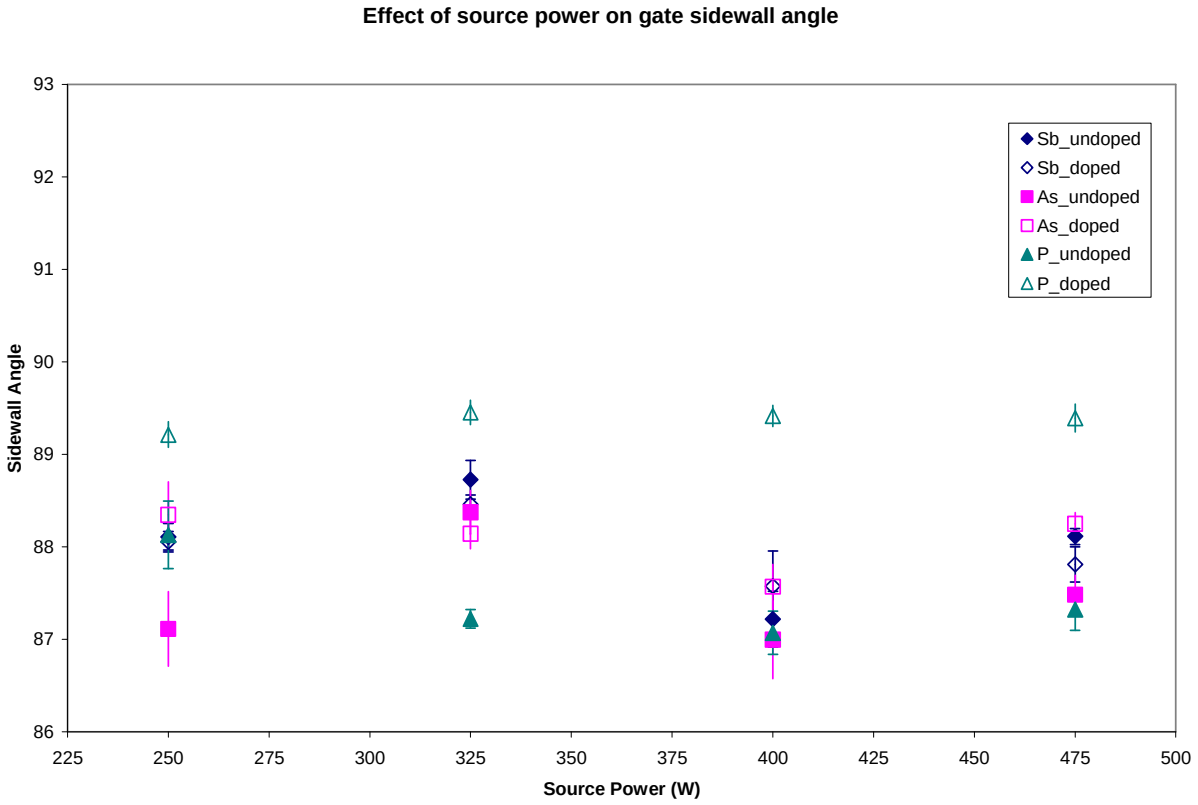

Figure 59: Sidewall angle as a function of source power for all dopant cases

The effect of source power on sidewall angle was examined by varying the source power between 250 and 475 W. CHF3 flow rates for all data was 66 sccm. Source power did not have as strong an effect on the sidewall angle as the CHF3 concentration. The sidewall angle fell between 87 and 89.5 degrees regardless of source power. Source power affected the doped and undoped gates differently for each dopant. The individual results for each dopant type will be discussed below.

For both experiments, the common setting between them—400 W source power and 66 sccm CHF3—yielded the lowest sidewall angle of the data set. All data were several degrees below the sidewall angle target for this technology of 89.5 degrees. Future experiments could explore the parameter space in more detail at the higher sidewall angle results. These results suggest that a source power of 325 W and CHF3 flow rate of 80 sccm would yield the least within-wafer variability for dual-doped gates and the highest achievable sidewall angle with this recipe.

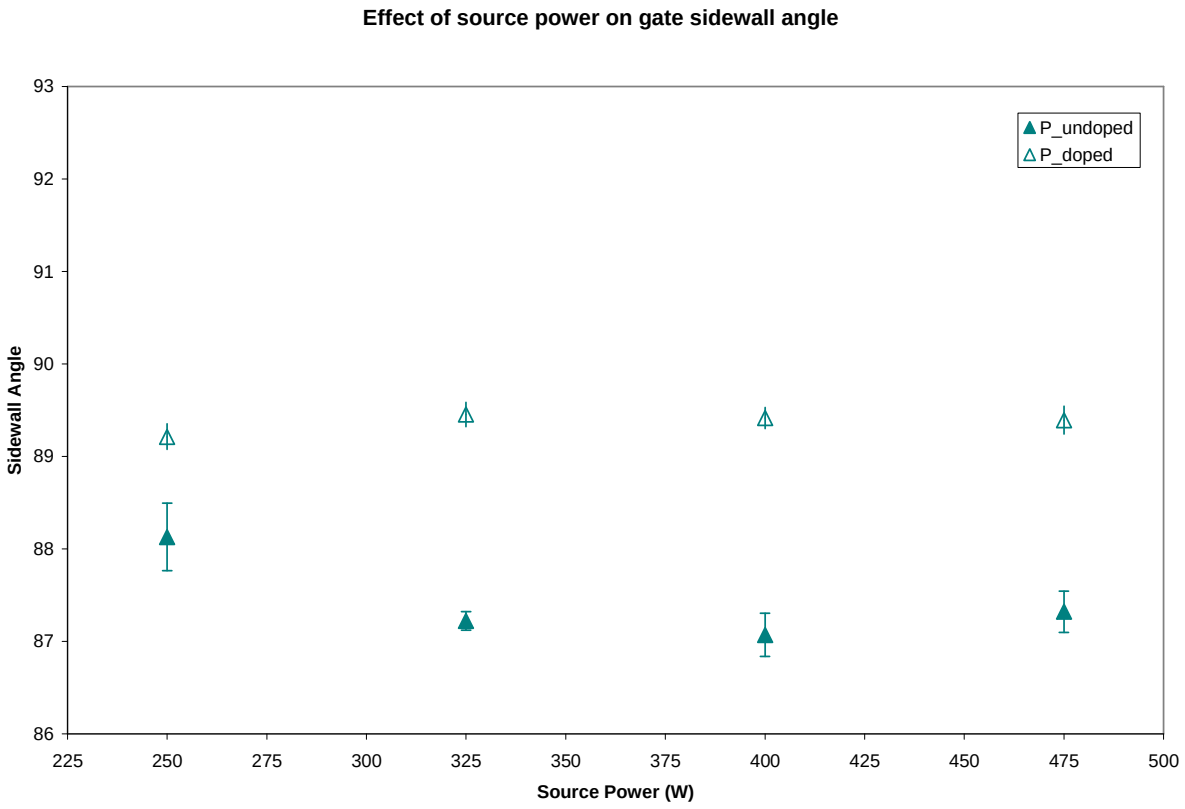

Figure 60: Sidewall angle as a function of source power for phosphorus doped samples

The phosphorus-doped wafers showed the strongest difference between doped and undoped structures. The doped structures were unaffected by the increase in source power, while the undoped gates showed a decrease in sidewall angle as power increased. The 250 W power setting minimizes the differences in the dual-doped gates in this case.

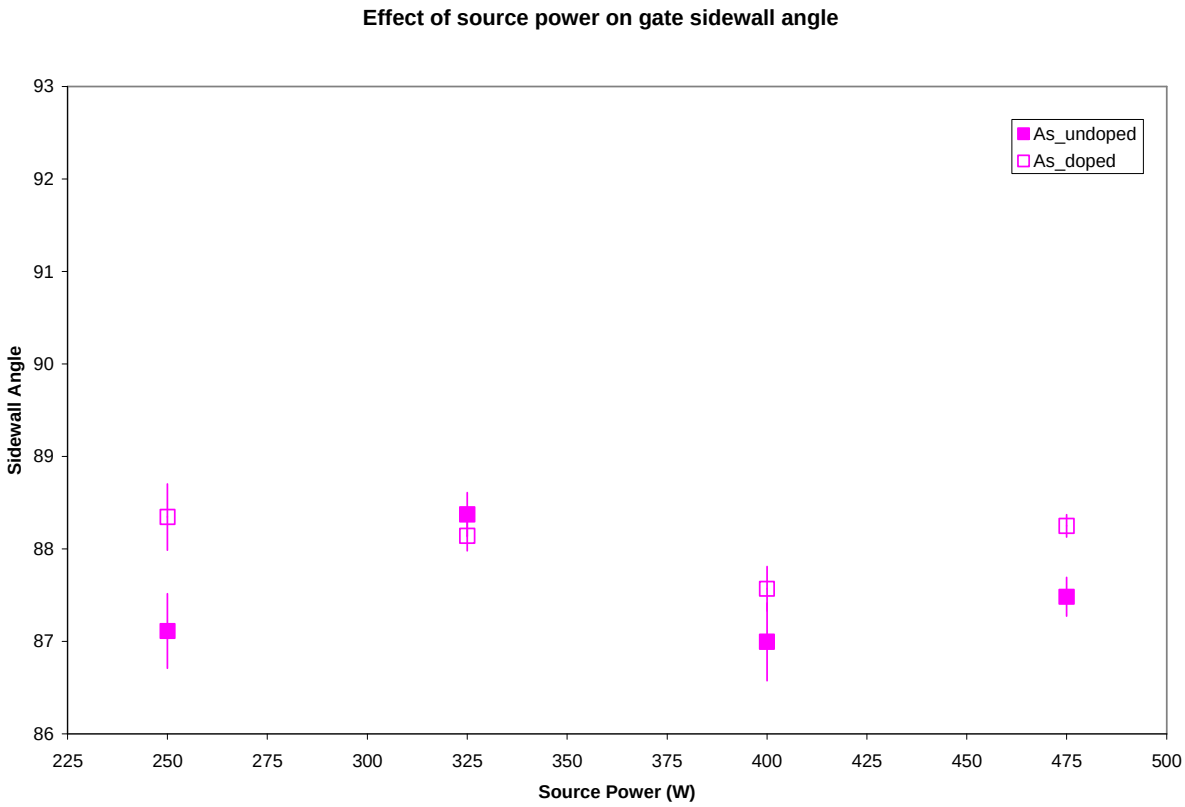

Figure 61: Sidewall angle as a function of source power for arsenic doped samples

For the arsenic-doped case, the increase in source power affected both structures on the wafer. In general, the doped gates had a sidewall angle closer to the target, except for the 325 W case. Here the undoped gates have slightly steeper sidewalls, although within the spread of the data, the doped and undoped gates have essentially the same angle for this power setting. The 325 W power setting minimizes the differences in the dual-doped gates in this case.

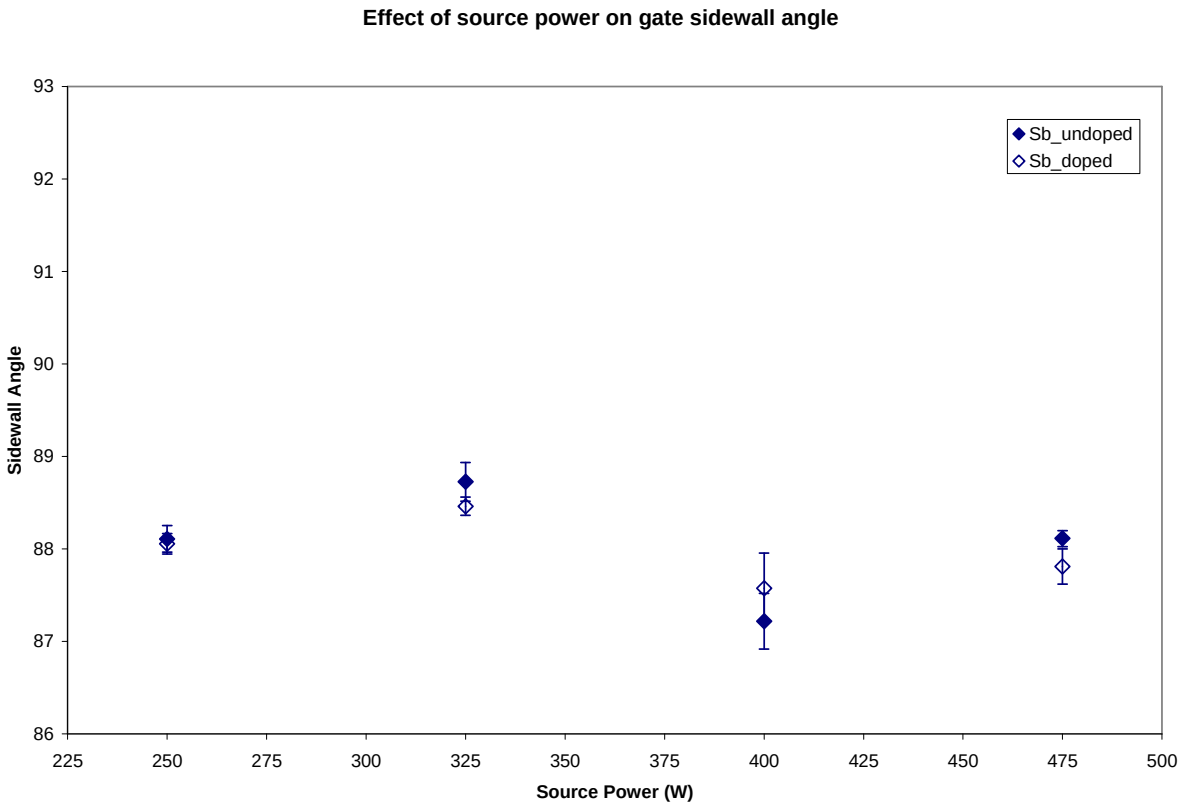

Figure 62: Sidewall angle as a function of source power for antimony doped samples

For the antimony-doped case, the increase in source power also affected both structures on the wafer. In general, the undoped gates had a sidewall angle closer to the target, except for the 400 W case. Here, the doped gates had slightly steeper sidewalls, although within the spread of the data, the doped and undoped gates have essentially the same angle for this power setting. The 250 W power setting minimizes the differences in the dual-doped gates in this case, although unlike the other dopant cases, the doped and undoped gates are statistically the same regardless of power setting.

The vertical distribution of the dopant within the gate has a strong affect on the profile evolution of the gate. SIMS data is available for the phosphorus-doped gates.

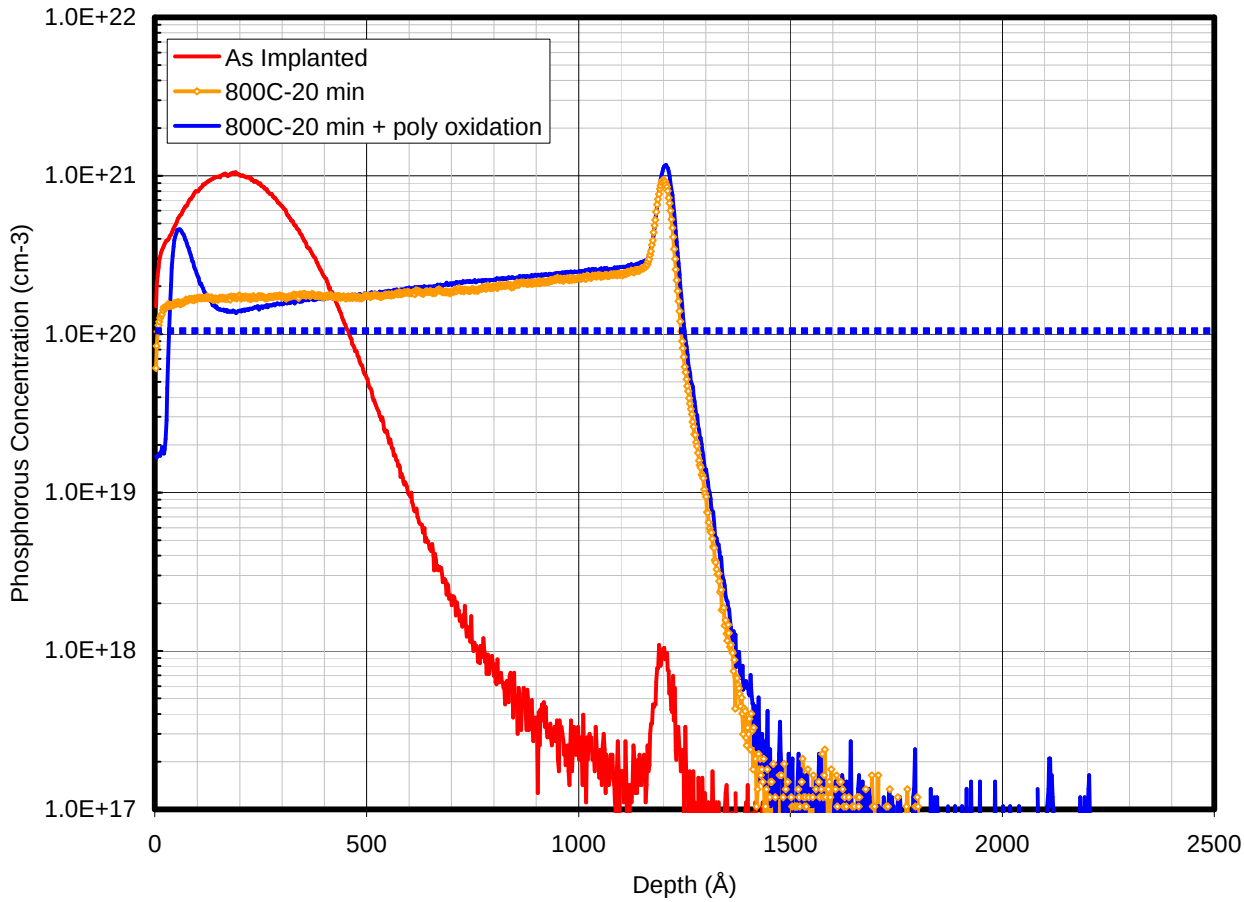

Figure 63: SIMS profile of phosphorus dopant distribution within the gate structure. "As implanted" refers to the condition before annealing, not to the chemical species arsenic.

The profile shows a Gaussian distribution of dopants after implant, but an increasing concentration of dopants from the top to the bottom of the gate once the sample has been annealed. After the poly-Si oxidation step, there is a spike in concentration at both interfaces of the gate.

CONCLUSIONS

Polysilicon gate etching for the 90nm lithography node and below requires extremely precise control of the gate CD and profile. Generally speaking, the current requirement for Gate CD control is that the 3 sigma should less than ~5nm for all gates, including across the chip, across the wafer, wafer-to-wafer, lot-to-lot, and tool-to-tool variations. Similarly, for gate sidewall angle control, the 3 sigma angle variation should be less than ~1 degree, inclusive of all sources of variation. This is particularly challenging for technologies which employ dual-doped gates, since the chemistry and physics of the etching process induces a different profile evolution between gates with different doping.

The goal of this project was to identify a parameter space where the differences in gate profile evolution across different polysilicon dopant types were minimized. Blanket etch rates and patterned wafers were used to determine the effect of different gate etch process variables on the gate profile. The materials studied were undoped polysilicon and polysilicon that had been doped with P, As, Sb, and B. Prediction models were created for the blanket etch rate studies that were used to optimize the processing conditions and to propose some simple mechanisms that identify which species are adsorbed on the surface.

REFERENCES

1. Lieberman, M.A. and A.J. Lichtenberg, *Principles of Plasma Discharges and Materials Processing*. 1994, New York: John Wiley & Sons, Inc.
2. Mauer, J.L., et al., *Mechanism of Silicon Etching by a Cf4 Plasma*. Journal of Vacuum Science & Technology, 1978. **15**(5): p. 1734-1738.
3. Bondur, J.A., *Dry Process Technology (Reactive Ion Etching)*. Journal of Vacuum Science & Technology, 1976. **13**(5): p. 1023-1029.
4. Holland, L. and S.M. Ojha, *Chemical Sputtering of Graphite in an Oxygen Plasma*. Vacuum, 1976. **26**(2): p. 53-60.
5. Hosokawa, N., R. Matsuzaki, and T. Asamaki, *Rf Sputter Etching by Fluoro-Chloro-Hydrocarbon Gases*. Japanese Journal of Applied Physics, 1974: p. 435-438.
6. Winters, H.F. and J.W. Coburn, Appl. Phys. Lett., 1979. **34**: p. 70.
7. Hori, T., *Gate dielectrics and MOS ULSIs : principles, technologies, and applications*. Springer series in electronics and photonics,. 1997, Berlin ; New York: Springer. xiv, 352 p.
8. Grove, A.S., et al., *Investigation of Thermally Oxidised Silicon Surfaces Using Metal-Oxide-Semiconductor Structures*. Solid-State Electronics, 1965. **8**(2): p. 145-&.
9. Gusev, E.P., et al., *Ultrathin high-K metal oxides on silicon: processing, characterization and integration issues*. Microelectronic Engineering, 2001. **59**(1-4): p. 341-349.
10. Murto, R.W., et al., *Challenges in gate stack engineering*. Solid State Technology, 2003. **46**(10): p. 43-+.
11. Zhong, H.C., et al., *Characterization of RuO2 electrodes on Zr silicate and ZrO2 dielectrics*. Applied Physics Letters, 2001. **78**(8): p. 1134-1136.
12. Winters, H.F. and J.W. Coburn, *Surface Science Aspects of Etching Reactions*. Surface Science Reports, 1992. **14**(4-6): p. 161-269.
13. Winters, H.F., J. Vac. Sci. Technol. B, 1985. **3**: p. 9.
14. Chuang, M.C. and J.W. Coburn, *Molecular-Beam Study of Gas-Surface Chemistry in the Ion-Assisted Etching of Silicon with Atomic and Molecular-Hydrogen and Chlorine*. Journal of Vacuum Science & Technology a-Vacuum Surfaces and Films, 1990. **8**(3): p. 1969-1976.
15. Winters, H.F. and I.C. Plumb, *Etching Reactions for Silicon with F-Atoms - Product Distributions and Ion Enhancement Mechanisms*. Journal of Vacuum Science & Technology B, 1991. **9**(2): p. 197-207.
16. Butterbaugh, J.W., D.C. Gray, and H.H. Sawin, *Plasma Surface Interactions in Fluorocarbon Etching of Silicon Dioxide*. Journal of Vacuum Science & Technology B, 1991. **9**(3): p. 1461-1470.
17. Kimura, Y.A., in *Chemical Engineering*. 2002, University of California: Berkeley. p. 25.
18. Kota, G.P., J.W. Coburn, and D.B. Graves, *Heterogeneous recombination of atomic bromine and fluorine*. Journal of Vacuum Science & Technology a-Vacuum Surfaces and Films, 1999. **17**(1): p. 282-290.
19. Kota, G.P., J.W. Coburn, and D.B. Graves, *The recombination of chlorine atoms at surfaces*. Journal of Vacuum Science & Technology a-Vacuum Surfaces and Films, 1998. **16**(1): p. 270-277.
20. Greer, F., et al., *Fundamental beam studies of radical enhanced atomic layer deposition of TiN*. Journal of Vacuum Science & Technology A, 2003. **21**(1): p. 96-105.

21. Cho, J.S., et al., *Surface modification of polymers by ion-assisted reaction*. Thin Solid Films, 2003. **445**(2): p. 332-341.
22. Coburn, J.W., K.M. Kiehlbaugh, Editor. 2004: Berkeley, CA.
23. O'Hanlon, J.F., *A User's Guide to Vacuum Technology*. Second Edition ed. 1989, New York: John Wiley & Sons.
24. Greer, H.F., *Experimental Beam Studies of Radical Enhanced Surface Processes*, in *Chemical Engineering*. 2002, University of California: Berkeley.
25. O'Hanlon, J.F., *A user's guide to vacuum technology*. 3rd ed. 2003, Hoboken, NJ: Wiley-Interscience. xviii, 516 p.
26. *Applications of Piezoelectric Quartz Crystal Microbalances*. Methods and Phenomena, Their Applications in Science and Technology, ed. C. Lu and A.W. Czanderna. Vol. 7. 1984, Amsterdam: Elsevier.
27. Kota, G.P., *Experimental Beam Studies of Plasma-Surface Interactions*, in *Chemical Engineering*. 1998, University of California: Berkeley. p. 316.
28. Czerwiec, T., F. Greer, and D.B. Graves, *Nitrogen dissociation in a low pressure cylindrical ICP discharge studied by actinometry and mass spectrometry*. Journal of Physics D-Applied Physics, 2005. **38**(24): p. 4278-4289.
29. Pozar, D.M., *Microwave engineering*. 3rd ed. 2005, Hoboken, NJ: J. Wiley. xvii, 700 p.
30. Moisan, M., Z. Zakrzewski, and R. Pantel, *THEORY AND CHARACTERISTICS OF AN EFFICIENT SURFACE-WAVE LAUNCHER (SURFATRON) PRODUCING LONG PLASMA COLUMNS*. Journal of Physics D-Applied Physics, 1979. **12**(2): p. 219-&.
31. Popov, O.A., *High density plasma sources : design, physics, and performance*. Materials science and process technology series. 1995, Park Ridge, N.J.: Noyes Publications. xx, 445 p.
32. Nuvolone, R., J. Vac. Sci. Technol., 1977. **14**: p. 1210.
33. Shin, W.C. and S.G. Yoon, *Characterization of RuO2 thin films prepared by hot-wall metallorganic chemical vapor deposition*. Journal of the Electrochemical Society, 1997. **144**(3): p. 1055-1060.
34. Krusinelbaum, L. and M. Wittmer, *Conducting Transition-Metal Oxides - Possibilities for Ruo2 in Vlsi Metallization*. Journal of the Electrochemical Society, 1988. **135**(10): p. 2610-2614.
35. Zhong, H.C., G. Heuss, and V. Misra, Ieee Electron Device Letters, 2000. **21**: p. 593.
36. Frohlich, K., et al., *Ru and RuO2 gate electrodes for advanced CMOS technology*. Materials Science and Engineering B-Solid State Materials for Advanced Technology, 2004. **109**(1-3): p. 117-121.
37. Yunogami, T. and K. Nojiri, *Anisotropic etching of RuO2 and Ru with high aspect ratio for gigabit dynamic random access memory*. Journal of Vacuum Science & Technology B, 2000. **18**(4): p. 1911-1914.
38. Saito, S. and K. Kuramasu, *Plasma-Etching of Ruo2 Thin-Films*. Japanese Journal of Applied Physics Part 1-Regular Papers Short Notes & Review Papers, 1992. **31**(1): p. 135-138.
39. Lee, E.J., J.W. Kim, and W.J. Lee, *Reactive ion etching mechanism of RuO2 thin films in oxygen plasma with the addition of CF4, Cl-2, and N-2*. Japanese Journal of Applied Physics Part 1-Regular Papers Short Notes & Review Papers, 1998. **37**(5A): p. 2634-2641.
40. Kim, H.W., B.S. Ju, and C.J. Kang, *High-rate Ru electrode etching using O-2/Cl-2 inductively coupled plasma*. Microelectronic Engineering, 2003. **65**(3): p. 319-326.
41. Bell, W.E. and M. Tagami, *High-Temperature Chemistry of Ruthenium-Oxygen System*. Journal of Physical Chemistry, 1963. **67**(11): p. 2432-&.
42. Schafer, H., G. Schneidereit, and W. Gerhardt, *Zur Chemie Der Platinmetalle - Ruo2 Chemischer Transport, Eigenschaften, Thermischer Zerfall*. Zeitschrift Fur Anorganische Und Allgemeine Chemie, 1963. **319**(5-6): p. 327-336.

43. Schafer, H., A. Tebben, and W. Gerhardt, *Zur Chemie Der Platinmetalle .5. Gleichgewichte Mit Ru(F), Ruo2(F), Ruo3(G) Und Ruo4(G)*. Zeitschrift Fur Anorganische Und Allgemeine Chemie, 1963. **321**(1-2): p. 41-55.
44. Pan, W. and S.B. Desu, *Reactive Ion Etching of Ruo2, Thin-Films Using the Gas-Mixture O-2 Cf3cfh2*. Journal of Vacuum Science & Technology B, 1994. **12**(6): p. 3208-3213.
45. Pan, W. and S.B. Desu, *Reactive ion etching of RuO2 films: The role of additive gases in O-2 discharge*. Physica Status Solidi a-Applied Research, 1997. **161**(1): p. 201-215.
46. Baborowski, J., et al., *Etching of RuO2 and Pt thin films with ECR/RF reactor*. Vacuum, 2000. **56**(1): p. 51-56.
47. Kim, H.W., et al., *Study of Ru etching using O-2/Cl-2 helicon plasmas*. Materials Science and Engineering B-Solid State Materials for Advanced Technology, 2002. **95**(3): p. 249-253.
48. Hsu, C.C., J.W. Coburn, and D.B. Graves, *Etching of ruthenium coatings in O-2- and Cl-2-containing plasmas*. Journal of Vacuum Science & Technology A, 2006. **24**(1): p. 1-8.
49. Hsu, C.C., et al., *Comparison of model and experiment for Ar, Ar/O-2 and Ar/O-2/Cl-2 inductively coupled plasmas*. Journal of Physics D-Applied Physics, 2006. **39**(15): p. 3272-3284.
50. Lim, K.T., et al., *The effect of CF4 addition on Ru etching with inductively coupled plasma*. Journal of the Korean Physical Society, 2003. **42**: p. S829-S832.
51. Koretsky, M.D. and J.A. Reimer, *Anomalous Etch Rates of Photoresist with Argon Dilution of Cf4/O2 Plasma Afterglows*. Applied Physics Letters, 1991. **59**(13): p. 1547-1549.
52. Koretsky, M.D. and J.A. Reimer, *A Simple-Model for the Etching of Photoresist with Plasma-Generated Reactants*. Journal of Applied Physics, 1992. **72**(11): p. 5081-5088.
53. Tokashiki, K. in *Proceeding of SEMI Technology Symposium*. 1996.
54. Hu, G.J. and R.H. Bruce, *DESIGN TRADEOFFS BETWEEN SURFACE AND BURIED-CHANNEL FETS*. Ieee Transactions on Electron Devices, 1985. **32**(3): p. 584-588.
55. Wong, C.Y., et al. *Doping of n/sup +/ and p/sup +/ polysilicon in a dual-gate CMOS process*. in *International Electron Devices Meeting. Technical Digest (IEEE Cat. No.88CH2528-8)*. 1988. San Francisco, CA,: Ieee.
56. Hyung, L., et al., *Advanced profile control and the impact of sidewall angle at gate etch for critical nodes*. Proceedings of the SPIE - The International Society for Optical Engineering, 2008. **6922**: p. 69220T-1-69220T-69220T-13.
57. Vitale, S.A. 2005.
58. Mui, D.S.L., et al., *Integrated optical metrology controls post etch CDs*. Semiconductor International, 2002. **25**(5): p. 83-83-83-4, 90.
59. Pogge, H.B., J.A. Bondur, and P.J. Burkhardt, *Reactive Ion Etching of Silicon with Cl2-Ar*. Journal of the Electrochemical Society, 1978. **125**(11): p. C470-C470.
60. Jinno, K., H. Kinoshita, and Y. Matsumoto, *ETCHING CHARACTERISTICS OF PHOSPHORUS CONTAINING POLYCRYSTALLINE SILICON IN A CF4 PLASMA*. Journal of the Electrochemical Society, 1978. **125**(5): p. 827-828.
61. Mogab, C.J. and H.J. Levinstein, *Anisotropic-Plasma Etching of Polysilicon*. Journal of Vacuum Science & Technology, 1980. **17**(3): p. 721-730.
62. Irene, E.A., et al., *AN ELECTRON-MICROSCOPE INVESTIGATION OF THE EFFECT OF PHOSPHORUS DOPING ON THE PLASMA-ETCHING OF POLYCRYSTALLINE SILICON*. Journal of the Electrochemical Society, 1981. **128**(9): p. 1971-1974.
63. Pogge, H.B., J.A. Bondur, and P.J. Burkhardt, *REACTIVE ION ETCHING OF SILICON WITH CL2/AR(1)*. Journal of the Electrochemical Society, 1983. **130**(7): p. 1592-1597.

64. Beinvogl, W. and B. Hasler, *REACTIVE ION ETCHING OF POLYSILICON AND TANTALUM SILICIDE*. Solid State Technology, 1983. **26**(4): p. 125-130.
65. Baldi, L. and D. Beardo, *Effects of Doping on Polysilicon Etch Rate in a Fluorine-Containing Plasma*. Journal of Applied Physics, 1985. **57**(6): p. 2221-2225.
66. Lee, Y.H. and M.M. Chen, *Silicon Doping Effects in Reactive Plasma-Etching*. Journal of Vacuum Science & Technology B, 1986. **4**(2): p. 468-475.
67. Gamble, H.S., N.E. Evans, and S.H. Raza, *Preferential Etching of Boron-Doped Polysilicon Electrodes for Ccds*. Journal of the Electrochemical Society, 1980. **127**(4): p. 990-992.
68. Flamm, D.L., P.L. Cowan, and J.A. Golovchenko, *ETCHING AND FILM FORMATION IN CF3BR PLASMAS - SOME QUALITATIVE OBSERVATIONS AND THEIR GENERAL IMPLICATIONS*. Journal of Vacuum Science & Technology, 1980. **17**(6): p. 1341-1347.
69. Bell, F.H., O. Joubert, and L. Vallier, *Polysilicon gate etching in high density plasmas .2. X-ray photoelectron spectroscopy investigation of silicon trenches etched using a chlorine-based chemistry*. Journal of Vacuum Science & Technology B, 1996. **14**(3): p. 1796-1806.
70. Bell, F.H., O. Joubert, and L. Vallier, *Polysilicon gate etching in high density plasmas .1. Process optimization using a chlorine-based chemistry*. Journal of Vacuum Science & Technology B, 1996. **14**(1): p. 96-101.
71. Berg, S., et al., *Dry Etching of N-Type and P-Type Polysilicon - Parameters Affecting the Etch Rate*. Journal of Vacuum Science & Technology a-Vacuum Surfaces and Films, 1987. **5**(4): p. 1600-1603.
72. Schwartz, G.C. and P.M. Schaible, *Reactive Ion Etching of Silicon*. Journal of Vacuum Science & Technology, 1979. **16**(2): p. 410-413.
73. Koike, A., et al., *ANISOTROPIC-PLASMA ETCHING OF POLYSILICON*. Journal of the Electrochemical Society, 1982. **129**(3): p. C105-C105.
74. Kraft, R., T. Boonstra, and S. Prengle, *Etching 0.35 mu m polysilicon gates on a high-density helicon etcher*. Journal of Vacuum Science & Technology B, 1996. **14**(1): p. 543-546.
75. Okazaki, Y., et al., *SUB-1/4-MU-M DUAL-GATE CMOS TECHNOLOGY USING IN-SITU DOPED POLYSILICON FOR NMOS AND PMOS GATES*. Ieee Transactions on Electron Devices, 1995. **42**(9): p. 1583-1590.
76. Hung, C.C., et al., *Simultaneous etching of polysilicon materials with different doping types by low-damage transformer-coupled plasma technique*. Microelectronic Engineering, 2002. **63**(4): p. 405-416.
77. Westerheim, A.C., et al., *High-density, inductively coupled plasma etch of sub half-micron critical layers: Transistor polysilicon gate definition and contact formation*. Journal of Vacuum Science & Technology B, 1998. **16**(5): p. 2699-2706.
78. Xu, S.L., et al., *Fluorocarbon polymer formation, characterization, and reduction in polycrystalline-silicon etching with CF4-added plasma*. Journal of Vacuum Science & Technology a-Vacuum Surfaces and Films, 2001. **19**(3): p. 871-877.
79. Cunge, G., et al., *Ion flux composition in HBr/Cl-2/O-2 and HBr/Cl-2/O-2/CF4 chemistries during silicon etching in industrial high-density plasmas*. Journal of Vacuum Science & Technology B, 2002. **20**(5): p. 2137-2148.
80. Detter, X., et al., *Impact of chemistry on profile control of resist masked silicon gates etched in high density halogen-based plasmas*. Journal of Vacuum Science & Technology B, 2003. **21**(5): p. 2174-2183.
81. Vallier, L., et al., *Chemical topography analyses of silicon gates etched in HBr/Cl-2/O-2 and HBr/Cl-2/O-2/CF4 high density plasmas*. Journal of Vacuum Science & Technology B, 2003. **21**(2): p. 904-911.

82. Bell, F.H. and O. Joubert, *Polysilicon gate etching in high density plasmas .5. Comparison between quantitative chemical analysis of photoresist and oxide masked polysilicon gates etched in HBr/Cl-2/O-2 plasmas*. Journal of Vacuum Science & Technology B, 1997. **15**(1): p. 88-97.
83. Guinn, K.V., C.C. Cheng, and V.M. Donnelly, *QUANTITATIVE CHEMICAL TOPOGRAPHY OF POLYCRYSTALLINE SI ANISOTROPICALLY ETCHED IN CL-2/O-2 HIGH-DENSITY PLASMAS*. Journal of Vacuum Science & Technology B, 1995. **13**(2): p. 214-226.
84. Joubert, O., et al., *Monitoring chamber walls coating deposited during plasma processes: Application to silicon gate etch processes*. Journal of Vacuum Science & Technology A, 2004. **22**(3): p. 553-563.
85. Montgomery, D.C., *Design and analysis of experiments*. 6th ed. 2005, Hoboken, NJ: John Wiley & Sons. xv, 643 p.
86. Box, G.E.P., J.S. Hunter, and W.G. Hunter, *Statistics for experimenters : design, innovation, and discovery*. 2nd ed. Wiley series in probability and statistics. 2005, Hoboken, N.J.: Wiley-Interscience. xvii, 633 p.
87. Ma, S.M., M. Jain, and J.D. Chinn, *Evaluation of plasma charging damage during polysilicon gate etching process in a decoupled plasma source reactor*. Journal of Vacuum Science & Technology A, 1998. **16**(3): p. 1440-1443.
88. Montgomery, D.C., et al., *The hierarchy principle in designed industrial experiments*. Quality and Reliability Engineering International, 2005. **21**(2): p. 197-201.
89. Myers, R.H., *Classical and modern regression with applications*. 2nd ed. The Duxbury advanced series in statistics and decision sciences. 1990, Boston: PWS-KENT. viii, 488 p.
90. Davis, J.C., et al., *A robust metric for measuring within-wafer uniformity*. IEEE Transactions on Components, Packaging & Manufacturing Technology, Part C (Manufacturing)|IEEE Transactions on Components, Packaging & Manufacturing Technology, Part C (Manufacturing), 1996. **19**(4): p. 10.1109/3476.558556.
91. Yamartino, J., et al. (2005) *Enhancing process control flexibility for sub-90nm applications*. Semiconductor Fabtech, 134-136.
92. Derringer, G. and R. Suich, *SIMULTANEOUS-OPTIMIZATION OF SEVERAL RESPONSE VARIABLES*. Journal of Quality Technology, 1980. **12**(4): p. 214-219.
93. Box, G.E.P. and D.W. Behnken, *SIMPLEX-SUM DESIGNS - A CLASS OF 2ND ORDER ROTATABLE DESIGNS DERIVABLE FROM THOSE OF 1ST ORDER*. Annals of Mathematical Statistics, 1960. **31**(4): p. 838-864.
94. Fogler, H.S., *Elements of chemical reaction engineering*. 4th ed. Prentice Hall PTR international series in the physical and chemical engineering sciences. 2006, Upper Saddle River, NJ: Prentice Hall PTR. xxxii, 1080 p.

APPENDIX

FULL FACTORIAL WITH COVARIATE FOR DOPED WAFERS

Response avg ER doping=1
Actual by Predicted Plot

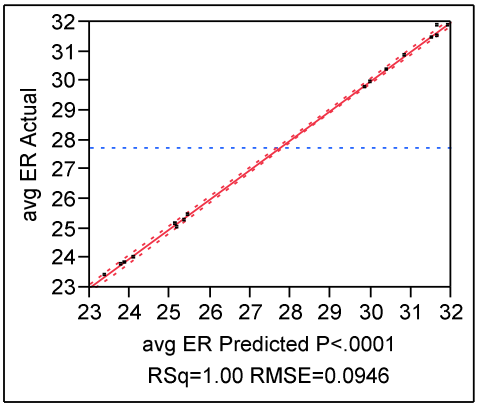

Summary of Fit

RSquare	0.999492
RSquare Adj	0.999239
Root Mean Square Error	0.094598
Mean of Response	27.73215
Observations (or Sum Wgts)	16

Analysis of Variance

Source	DF	Sum of Squares	Mean Square	F Ratio
Model	5	176.18782	35.2376	3937.727
Error	10	0.08949	0.0089	**Prob > F**
C. Total	15	176.27730		<.0001*

Parameter Estimates

Term	Estimate	Std Error	t Ratio	Prob>|t|
Intercept	27.687939	0.029106	951.27	<.0001*
source power	3.254943	0.024276	134.08	<.0001*
CHF3	-0.696408	0.024422	-28.52	<.0001*
doped starting thickness(2458.43,2517.83)	0.1741617	0.043909	3.97	0.0027*
O2*doped starting thickness	0.2259228	0.036414	6.20	0.0001*
O2*CHF3*doped starting thickness	0.3763801	0.03835	9.81	<.0001*

Effect Tests

Source	Nparm	DF	Sum of Squares	F Ratio	Prob > F
source power	1	1	160.87477	17977.43	<.0001*
CHF3	1	1	7.27658	813.1426	<.0001*
doped starting thickness(2458.43,2517.83)	1	1	0.14079	15.7325	0.0027*
O2*doped starting thickness	1	1	0.34447	38.4936	0.0001*

Source	Nparm	DF	Sum of Squares	F Ratio	Prob > F
O2*CHF3*doped starting thickness	1	1	0.86194	96.3204	<.0001*

Press

Press	Press RMSE
0.2566416298	0.12664952

Residual by Predicted Plot

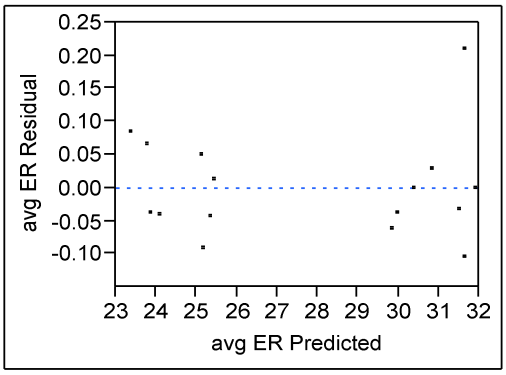

Distributions doping=1
Studentized Resid avg ER By doping

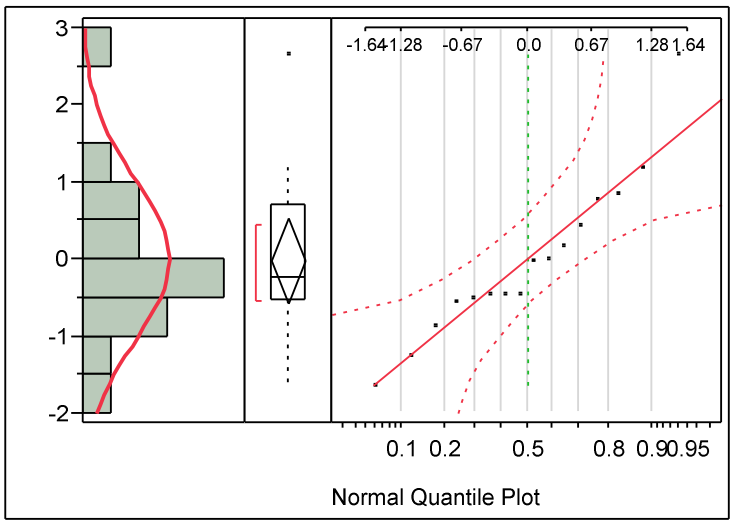

Normal(-0.0076,1.04237)

Quantiles

100.0%	maximum	2.662
99.5%		2.662
97.5%		2.662

90.0%		1.632
75.0%	quartile	0.697
50.0%	median	-0.236
25.0%	quartile	-0.534
10.0%		-1.376
2.5%		-1.644
0.5%		-1.644
0.0%	minimum	-1.644

Moments

Mean	-0.007647
Std Dev	1.0423685
Std Err Mean	0.2605921
Upper 95% Mean	0.5477921
Lower 95% Mean	-0.563086
N	16

Fitted Normal
Parameter Estimates

Type	Parameter	Estimate	Lower 95%	Upper 95%
Location	μ	-0.007647	-0.563086	0.5477921
Dispersion	σ	1.0423685	0.7700027	1.6132645

-2log(Likelihood) = 45.7338889596917

Goodness-of-Fit Test

Shapiro-Wilk W Test

W	Prob<W
0.938895	0.3357

Note: Ho = The data is from the Normal distribution. Small p-values reject Ho.

Fit Y by X Group
Oneway Analysis of Studentized Resid avg ER By doping By source power doping=1

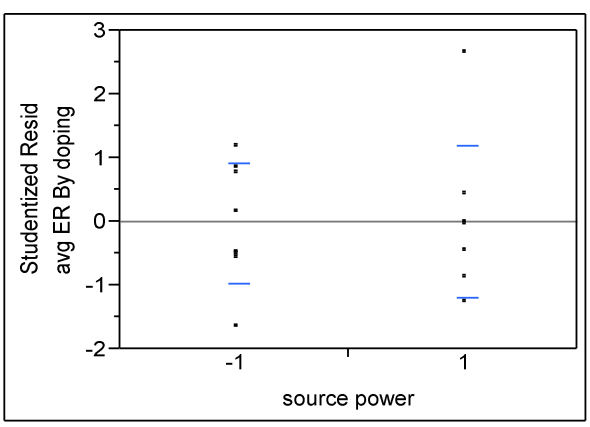

Tests that the Variances are Equal

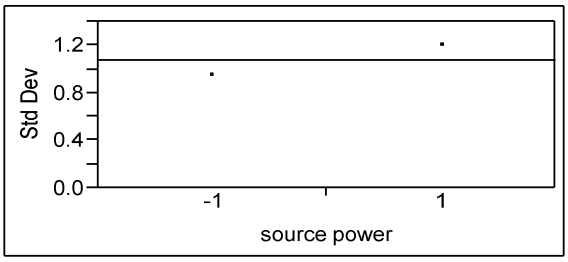

Level	Count	Std Dev	MeanAbsDif to Mean	MeanAbsDif to Median
-1	8	0.945871	0.7701808	0.7701808
1	8	1.197192	0.7718368	0.7638205

Test	F Ratio	DFNum	DFDen	p-Value
O'Brien[.5]	0.2306	1	14	0.6385
Brown-Forsythe	0.0003	1	14	0.9864
Levene	0.0000	1	14	0.9963
Bartlett	0.3594	1	.	0.5488
F Test 2-sided	1.6020	7	7	0.5492

Welch's Test

Welch Anova testing Means Equal, allowing Std Devs Not Equal

F Ratio	DFNum	DFDen	Prob > F
0.0021	1	13.289	0.9644

t Test
0.0454

Oneway Analysis of Studentized Resid avg ER By doping By CF4 doping=1

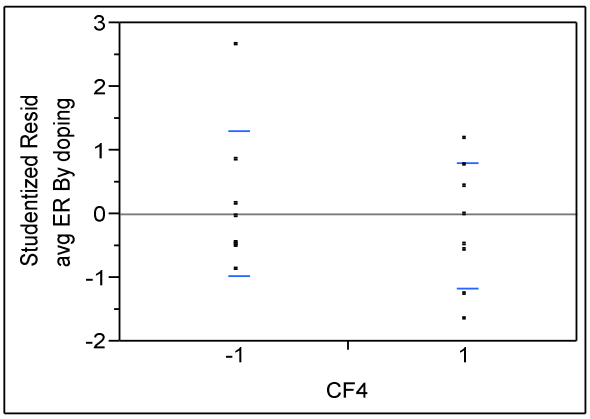

Tests that the Variances are Equal

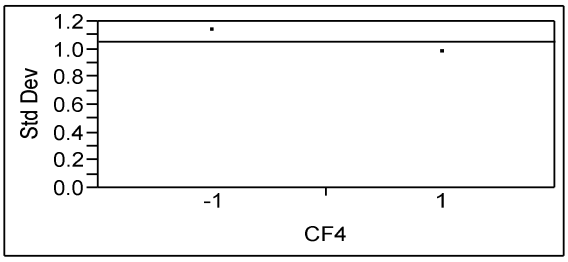

Level	Count	Std Dev	MeanAbsDif to Mean	MeanAbsDif to Median
-1	8	1.136577	0.7936461	0.7446292
1	8	0.981119	0.7893722	0.7893722

Test	F Ratio	DFNum	DFDen	p-Value
O'Brien[.5]	0.1132	1	14	0.7415
Brown-Forsythe	0.0146	1	14	0.9057
Levene	0.0002	1	14	0.9896
Bartlett	0.1408	1	.	0.7075
F Test 2-sided	1.3420	7	7	0.7077

Welch's Test

Welch Anova testing Means Equal, allowing Std Devs Not Equal

F Ratio	DFNum	DFDen	Prob > F
0.4588	1	13.708	0.5095

t Test
0.6774

Oneway Analysis of Studentized Resid avg ER By doping By O2 doping=1

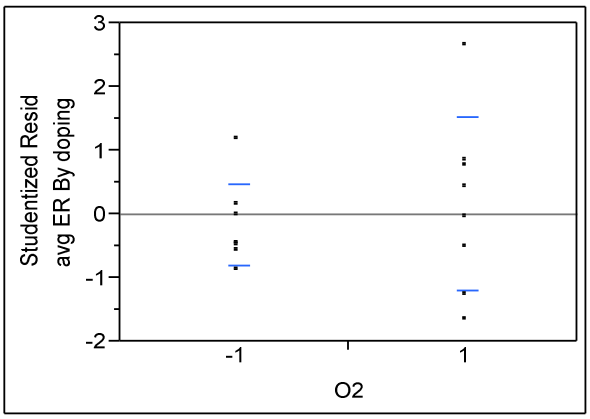

Tests that the Variances are Equal

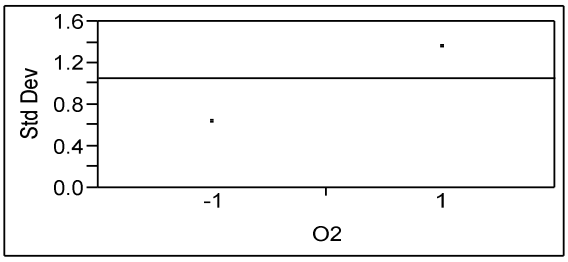

Level	Count	Std Dev	MeanAbsDif to Mean	MeanAbsDif to Median
-1	8	0.640029	0.473376	0.405602
1	8	1.361033	1.021711	1.021711

Test	F Ratio	DFNum	DFDen	p-Value
O'Brien[.5]	2.1046	1	14	0.1689
Brown-Forsythe	3.1300	1	14	0.0986
Levene	2.9589	1	14	0.1074
Bartlett	3.4120	1	.	0.0647
F Test 2-sided	4.5221	7	7	0.0646

Welch's Test

Welch Anova testing Means Equal, allowing Std Devs Not Equal

F Ratio	DFNum	DFDen	Prob > F
0.4099	1	9.9516	0.5365

t Test
0.6403

Oneway Analysis of Studentized Resid avg ER By doping By CHF3 doping=1

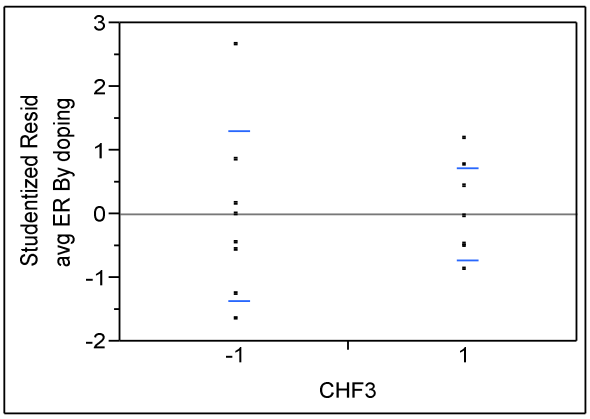

Tests that the Variances are Equal

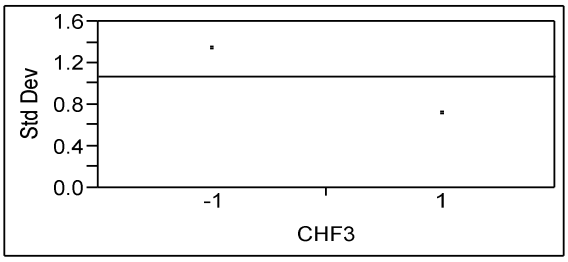

Level	Count	Std Dev	MeanAbsDif to Mean	MeanAbsDif to Median
-1	8	1.343540	0.9482659	0.9482659
1	8	0.722775	0.5939920	0.5857355

Test	F Ratio	DFNum	DFDen	p-Value
O'Brien[.5]	1.3790	1	14	0.2599
Brown-Forsythe	1.0258	1	14	0.3283
Levene	1.1199	1	14	0.3079
Bartlett	2.3650	1	.	0.1241
F Test 2-sided	3.4554	7	7	0.1241

Welch's Test

Welch Anova testing Means Equal, allowing Std Devs Not Equal

F Ratio	DFNum	DFDen	Prob > F
0.0047	1	10.739	0.9467

t Test
0.0684

Response avg ER doping=-1
Whole Model
Actual by Predicted Plot

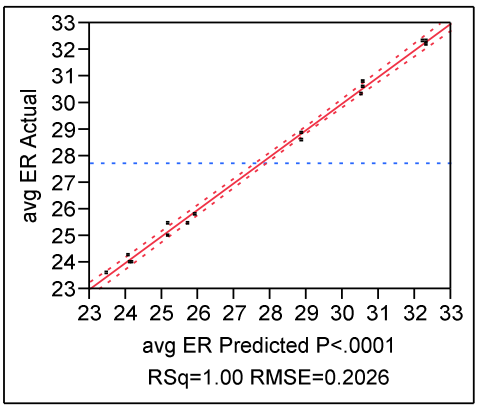

Summary of Fit

RSquare	0.997057
RSquare Adj	0.996321
Root Mean Square Error	0.202612
Mean of Response	27.73485
Observations (or Sum Wgts)	16

Analysis of Variance

Source	DF	Sum of Squares	Mean Square	F Ratio
Model	3	166.88685	55.6289	1355.097
Error	12	0.49262	0.0411	**Prob > F**
C. Total	15	167.37947		<.0001*

Parameter Estimates

Term	Estimate	Std Error	t Ratio	Prob>|t|
Intercept	27.360871	0.059179	462.34	<.0001*
source power	3.231408	0.053214	60.73	<.0001*
CHF3	-0.851979	0.050994	-16.71	<.0001*
undoped starting thickness(2379.68,2558.41)	0.9010404	0.073729	12.22	<.0001*

Effect Tests

Source	Nparm	DF	Sum of Squares	F Ratio	Prob > F
source power	1	1	151.37970	3687.543	<.0001*
CHF3	1	1	11.45921	279.1414	<.0001*
undoped starting thickness(2379.68,2558.41)	1	1	6.13110	149.3510	<.0001*

Press

Press	Press RMSE
0.8520830077	0.23077086

Residual by Predicted Plot

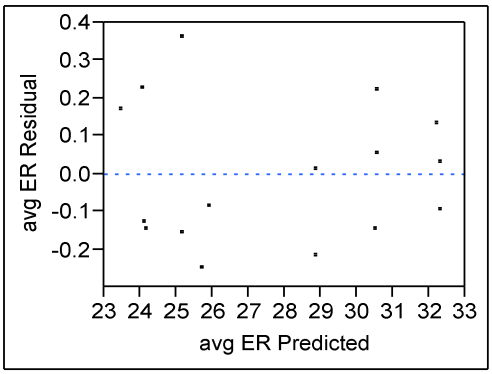

Are the residuals normally distributed?

Distributions doping=-1
Studentized Resid avg ER By doping +Co

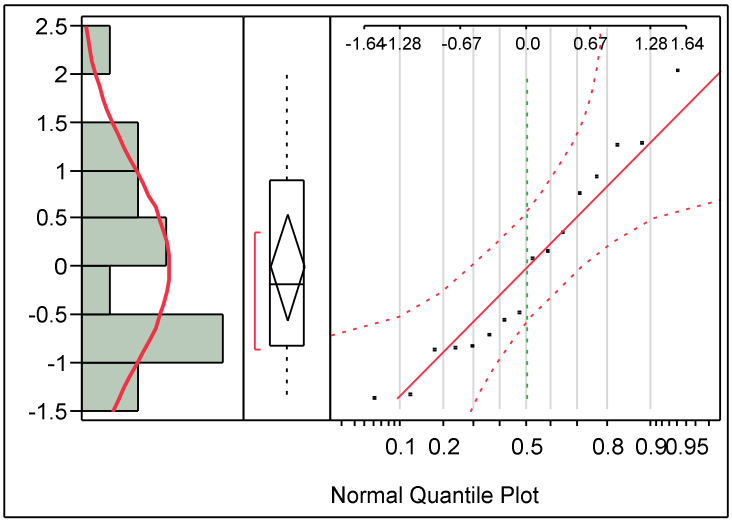

Normal(-0.0013,1.02456)

Quantiles

100.0%	maximum	2.039
99.5%		2.039
97.5%		2.039
90.0%		1.515
75.0%	quartile	0.898
50.0%	median	-0.190
25.0%	quartile	-0.830
10.0%		-1.334
2.5%		-1.364

0.5%		-1.364
0.0%	minimum	-1.364

Moments

Mean	-0.001267
Std Dev	1.0245611
Std Err Mean	0.2561403
Upper 95% Mean	0.5446828
Lower 95% Mean	-0.547217
N	16

Fitted Normal
Parameter Estimates

Type	Parameter	Estimate	Lower 95%	Upper 95%
Location	μ	-0.001267	-0.547217	0.5446828
Dispersion	σ	1.0245611	0.7568483	1.5857043

-2log(Likelihood) = 45.1824921895703

Goodness-of-Fit Test

Shapiro-Wilk W Test

W	Prob<W
0.939047	0.3375

Note: Ho = The data is from the Normal distribution. Small p-values reject Ho.

Do they have constant variance?

Fit Y by X Group
Oneway Analysis of Studentized Resid avg ER By doping +Co By source power doping=-1

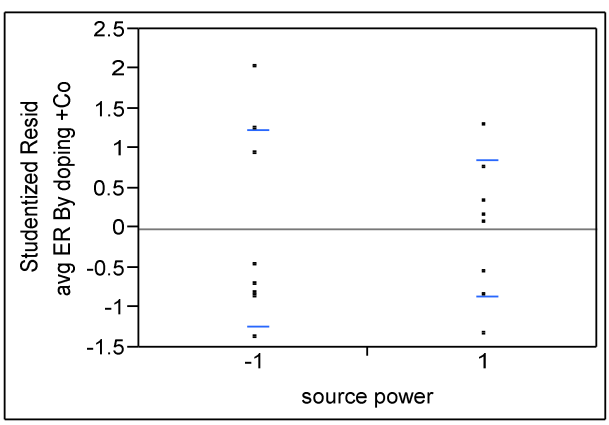

Tests that the Variances are Equal

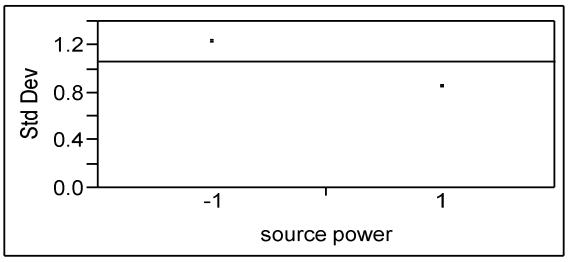

Level	Count	Std Dev	MeanAbsDif to Mean	MeanAbsDif to Median
-1	8	1.230670	1.056887	0.9394170
1	8	0.857215	0.671626	0.6485847

Test	F Ratio	DFNum	DFDen	p-Value
O'Brien[.5]	1.5243	1	14	0.2373
Brown-Forsythe	0.5757	1	14	0.4606
Levene	2.5968	1	14	0.1294
Bartlett	0.8364	1	.	0.3604
F Test 2-sided	2.0611	7	7	0.3608

Welch's Test

Welch Anova testing Means Equal, allowing Std Devs Not Equal

F Ratio	DFNum	DFDen	Prob > F
0.0003	1	12.498	0.9866

t Test
0.0171

Oneway Analysis of Studentized Resid avg ER By doping +Co By CF4 doping=-1

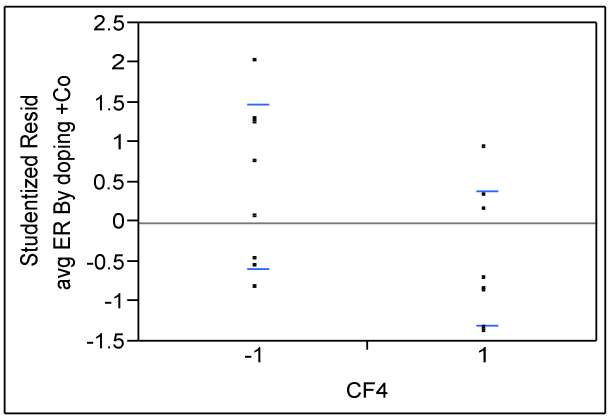

Tests that the Variances are Equal

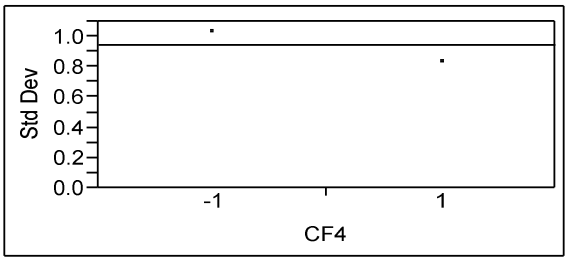

Level	Count	Std Dev	MeanAbsDif to Mean	MeanAbsDif to Median
-1	8	1.038590	0.8863666	0.8863666
1	8	0.840201	0.7052373	0.6426952

Test	F Ratio	DFNum	DFDen	p-Value
O'Brien[.5]	0.7150	1	14	0.4120
Brown-Forsythe	0.8966	1	14	0.3598
Levene	0.8245	1	14	0.3792
Bartlett	0.2914	1	.	0.5893
F Test 2-sided	1.5280	7	7	0.5897

Welch's Test

Welch Anova testing Means Equal, allowing Std Devs Not Equal

F Ratio	DFNum	DFDen	Prob > F
3.6463	1	13.415	0.0778

t Test
1.9095

Oneway Analysis of Studentized Resid avg ER By doping +Co By O2 doping=-1

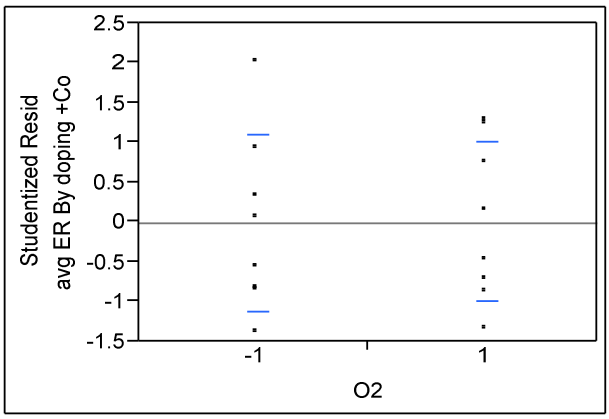

Tests that the Variances are Equal

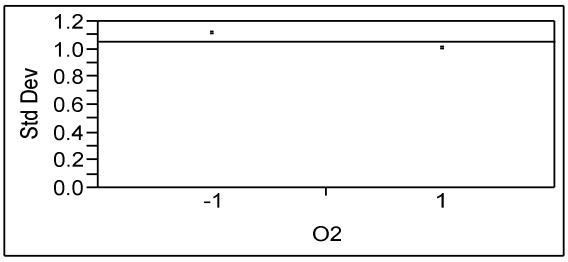

Level	Count	Std Dev	MeanAbsDif to Mean	MeanAbsDif to Median
-1	8	1.114928	0.8730296	0.8730296
1	8	1.002840	0.8532200	0.8532200

Test	F Ratio	DFNum	DFDen	p-Value
O'Brien[.5]	0.1231	1	14	0.7310
Brown-Forsythe	0.0050	1	14	0.9446
Levene	0.0058	1	14	0.9406
Bartlett	0.0732	1	.	0.7867
F Test 2-sided	1.2360	7	7	0.7869

Welch's Test

Welch Anova testing Means Equal, allowing Std Devs Not Equal

F Ratio	DFNum	DFDen	Prob > F
0.0041	1	13.846	0.9498

t Test
0.0641

Oneway Analysis of Studentized Resid avg ER By doping +Co By CHF3 doping=-1

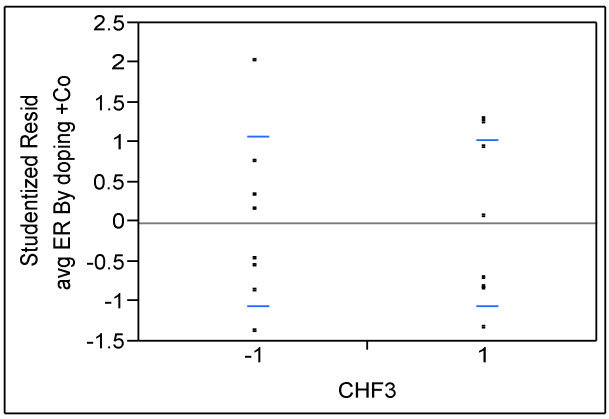

Tests that the Variances are Equal

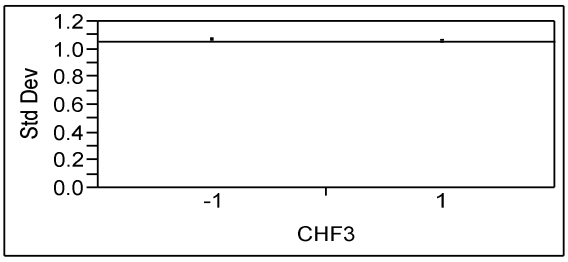

Level	Count	Std Dev	MeanAbsDif to Mean	MeanAbsDif to Median
-1	8	1.069363	0.8199000	0.8199000
1	8	1.051469	0.9063496	0.9063496

Test	F Ratio	DFNum	DFDen	p-Value
O'Brien[.5]	0.0032	1	14	0.9556
Brown-Forsythe	0.0892	1	14	0.7696
Levene	0.1103	1	14	0.7447
Bartlett	0.0019	1	.	0.9656
F Test 2-sided	1.0343	7	7	0.9656

Welch's Test

Welch Anova testing Means Equal, allowing Std Devs Not Equal

F Ratio	DFNum	DFDen	Prob > F
0.0018	1	13.996	0.9668

t Test
0.0424

Response I median doping=1
Whole Model
Actual by Predicted Plot

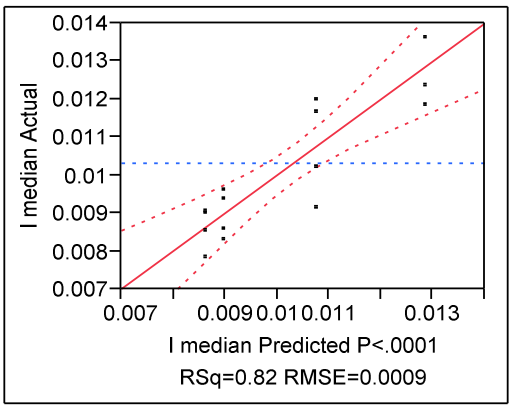

Summary of Fit

RSquare	0.822114
RSquare Adj	0.777642
Root Mean Square Error	0.000906
Mean of Response	0.010295
Observations (or Sum Wgts)	16

Analysis of Variance

Source	DF	Sum of Squares	Mean Square	F Ratio
Model	3	0.00004556	0.000015	18.4863
Error	12	0.00000986	8.215e-7	**Prob > F**
C. Total	15	0.00005542		<.0001*

Parameter Estimates

Term	Estimate	Std Error	t Ratio	Prob>|t|
Intercept	0.0102946	0.000227	45.43	<.0001*
source power	0.0004399	0.000227	1.94	0.0761
O2	0.0006187	0.000227	2.73	0.0183*
source power*O2	0.0015071	0.000227	6.65	<.0001*

Residual by Predicted Plot

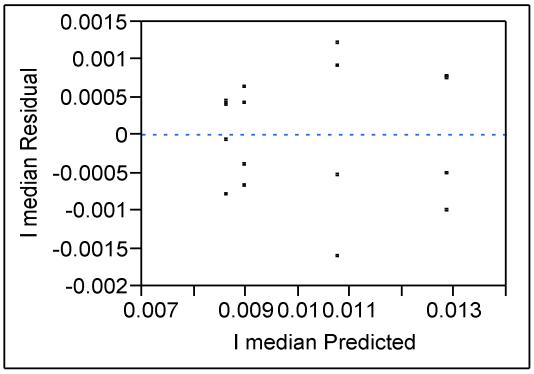

Press

Press	Press RMSE
0.000017526	0.0010466

Distributions doping=1
Studentized Resid I median By doping final

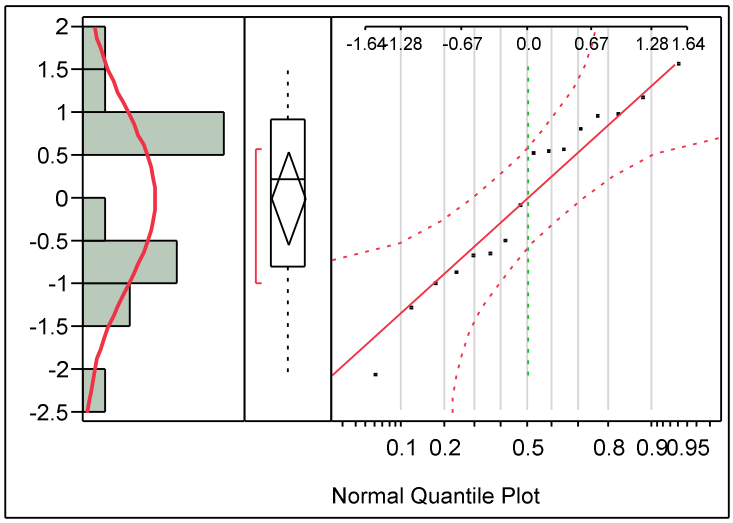

Normal(2.4e-15,1.0328)

Quantiles

100.0%	maximum	1.563
99.5%		1.563
97.5%		1.563
90.0%		1.285
75.0%	quartile	0.919
50.0%	median	0.218
25.0%	quartile	-0.813
10.0%		-1.510
2.5%		-2.056

0.5%		-2.056
0.0%	minimum	-2.056

Moments

Mean	2.387e-15
Std Dev	1.0327956
Std Err Mean	0.2581989
Upper 95% Mean	0.5503379
Lower 95% Mean	-0.550338
N	16

Fitted Normal
Parameter Estimates

Type	Parameter	Estimate	Lower 95%	Upper 95%
Location	μ	2.387e-15	-0.550338	0.5503379
Dispersion	σ	1.0327956	0.7629311	1.5984486

-2log(Likelihood) = 45.4386494007495

Goodness-of-Fit Test

Shapiro-Wilk W Test

W	Prob<W
0.950532	0.4982

Note: Ho = The data is from the Normal distribution. Small p-values reject Ho.

Fit Y by X Group
Oneway Analysis of Studentized Resid I median By doping final By source power doping=1

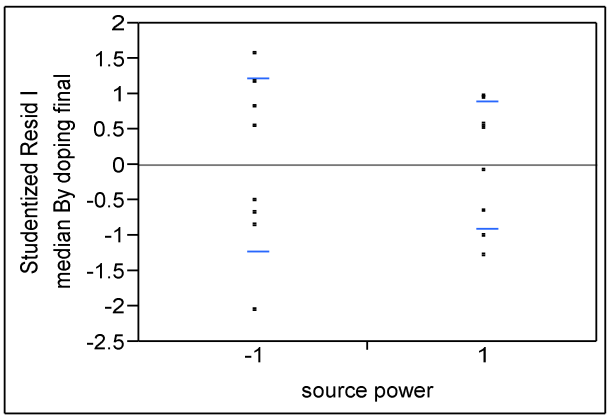

Tests that the Variances are Equal

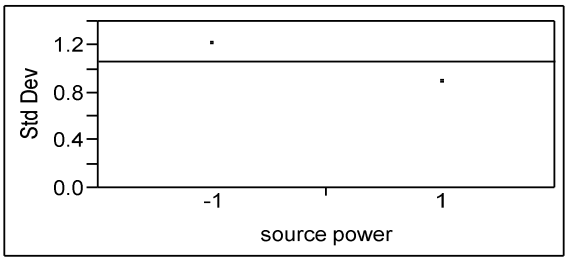

Level	Count	Std Dev	MeanAbsDif to Mean	MeanAbsDif to Median
-1	8	1.221796	1.024128	1.024128
1	8	0.890466	0.756365	0.756365

Test	F Ratio	DFNum	DFDen	p-Value
O'Brien[.5]	1.1657	1	14	0.2985
Brown-Forsythe	1.1750	1	14	0.2967
Levene	1.3240	1	14	0.2692
Bartlett	0.6431	1	.	0.4226
F Test 2-sided	1.8826	7	7	0.4229

Welch's Test

Welch Anova testing Means Equal, allowing Std Devs Not Equal

F Ratio	DFNum	DFDen	Prob > F
0.0000	1	12.8	1.0000

t Test
0.0000

Oneway Analysis of Studentized Resid I median By doping final By CF4 doping=1

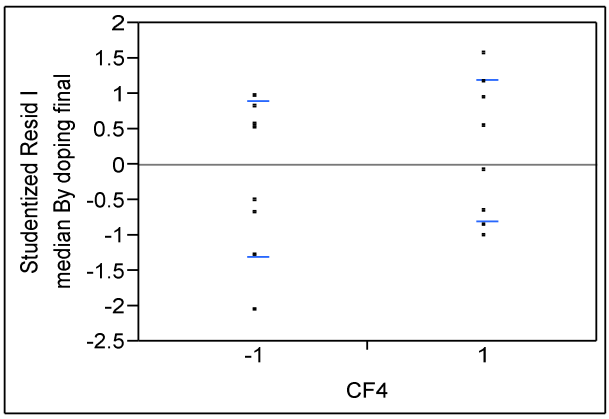

Tests that the Variances are Equal

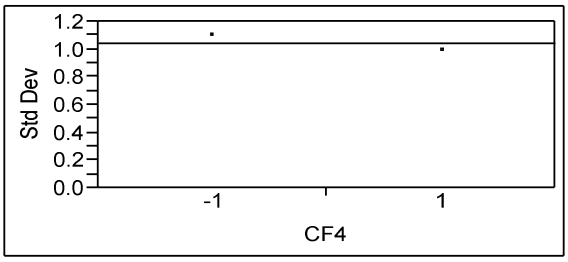

Level	Count	Std Dev	MeanAbsDif to Mean	MeanAbsDif to Median
-1	8	1.099197	0.9248919	0.9248919
1	8	0.991452	0.8556012	0.8556012

Test	F Ratio	DFNum	DFDen	p-Value
O'Brien[.5]	0.1753	1	14	0.6818
Brown-Forsythe	0.0897	1	14	0.7690
Levene	0.1019	1	14	0.7543
Bartlett	0.0694	1	.	0.7922
F Test 2-sided	1.2292	7	7	0.7924

Welch's Test

Welch Anova testing Means Equal, allowing Std Devs Not Equal

F Ratio	DFNum	DFDen	Prob > F
0.6038	1	13.854	0.4502

t Test
0.7771

Oneway Analysis of Studentized Resid I median By doping final By O2 doping=1

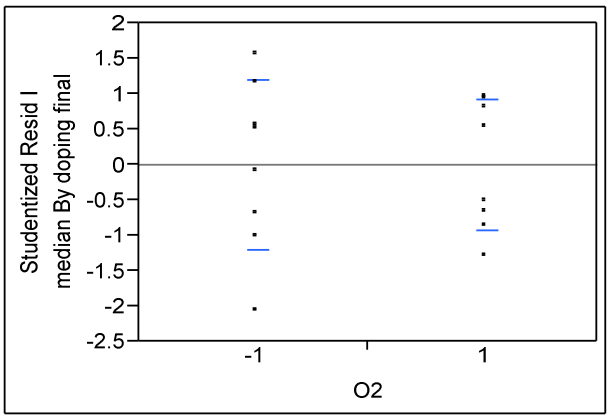

Tests that the Variances are Equal

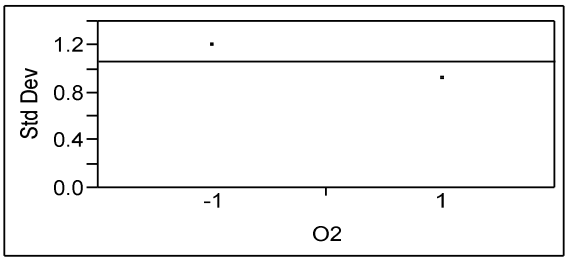

Level	Count	Std Dev	MeanAbsDif to Mean	MeanAbsDif to Median
-1	8	1.201375	0.9552122	0.9552122
1	8	0.917831	0.8252810	0.8252810

Test	F Ratio	DFNum	DFDen	p-Value
O'Brien[.5]	0.8378	1	14	0.3755
Brown-Forsythe	0.2600	1	14	0.6181
Levene	0.2907	1	14	0.5982
Bartlett	0.4679	1	.	0.4940
F Test 2-sided	1.7133	7	7	0.4943

Welch's Test

Welch Anova testing Means Equal, allowing Std Devs Not Equal

F Ratio	DFNum	DFDen	Prob > F
0.0000	1	13.095	1.0000

t Test
0.0000

Oneway Analysis of Studentized Resid I median By doping final By CHF3 doping=1

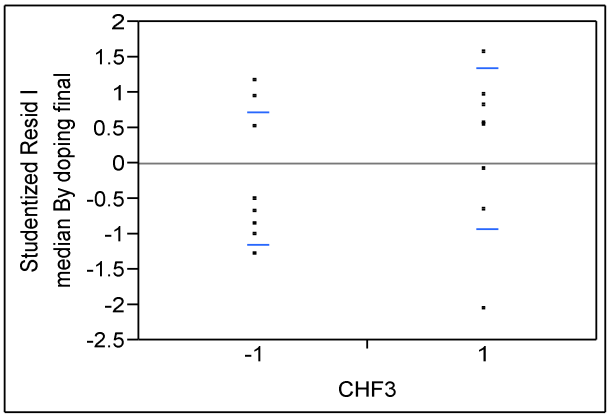

Tests that the Variances are Equal

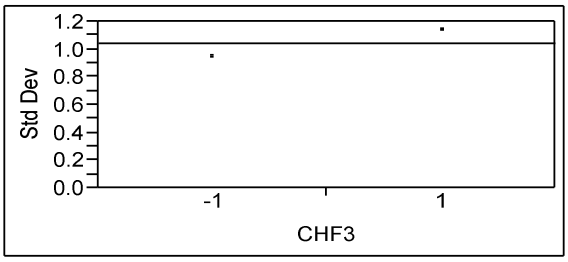

Level	Count	Std Dev	MeanAbsDif to Mean	MeanAbsDif to Median
-1	8	0.947043	0.8178371	0.7435259
1	8	1.134638	0.8573328	0.7716145

Test	F Ratio	DFNum	DFDen	p-Value
O'Brien[.5]	0.2381	1	14	0.6332
Brown-Forsythe	0.0054	1	14	0.9427
Levene	0.0215	1	14	0.8855
Bartlett	0.2122	1	.	0.6450
F Test 2-sided	1.4354	7	7	0.6454

Welch's Test

Welch Anova testing Means Equal, allowing Std Devs Not Equal

F Ratio	DFNum	DFDen	Prob > F
0.6501	1	13.566	0.4340

t Test
0.8063

Response I median doping=-1
Whole Model
Actual by Predicted Plot

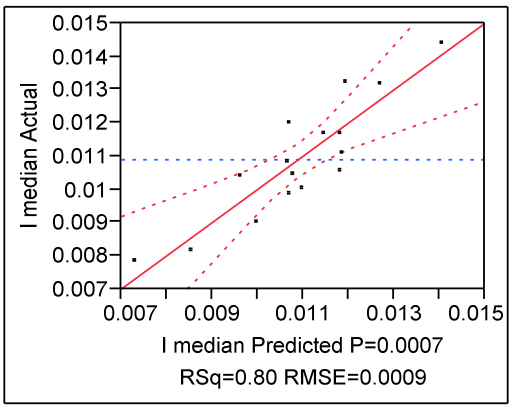

Summary of Fit

RSquare	0.801282
RSquare Adj	0.729021
Root Mean Square Error	0.000932
Mean of Response	0.010908
Observations (or Sum Wgts)	16

Analysis of Variance

Source	DF	Sum of Squares	Mean Square	F Ratio
Model	4	0.00003855	9.6369e-6	11.0887
Error	11	0.00000956	8.6908e-7	**Prob > F**
C. Total	15	0.00004811		0.0007*

Parameter Estimates

Term	Estimate	Std Error	t Ratio	Prob>|t|
Intercept	0.0106443	0.000243	43.88	<.0001*
O2	0.0006611	0.000234	2.83	0.0165*
CHF3	0.0005324	0.000239	2.23	0.0478*
source power*O2	0.0010256	0.000239	4.30	0.0013*
source power*undoped starting thickness	-0.001193	0.000304	-3.92	0.0024*

Effect Tests

Source	Nparm	DF	Sum of Squares	F Ratio	Prob > F
O2	1	1	0.00000694	7.9894	0.0165*
CHF3	1	1	0.00000431	4.9575	0.0478*
source power*O2	1	1	0.00001606	18.4816	0.0013*
source power*undoped starting thickness	1	1	0.00001338	15.3909	0.0024*

Residual by Predicted Plot

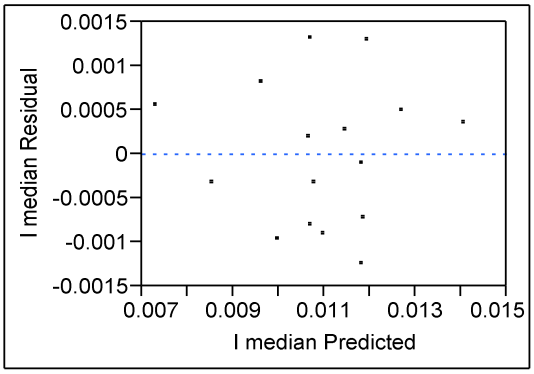

Press

Press	Press RMSE
0.000019044	0.00109099

Distributions doping=-1
Studentized Resid I median By doping final

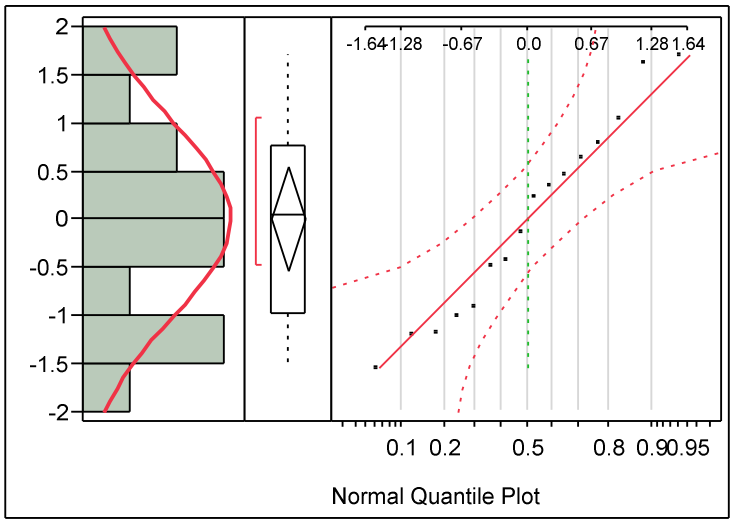

Normal(0.00706,1.01621)

Quantiles

100.0%	maximum	1.705
99.5%		1.705
97.5%		1.705
90.0%		1.661
75.0%	quartile	0.762
50.0%	median	0.056
25.0%	quartile	-0.977
10.0%		-1.290
2.5%		-1.532
0.5%		-1.532

0.0%	minimum	-1.532

Moments

Mean	0.0070637
Std Dev	1.016208
Std Err Mean	0.254052
Upper 95% Mean	0.5485628
Lower 95% Mean	-0.534435
N	16

Fitted Normal
Parameter Estimates

Type	Parameter	Estimate	Lower 95%	Upper 95%
Location	μ	0.0070637	-0.534435	0.5485628
Dispersion	σ	1.016208	0.7506778	1.5727763

-2log(Likelihood) = 44.9205321876189

Goodness-of-Fit Test

Shapiro-Wilk W Test

W	Prob<W
0.954369	0.5619

Note: Ho = The data is from the Normal distribution. Small p-values reject Ho.

Fit Y by X Group
Oneway Analysis of Studentized Resid I median By doping final By source power doping=-1

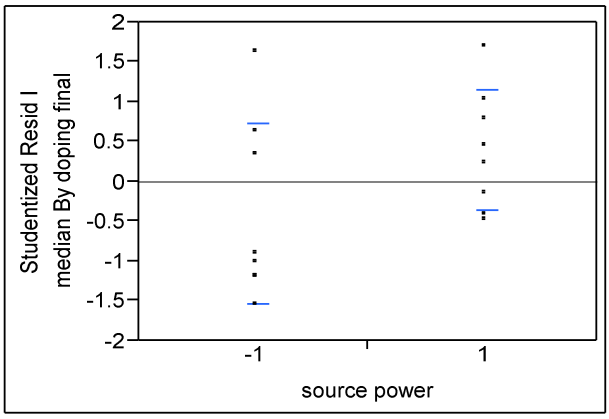

Tests that the Variances are Equal

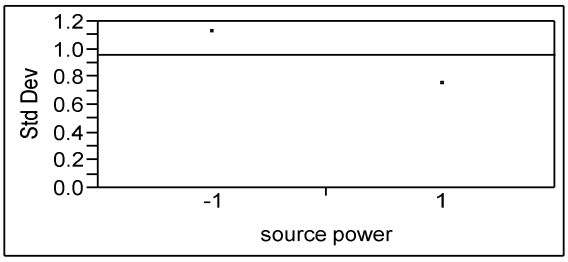

Level	Count	Std Dev	MeanAbsDif to Mean	MeanAbsDif to Median
-1	8	1.130542	0.9566906	0.8299130
1	8	0.755114	0.5971162	0.5971162

Test	F Ratio	DFNum	DFDen	p-Value
O'Brien[.5]	1.3661	1	14	0.2620
Brown-Forsythe	0.4276	1	14	0.5238
Levene	2.6197	1	14	0.1278
Bartlett	1.0365	1	.	0.3086
F Test 2-sided	2.2416	7	7	0.3089

Welch's Test

Welch Anova testing Means Equal, allowing Std Devs Not Equal

F Ratio	DFNum	DFDen	Prob > F
2.7613	1	12.209	0.1220

t Test
1.6617

Oneway Analysis of Studentized Resid I median By doping final By CF4 doping=-1

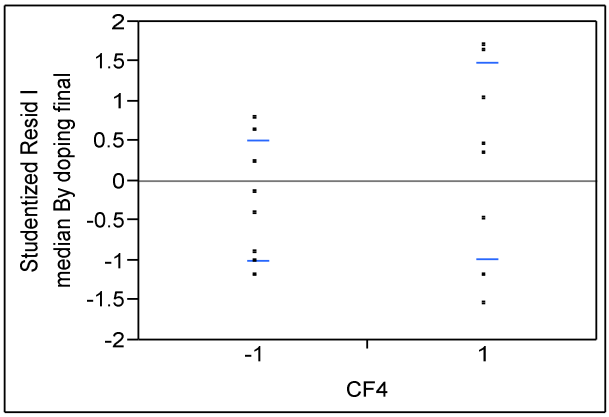

Tests that the Variances are Equal

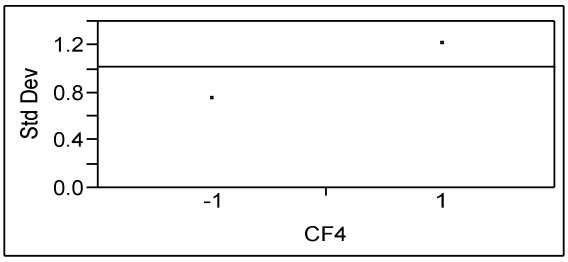

Level	Count	Std Dev	MeanAbsDif to Mean	MeanAbsDif to Median
-1	8	0.757945	0.6299096	0.6299096
1	8	1.224430	0.9865387	0.9602857

Test	F Ratio	DFNum	DFDen	p-Value
O'Brien[.5]	2.9442	1	14	0.1082
Brown-Forsythe	1.4647	1	14	0.2462
Levene	2.0031	1	14	0.1788
Bartlett	1.4486	1	.	0.2288
F Test 2-sided	2.6097	7	7	0.2289

Welch's Test

Welch Anova testing Means Equal, allowing Std Devs Not Equal

F Ratio	DFNum	DFDen	Prob > F
0.9396	1	11.678	0.3520

t Test
0.9693

Oneway Analysis of Studentized Resid I median By doping final By O2 doping=-1

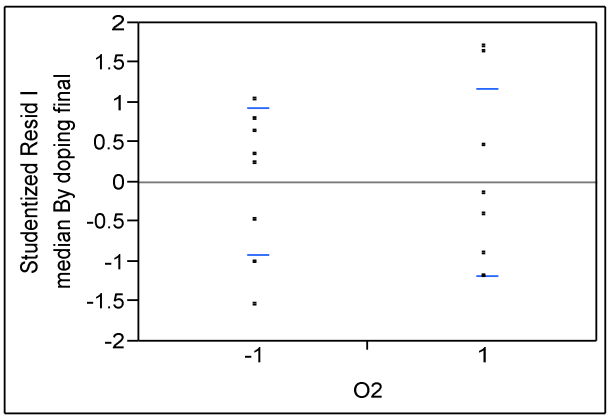

Tests that the Variances are Equal

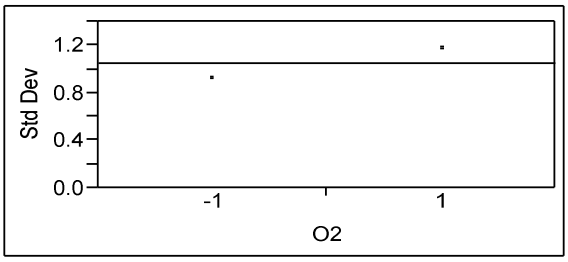

Level	Count	Std Dev	MeanAbsDif to Mean	MeanAbsDif to Median
-1	8	0.918693	0.7590299	0.7012517
1	8	1.169974	0.9512717	0.9179817

Test	F Ratio	DFNum	DFDen	p-Value
O'Brien[.5]	0.7812	1	14	0.3917
Brown-Forsythe	0.4329	1	14	0.5212
Levene	0.5683	1	14	0.4634
Bartlett	0.3783	1	.	0.5385
F Test 2-sided	1.6219	7	7	0.5389

Welch's Test

Welch Anova testing Means Equal, allowing Std Devs Not Equal

F Ratio	DFNum	DFDen	Prob > F
0.0003	1	13.254	0.9866

t Test
0.0171

Oneway Analysis of Studentized Resid I median By doping final By CHF3 doping=-1

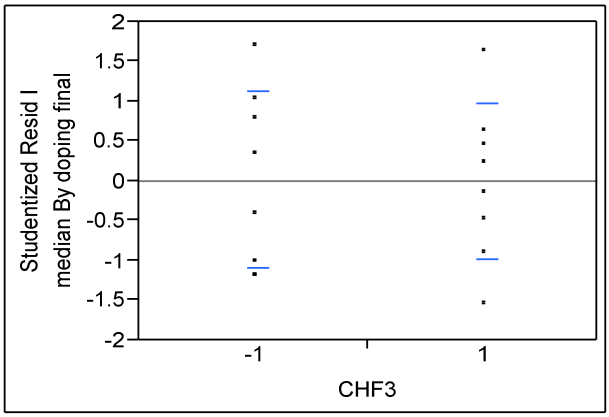

Tests that the Variances are Equal

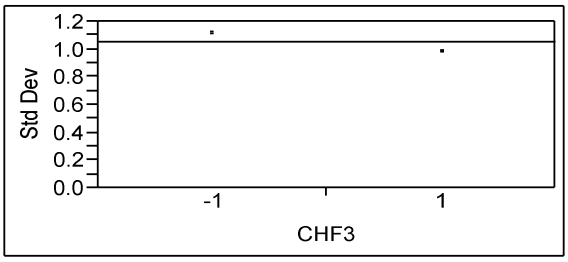

Level	Count	Std Dev	MeanAbsDif to Mean	MeanAbsDif to Median
-1	8	1.115122	0.9590353	0.9590353
1	8	0.984443	0.7535176	0.7535176

Test	F Ratio	DFNum	DFDen	p-Value
O'Brien[.5]	0.2071	1	14	0.6560
Brown-Forsythe	0.6514	1	14	0.4331
Levene	0.6592	1	14	0.4304
Bartlett	0.1012	1	.	0.7503
F Test 2-sided	1.2831	7	7	0.7506

Welch's Test

Welch Anova testing Means Equal, allowing Std Devs Not Equal

F Ratio	DFNum	DFDen	Prob > F
0.0016	1	13.788	0.9683

t Test
0.0404

P-DOPED WAFERS

Response P doped
Actual by Predicted Plot

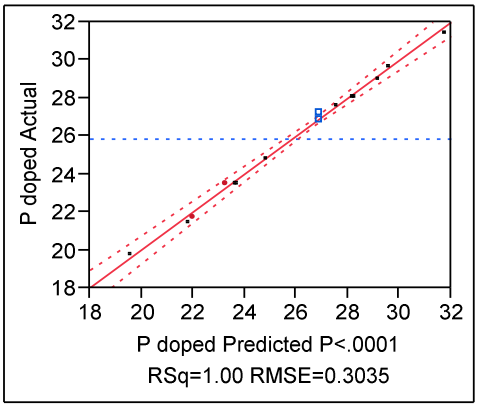

Summary of Fit

RSquare	0.995551
RSquare Adj	0.991659
Root Mean Square Error	0.30353
Mean of Response	25.83501
Observations (or Sum Wgts)	16

Analysis of Variance

Source	DF	Sum of Squares	Mean Square	F Ratio
Model	7	164.93642	23.5623	255.7491
Error	8	0.73705	0.0921	**Prob > F**
C. Total	15	165.67347		<.0001*

Parameter Estimates

Term	Estimate	Std Error	t Ratio	Prob>|t|
Intercept	26.802964	0.122334	219.10	<.0001*
CHF3(0,80)	-1.229428	0.112052	-10.97	<.0001*
source power(250,400)	4.0305455	0.104373	38.62	<.0001*
CHF3*He/O2	0.7135152	0.156677	4.55	0.0019*
source power*He/O2	1.4943899	0.154467	9.67	<.0001*
He/O2*He/O2	-1.610535	0.182245	-8.84	<.0001*
source power*source power*P starting thickness	1.316621	0.405092	3.25	0.0117*
He/O2*He/O2*P starting thickness	-2.462416	0.371787	-6.62	0.0002*

Effect Tests

Source	Nparm	DF	Sum of Squares	F Ratio	Prob > F
CHF3(0,80)	1	1	11.09103	120.3836	<.0001*
source power(250,400)	1	1	137.38989	1491.249	<.0001*
CHF3*He/O2	1	1	1.91074	20.7394	0.0019*
source power*He/O2	1	1	8.62307	93.5960	<.0001*
He/O2*He/O2	1	1	7.19503	78.0959	<.0001*
source power*source power*P starting thickness	1	1	0.97324	10.5637	0.0117*

Source	Nparm	DF	Sum of Squares	F Ratio	Prob > F
He/O2*He/O2*P starting thickness	1	1	4.04148	43.8668	0.0002*

Residual by Predicted Plot

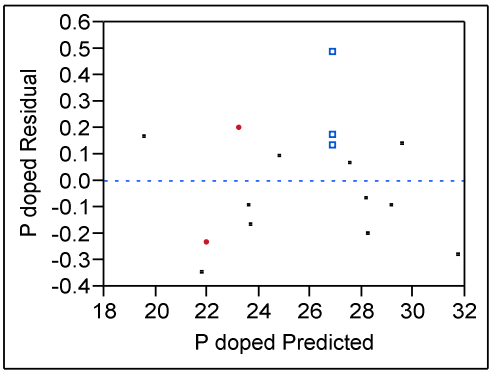

Press

Press	Press RMSE
3.3026754083	0.45433161

Distributions

Studentized Resid P doped

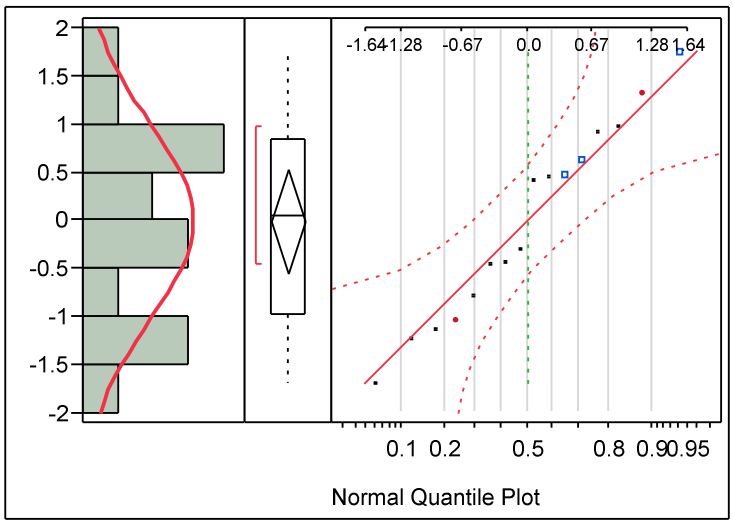

Normal(-0.0026,1.01705)

Quantiles

100.0%	maximum	1.770
99.5%		1.770
97.5%		1.770
90.0%		1.460
75.0%	quartile	0.845

50.0%	median	0.054
25.0%	quartile	-0.968
10.0%		-1.365
2.5%		-1.694
0.5%		-1.694
0.0%	minimum	-1.694

Moments

Mean	-0.00258
Std Dev	1.0170535
Std Err Mean	0.2542634
Upper 95% Mean	0.5393695
Lower 95% Mean	-0.54453
N	16

Fitted Normal
Parameter Estimates

Type	Parameter	Estimate	Lower 95%	Upper 95%
Location	μ	-0.00258	-0.54453	0.5393695
Dispersion	σ	1.0170535	0.7513024	1.5740848

-2log(Likelihood) = 44.9471441212897

Goodness-of-Fit Test

Shapiro-Wilk W Test

W	Prob<W
0.963926	0.7332

Note: Ho = The data is from the Normal distribution. Small p-values reject Ho.

Fit Y by X Group
Oneway Analysis of Studentized Resid P doped By CHF3

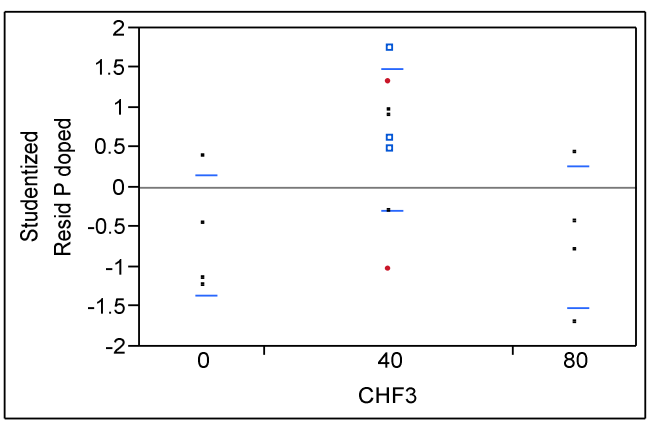

Tests that the Variances are Equal

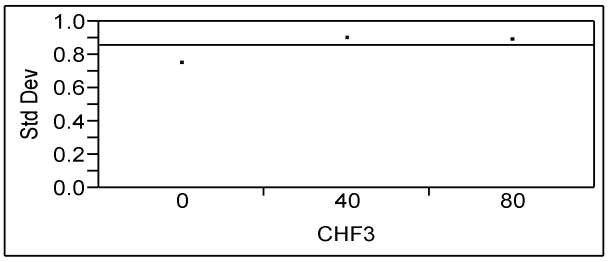

Level	Count	Std Dev	MeanAbsDif to Mean	MeanAbsDif to Median
0	4	0.7533531	0.5770181	0.5770181
40	8	0.8950393	0.6574493	0.6441406
80	4	0.8880131	0.6255375	0.6255375

Test	F Ratio	DFNum	DFDen	Prob > F
O'Brien[.5]	0.0731	2	13	0.9299
Brown-Forsythe	0.0203	2	13	0.9799
Levene	0.0339	2	13	0.9667
Bartlett	0.0559	2	.	0.9456

Warning: Small sample sizes. Use Caution.

Welch's Test

Welch Anova testing Means Equal, allowing Std Devs Not Equal

F Ratio	DFNum	DFDen	Prob > F
3.6295	2	6.742	0.0851

Oneway Analysis of Studentized Resid P doped By source power

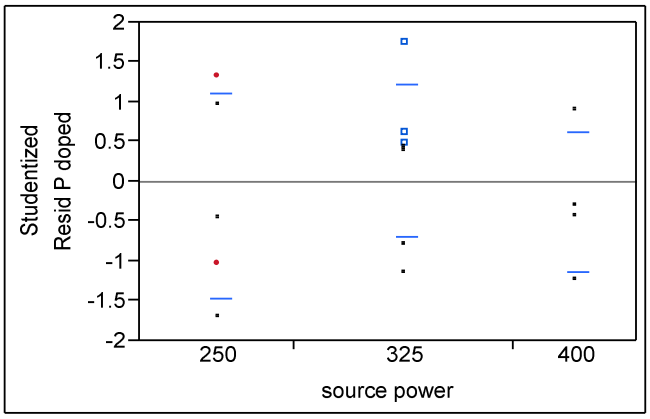

Tests that the Variances are Equal

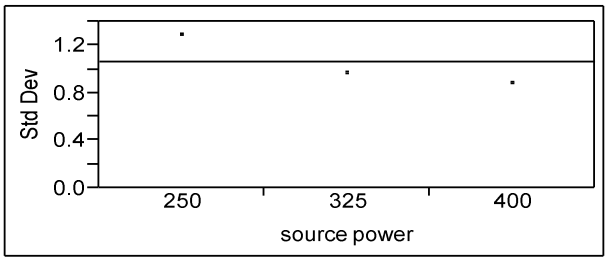

Level	Count	Std Dev	MeanAbsDif to Mean	MeanAbsDif to Median
250	5	1.293578	1.060434	1.120926
325	7	0.963732	0.699587	0.640154
400	4	0.880563	0.584898	0.566081

Test	F Ratio	DFNum	DFDen	Prob > F
O'Brien[.5]	0.6934	2	13	0.5174
Brown-Forsythe	1.1338	2	13	0.3517
Levene	0.9193	2	13	0.4232
Bartlett	0.2919	2	.	0.7469

Warning: Small sample sizes. Use Caution.

Welch's Test

Welch Anova testing Means Equal, allowing Std Devs Not Equal

F Ratio	DFNum	DFDen	Prob > F
0.4494	2	7.4301	0.6543

Oneway Analysis of Studentized Resid P doped By He/O2

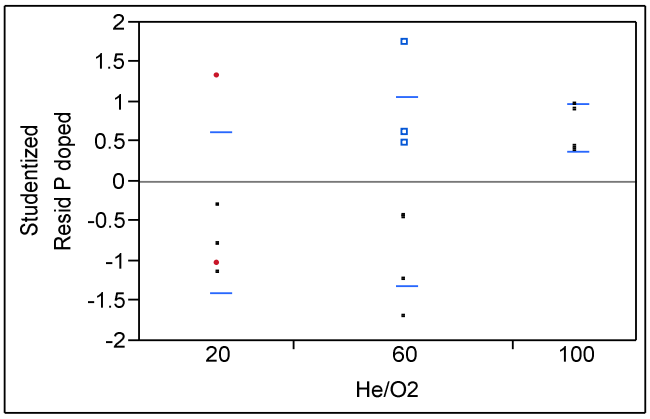

Tests that the Variances are Equal

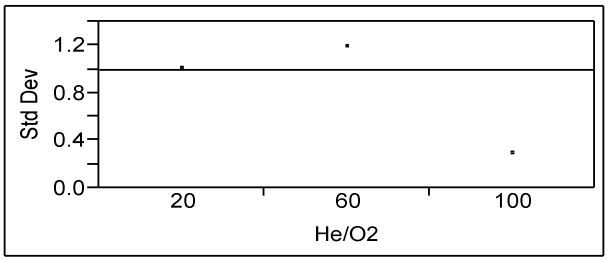

Level	Count	Std Dev	MeanAbsDif to Mean	MeanAbsDif to Median
20	5	1.008311	0.7176539	0.6851800
60	7	1.187471	0.9429319	0.9020162
100	4	0.298288	0.2566854	0.2566854

Test	F Ratio	DFNum	DFDen	Prob > F
O'Brien[.5]	0.9710	2	13	0.4045
Brown-Forsythe	1.1462	2	13	0.3480
Levene	2.0915	2	13	0.1631
Bartlett	2.2131	2	.	0.1094

Warning: Small sample sizes. Use Caution.

Welch's Test

Welch Anova testing Means Equal, allowing Std Devs Not Equal

F Ratio	DFNum	DFDen	Prob > F
3.3536	2	7.4937	0.0912

Bivariate Fit of Studentized Resid P doped By P starting thickness

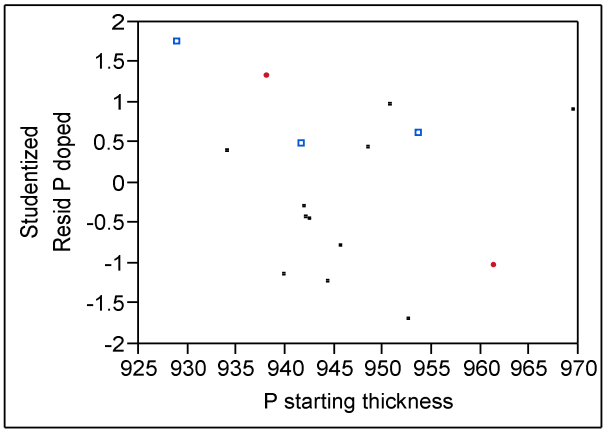

Response As doped
Whole Model
Actual by Predicted Plot

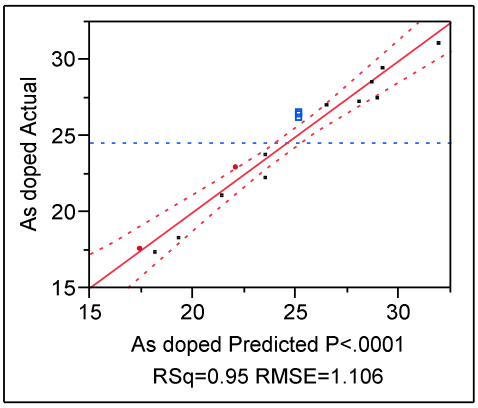

Summary of Fit

RSquare	0.947393
RSquare Adj	0.934241
Root Mean Square Error	1.105987
Mean of Response	24.60201
Observations (or Sum Wgts)	16

Analysis of Variance

Source	DF	Sum of Squares	Mean Square	F Ratio
Model	3	264.34208	88.1140	72.0353
Error	12	14.67848	1.2232	**Prob > F**
C. Total	15	279.02056		<.0001*

Parameter Estimates

Term	Estimate	Std Error	t Ratio	Prob>|t|
Intercept	25.039043	0.279213	89.68	<.0001*
CHF3(0,80)	-1.603478	0.39545	-4.05	0.0016*
source power(250,400)	5.2520179	0.378761	13.87	<.0001*
He/O2*He/O2*As starting thickness	-2.337496	0.561924	-4.16	0.0013*

Effect Tests

Source	Nparm	DF	Sum of Squares	F Ratio	Prob > F
CHF3(0,80)	1	1	20.11143	16.4416	0.0016*
source power(250,400)	1	1	235.19174	192.2748	<.0001*
He/O2*He/O2*As starting thickness	1	1	21.16638	17.3040	0.0013*

Residual by Predicted Plot

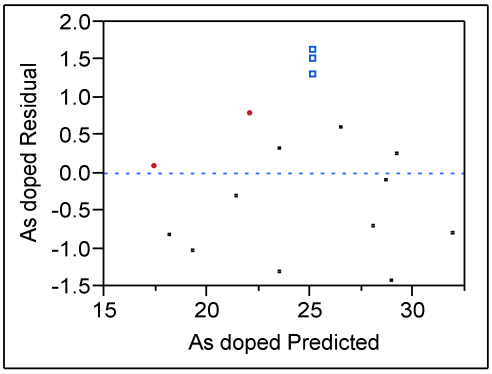

Press

Press	Press RMSE
24.262575533	1.2314264

Distributions
Studentized Resid As doped

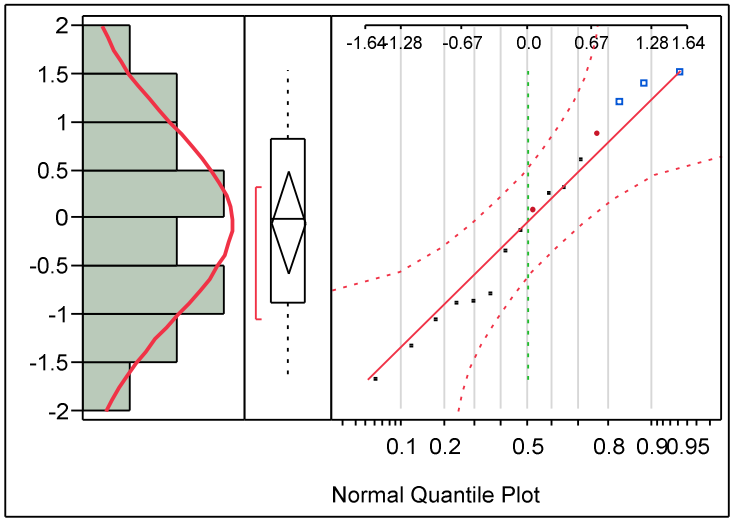

Normal(-0.0416,1.00511)

Quantiles

100.0%	maximum	1.533
99.5%		1.533
97.5%		1.533
90.0%		1.460
75.0%	quartile	0.817
50.0%	median	-0.011
25.0%	quartile	-0.877
10.0%		-1.432
2.5%		-1.676

0.5%		-1.676
0.0%	minimum	-1.676

Moments

Mean	-0.041614
Std Dev	1.0051093
Std Err Mean	0.2512773
Upper 95% Mean	0.4939709
Lower 95% Mean	-0.577199
N	16

Fitted Normal
Parameter Estimates

Type	Parameter	Estimate	Lower 95%	Upper 95%
Location	μ	-0.041614	-0.577199	0.4939709
Dispersion	σ	1.0051093	0.7424791	1.5555988

-2log(Likelihood) = 44.5691128693473

Goodness-of-Fit Test

Shapiro-Wilk W Test

W	Prob<W
0.958493	0.6345

Note: Ho = The data is from the Normal distribution. Small p-values reject Ho.

Fit Y by X Group
Oneway Analysis of Studentized Resid As doped By CHF3

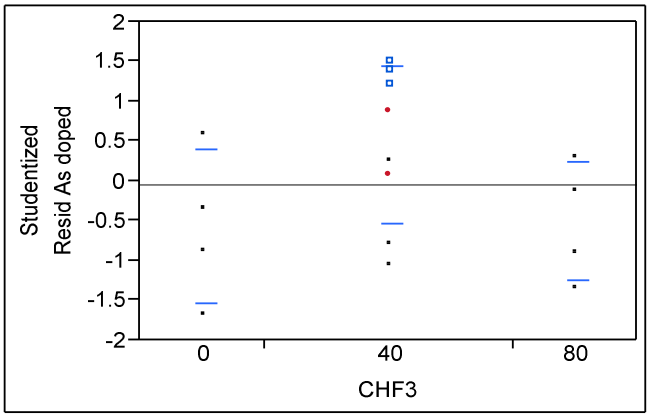

Tests that the Variances are Equal

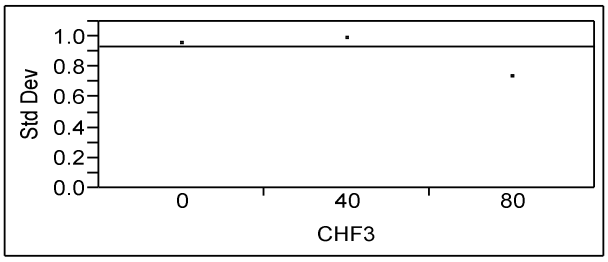

Level	Count	Std Dev	MeanAbsDif to Mean	MeanAbsDif to Median
0	4	0.9578421	0.7010379	0.7010379
40	8	0.9889743	0.8191364	0.8191364
80	4	0.7411726	0.6027021	0.6027021

Test	F Ratio	DFNum	DFDen	Prob > F
O'Brien[.5]	0.2890	2	13	0.7537
Brown-Forsythe	0.3304	2	13	0.7245
Levene	0.3468	2	13	0.7133
Bartlett	0.1460	2	.	0.8642

Warning: Small sample sizes. Use Caution.

Welch's Test

Welch Anova testing Means Equal, allowing Std Devs Not Equal

F Ratio	DFNum	DFDen	Prob > F
2.1048	2	6.9173	0.1932

Oneway Analysis of Studentized Resid As doped By source power

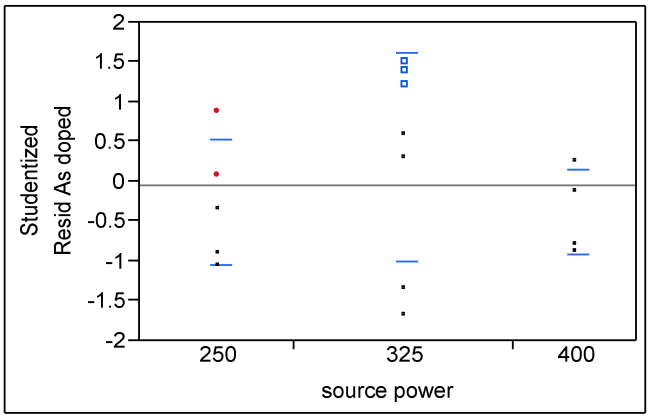

Tests that the Variances are Equal

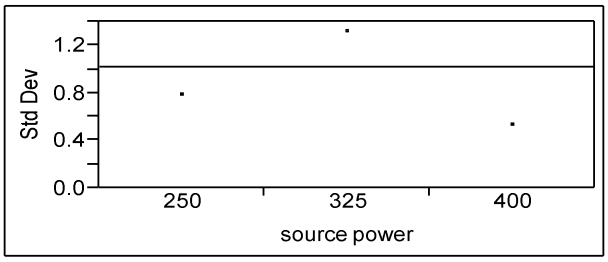

Level	Count	Std Dev	MeanAbsDif to Mean	MeanAbsDif to Median
250	5	0.782910	0.599190	0.669906
325	7	1.311667	1.031621	1.024918
400	4	0.538093	0.445493	0.445493

Test	F Ratio	DFNum	DFDen	Prob > F
O'Brien[.5]	1.8921	2	13	0.1900
Brown-Forsythe	1.4170	2	13	0.2775
Levene	1.8750	2	13	0.1925
Bartlett	1.3705	2	.	0.2540

Warning: Small sample sizes. Use Caution.

Welch's Test

Welch Anova testing Means Equal, allowing Std Devs Not Equal

F Ratio	DFNum	DFDen	Prob > F
0.6741	2	8.6012	0.5346

Oneway Analysis of Studentized Resid As doped By He/O2

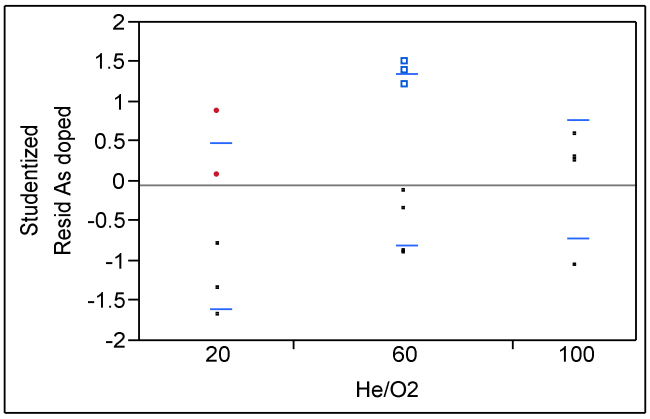

Tests that the Variances are Equal

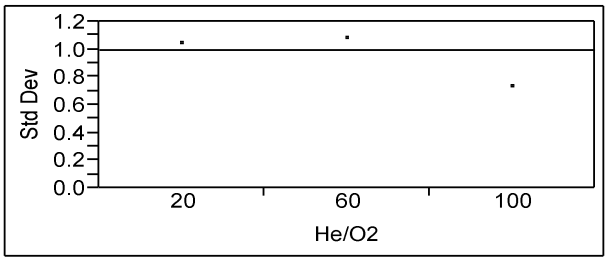

Level	Count	Std Dev	MeanAbsDif to Mean	MeanAbsDif to Median
20	5	1.049468	0.8409171	0.9072324
60	7	1.080637	0.9555578	0.9303739
100	4	0.736930	0.5406200	0.4287571

Test	F Ratio	DFNum	DFDen	Prob > F
O'Brien[.5]	0.6638	2	13	0.5315
Brown-Forsythe	1.1496	2	13	0.3470
Levene	1.4797	2	13	0.2636
Bartlett	0.2500	2	.	0.7788

Warning: Small sample sizes. Use Caution.

Welch's Test

Welch Anova testing Means Equal, allowing Std Devs Not Equal

F Ratio	DFNum	DFDen	Prob > F
0.8780	2	8.119	0.4517

Bivariate Fit of Studentized Resid As doped By As starting thickness

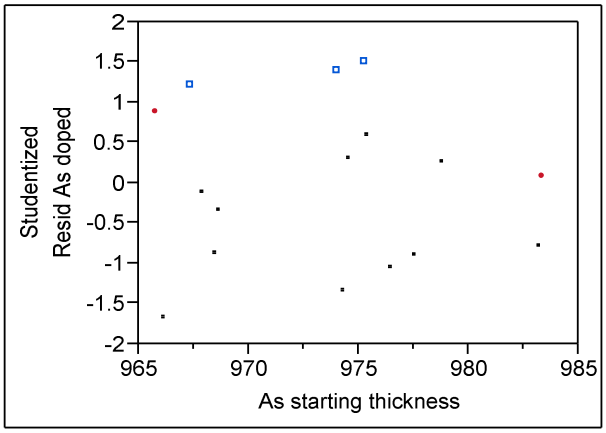

Response Sb doped
Actual by Predicted Plot

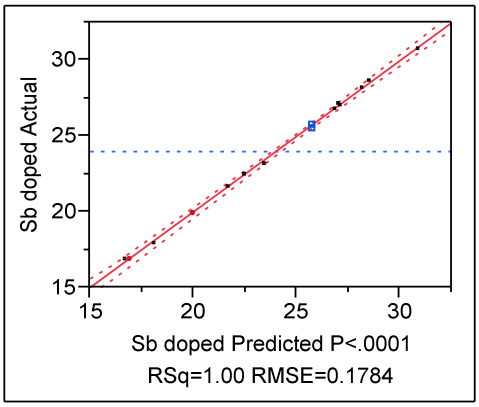

Summary of Fit

RSquare	0.999214
RSquare Adj	0.998315
Root Mean Square Error	0.178431
Mean of Response	24.02695
Observations (or Sum Wgts)	16

Analysis of Variance

Source	DF	Sum of Squares	Mean Square	F Ratio
Model	8	283.16773	35.3960	1111.766
Error	7	0.22286	0.0318	**Prob > F**
C. Total	15	283.39059		<.0001*

Parameter Estimates

Term	Estimate	Std Error	t Ratio	Prob>|t|
Intercept	25.67004	0.092204	278.40	<.0001*
CHF3(0,80)	-1.90997	0.063133	-30.25	<.0001*
source power(250,400)	5.1737588	0.061488	84.14	<.0001*
He/O2(20,100)	0.3676749	0.060963	6.03	0.0005*
CHF3*CHF3	0.4375898	0.090548	4.83	0.0019*
CHF3*source power	0.553125	0.089215	6.20	0.0004*
source power*source power	-1.78035	0.09208	-19.33	<.0001*
CHF3*He/O2	0.4658284	0.089838	5.19	0.0013*
He/O2*He/O2*Sb starting thickness	-1.635677	0.092781	-17.63	<.0001*

Effect Tests

Source	Nparm	DF	Sum of Squares	F Ratio	Prob > F
CHF3(0,80)	1	1	29.13933	915.2487	<.0001*
source power(250,400)	1	1	225.41052	7080.008	<.0001*
He/O2(20,100)	1	1	1.15806	36.3741	0.0005*
CHF3*CHF3	1	1	0.74357	23.3551	0.0019*
CHF3*source power	1	1	1.22379	38.4385	0.0004*
source power*source power	1	1	11.90192	373.8321	<.0001*
CHF3*He/O2	1	1	0.85599	26.8863	0.0013*
He/O2*He/O2*Sb starting thickness	1	1	9.89498	310.7954	<.0001*

Residual by Predicted Plot

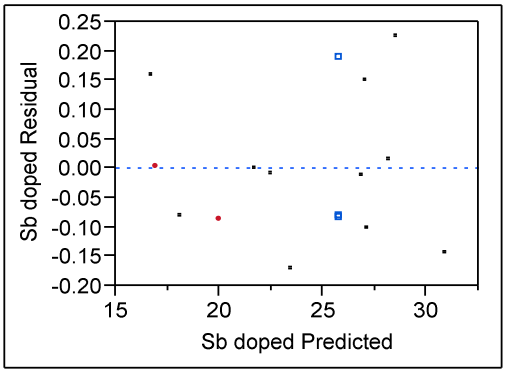

Press

Press	Press RMSE
1.4947218222	0.30564704

Distributions
Studentized Resid Sb doped

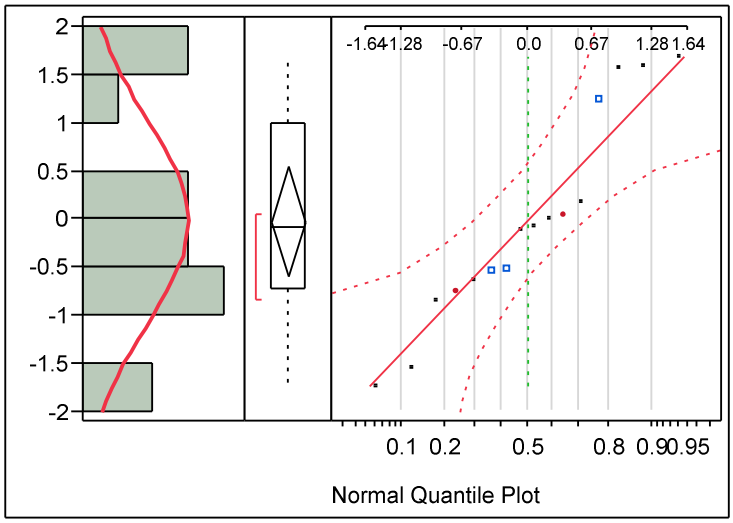

Normal(-0.0202,1.06669)

Quantiles

100.0%	maximum	1.699
99.5%		1.699
97.5%		1.699
90.0%		1.622
75.0%	quartile	0.991
50.0%	median	-0.095
25.0%	quartile	-0.717
10.0%		-1.596
2.5%		-1.736
0.5%		-1.736

0.0%	minimum	-1.736

Moments

Mean	-0.020177
Std Dev	1.0666931
Std Err Mean	0.2666733
Upper 95% Mean	0.5482238
Lower 95% Mean	-0.588578
N	16

Fitted Normal
Parameter Estimates

Type	Parameter	Estimate	Lower 95%	Upper 95%
Location	μ	-0.020177	-0.588578	0.5482238
Dispersion	σ	1.0666931	0.7879714	1.6509116

-2log(Likelihood) = 46.472059367718

Goodness-of-Fit Test

Shapiro-Wilk W Test

W	Prob<W
0.922442	0.1846

Note: Ho = The data is from the Normal distribution. Small p-values reject Ho.

Fit Y by X Group
Oneway Analysis of Studentized Resid Sb doped By CHF3

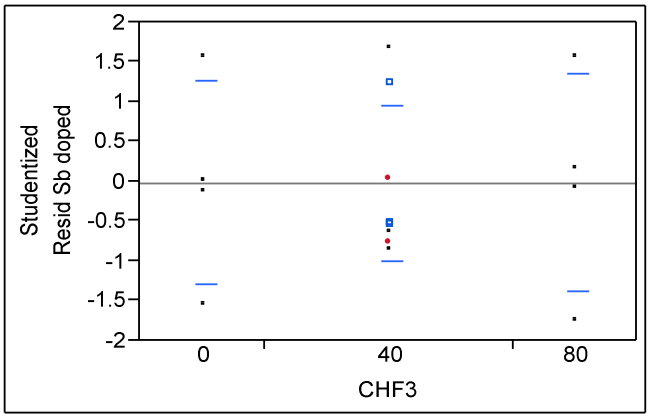

Tests that the Variances are Equal

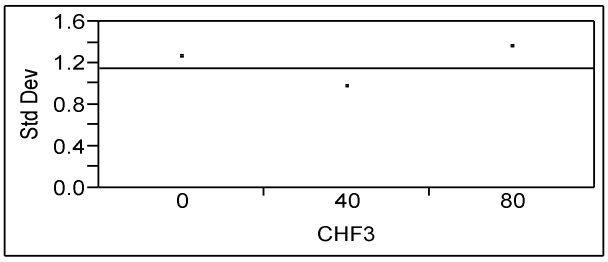

Level	Count	Std Dev	MeanAbsDif to Mean	MeanAbsDif to Median
0	4	1.271676	0.8100775	0.8100775
40	8	0.973575	0.7712332	0.6536279
80	4	1.363806	0.8973422	0.8973422

Test	F Ratio	DFNum	DFDen	Prob > F
O'Brien[.5]	0.3523	2	13	0.7096
Brown-Forsythe	0.1180	2	13	0.8896
Levene	0.0427	2	13	0.9583
Bartlett	0.2715	2	.	0.7622

Warning: Small sample sizes. Use Caution.

Welch's Test

Welch Anova testing Means Equal, allowing Std Devs Not Equal

F Ratio	DFNum	DFDen	Prob > F
0.0004	2	5.6788	0.9996

Oneway Analysis of Studentized Resid Sb doped By source power

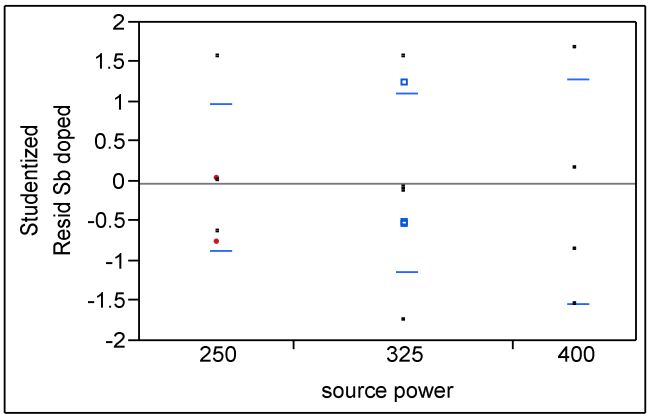

Tests that the Variances are Equal

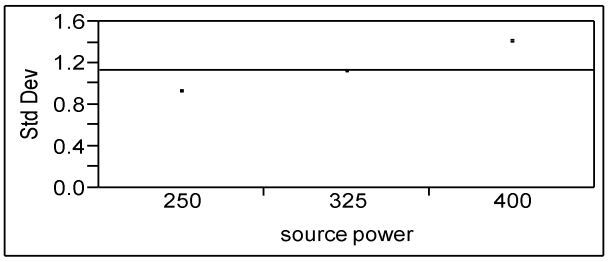

Level	Count	Std Dev	MeanAbsDif to Mean	MeanAbsDif to Median
250	5	0.929873	0.613441	0.606035
325	7	1.126183	0.818221	0.792448
400	4	1.405787	1.066310	1.066310

Test	F Ratio	DFNum	DFDen	Prob > F
O'Brien[.5]	0.4310	2	13	0.6588
Brown-Forsythe	0.4748	2	13	0.6324
Levene	0.5038	2	13	0.6156
Bartlett	0.2685	2	.	0.7645

Warning: Small sample sizes. Use Caution.

Welch's Test

Welch Anova testing Means Equal, allowing Std Devs Not Equal

F Ratio	DFNum	DFDen	Prob > F
0.0225	2	7.0721	0.9778

Oneway Analysis of Studentized Resid Sb doped By He/O2

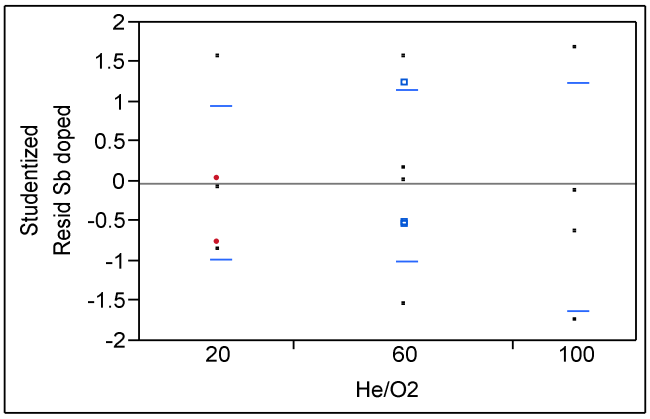

Tests that the Variances are Equal

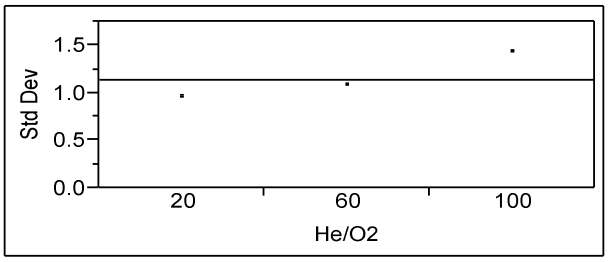

Level	Count	Std Dev	MeanAbsDif to Mean	MeanAbsDif to Median
20	5	0.969167	0.6548548	0.6653454
60	7	1.078550	0.8059988	0.8227550
100	4	1.431907	0.9857112	0.9857112

Test	F Ratio	DFNum	DFDen	Prob > F
O'Brien[.5]	0.4270	2	13	0.6613
Brown-Forsythe	0.2377	2	13	0.7918
Levene	0.2507	2	13	0.7820
Bartlett	0.2655	2	.	0.7669

Warning: Small sample sizes. Use Caution.

Welch's Test

Welch Anova testing Means Equal, allowing Std Devs Not Equal

F Ratio	DFNum	DFDen	Prob > F
0.0476	2	6.9729	0.9538

Bivariate Fit of Studentized Resid Sb doped By Sb starting thickness

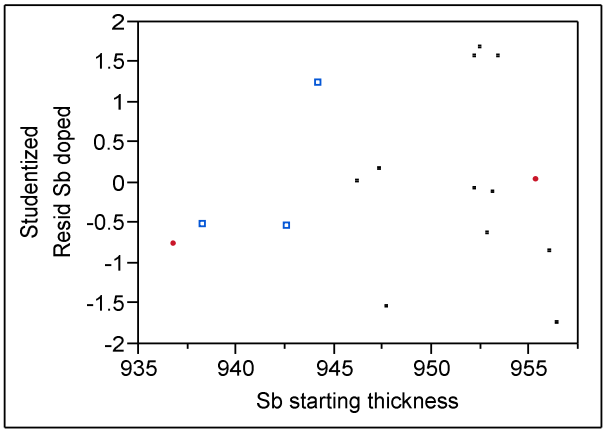

Response B doped
Actual by Predicted Plot

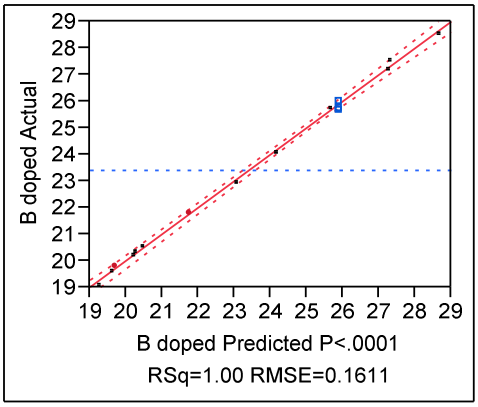

Summary of Fit

RSquare	0.998691
RSquare Adj	0.997545
Root Mean Square Error	0.161101
Mean of Response	23.43159
Observations (or Sum Wgts)	16

Analysis of Variance

Source	DF	Sum of Squares	Mean Square	F Ratio
Model	7	158.37545	22.6251	871.7557
Error	8	0.20763	0.0260	**Prob > F**
C. Total	15	158.58308		<.0001*

Parameter Estimates

Term	Estimate	Std Error	t Ratio	Prob>|t|
Intercept	25.857381	0.068866	375.47	<.0001*
source power(250,400)	3.1655813	0.06181	51.22	<.0001*
CHF3*source power	-1.825481	0.1158	-15.76	<.0001*
CHF3*B starting thickness	-0.850294	0.130445	-6.52	0.0002*
CHF3*source power*B starting thickness	-1.871816	0.24753	-7.56	<.0001*
source power*source power*B starting thickness	3.0337432	0.149792	20.25	<.0001*
CHF3*He/O2*B starting thickness	0.8376722	0.128938	6.50	0.0002*
He/O2*He/O2*B starting thickness	-6.471119	0.178254	-36.30	<.0001*

Effect Tests

Source	Nparm	DF	Sum of Squares	F Ratio	Prob > F
source power(250,400)	1	1	68.075343	2622.979	<.0001*
CHF3*source power	1	1	6.449614	248.5070	<.0001*
CHF3*B starting thickness	1	1	1.102758	42.4898	0.0002*
CHF3*source power*B starting thickness	1	1	1.484112	57.1836	<.0001*
source power*source power*B starting thickness	1	1	10.645788	410.1878	<.0001*
CHF3*He/O2*B starting thickness	1	1	1.095424	42.2073	0.0002*
He/O2*He/O2*B starting thickness	1	1	34.203942	1317.896	<.0001*

Residual by Predicted Plot

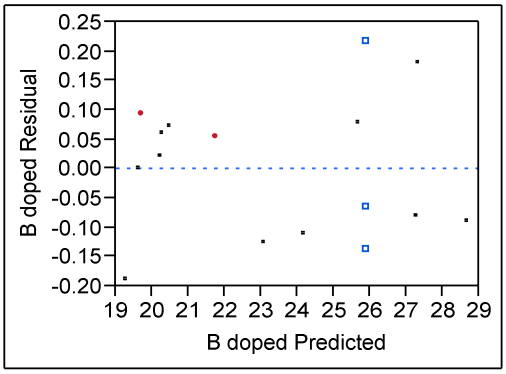

Press

Press	Press RMSE
2.6198739282	0.40465062

Distributions
Studentized Resid B doped

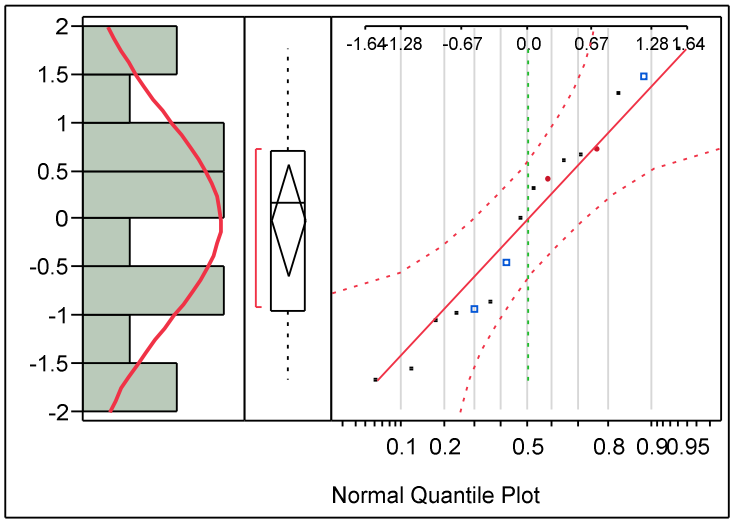

Normal(-0.0111,1.08769)

Quantiles

100.0%	maximum	1.767
99.5%		1.767
97.5%		1.767
90.0%		1.582
75.0%	quartile	0.708
50.0%	median	0.160
25.0%	quartile	-0.959
10.0%		-1.592

2.5%		-1.672
0.5%		-1.672
0.0%	minimum	-1.672

Moments

Mean	-0.011071
Std Dev	1.0876867
Std Err Mean	0.2719217
Upper 95% Mean	0.5685162
Lower 95% Mean	-0.590658
N	16

Fitted Normal
Parameter Estimates

Type	Parameter	Estimate	Lower 95%	Upper 95%
Location	μ	-0.011071	-0.590658	0.5685162
Dispersion	σ	1.0876867	0.8034794	1.6834032

-2log(Likelihood) = 47.0957337775915

Goodness-of-Fit Test

Shapiro-Wilk W Test

W	Prob<W
0.949179	0.4768

Note: Ho = The data is from the Normal distribution. Small p-values reject Ho.

Fit Y by X Group
Oneway Analysis of Studentized Resid B doped By CHF3

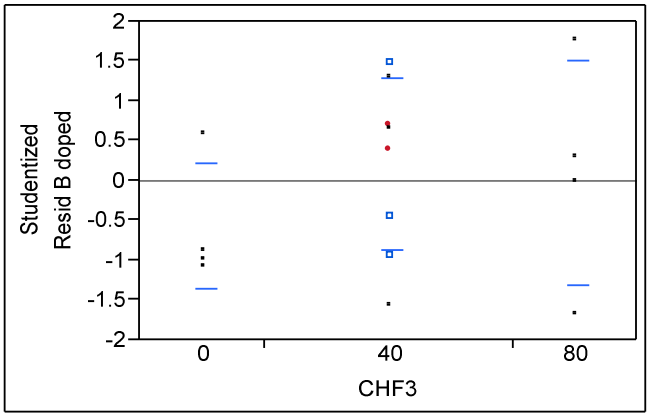

Tests that the Variances are Equal

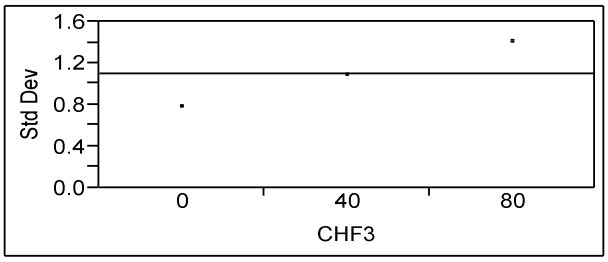

Level	Count	Std Dev	MeanAbsDif to Mean	MeanAbsDif to Median
0	4	0.789541	0.5890330	0.4439684
40	8	1.080930	0.8849628	0.8364121
80	4	1.411090	0.9352082	0.9352082

Test	F Ratio	DFNum	DFDen	Prob > F
O'Brien[.5]	0.6380	2	13	0.5441
Brown-Forsythe	0.4949	2	13	0.6207
Levene	0.4004	2	13	0.6781
Bartlett	0.4366	2	.	0.6463

Warning: Small sample sizes. Use Caution.

Welch's Test

Welch Anova testing Means Equal, allowing Std Devs Not Equal

F Ratio	DFNum	DFDen	Prob > F
0.9903	2	6.5526	0.4209

Oneway Analysis of Studentized Resid B doped By source power

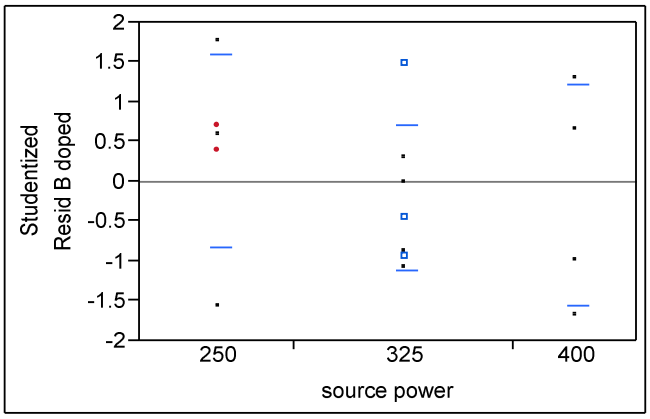

Tests that the Variances are Equal

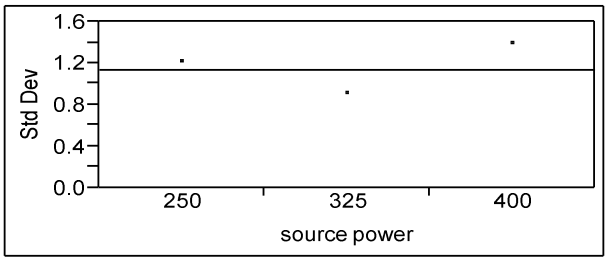

Level	Count	Std Dev	MeanAbsDif to Mean	MeanAbsDif to Median
250	5	1.209247	0.778655	0.751554
325	7	0.908414	0.697914	0.728416
400	4	1.388204	1.154893	1.154893

Test	F Ratio	DFNum	DFDen	Prob > F
O'Brien[.5]	0.5287	2	13	0.6015
Brown-Forsythe	0.6190	2	13	0.5536
Levene	0.7529	2	13	0.4905
Bartlett	0.3723	2	.	0.6891

Warning: Small sample sizes. Use Caution.

Welch's Test

Welch Anova testing Means Equal, allowing Std Devs Not Equal

F Ratio	DFNum	DFDen	Prob > F
0.4053	2	6.5026	0.6825

Oneway Analysis of Studentized Resid B doped By He/O2

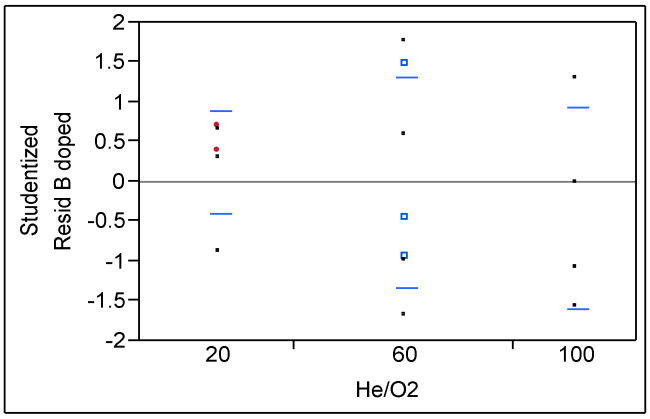

Tests that the Variances are Equal

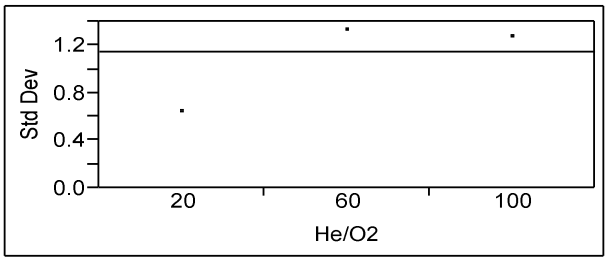

Level	Count	Std Dev	MeanAbsDif to Mean	MeanAbsDif to Median
20	5	0.645690	0.445222	0.408123
60	7	1.323477	1.120957	1.131309
100	4	1.269248	0.983707	0.983707

Test	F Ratio	DFNum	DFDen	Prob > F
O'Brien[.5]	1.3481	2	13	0.2938
Brown-Forsythe	2.0472	2	13	0.1687
Levene	2.7032	2	13	0.1043
Bartlett	0.9895	2	.	0.3718

Warning: Small sample sizes. Use Caution.

Welch's Test

Welch Anova testing Means Equal, allowing Std Devs Not Equal

F Ratio	DFNum	DFDen	Prob > F
0.3502	2	6.9652	0.7163

Bivariate Fit of Studentized Resid B doped By B starting thickness

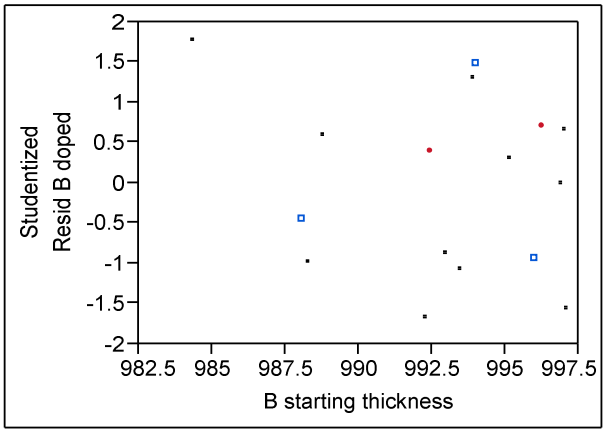

Response undoped
Actual by Predicted Plot

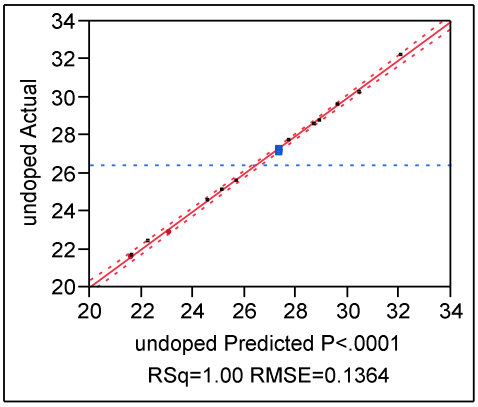

Summary of Fit

RSquare	0.99891
RSquare Adj	0.998183
Root Mean Square Error	0.136393
Mean of Response	26.43331
Observations (or Sum Wgts)	16

Analysis of Variance

Source	DF	Sum of Squares	Mean Square	F Ratio
Model	6	153.43582	25.5726	1374.653
Error	9	0.16743	0.0186	**Prob > F**
C. Total	15	153.60325		<.0001*

Parameter Estimates

Term	Estimate	Std Error	t Ratio	Prob>|t|
Intercept	27.266061	0.070382	387.40	<.0001*
CHF3(0,80)	-1.378007	0.04834	-28.51	<.0001*
source power(250,400)	3.6758843	0.049828	73.77	<.0001*
He/O2(20,100)	0.4580102	0.046655	9.82	<.0001*
source power*source power	-0.505072	0.072403	-6.98	<.0001*
source power*source power*undoped starting thickness	-0.549137	0.108536	-5.06	0.0007*
He/O2*He/O2*undoped starting thickness	-0.723457	0.124441	-5.81	0.0003*

Effect Tests

Source	Nparm	DF	Sum of Squares	F Ratio	Prob > F
CHF3(0,80)	1	1	15.11695	812.6091	<.0001*
source power(250,400)	1	1	101.24353	5442.330	<.0001*
He/O2(20,100)	1	1	1.79283	96.3731	<.0001*
source power*source power	1	1	0.90526	48.6623	<.0001*
source power*source power*undoped starting thickness	1	1	0.47621	25.5986	0.0007*
He/O2*He/O2*undoped starting thickness	1	1	0.62876	33.7988	0.0003*

Residual by Predicted Plot

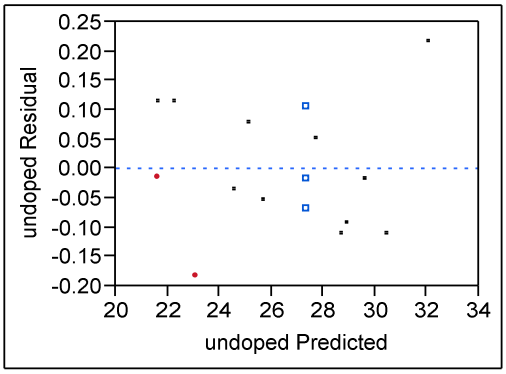

Press

Press	Press RMSE
0.5392247273	0.18357981

Distributions
Studentized Resid undoped

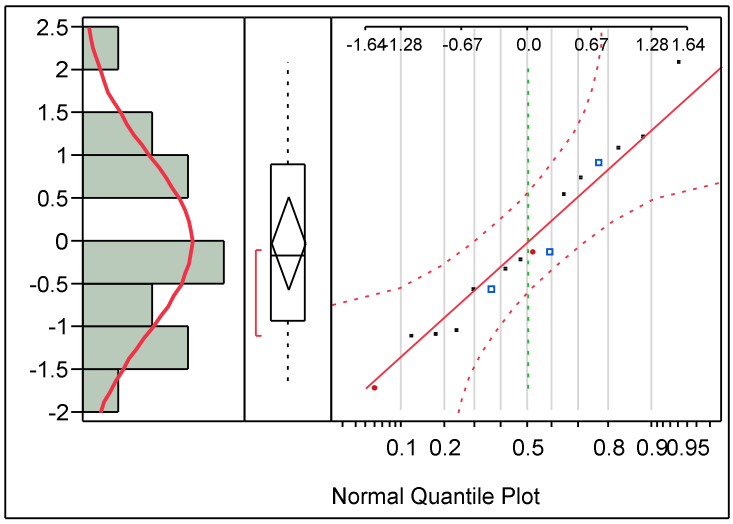

Normal(-0.0176,1.03129)

Quantiles

100.0%	maximum	2.088
99.5%		2.088
97.5%		2.088
90.0%		1.474
75.0%	quartile	0.885
50.0%	median	-0.168
25.0%	quartile	-0.927
10.0%		-1.284
2.5%		-1.717
0.5%		-1.717

0.0%	minimum	-1.717

Moments

Mean	-0.017597
Std Dev	1.0312925
Std Err Mean	0.2578231
Upper 95% Mean	0.5319398
Lower 95% Mean	-0.567134
N	16

Fitted Normal
Parameter Estimates

Type	Parameter	Estimate	Lower 95%	Upper 95%
Location	μ	-0.017597	-0.567134	0.5319398
Dispersion	σ	1.0312925	0.7618208	1.5961223

-2log(Likelihood) = 45.3920436872466

Goodness-of-Fit Test

Shapiro-Wilk W Test

W	Prob<W
0.967663	0.7995

Note: Ho = The data is from the Normal distribution. Small p-values reject Ho.

Fit Y by X Group
Oneway Analysis of Studentized Resid undoped By CHF3

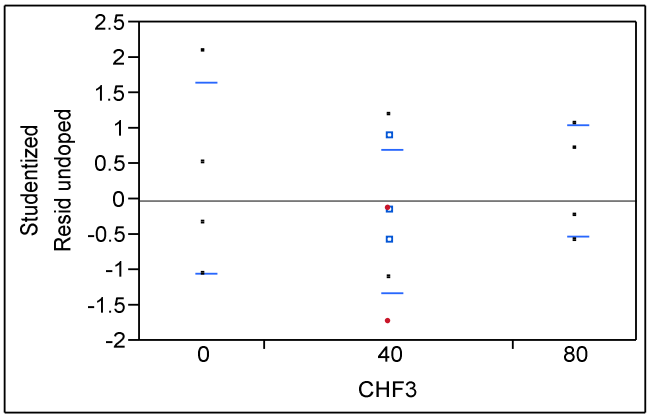

Tests that the Variances are Equal

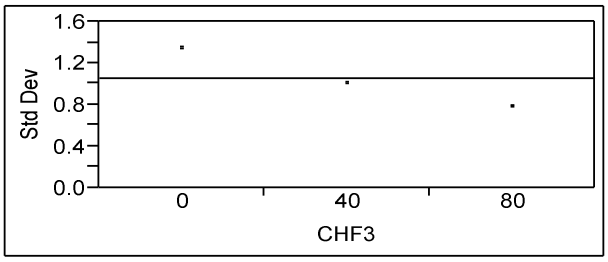

Level	Count	Std Dev	MeanAbsDif to Mean	MeanAbsDif to Median
0	4	1.349612	1.000542	1.000542
40	8	1.014457	0.795798	0.795798
80	4	0.779982	0.651775	0.651775

Test	F Ratio	DFNum	DFDen	Prob > F
O'Brien[.5]	0.7505	2	13	0.4915
Brown-Forsythe	0.4110	2	13	0.6713
Levene	0.4311	2	13	0.6587
Bartlett	0.4031	2	.	0.6682

Warning: Small sample sizes. Use Caution.

Welch's Test

Welch Anova testing Means Equal, allowing Std Devs Not Equal

F Ratio	DFNum	DFDen	Prob > F
0.6522	2	6.474	0.5520

Oneway Analysis of Studentized Resid undoped By source power

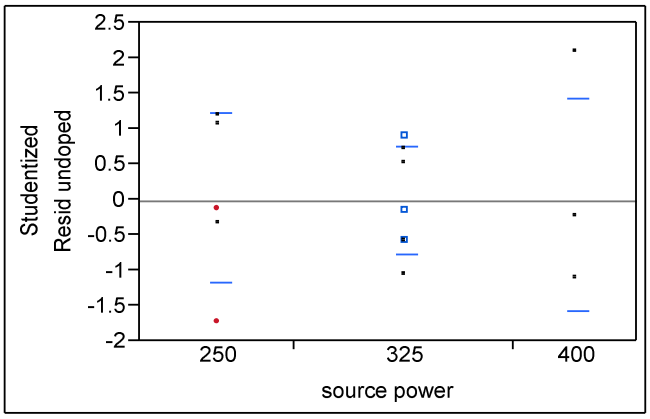

Tests that the Variances are Equal

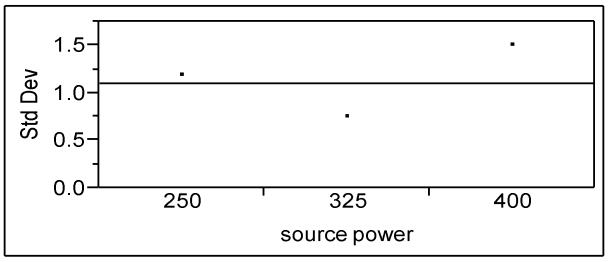

Level	Count	Std Dev	MeanAbsDif to Mean	MeanAbsDif to Median
250	5	1.195024	0.898822	0.911854
325	7	0.757296	0.640108	0.688124
400	4	1.502977	1.083311	1.015973

Test	F Ratio	DFNum	DFDen	Prob > F
O'Brien[.5]	0.9820	2	13	0.4007
Brown-Forsythe	0.3335	2	13	0.7224
Levene	0.8000	2	13	0.4703
Bartlett	0.9479	2	.	0.3876

Warning: Small sample sizes. Use Caution.

Welch's Test

Welch Anova testing Means Equal, allowing Std Devs Not Equal

F Ratio	DFNum	DFDen	Prob > F
0.0055	2	6.0027	0.9945

Oneway Analysis of Studentized Resid undoped By He/O2

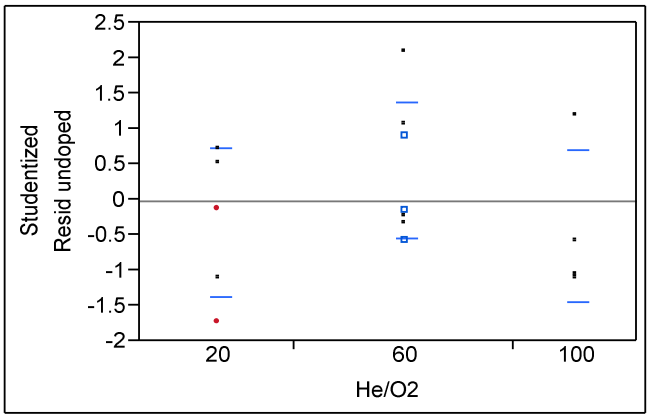

Tests that the Variances are Equal

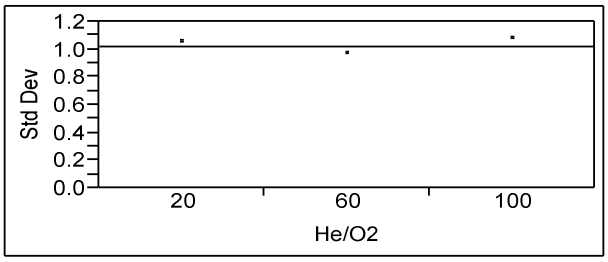

Level	Count	Std Dev	MeanAbsDif to Mean	MeanAbsDif to Median
20	5	1.051833	0.8569880	0.9466839
60	7	0.974286	0.8196068	0.7582219
100	4	1.084084	0.7937516	0.6945213

Test	F Ratio	DFNum	DFDen	Prob > F
O'Brien[.5]	0.0429	2	13	0.9581
Brown-Forsythe	0.1625	2	13	0.8517
Levene	0.0218	2	13	0.9785
Bartlett	0.0247	2	.	0.9756

Warning: Small sample sizes. Use Caution.

Welch's Test

Welch Anova testing Means Equal, allowing Std Devs Not Equal

F Ratio	DFNum	DFDen	Prob > F
1.0221	2	7.2011	0.4067

Bivariate Fit of Studentized Resid undoped By undoped starting thickness

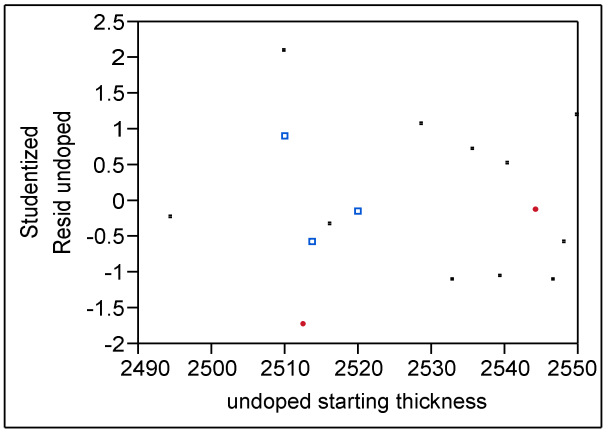

P-DOPED WAFERS

Response P doped I median
Actual by Predicted Plot

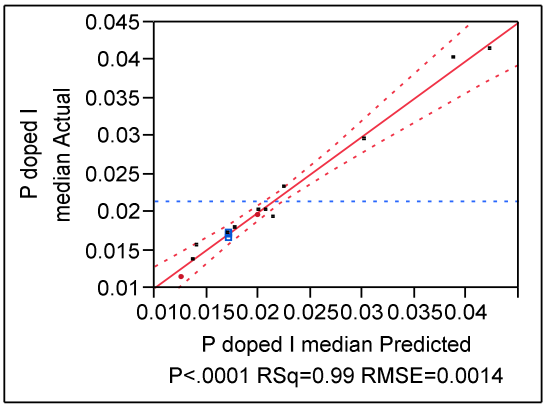

Summary of Fit

RSquare	0.987791
RSquare Adj	0.973837
Root Mean Square Error	0.001394
Mean of Response	0.021332
Observations (or Sum Wgts)	16

Analysis of Variance

Source	DF	Sum of Squares	Mean Square	F Ratio
Model	8	0.00110005	0.000138	70.7923
Error	7	0.00001360	1.942e-6	**Prob > F**
C. Total	15	0.00111365		<.0001*

Parameter Estimates

Term	Estimate	Std Error	t Ratio	Prob>|t|
Intercept	0.0169995	0.000672	25.30	<.0001*
source power(250,400)	-0.011516	0.000609	-18.90	<.0001*
He/O2(20,100)	0.0100713	0.000647	15.57	<.0001*
CHF3*CHF3	0.0069014	0.000788	8.76	<.0001*
source power*source power	-0.002366	0.00084	-2.82	0.0259*
CHF3*He/O2	-0.011982	0.000871	-13.76	<.0001*
source power*P starting thickness	-0.032686	0.001975	-16.55	<.0001*
He/O2*P starting thickness	0.0327944	0.002056	15.95	<.0001*
He/O2*He/O2*P starting thickness	0.006591	0.001079	6.11	0.0005*

Effect Tests

Source	Nparm	DF	Sum of Squares	F Ratio	Prob > F
source power(250,400)	1	1	0.00069369	357.1313	<.0001*
He/O2(20,100)	1	1	0.00047087	242.4181	<.0001*
CHF3*CHF3	1	1	0.00014918	76.8008	<.0001*
source power*source power	1	1	0.00001542	7.9406	0.0259*

Source	Nparm	DF	Sum of Squares	F Ratio	Prob > F
CHF3*He/O2	1	1	0.00036778	189.3445	<.0001*
source power*P starting thickness	1	1	0.00053190	273.8384	<.0001*
He/O2*P starting thickness	1	1	0.00049405	254.3525	<.0001*
He/O2*He/O2*P starting thickness	1	1	0.00007244	37.2922	0.0005*

Residual by Predicted Plot

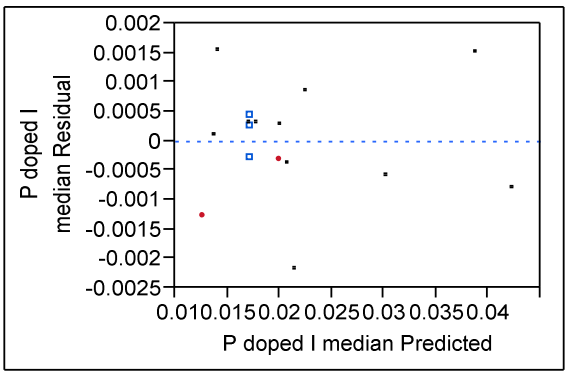

Press

Press	Press RMSE
0.0001082517	0.0026011

Distributions
Studentized Resid P doped I median

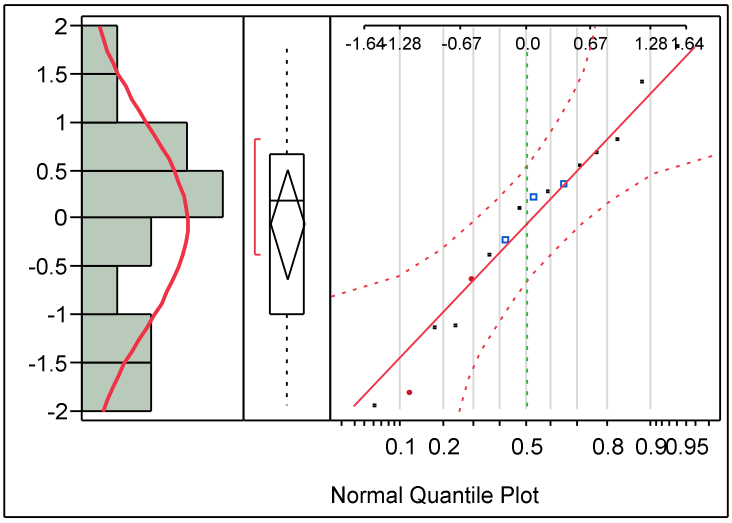

Normal(-0.0551,1.06609)

Quantiles

100.0%	maximum	1.795
99.5%		1.795

97.5%		1.795
90.0%		1.534
75.0%	quartile	0.658
50.0%	median	0.177
25.0%	quartile	-0.987
10.0%		-1.842
2.5%		-1.943
0.5%		-1.943
0.0%	minimum	-1.943

Moments

Mean	-0.055082
Std Dev	1.0660885
Std Err Mean	0.2665221
Upper 95% Mean	0.5129967
Lower 95% Mean	-0.62316
N	16

Fitted Normal
Parameter Estimates

Type	Parameter	Estimate	Lower 95%	Upper 95%
Location	μ	-0.055082	-0.62316	0.5129967
Dispersion	σ	1.0660885	0.7875247	1.6499758

-2log(Likelihood) = 46.4539152050714

Goodness-of-Fit Test

Shapiro-Wilk W Test

W	Prob<W
0.971824	0.8672

Note: Ho = The data is from the Normal distribution. Small p-values reject Ho.

Fit Y by X Group
Oneway Analysis of Studentized Resid P doped I median By CHF3

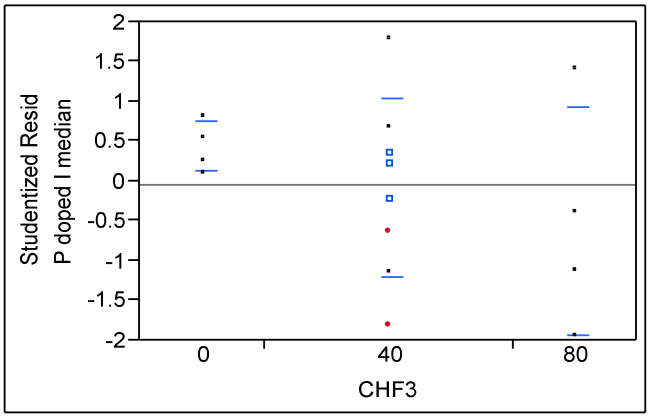

Tests that the Variances are Equal

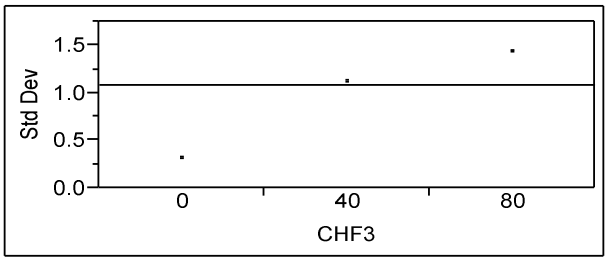

Level	Count	Std Dev	MeanAbsDif to Mean	MeanAbsDif to Median
0	4	0.314106	0.248980	0.248980
40	8	1.120236	0.857513	0.857513
80	4	1.433277	1.023192	1.023192

Test	F Ratio	DFNum	DFDen	Prob > F
O'Brien[.5]	1.1416	2	13	0.3493
Brown-Forsythe	1.7311	2	13	0.2155
Levene	1.8410	2	13	0.1977
Bartlett	2.3475	2	.	0.0956

Warning: Small sample sizes. Use Caution.

Welch's Test

Welch Anova testing Means Equal, allowing Std Devs Not Equal

F Ratio	DFNum	DFDen	Prob > F
1.3327	2	6.2748	0.3293

Oneway Analysis of Studentized Resid P doped I median By source power

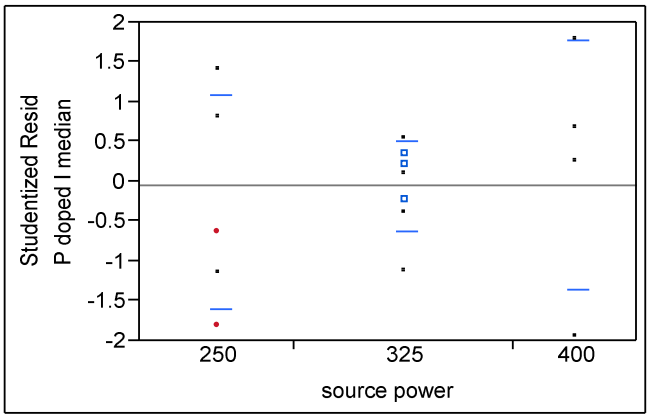

Tests that the Variances are Equal

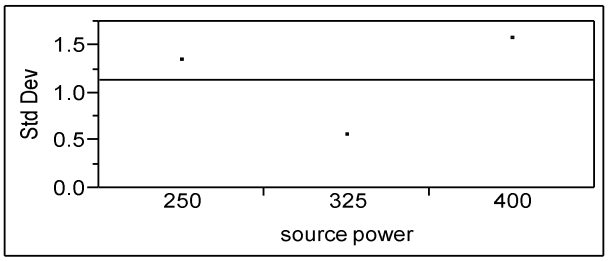

Level	Count	Std Dev	MeanAbsDif to Mean	MeanAbsDif to Median
250	5	1.346987	1.106871	1.136725
325	7	0.567066	0.436220	0.428919
400	4	1.568838	1.073659	1.038646

Test	F Ratio	DFNum	DFDen	Prob > F
O'Brien[.5]	1.6974	2	13	0.2213
Brown-Forsythe	1.9222	2	13	0.1856
Levene	2.4493	2	13	0.1251
Bartlett	2.1927	2	.	0.1116

Warning: Small sample sizes. Use Caution.

Welch's Test

Welch Anova testing Means Equal, allowing Std Devs Not Equal

F Ratio	DFNum	DFDen	Prob > F
0.0992	2	5.3553	0.9072

Oneway Analysis of Studentized Resid P doped I median By He/O2

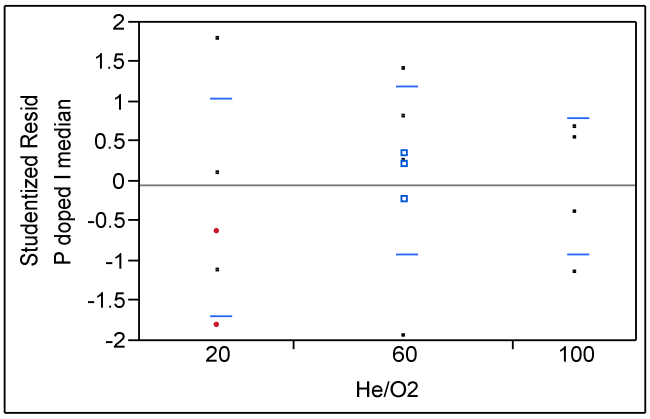

Tests that the Variances are Equal

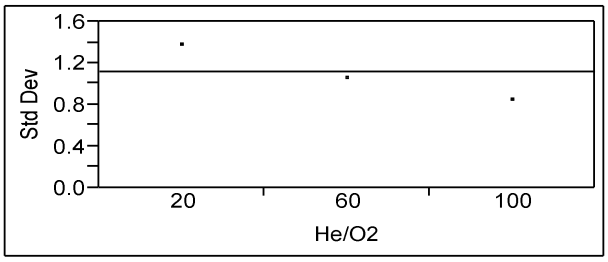

Level	Count	Std Dev	MeanAbsDif to Mean	MeanAbsDif to Median
20	5	1.374882	1.022950	1.061821
60	7	1.053707	0.695321	0.654586
100	4	0.854822	0.690162	0.690162

Test	F Ratio	DFNum	DFDen	Prob > F
O'Brien[.5]	0.3750	2	13	0.6945
Brown-Forsythe	0.5163	2	13	0.6085
Levene	0.4117	2	13	0.6709
Bartlett	0.3591	2	.	0.6983

Warning: Small sample sizes. Use Caution.

Welch's Test

Welch Anova testing Means Equal, allowing Std Devs Not Equal

F Ratio	DFNum	DFDen	Prob > F
0.1935	2	7.666	0.8280

Bivariate Fit of Studentized Resid P doped I median By P starting thickness

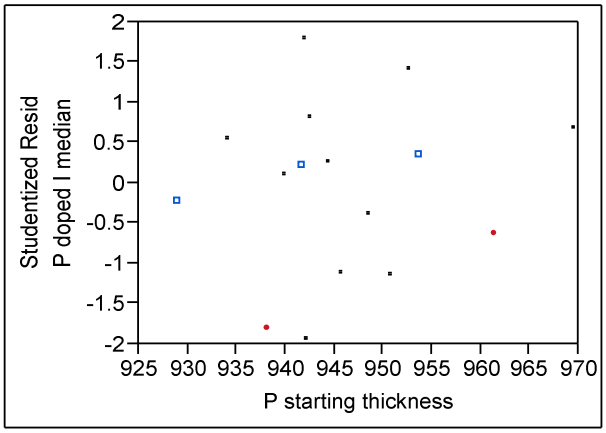

Response As doped I median
Actual by Predicted Plot

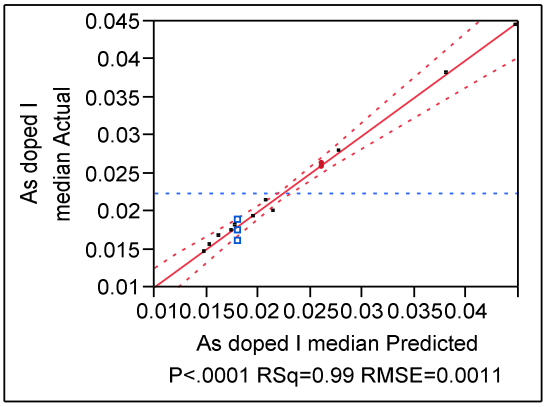

Summary of Fit

RSquare	0.993199
RSquare Adj	0.982996
Root Mean Square Error	0.001103
Mean of Response	0.022441
Observations (or Sum Wgts)	16

Analysis of Variance

Source	DF	Sum of Squares	Mean Square	F Ratio
Model	9	0.00106571	0.000118	97.3511
Error	6	0.00000730	1.216e-6	**Prob > F**
C. Total	15	0.00107300		<.0001*

Parameter Estimates

Term	Estimate	Std Error	t Ratio	Prob>|t|
Intercept	0.0179464	0.000452	39.73	<.0001*
CHF3(0,80)	0.0067773	0.000602	11.26	<.0001*
CHF3*source power	0.0145185	0.00066	22.00	<.0001*
CHF3*He/O2	-0.004831	0.000707	-6.83	0.0005*
He/O2*He/O2	0.0081418	0.000693	11.75	<.0001*
CHF3*As starting thickness	0.0279342	0.001298	21.52	<.0001*
He/O2*As starting thickness	-0.005541	0.001315	-4.21	0.0056*
CHF3*He/O2*As starting thickness	0.0333202	0.002042	16.31	<.0001*
source power*He/O2*As starting thickness	0.0054968	0.000739	7.43	0.0003*
He/O2*He/O2*As starting thickness	-0.011108	0.001537	-7.23	0.0004*

Effect Tests

Source	Nparm	DF	Sum of Squares	F Ratio	Prob > F
CHF3(0,80)	1	1	0.00015431	126.8665	<.0001*
CHF3*source power	1	1	0.00058890	484.1549	<.0001*
CHF3*He/O2	1	1	0.00005680	46.6952	0.0005*
He/O2*He/O2	1	1	0.00016790	138.0355	<.0001*
CHF3*As starting thickness	1	1	0.00056319	463.0192	<.0001*
He/O2*As starting thickness	1	1	0.00002159	17.7528	0.0056*
CHF3*He/O2*As starting thickness	1	1	0.00032374	266.1617	<.0001*
source power*He/O2*As starting thickness	1	1	0.00006723	55.2692	0.0003*

Source	Nparm	DF	Sum of Squares	F Ratio	Prob > F
He/O2*He/O2*As starting thickness	1	1	0.00006353	52.2305	0.0004*

Residual by Predicted Plot

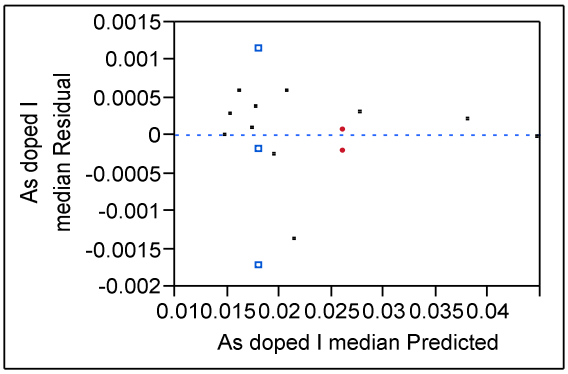

Press

Press	Press RMSE
0.0000926861	0.00240684

Distributions

Studentized Resid As doped I median

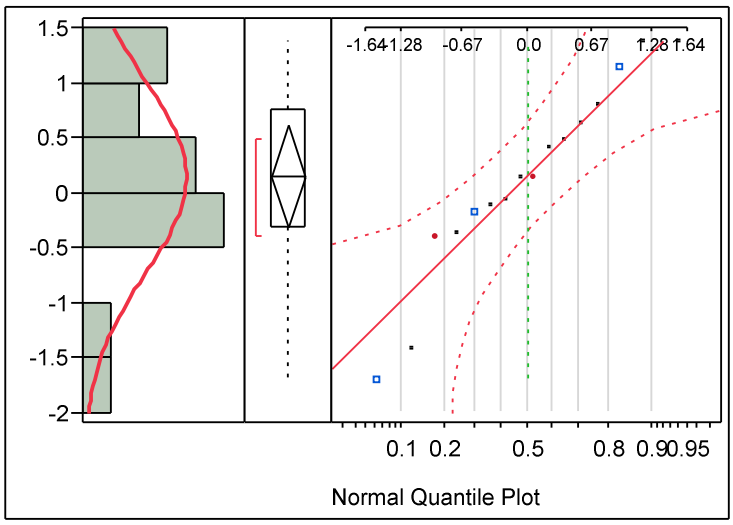

Normal(0.14801,0.87181)

Quantiles

100.0%	maximum	1.378
99.5%		1.378
97.5%		1.378
90.0%		1.375
75.0%	quartile	0.763

50.0%	median	0.141
25.0%	quartile	-0.308
10.0%		-1.489
2.5%		-1.683
0.5%		-1.683
0.0%	minimum	-1.683

Moments

Mean	0.148006
Std Dev	0.87181
Std Err Mean	0.2179525
Upper 95% Mean	0.6125608
Lower 95% Mean	-0.316549
N	16

Fitted Normal
Parameter Estimates

Type	Parameter	Estimate	Lower 95%	Upper 95%
Location	μ	0.148006	-0.316549	0.6125608
Dispersion	σ	0.87181	0.6440103	1.3492927

-2log(Likelihood) = 40.0161516385079

Goodness-of-Fit Test

Shapiro-Wilk W Test

W	Prob<W
0.943777	0.3979

Note: Ho = The data is from the Normal distribution. Small p-values reject Ho.

Fit Y by X Group
Oneway Analysis of Studentized Resid As doped I median By CHF3

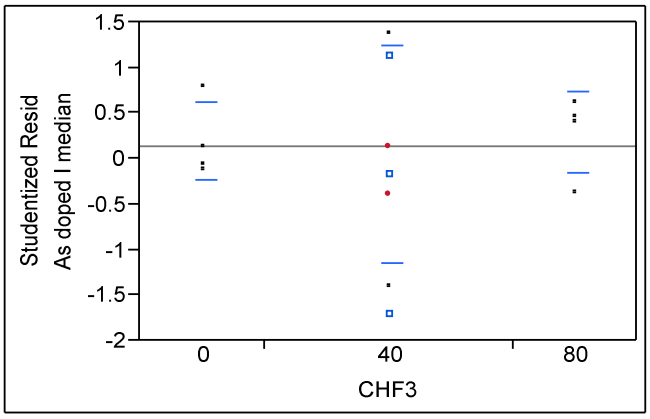

Tests that the Variances are Equal

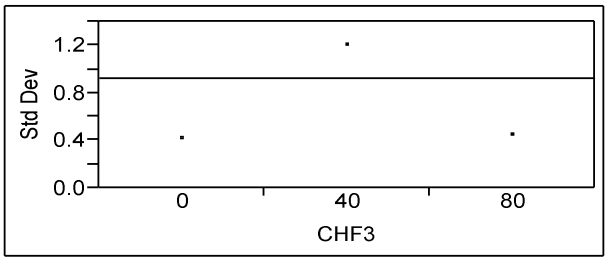

Level	Count	Std Dev	MeanAbsDif to Mean	MeanAbsDif to Median
0	4	0.421939	0.3059250	0.2783581
40	8	1.201807	0.9612537	0.9612537
80	4	0.443184	0.3254948	0.2621421

Test	F Ratio	DFNum	DFDen	Prob > F
O'Brien[.5]	3.0381	2	13	0.0827
Brown-Forsythe	3.5723	2	13	0.0580
Levene	3.5617	2	13	0.0584
Bartlett	2.4900	2	.	0.0829

Warning: Small sample sizes. Use Caution.

Welch's Test

Welch Anova testing Means Equal, allowing Std Devs Not Equal

F Ratio	DFNum	DFDen	Prob > F
0.1302	2	8.3503	0.8796

Oneway Analysis of Studentized Resid As doped I median By source power

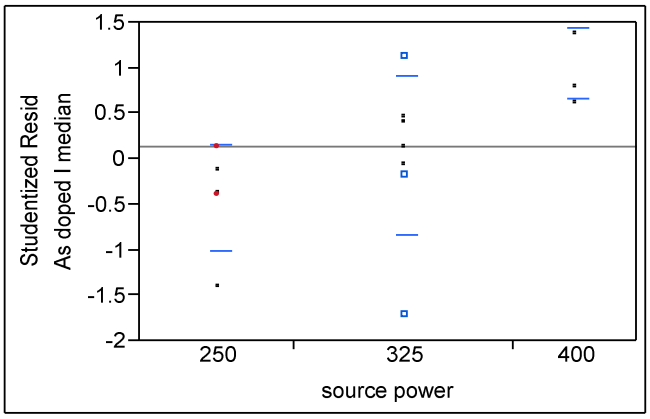

Tests that the Variances are Equal

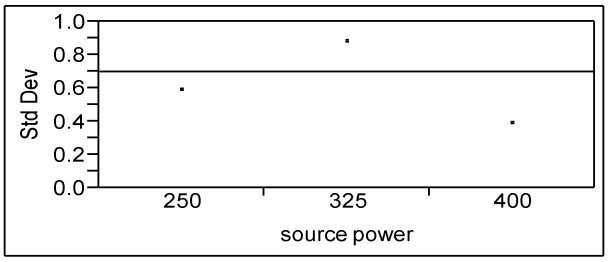

Level	Count	Std Dev	MeanAbsDif to Mean	MeanAbsDif to Median
250	5	0.5891937	0.3928205	0.3702429
325	7	0.8770239	0.5789705	0.5928192
400	4	0.3853823	0.3280823	0.3280823

Test	F Ratio	DFNum	DFDen	Prob > F
O'Brien[.5]	0.5300	2	13	0.6008
Brown-Forsythe	0.5043	2	13	0.6153
Levene	0.4284	2	13	0.6604
Bartlett	1.0856	2	.	0.3377

Warning: Small sample sizes. Use Caution.

Welch's Test

Welch Anova testing Means Equal, allowing Std Devs Not Equal

F Ratio	DFNum	DFDen	Prob > F
10.2663	2	8.5487	0.0053*

Oneway Analysis of Studentized Resid As doped I median By He/O2

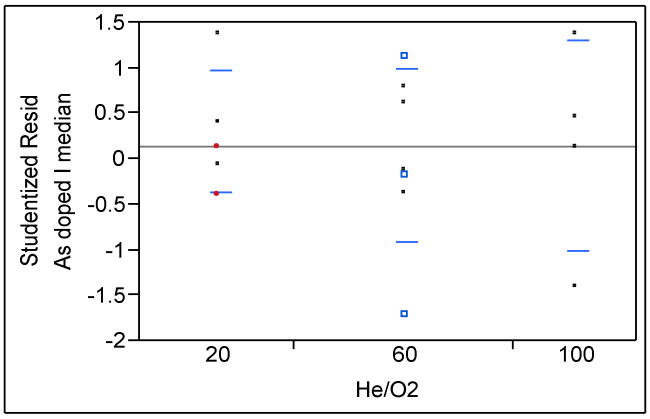

Tests that the Variances are Equal

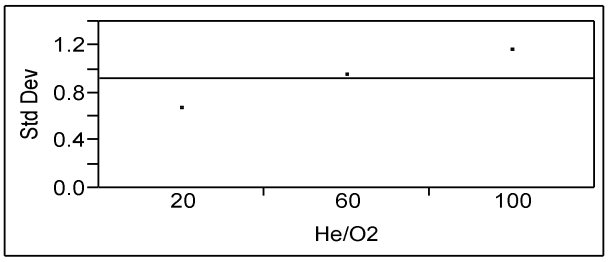

Level	Count	Std Dev	MeanAbsDif to Mean	MeanAbsDif to Median
20	5	0.668748	0.4781849	0.4865939
60	7	0.946903	0.7075795	0.6925224
100	4	1.159938	0.7807165	0.7807165

Test	F Ratio	DFNum	DFDen	Prob > F
O'Brien[.5]	0.4815	2	13	0.6284
Brown-Forsythe	0.2993	2	13	0.7463
Levene	0.3770	2	13	0.6932
Bartlett	0.4728	2	.	0.6233

Warning: Small sample sizes. Use Caution.

Welch's Test

Welch Anova testing Means Equal, allowing Std Devs Not Equal

F Ratio	DFNum	DFDen	Prob > F
0.1434	2	7.0424	0.8689

Bivariate Fit of Studentized Resid As doped I median By As starting thickness

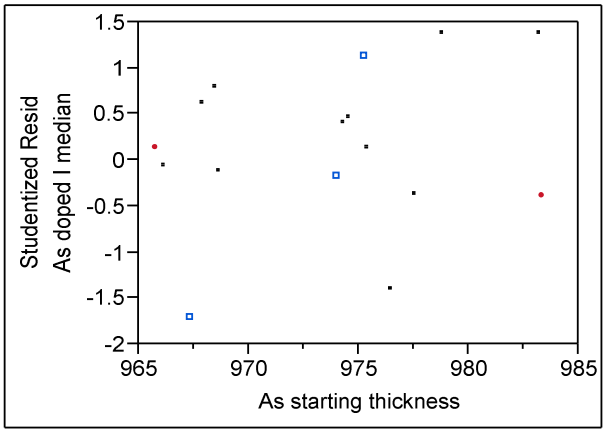

Response Sb doped I median
Actual by Predicted Plot

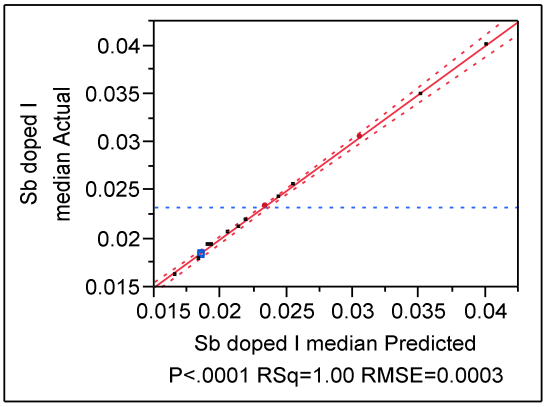

Summary of Fit

RSquare	0.999228
RSquare Adj	0.99807
Root Mean Square Error	0.000293
Mean of Response	0.023198
Observations (or Sum Wgts)	16

Analysis of Variance

Source	DF	Sum of Squares	Mean Square	F Ratio
Model	9	0.00066860	0.000074	862.9289
Error	6	0.00000052	8.609e-8	**Prob > F**
C. Total	15	0.00066912		<.0001*

Parameter Estimates

Term	Estimate	Std Error	t Ratio	Prob>|t|
Intercept	0.0184928	0.000165	111.94	<.0001*
CHF3(0,80)	0.0070002	0.000154	45.42	<.0001*
CHF3*CHF3	0.0140141	0.000294	47.67	<.0001*
CHF3*source power	0.0025243	0.000234	10.78	<.0001*
He/O2*He/O2	0.0083209	0.000227	36.67	<.0001*
source power*Sb starting thickness	-0.003431	0.00018	-19.05	<.0001*
CHF3*CHF3*Sb starting thickness	-0.08841	0.001404	-62.96	<.0001*
CHF3*source power*Sb starting thickness	-0.131897	0.002186	-60.33	<.0001*
source power*source power*Sb starting thickness	-0.073259	0.001215	-60.28	<.0001*
He/O2*He/O2*Sb starting thickness	0.0660363	0.001221	54.08	<.0001*

Effect Tests

Source	Nparm	DF	Sum of Squares	F Ratio	Prob > F
CHF3(0,80)	1	1	0.00017758	2062.761	<.0001*
CHF3*CHF3	1	1	0.00019562	2272.317	<.0001*
CHF3*source power	1	1	0.00001001	116.2416	<.0001*
He/O2*He/O2	1	1	0.00011578	1344.920	<.0001*
source power*Sb starting thickness	1	1	0.00003123	362.7338	<.0001*
CHF3*CHF3*Sb starting thickness	1	1	0.00034121	3963.427	<.0001*
CHF3*source power*Sb starting thickness	1	1	0.00031331	3639.424	<.0001*
source power*source power*Sb starting thickness	1	1	0.00031281	3633.590	<.0001*

Source	Nparm	DF	Sum of Squares	F Ratio	Prob > F
He/O2*He/O2*Sb starting thickness	1	1	0.00025181	2924.971	<.0001*

Residual by Predicted Plot

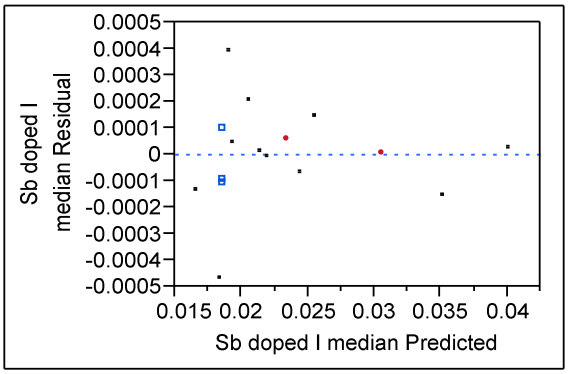

Press

Press	Press RMSE
0.0000320594	0.00141552

Distributions
Studentized Resid Sb doped I median

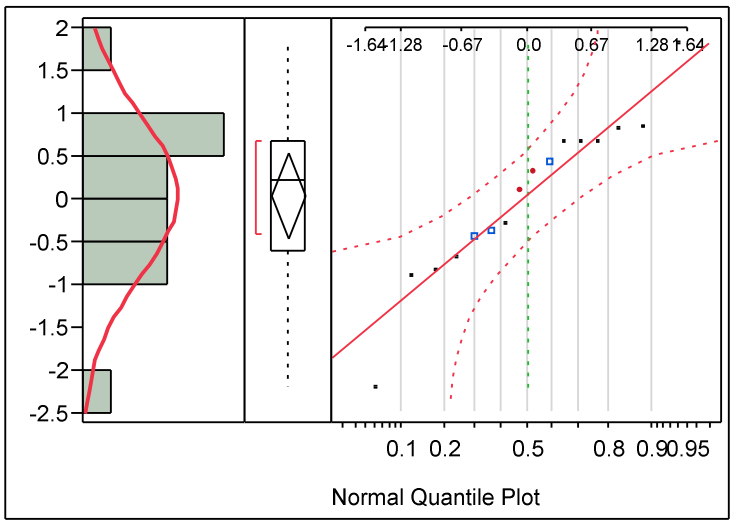

Normal(0.04733,0.94875)

Quantiles

100.0%	maximum	1.819
99.5%		1.819
97.5%		1.819
90.0%		1.135
75.0%	quartile	0.678

50.0%	median	0.212
25.0%	quartile	-0.611
10.0%		-1.278
2.5%		-2.203
0.5%		-2.203
0.0%	minimum	-2.203

Moments

Mean	0.0473298
Std Dev	0.9487474
Std Err Mean	0.2371868
Upper 95% Mean	0.5528816
Lower 95% Mean	-0.458222
N	16

Fitted Normal
Parameter Estimates

Type	Parameter	Estimate	Lower 95%	Upper 95%
Location	μ	0.0473298	-0.458222	0.5528816
Dispersion	σ	0.9487474	0.7008443	1.468368

-2log(Likelihood) = 42.7224260052492

Goodness-of-Fit Test

Shapiro-Wilk W Test

W	Prob<W
0.953742	0.5512

Note: Ho = The data is from the Normal distribution. Small p-values reject Ho.

Fit Y by X Group
Oneway Analysis of Studentized Resid Sb doped I median By CHF3

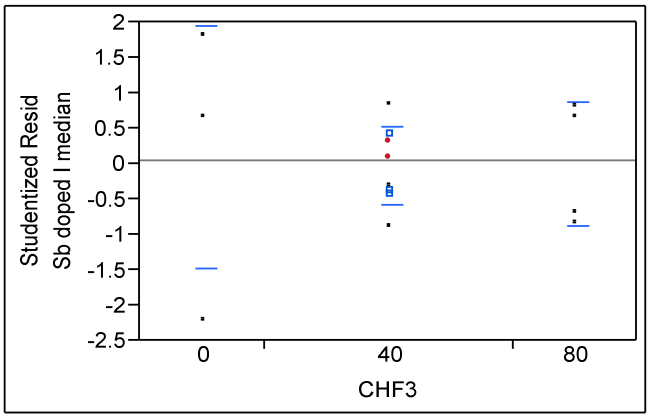

Tests that the Variances are Equal

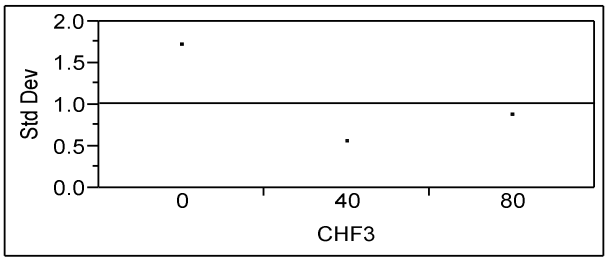

Level	Count	Std Dev	MeanAbsDif to Mean	MeanAbsDif to Median
0	4	1.716875	1.222872	1.005361
40	8	0.556525	0.455941	0.455941
80	4	0.872535	0.752022	0.752022

Test	F Ratio	DFNum	DFDen	Prob > F
O'Brien[.5]	1.9559	2	13	0.1809
Brown-Forsythe	0.8961	2	13	0.4320
Levene	3.0185	2	13	0.0838
Bartlett	2.7054	2	.	0.0668

Warning: Small sample sizes. Use Caution.

Welch's Test

Welch Anova testing Means Equal, allowing Std Devs Not Equal

F Ratio	DFNum	DFDen	Prob > F
0.0421	2	4.8834	0.9591

Oneway Analysis of Studentized Resid Sb doped I median By source power

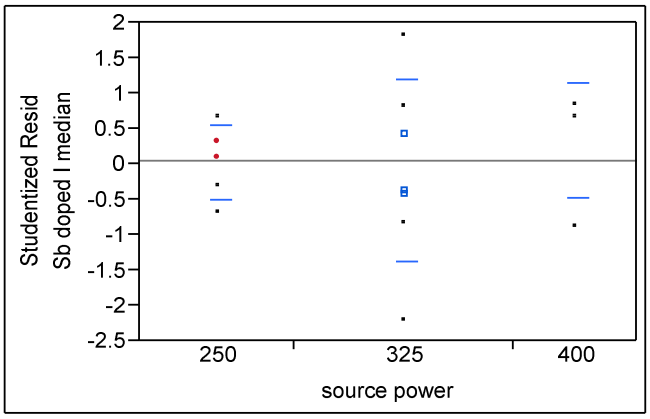

Tests that the Variances are Equal

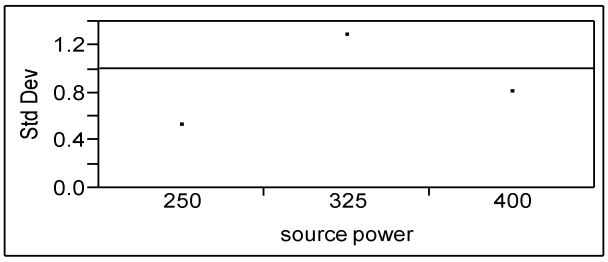

Level	Count	Std Dev	MeanAbsDif to Mean	MeanAbsDif to Median
250	5	0.527368	0.4088096	0.4345255
325	7	1.287628	0.9692165	0.9406204
400	4	0.810664	0.6052330	0.4307909

Test	F Ratio	DFNum	DFDen	Prob > F
O'Brien[.5]	1.0698	2	13	0.3714
Brown-Forsythe	1.0689	2	13	0.3717
Levene	1.5127	2	13	0.2567
Bartlett	1.5180	2	.	0.2192

Warning: Small sample sizes. Use Caution.

Welch's Test

Welch Anova testing Means Equal, allowing Std Devs Not Equal

F Ratio	DFNum	DFDen	Prob > F
0.2586	2	7.425	0.7788

Oneway Analysis of Studentized Resid Sb doped I median By He/O2

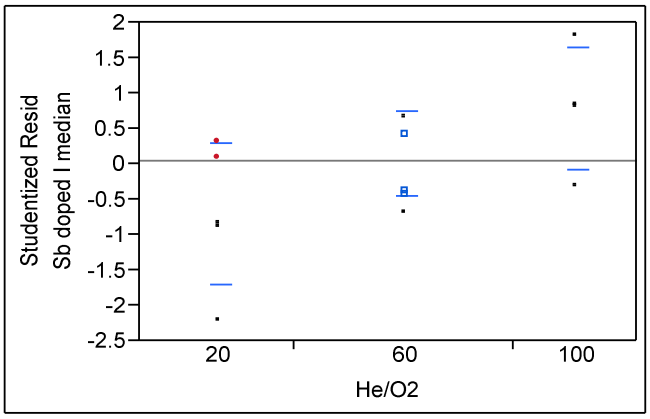

Tests that the Variances are Equal

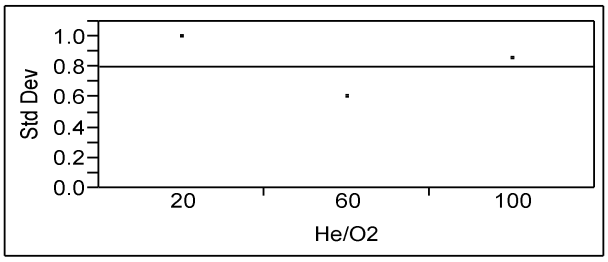

Level	Count	Std Dev	MeanAbsDif to Mean	MeanAbsDif to Median
20	5	0.9986673	0.7265982	0.7130405
60	7	0.6024282	0.5391821	0.5293767
100	4	0.8623312	0.5453209	0.5307382

Test	F Ratio	DFNum	DFDen	Prob > F
O'Brien[.5]	0.7120	2	13	0.5088
Brown-Forsythe	0.2121	2	13	0.8116
Levene	0.3027	2	13	0.7439
Bartlett	0.5844	2	.	0.5574

Warning: Small sample sizes. Use Caution.

Welch's Test

Welch Anova testing Means Equal, allowing Std Devs Not Equal

F Ratio	DFNum	DFDen	Prob > F
2.6466	2	6.4015	0.1453

Bivariate Fit of Studentized Resid Sb doped I median By Sb starting thickness

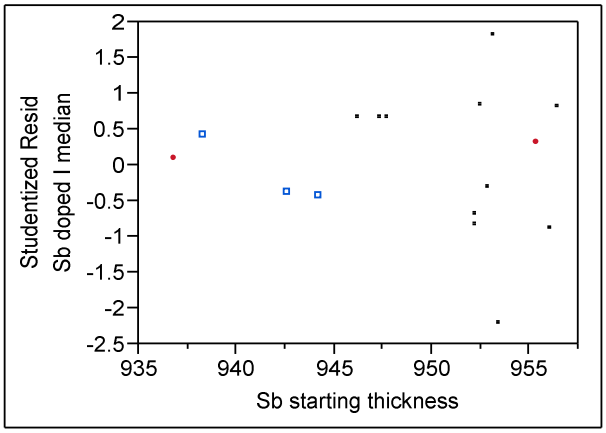

Response B doped I median
Actual by Predicted Plot

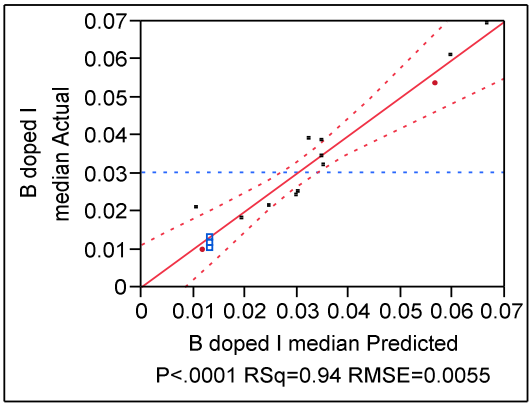

Summary of Fit

RSquare	0.944943
RSquare Adj	0.908238
Root Mean Square Error	0.005516
Mean of Response	0.03029
Observations (or Sum Wgts)	16

Analysis of Variance

Source	DF	Sum of Squares	Mean Square	F Ratio
Model	6	0.00469971	0.000783	25.7443
Error	9	0.00027383	0.000030	**Prob > F**
C. Total	15	0.00497354		<.0001*

Parameter Estimates

Term	Estimate	Std Error	t Ratio	Prob>|t|
Intercept	0.0130334	0.003058	4.26	0.0021*
CHF3*CHF3	0.0250061	0.003175	7.88	<.0001*
CHF3*source power	0.0289288	0.003756	7.70	<.0001*
source power*source power	-0.021924	0.004863	-4.51	0.0015*
source power*B starting thickness	-0.017991	0.002909	-6.18	0.0002*
CHF3*CHF3*B starting thickness	-0.065518	0.007719	-8.49	<.0001*
He/O2*He/O2*B starting thickness	0.0572969	0.005874	9.75	<.0001*

Effect Tests

Source	Nparm	DF	Sum of Squares	F Ratio	Prob > F
CHF3*CHF3	1	1	0.00188735	62.0317	<.0001*
CHF3*source power	1	1	0.00180514	59.3296	<.0001*
source power*source power	1	1	0.00061827	20.3207	0.0015*
source power*B starting thickness	1	1	0.00116360	38.2443	0.0002*
CHF3*CHF3*B starting thickness	1	1	0.00219174	72.0362	<.0001*
He/O2*He/O2*B starting thickness	1	1	0.00289516	95.1555	<.0001*

Residual by Predicted Plot

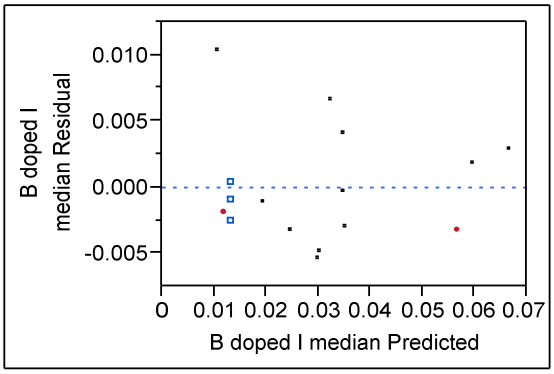

Press

Press	Press RMSE
0.0008659337	0.00735669

Distributions
Studentized Resid B doped I median

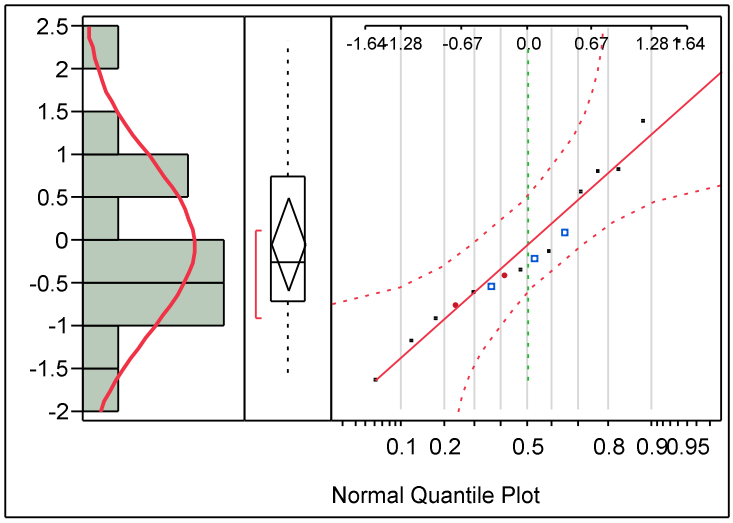

Normal(-0.0427,1.01284)

Quantiles

100.0%	maximum	2.318
99.5%		2.318
97.5%		2.318
90.0%		1.676
75.0%	quartile	0.737
50.0%	median	-0.268
25.0%	quartile	-0.719
10.0%		-1.316

2.5%		-1.627
0.5%		-1.627
0.0%	minimum	-1.627

Moments

Mean	-0.042721
Std Dev	1.0128379
Std Err Mean	0.2532095
Upper 95% Mean	0.4969825
Lower 95% Mean	-0.582424
N	16

Fitted Normal
Parameter Estimates

Type	Parameter	Estimate	Lower 95%	Upper 95%
Location	μ	-0.042721	-0.582424	0.4969825
Dispersion	σ	1.0128379	0.7481883	1.5675603

-2log(Likelihood) = 44.8142312207707

Goodness-of-Fit Test

Shapiro-Wilk W Test

W	Prob<W
0.956700	0.6025

Note: Ho = The data is from the Normal distribution. Small p-values reject Ho.

Fit Y by X Group
Oneway Analysis of Studentized Resid B doped I median By CHF3

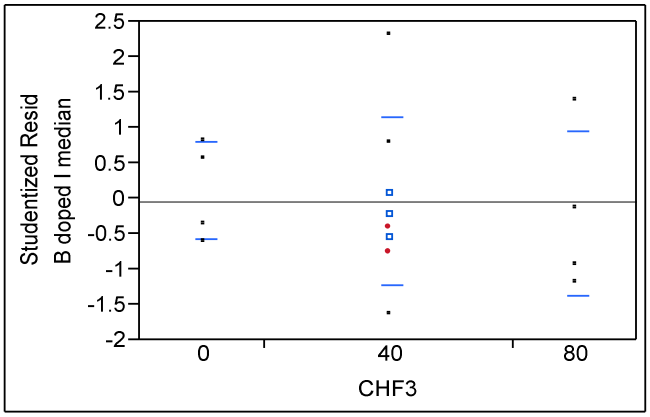

Tests that the Variances are Equal

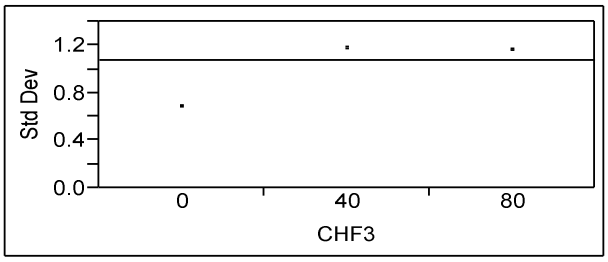

Level	Count	Std Dev	MeanAbsDif to Mean	MeanAbsDif to Median
0	4	0.692392	0.5853754	0.5853754
40	8	1.177268	0.8306001	0.7924599
80	4	1.162071	0.8450443	0.8450443

Test	F Ratio	DFNum	DFDen	Prob > F
O'Brien[.5]	0.3078	2	13	0.7403
Brown-Forsythe	0.1497	2	13	0.8624
Levene	0.2246	2	13	0.8019
Bartlett	0.4655	2	.	0.6278

Warning: Small sample sizes. Use Caution.

Welch's Test

Welch Anova testing Means Equal, allowing Std Devs Not Equal

F Ratio	DFNum	DFDen	Prob > F
0.1048	2	7.0635	0.9019

Oneway Analysis of Studentized Resid B doped I median By source power

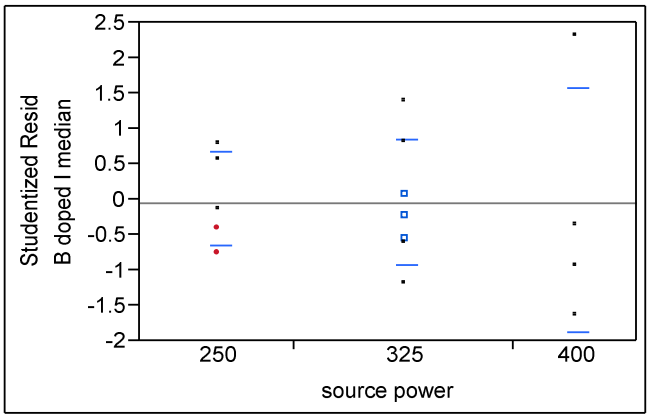

Tests that the Variances are Equal

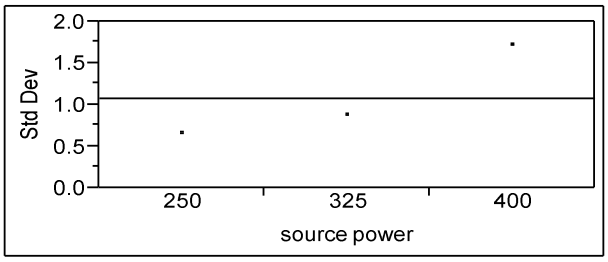

Level	Count	Std Dev	MeanAbsDif to Mean	MeanAbsDif to Median
250	5	0.652959	0.532501	0.563629
325	7	0.887436	0.685771	0.703494
400	4	1.722257	1.230494	1.128768

Test	F Ratio	DFNum	DFDen	Prob > F
O'Brien[.5]	1.6008	2	13	0.2391
Brown-Forsythe	0.7492	2	13	0.4921
Levene	1.6804	2	13	0.2243
Bartlett	1.6740	2	.	0.1875

Warning: Small sample sizes. Use Caution.

Welch's Test

Welch Anova testing Means Equal, allowing Std Devs Not Equal

F Ratio	DFNum	DFDen	Prob > F
0.0149	2	6.5515	0.9852

Oneway Analysis of Studentized Resid B doped I median By He/O2

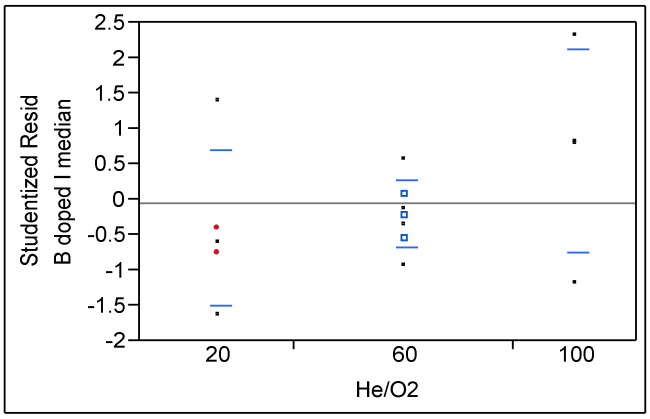

Tests that the Variances are Equal

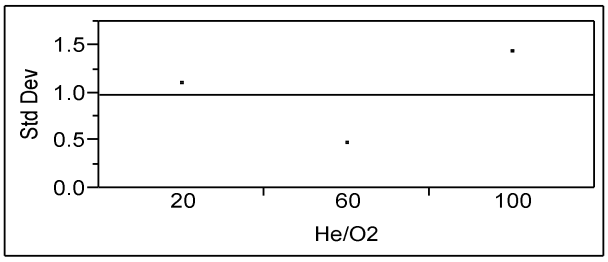

Level	Count	Std Dev	MeanAbsDif to Mean	MeanAbsDif to Median
20	5	1.109219	0.7207286	0.7041148
60	7	0.468789	0.3346988	0.3422950
100	4	1.436123	0.9356586	0.8821733

Test	F Ratio	DFNum	DFDen	Prob > F
O'Brien[.5]	1.3158	2	13	0.3017
Brown-Forsythe	0.8602	2	13	0.4458
Levene	1.1909	2	13	0.3350
Bartlett	2.4747	2	.	0.0842

Warning: Small sample sizes. Use Caution.

Welch's Test

Welch Anova testing Means Equal, allowing Std Devs Not Equal

F Ratio	DFNum	DFDen	Prob > F
0.7456	2	5.2968	0.5185

Bivariate Fit of Studentized Resid B doped I median By B starting thickness

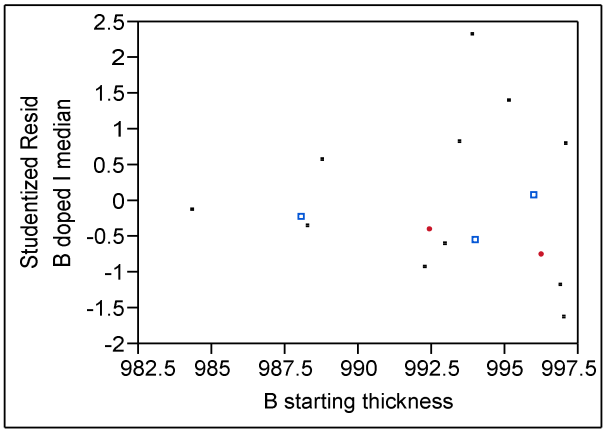

Response undoped I median
Actual by Predicted Plot

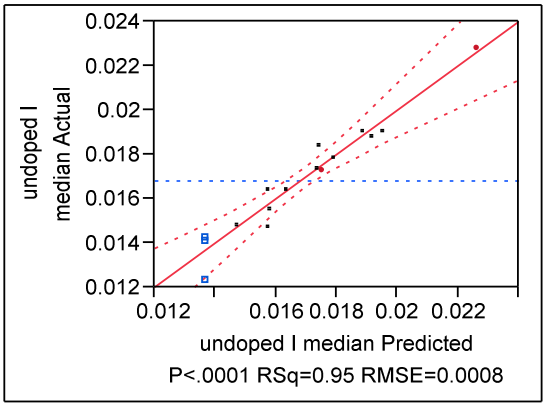

Summary of Fit

RSquare	0.946112
RSquare Adj	0.910187
Root Mean Square Error	0.00076
Mean of Response	0.016836
Observations (or Sum Wgts)	16

Analysis of Variance

Source	DF	Sum of Squares	Mean Square	F Ratio
Model	6	0.00009122	0.000015	26.3357
Error	9	0.00000520	5.773e-7	**Prob > F**
C. Total	15	0.00009642		<.0001*

Parameter Estimates

Term	Estimate	Std Error	t Ratio	Prob>|t|
Intercept	0.013637	0.00036	37.88	<.0001*
He/O2(20,100)	-0.002218	0.000544	-4.08	0.0028*
source power*source power	0.0031845	0.000399	7.98	<.0001*
He/O2*undoped starting thickness	0.0041089	0.000771	5.33	0.0005*
CHF3*source power*undoped starting thickness	-0.002339	0.000715	-3.27	0.0097*
source power*He/O2*undoped starting thickness	0.004708	0.000536	8.78	<.0001*
He/O2*He/O2*undoped starting thickness	0.0038588	0.000513	7.53	<.0001*

Effect Tests

Source	Nparm	DF	Sum of Squares	F Ratio	Prob > F
He/O2(20,100)	1	1	0.00000960	16.6298	0.0028*
source power*source power	1	1	0.00003679	63.7298	<.0001*
He/O2*undoped starting thickness	1	1	0.00001641	28.4305	0.0005*
CHF3*source power*undoped starting thickness	1	1	0.00000618	10.6997	0.0097*
source power*He/O2*undoped starting thickness	1	1	0.00004452	77.1132	<.0001*
He/O2*He/O2*undoped starting thickness	1	1	0.00003269	56.6329	<.0001*

Residual by Predicted Plot

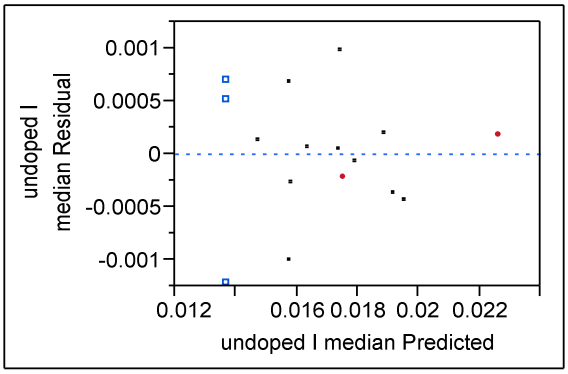

Press

Press	Press RMSE
0.0000146335	0.00095634

Distributions
Studentized Resid undoped I median

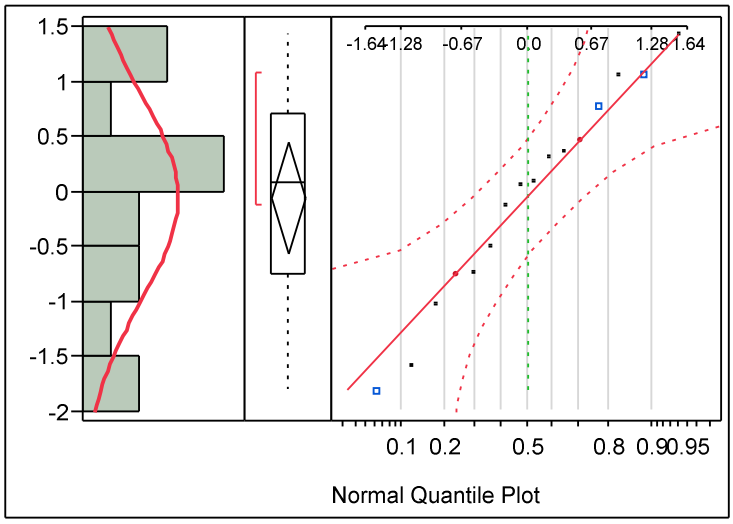

Normal(-0.0508,0.94628)

Quantiles

100.0%	maximum	1.424
99.5%		1.424
97.5%		1.424
90.0%		1.182
75.0%	quartile	0.708
50.0%	median	0.083
25.0%	quartile	-0.742
10.0%		-1.638

2.5%		-1.791
0.5%		-1.791
0.0%	minimum	-1.791

Moments

Mean	-0.05081
Std Dev	0.9462757
Std Err Mean	0.2365689
Upper 95% Mean	0.4534248
Lower 95% Mean	-0.555045
N	16

Fitted Normal
Parameter Estimates

Type	Parameter	Estimate	Lower 95%	Upper 95%
Location	μ	-0.05081	-0.555045	0.4534248
Dispersion	σ	0.9462757	0.6990185	1.4645426

-2log(Likelihood) = 42.6389519260855

Goodness-of-Fit Test

Shapiro-Wilk W Test

W	Prob<W
0.968086	0.8067

Note: Ho = The data is from the Normal distribution. Small p-values reject Ho.

Fit Y by X Group
Oneway Analysis of Studentized Resid undoped I median By CHF3

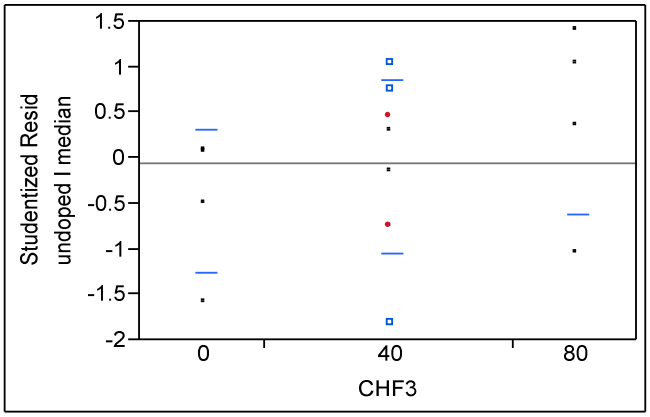

Tests that the Variances are Equal

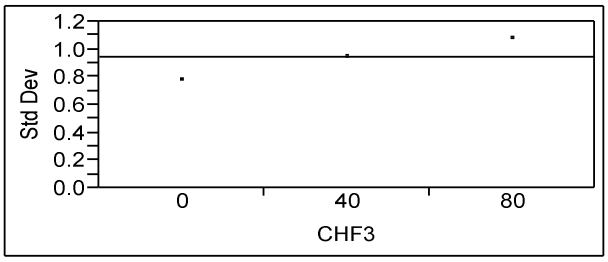

Level	Count	Std Dev	MeanAbsDif to Mean	MeanAbsDif to Median
0	4	0.780399	0.5569391	0.5569391
40	8	0.952911	0.7571838	0.7571838
80	4	1.077582	0.7824121	0.7824121

Test	F Ratio	DFNum	DFDen	Prob > F
O'Brien[.5]	0.2051	2	13	0.8171
Brown-Forsythe	0.2039	2	13	0.8181
Levene	0.2536	2	13	0.7797
Bartlett	0.1373	2	.	0.8717

Warning: Small sample sizes. Use Caution.

Welch's Test

Welch Anova testing Means Equal, allowing Std Devs Not Equal

F Ratio	DFNum	DFDen	Prob > F
0.8981	2	6.5972	0.4519

Oneway Analysis of Studentized Resid undoped I median By source power

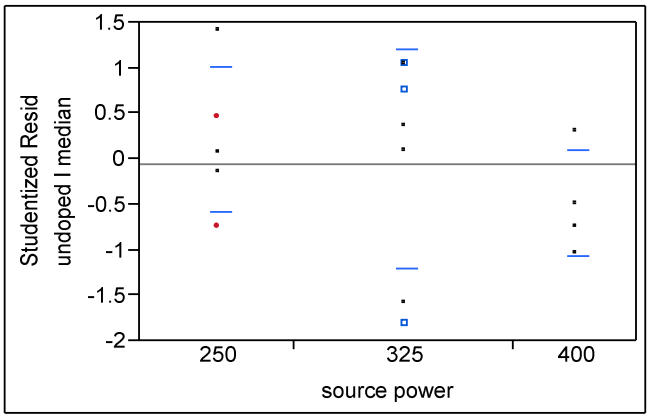

Tests that the Variances are Equal

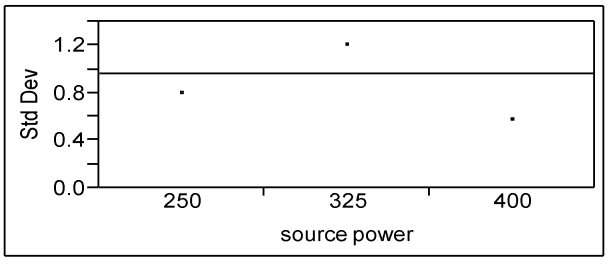

Level	Count	Std Dev	MeanAbsDif to Mean	MeanAbsDif to Median
250	5	0.803549	0.5823299	0.5932392
325	7	1.205721	0.9628266	0.9236141
400	4	0.577587	0.4015302	0.3977364

Test	F Ratio	DFNum	DFDen	Prob > F
O'Brien[.5]	1.3226	2	13	0.3000
Brown-Forsythe	0.9668	2	13	0.4060
Levene	1.6994	2	13	0.2210
Bartlett	0.9374	2	.	0.3916

Warning: Small sample sizes. Use Caution.

Welch's Test

Welch Anova testing Means Equal, allowing Std Devs Not Equal

F Ratio	DFNum	DFDen	Prob > F
1.1488	2	8.5445	0.3615

Oneway Analysis of Studentized Resid undoped I median By He/O2

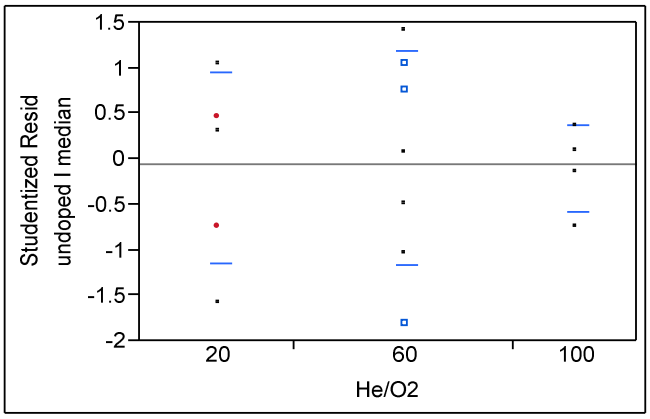

Tests that the Variances are Equal

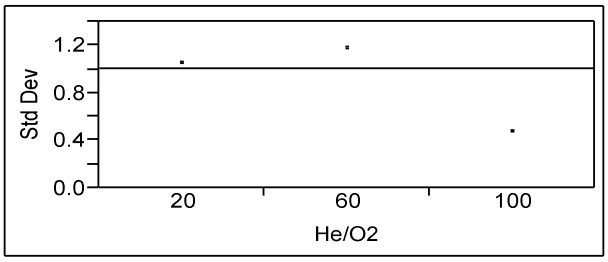

Level	Count	Std Dev	MeanAbsDif to Mean	MeanAbsDif to Median
20	5	1.050681	0.8506888	0.796972
60	7	1.176346	0.9504063	1.021575
100	4	0.472210	0.3337752	0.333775

Test	F Ratio	DFNum	DFDen	Prob > F
O'Brien[.5]	1.2043	2	13	0.3313
Brown-Forsythe	2.1119	2	13	0.1606
Levene	2.2121	2	13	0.1490
Bartlett	1.1416	2	.	0.3193

Warning: Small sample sizes. Use Caution.

Welch's Test

Welch Anova testing Means Equal, allowing Std Devs Not Equal

F Ratio	DFNum	DFDen	Prob > F
0.0224	2	8.1806	0.9779
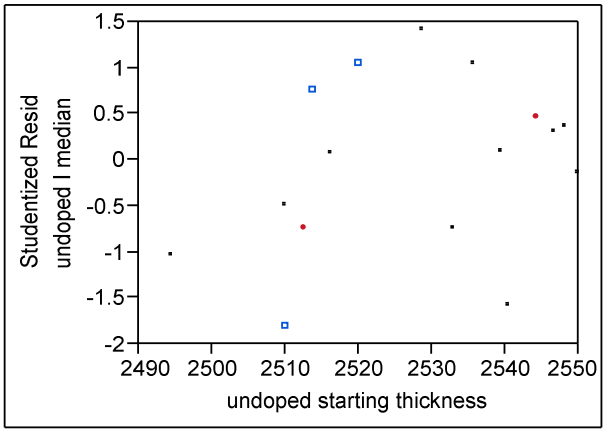
Bivariate Fit of Studentized Resid undoped I median By undoped starting thickness